Volume 97, Number 5, September–October 1992
Journal of Research of the National Institute of Standards and Technology

Contents

Articles

The Characterization of a Piston Displacement-Type Flowmeter Calibration Facility and the Calibration and Use of Pulsed Output Type Flowmeters — **G. E. Mattingly** — 509

A General Waveguide Circuit Theory — **Roger B. Marks and Dylan F. Williams** — 533

Resistive Liquid-Vapor Surface Sensors for Liquid Nitrogen and Hydrogen — **J. D. Siegwarth, R. O. Voth, and S. M. Snyder** — 563

Fracture Toughness of Advanced Ceramics at Room Temperature — **George D. Quinn, Jonathan Salem, Isa Bar-on, Kyu Cho, Michael Foley, and Ho Fang** — 579

Errata

Erratum: Optical Calibration of a Submicrometer Magnification Standard — **Jon Geist, Barbara Belzer, Mary Lou Miller, and Peter Roitman** — 609

Conference Reports

Data Administration Management Association Symposium — **Judith Newton** — 611

News Briefs

GENERAL DEVELOPMENTS — 615

Consortium to Develop Ceramic Machining Data
Industry/NIST to Improve Advanced Polymer Systems
Frequency Calibrations Using LORAN-C Explained

Technology Centers Created for California, Minnesota — 616
CRADA Partners to Study Concrete Failure During Fire
Have You Heard? New Noise Standard Developed
"Superconductivity Report" Now Available on VHS
Two Views of Protein Puzzles Prove Better Than One

New Biosensor Consortium Seeks Members 617
NIST/Industry to Study Cryptography Infrastructures
Standards Needs on Diamond Films Cited
Critical Technologies Dominate ATP Proposals

Exploring Math and Manufacturing in the Classroom 618
Mobile Machinery Group Defines Standards Issues
Proposals Sought for Precision Measurement Grants
Security Training Compendium Available from NIST
Fifteen Inventions Now Available for Licensing

NIST and Auto Industry Cooperate on Welding Research 619
NIST to Lead Development of New IEEE Standard for Power-Frequency Field-Measuring Instruments
NIST Scientist Shares Patent and R&D 100 Award on Diamond-Turning of Ferrous Metals

Non-Methane Organic Compound Gas Standards Developed to Support Atmospheric Measurements of Auto Emissions 620
Carbonyl Sulfide Measured in Automotive Emissions Using Tunable Diode Laser Absorption Spectroscopy
Gold-Platinum Thermocouples: A New High-Stability, High-Accuracy Industrial Transfer Standard

Dark-State Vibrational Quasi-Continuum Probed with Molecular "Searchlight" Technique 621
Magnetism in Nanometer-Sized Iron Particles
Third Industry Workshop Identifies Challenges for Improved Polymer Composite Processing

Pulsed Laser Deposition of Nanocomposite Thin Films 622
Gas-Coupled Acoustic Microscope
High-Resolution Experimental Mechanics by E-Beam Moiré
Non-Intrusive Technique Developed for Surface Cooling Studies

NIST Develops Fingerprint Classification System for the Federal Bureau of Investigation (FBI) 623
Raster Graphics Validation Program Developed
Hardware Description Language Approved as FIPS
Validated Products List Expanded
Guidance on Computer Security Training Published

77th National Conference on Weights and Measures Meets in Nashville 624
NIST Transfers Measurement Expertise to Power Electronics Industry
NIST Assists Industry with Measurements of Media and Heads for High-Density Magnetic Recording

NIST Helps Assure Lottery Fairness 625
Robot Chauffeur
Rate of Key Physiological Reaction Determined
NIST Participates in X-Ray Beamline Development at the Advanced Photon Source

Subpicosecond Probes of Laser Surface Heating 626
Using Lasers to Confine Atoms on a Lattice of Light
Broadband Picosecond Infrared Spectroscopy of Solution-Phase Photochemistry

NIST/NPL Intercomparison of Radiance Temperature Scales 627
NIST Strongly Represented at Solid State Dosimetry Conference
Anomalies in Resonance Ionization Mass Spectrometry Measurements Explained

NIST Develops Transport Standards for Phase Noise Measurement Systems 628
Synchronization Interface Standards for Telecommunications Networks
Enhanced Magnetocaloric Effect in Iron-Doped Garnet Materials

Small-Angle Neutron Scattering Studies of Nanostructured Ceramics 629
NIST Recommends Moisture Control Measures for Manufactured Housing
NIST and Taiwan Collaborate on Open Systems Interconnection (OSI) Routing Protocols
Spatial Data Transfer Standard Approved as Federal Information Processing Standard (FIPS)

New Publication Focuses on Graphical User Interfaces (GUIs) 630
Catalog of Code Sets Updated
Mainframe Computer Tapes Subject of New Publication

STANDARD REFERENCE MATERIALS 630

Accurate DNA Fingerprints Assured by New SRM
Standard Reference Material 1842, X-Ray Stage Calibration Board

Standard Reference Material 676, Alumina Internal Standard for Quantitative Analysis by X-Ray Powder Diffraction 631
Standard Reference Material 659, Particle Size Distribution Standard for Sedigraph Calibration
Standard Reference Material 2579—Lead Paint Film on Mylar Sheet for Portable X-Ray Fluorescence Analyzers

STANDARD REFERENCE DATA 631

Chemical Kinetics PC Database Expanded

PC Database Available on Transient Molecules 632

Calendar 633

Volume 97, Number 5, September–October 1992
Journal of Research of the National Institute of Standards and Technology

[J. Res. Natl. Inst. Stand. Technol. 97, 509 (1992)]

The Characterization of a Piston Displacement-Type Flowmeter Calibration Facility and the Calibration and Use of Pulsed Output Type Flowmeters

Volume 97 Number 5 September–October 1992

G. E. Mattingly

National Institute of Standards and Technology,
Gaithersburg, MD 20899

Critical measurement performance of fluid flowmeters requires proper and quantified verification data. These data should be generated using calibration and traceability techniques established for these verification purposes. In these calibration techniques, the calibration facility should be well-characterized and its components and performance properly traced to pertinent higher standards. The use of this calibrator to calibrate flowmeters should be appropriately established and the manner in which the calibrated flowmeter is used should be specified in accord with the conditions of the calibration.

These three steps: 1) characterizing the calibration facility itself, 2) using the characterized facility to calibrate a flowmeter, and 3) using the calibrated flowmeter to make a measurement are described and the pertinent equations are given for an encoded-stroke, piston displacement-type calibrator and a pulsed output flowmeter. It is concluded that, given these equations and proper instrumentation of this type of calibrator, very high levels of performance can be attained and, in turn, these can be used to achieve high fluid flow rate measurement accuracy with pulsed output flowmeters.

Key words: flow measurement; fluid meter characterization; meter performance; output flowmeter; turbine flowmeter; volumetric calibrator.

Accepted: June 29, 1992

Contents

Glossary 510
1. Introduction 512
2. Calibrator Characterization 513
   2.1 Geometrical Determination at Reference Conditions 513
   2.2 Geometrical Determination at Non-Reference Conditions 514
   2.3 Determination of Calibrator Constant by the Draw Technique in Reference Conditions 515
   2.4 Determination of Calibrator Constant by the Draw Technique in Non-Reference Conditions 516
3. Calibrator Use in Calibrating a Turbine-Type Flowmeter 518
   3.1 Reference Conditions 518
   3.2 Non-Reference Conditions 521
4. Using a Turbine-Type Flowmeter to Make a Measurement 522
   4.1 Reference Conditions 522
   4.2 Non-Reference Conditions 523
5. Discussion 523
6. Conclusions 525
7. Appendix A. Cross-Sectional Area Changes in the Cylinder of the Calibrator 526
8. Appendix B. Turbine Meter Data Processing 527
9. Appendix C. Equations Summary 529
10. References 531

Glossary

Symbol	*Description*	*Dimensions*
A_{C0}, A_C	Calibrator cross-sectional areas at reference and non-reference conditions, respectively. Over-bars, where used, denote averages over piston stroke length.	L^2
A_{t0}, A_t	Cross-sectional areas of tubes connected to calibrator piston at reference and non-reference conditions, respectively.	L^2
C_0, C	Circumference of cylindrical body in unstressed and stressed conditions, respectively.	L
d_0, d	Diameter of rod connected to calibrator piston at reference and non-reference conditions, respectively.	L
D_0, D	Inner diameter of calibrator cylinder at reference and non-reference conditions, respectively.	L
D_{M0}, D_M	Inside diameter of flowmeter at reference and non-reference conditions, respectively.	L
d_{M0}, d_M	Outside diameter of turbine propeller at reference and non-reference conditions, respectively.	L
D_{C0}, D_C	Inside diameter of the cylinder of the calibrator at reference and non-reference conditions, respectively.	L
D_{T0}, D_T	Outside diameter of the tube connected to the calibrator piston at reference and non-reference conditions, respectively.	L
E_C	Modulus of elasticity of the material of the calibrator cylinder at pertinent conditions..	F/L^2
E_F	Modulus of elasticity of the fluid at pertinent conditions.	F/L^2
E_M	Modulus of elasticity of the material of the body of the flowmeter at pertinent conditions.	F/L^2
E_T	Modulus of elasticity of the material of the tube connected to the calibrator piston at pertinent conditions.	F/L^2
f_{E0}, f_E	Frequency of pulses from encoder at reference and non-reference conditions, respectively.	pulses/t
f_{M0}, f_M	Frequencies of pulses from the flowmeter at reference and non-reference conditions respectively.	pulses/t
K_{E0}, K_E	Encoder constant at reference and non-reference conditions, respectively.	pulses/L
K_{C0}, K_C	Calibrator constant at reference and non-reference conditions, respectively.	$pulses/L^3$
K'_C	Calibrator constant in pulses per fluid volume collected in collection vessel.	$pulses/L^3$
K_{M0}, K_M	Meter factor at reference and non-reference conditions, respectively. Where over-bars are used is meant the average value over a Reynolds number range.	$pulses/L^3$
L_{E0}, L_E	Piston stroke length at reference and non-reference conditions, respectively.	L

$N_{\mathrm{E0}}, N_{\mathrm{E}}$	Totalized encoder pulses at reference and non-reference conditions, respectively.	pulses
$N_{\mathrm{M0}}, N_{\mathrm{M}}$	Totalized meter pulses at reference and non-reference conditions, respectively.	pulses
$\boldsymbol{n}$	Unit vector.	dimensionless
$P_{\mathrm{C0}}, P_{\mathrm{C}}$	Pressure of the fluid in the cylinder of the calibrator at reference and non-reference conditions, respectively.	F/L^2
$P_{\mathrm{COLL'T}}$	Pressure of fluid in collection vessel.	F/L^2
$P_{\mathrm{M0}}, P_{\mathrm{M}}$	Pressure of the fluid in the flowmeter at reference and non-reference conditions, respectively.	F/L^2
Re	Reynolds number.	dimensionless
Ro	Roshko number.	dimensionless
St	Strouhal number. Where over-bars are used is meant the average value over a Reynolds number range.	dimensionless
S	Surface area of control volume.	L^2
T_{r}	Temperature of meter rotor or of rod connected to calibrator piston.	°C (°F)
$T_{\mathrm{C0}}, T_{\mathrm{C}}$	Temperature of the cylinder of the calibrator at reference and non-reference conditions, respectively.	°C (°F)
$T_{\mathrm{E0}}, T_{\mathrm{E}}$	Temperature of the encoder at reference and non-reference conditions, respectively.	°C (°F)
t_{C0}	Thickness of the cylinder of the calibrator at reference conditions.	L
t_{T0}	Thickness of the tube connected to the to the calibrator piston at reference conditions.	L

t	Time.	t
$T_{\mathrm{COLL'T}}$	Temperature of fluid in collection vessel.	°C (°F)
$T_{\mathrm{M0}}, T_{\mathrm{M}}$	Temperature of the flowmeter at reference and non-reference conditions, respectively.	°C (°F)
t_{M0}	Thickness of the body of the flowmeter at reference conditions.	L
U_{M0}	Average velocity of fluid through the flowmeter at reference conditions.	L/t
$V_{\mathrm{C0}}, V_{\mathrm{C}}$	Calibrator piston displacement at reference and non-reference conditions, respectively.	L^3
$\boldsymbol{v}$	Fluid velocity vector.	L/t
V	Control volume.	L^3
$\dot{V}_{\mathrm{C0}}, V_{\mathrm{C0}}$	Fluid volumetric flowrate and volume, respectively, in the calibrator cylinder at reference condition.	$L^3/t, L^3$
$\dot{V}_{\mathrm{COLL'T0}}$, $V_{\mathrm{COLL'T0}}$	Fluid volumetric flowrate and volume, respectively, into collection vessel at reference conditions.	$L^3/t, L^3$
$\dot{V}_{\mathrm{C}}, V_{\mathrm{C}}$	Fluid volumetric flowrate and volume, respectively, in the calibrator cylinder at non-reference conditions.	$L^3/t, L^3$
$\dot{V}_{\mathrm{M0}}, V_{\mathrm{M0}}$	Fluid volumetric flowrate and volume, respectively, in flowmeter at reference conditions.	$L^3/t, L^3$
$\dot{V}_{\mathrm{M}}, V_{\mathrm{M}}$	Fluid volumetric flowrate and volume, respectively, through the flowmeter at non-reference conditions.	$L^3/t, L^3$
α_{E}	Linear expansion coefof the encoder at pertinent conditions.	$^{\circ}\mathrm{C}^{-1}$ ($^{\circ}\mathrm{F}^{-1}$)
α_{C}	Linear expansion coefficient for the material of the calibrator cylinder at pertinent conditions.	$^{\circ}\mathrm{C}^{-1}$ ($^{\circ}\mathrm{F}^{-1}$)

α_F	Linear expansion coefficient of fluid.	$°C^{-1}$ ($°F^{-1}$)
α_M	Linear expansion coefficient for the material of the body of the flowmeter.	$°C^{-1}$ ($°F^{-1}$)
α_r	Linear expansion coefficient for the material of rotor or turbine wheel.	$°C^{-1}$ ($°F^{-1}$)
β	Ratio of turbine propeller diameter to inside diameter of meter.	dimensionless
ϵ_θ	Hoop strain in cylindrical body.	dimensionless
ρ	Fluid density.	M/L^3
ρ_{C0}, ρ_C	Fluid density in calibrator at reference and non-reference conditions, respectively.	M/L^3
$\rho_{COLL'T0}$, $\rho_{COLL'T}$	Density of fluid collected in collection vessel at reference and non-reference conditions, respectively.	M/L^3
ρ_{M0}, ρ_M	Density of the fluid in the flowmeter at reference and non-reference conditions, respectively.	M/L^3
σ_θ	Hoop stress in cylindrical body.	F/L^2
ν_0, ν	Fluid kinematic viscosity at reference and non-reference conditions, respectively.	L^2/t
μ_0, μ	Fluid absolute viscosity at reference and non-reference conditions, respectively.	Ft/L^2

1. Introduction

Fluid flowmeter calibration methods use a variety of techniques; they include wide ranges of operational parameters; they cover wide ranges of precision and accuracy, [1-3]. Increasingly, the diverse improvements being sought for flowmeters are producing corresponding improvements in the characteristics of flowmeter calibration systems. Of these systems, the piston displacement-type calibrator offers advantages such as compactness, mobility, efficient change of fluid, and prospects for state-of-the-art performance characteristics.

To characterize the performance of a piston displacement calibrator, which produces a pulsed output signal that is proportional to the volumetric flowrate, the objective is, generally, to determine the "pulses per volume displacement" ratio (or its reciprocal) where the pulse output is assumed to come from a source such as a linear encoder. This pulse output is also assumed to be proportional to the piston displacement. High accuracy calibrator performance requires examination of these assumptions.

A number of techniques can be used to determine volumetric displacement. It is assumed in what follows that the displaced fluid is a liquid, but the principles apply to gases or mixtures of gases and liquids as well. It is also assumed that both temperature and pressure effects on all the components of the piston displacement system, the cylinder, encoder, and fluid should be considered in order that high accuracy performance can be achieved.

Depending upon the desired uncertainty level for the performance of the calibrator, one or more of the pressure and temperature effects on the components of the system may be negligible. When this is so, it may be permissible to disregard such effects to simplify data processing or to reduce the size of the controlling software for the system. Alternatively, and more preferably, all effects can be included in computer software. In this way, the terms which are negligible will not influence the results when higher levels of uncertainty, i.e., less precise performance can be tolerated or is desirable from benefits vs. costs perspectives. More importantly, where high accuracy is required, more of the figures available via the software capabilities can be accepted as significant.

The volumetric-type calibrator system, using encoded piston displacement as both the flow source and as the flow determination scheme, is sketched in Fig. 1. The piston motion produces and measures a fluid volumetric flowrate that is proportional to the encoder frequency. The piston in the cylinder has a seal that is assumed to seal perfectly for all piston velocities. The corresponding fluid flowrate through the meter and the meter output frequency enable a calibration of the flowmeter. Using these elements, three steps are considered.

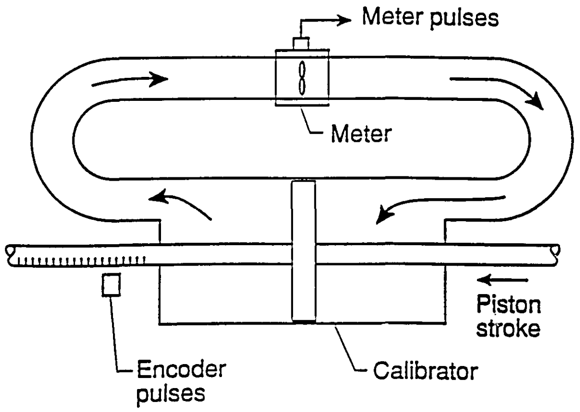

Fig. 1. Sketch of encoded-stroke calibrator in operation.

The first step is determining the calibrator factor which is an "encoder pulses per volume displaced" ratio (or its reciprocal) at the defined set of reference conditions. These results can be obtained experimentally in a number of ways: (1) by physical measurement, (2) by the so-called "draw" technique, or (3) by using a transfer standard such as a single or, preferably, a tandem arrangement of calibrated turbine flowmeters.

The second step is the use of the characterized calibrator to calibrate a pulsed-output flowmeter such as a turbine meter or other device where the meter factor is a "pulses per volume" quantity or its reciprocal. This process is done with one or more selected fluids and at specified conditions. In what follows turbine flowmeters will be considered. Conventionally, turbine meter results are produced in the form of a meter factor which has units of pulses per volume or volume per pulses (referenced to specified conditions). This meter factor is determined over the desired ranges of fluid conditions and flowrate expressed in terms of a ratio of inertial-to-viscous effects such as a Reynolds number, or equivalent parameter.

The third step is the use of the characterized turbine flowmeter to calculate a fluid flowrate under actual conditions of use. The results can be produced with respect to specified reference conditions or to the actual conditions, depending upon the needs of the meter operator.

The purpose of this paper is to describe these three steps and give the pertinent relationships that pertain to each procedure. The resulting equations are intended to be used in the software packages used with these types of calibrators and metering units. In this way, it is expected that the measurement performance of both the calibrators and the metering units can be maximized.

2. Calibrator Characterization

2.1 Geometrical Determination at Reference Conditions

To perform the required measurements at reference conditions and then calculate the calibrator factor in units of pulses per fluid volume displaced, the system analyzed is that sketched in Fig. 2. The assumption of reference conditions is a conceptual situation that is impractical to achieve precisely but is done solely for convenience, as will be clear in what follows. For the conditions selected to be the reference conditions which are denoted by the "0" subscript, a specific piston stroke produces a displacement volume, V_{C0}, and the encoder produces the corresponding number of pulses, N_{E0}. A list of symbols is given in the Glossary. The reference conditions of calibrator temperature and the pressure in the calibrator are T_{C0} and P_{C0}, respectively. These properties are assumed to be constant and steady in the calibrator volume. These conditions should be monitored, quantified, and assessed with respect to the performance level of the calibrator. Furthermore, the fluid inside and outside the calibrator is assumed to have the same temperature as the cylinder of the calibrator and no heat is being transferred to or from the calibrator. In all that follows, the reference conditions of T_0 and P_0 will be assumed to be the same for all components.

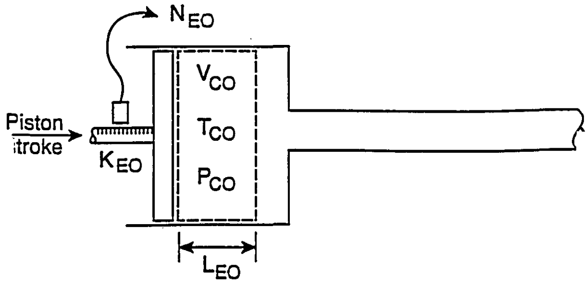

Fig. 2. Encoded-stroke calibrator configuration at reference conditions.

The specified piston stroke, L_{E0}, produces the pulse total, N_{E0}, where

$$N_{E0}=L_{E0}K_{E0}, \tag{1}$$

and K_{E0} is the encoder constant in pulses per length at the reference temperature condition, T_0. The calibration constant can be written

$$K_{C0}=\frac{N_{E0}}{V_{C0}}=\frac{L_{E0}K_{E0}}{\bar{A}_{C0}L_{E0}}=\frac{K_{E0}}{\bar{A}_{C0}}, \tag{2}$$

in units of pulses per volume, where, at the reference conditions, $\bar{A}_{C0}$ is the averaged cylinder cross-sectional area over the piston stroke, L_{E0}. This calibrator constant, K_{C0} is assumed to be constant over the operating range of the calibrator.

For the calibrator configuration shown in Fig. 1, the area $\bar{A}_{C0}$ is an annular one between the cylinder of the calibrator and the rod or tube attached to the piston. The precision with which K_{C0} is determined can be written using root-sum-square combinations of component precisions:

$$\frac{\Delta K_{C0}}{K_{C0}} < \left[\left(\frac{\Delta N_{E0}}{N_{E0}}\right)^2 + \left(\frac{\Delta V_{C0}}{V_{C0}}\right)^2\right]^{1/2}$$

$$= \left[\left(\frac{\Delta K_{E0}}{K_{E0}}\right)^2 + \left(\frac{\Delta \bar{A}_{C0}}{\bar{A}_{C0}}\right)^2\right]^{1/2}, \qquad (3)$$

where the numerators of the respective terms refer to the maximum errors of each of the component measurements. Equation (3) indicates that high levels of precision in K_{C0} can be attained when large pulse sums, N_{E0}, and large displaced volumes, V_{C0}, are used. Correspondingly, these precision levels can be achieved with accurate and sensitive linear encoders and accurately measured and large cross-sectional areas.

2.2 Geometrical Determination at Non-Reference Conditions

To perform the required measurements at non-reference temperature and pressure conditions, it is assumed that these conditions are constant and steady as shown in Fig. 3. For a specified piston stroke, L_E, the corresponding encoder pulse total, N_E, is

$$N_E = L_E K_E\,, \qquad (4)$$

where the encoder constant, K_E, is assumed to depend only on temperature according to

$$K_E = K_{E0}\,[1 - \alpha_E (T_E - T_{E0})\,, \qquad (5)$$

where α_E is the pertinent linear expansion coefficient for the encoder and T_E and T_{E0} are, respectively, the encoder temperatures at non-reference and reference conditions.

The cross-sectional area change of the calibrator cylinder that is produced by temperature, T_C, and internal fluid pressure, P_C, in excess of the reference values is analyzed in Appendix A. In what follows, it is assumed that the annular area contained between the calibrator cylinder and the rod or tube connected to the piston is changed with temperature in the usual way and the pressure effect is considered to enlarge only the cylinder of the calibrator. The pressure effect on the tube or rod is taken to be negligible. The cross-sectional area of the cylinder of the calibrator averaged over the stroke length is given, to first order in temperature and pressure separately, by

$$\bar{A}_C = \bar{A}_{C0}\,[1 + 2\alpha_C (T_C - T_0)]\left[1 + \frac{(P_C - P_0) D_{C0}}{t_{C0} E_C}\right], \qquad (6)$$

where α_C is the linear expansion coefficient for the material of the calibrator cylinder, D_{C0} and t_{C0} are, respectively, the inside diameter and wall thickness of the calibrator cylinder at reference conditions and E_C is the modulus of elasticity of the material of the calibrator cylinder. In Eq. (6) the compressive effects of the pressure in the cylinder on the rod attached to the piston are assumed negligible.

If it is assumed that the linear expansion coefficient of the cylinder material is $2 \times 10^{-5}\ ^\circ\mathrm{C}^{-1}$, a systematic temperature difference of only 2.5 °C would produce a corresponding systematic error of ±0.01% in the calibrator area. Similarly, if it is assumed that the modulus of elasticity for the calibrator material is 2×10^{11} Pa (2×10^6 atm) and if the calibrator has a diameter to thickness ratio of 20, a systematic pressure error of only 1 MPa (10 atm) will produce a systematic error of ±0.01% in the calibrator area. Such calibrator area errors will propagate through all of the successive relationships for calibrating and using meters, and these relationships will be further altered by additional temperature and pressure effects.

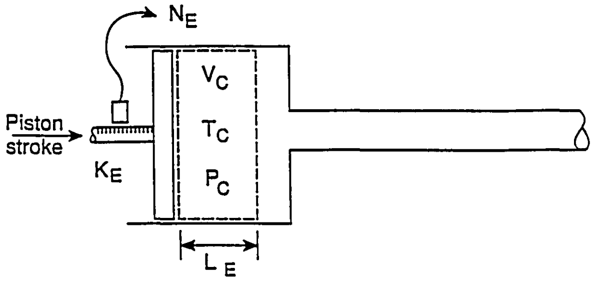

Fig. 3. Encoded-stroke calibrator configuration at non-reference conditions.

The calibrator constant, K_C, at non-reference conditions in units of pulses per volume can be written

$$K_C = \frac{N_E}{V_C}, \tag{7}$$

since V_C is the displacement at non-reference conditions. Therefore

$$K_C = \frac{K_E}{A_C}. \tag{8}$$

Combining Eq. (8) with Eqs. (2), (5), and (6) produces

$$K_C = \frac{K_{C0}\left[1-\alpha_E\left(T_E-T_0\right)\right]}{\left[1+2\alpha_C\left(T_C-T_0\right]\left[1+\frac{\left(P_C-P_0\right)D_{C0}}{t_{C0}E_C}\right]}, \tag{9}$$

or, to first order approximation:

$$K_{C0} \approx K_C \frac{\left[1+\alpha_E\left(T_E-T_0\right)\right]}{\left[1-2\alpha_C\left(T_C-T_0\right]\left[1-\frac{\left(P_C-P_0\right)D_{C0}}{t_{C0}E_C}\right]}. \tag{10}$$

For temperatures and pressures higher than reference conditions the calibrator constant, K_C, is less than the value at reference conditions. In both of the above geometrical methods for obtaining calibrator constants, fluid properties are not involved.

The value for K_{C0} given by Eqs. (2) or (10) should be put into the software that operates the displacement calibrator, together with pertinent material constants and component dimensions. Then the computation for the calibrator constant K_C at non-reference conditions can be done using appropriate measurements for encoder temperature, in addition to the pressure and temperature in the calibrator, as shown in Eq. (9). These values of K_{C0} or K_C will be used for the accurate calibrations of flowmeters.

2.3 Determination of Calibrator Constant by the Draw Technique at Reference Conditions

The configuration for the draw technique is shown in Fig. 4, where the piston stroke displaces an amount of fluid through a valve into the collection tank; the corresponding encoder pulses total N_{EO}. All temperatures and pressures are the reference values. In all that follows, it is assumed that the seal of the piston in the calibrator seals perfectly and is sufficiently pliant to continue to seal perfectly when changes in temperature and internal pressure occur and change the diameter of the cylinder of the calibrator. Applying conservation of mass principles to the constant volume shown in figure 4, we obtain:

$$\frac{\partial}{\partial t}\int_V \rho \, dV - \int_S \rho \boldsymbol{v} \cdot \boldsymbol{n} \, dS = 0, \tag{11}$$

where ρ is the fluid density, V is the control volume surrounded by the control surface, S,$\boldsymbol{v}$ is the fluid velocity vector, and $\boldsymbol{n}$ is the unit vector normal to S with positive direction pointing to the interior of V. When

$$\frac{\partial}{\partial t}\int_V \rho \, dV = 0, \tag{12}$$

there is no change of the mass within the control volume in time. This means the effects of fluid friction or of heat transfer are negligible or, taken in total, do not alter in time the mass contained within the control volume. Under such conditions, the inlet and outlet mass fluxes through the control surface, S are the same, that is

$$\rho_{C0}\dot{V}_{C0} = \rho_{\mathrm{COLL'T0}}\dot{V}_{\mathrm{COLL'T0}}, \tag{13}$$

where ρ_{C0} and $\rho_{\mathrm{COLL'T0}}$ are the fluid densities, respectively, in the calibrator and collection tank at the same reference conditions and therefore are equal. The quantities $\dot{V}_{C0}$ and $\dot{V}_{\mathrm{COLL'T0}}$ are the volumetric flowrates out of the calibrator and into the collection tank, respectively.

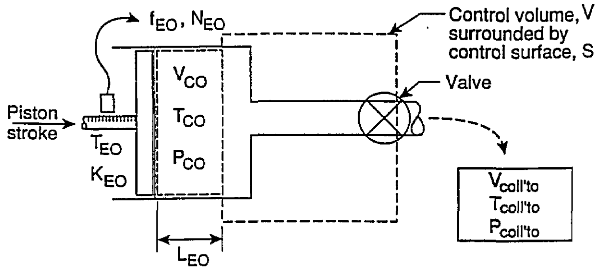

Fig. 4. Experimental arrangement for the draw technique at reference conditions.

Therefore, since the times of displacement and collection are assumed to be the same,

$$V_{C0} = V_{\mathrm{COLL'T0}}, \tag{14}$$

and the calibrator constant, in units of pulses per displacement volume can be written

$$K_{C0} = N_{E0}/V_{COLL'T0}\,, \qquad (15)$$

where

$$V_{COLL'T0} = \bar{A}_{C0} L_{E0}\,. \qquad (16)$$

Therefore, using Eq. (13)-(16), we obtain

$$K_{C0} = K_{E0}/\bar{A}_{C0}\,, \qquad (17)$$

in agreement with Eq. (2). Accordingly, results obtained via this procedure should duplicate those obtained via the geometrical measurement techniques.

It is generally assumed that the calibrator constant K_{C0} is independent of the piston speed or the fluid properties. If this assumption is not valid then it is necessary to characterize the dependence. This should be done in a manner analogous to the procedures used to characterize turbine meters as given below.

It should be noted that, for the control volume shown in Fig. 4, if

$$\frac{\partial}{\partial t}\int_V \rho \mathrm{d}V \neq 0\,, \qquad (18)$$

then the mass flux displaced in the cylinder of the calibrator is not equal to that delivered to the collection tank. Furthermore, if the fluid density in the control volume decreases because of a temperature rise then the mass flux to the collection tank would be more than that displaced in the calibrator cylinder. As will be seen below, this produces a turbine-type meter calibration result in pulses per volume units that is larger than it should be. Conversely, if the fluid density in the control volume increases, then the mass flux delivered to the collection vessel is less than that displaced in the calibrator cylinder. This produces a low calibration result for a turbine meter constant in pulses per volume units.

2.4 Determination of Calibrator Constant by the Draw Technique at Non-Reference Conditions

The configuration for the draw technique in non-reference conditions is shown in Fig. 5. As before, the piston stroke displaces a volume of fluid in the cylinder and the corresponding encoder pulses total N_E. The temperature and pressure of the fluid in the cylinder are T_C and P_C, respectively. Applying conservation of mass principles to the control volume in Fig. 5, for the condition where there is no change with time of the mass within the control volume, Eq. (11) and (12) indicate that

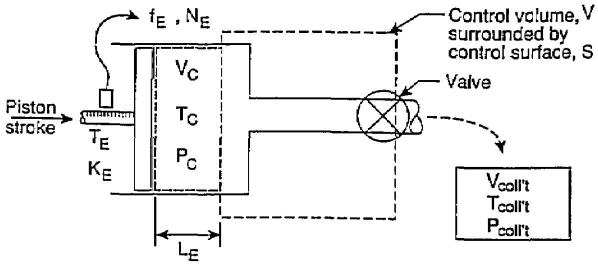

Fig. 5. Experimental arrangement for the draw technique at non-reference conditions.

$$\rho_C \dot{V}_C = \rho_{COLL'T} \dot{V}_{COLL'T}\,, \qquad (19)$$

or when the displacement and collected volumes are simultaneous

$$\rho_C V_C = \rho_{COLL'T} V_{COLL'T}\,, \qquad (20)$$

where ρ_C and $\rho_{COLL'T}$ are, respectively, the density of the fluid displaced within the cylinder of the calibrator and flowing from the valve and into the collection tank. The volume $V_{COLL'T}$ can be determined using volumetric or gravimetric techniques, or both. It is noted that constant conditions of temperature and pressure need to be maintained in the calibrator and in the collection vessel for accurate results.

With the volume $V_{COLL'T}$ determined, V_C can be computed via

$$V_C = (\rho_{COLL'T}/\rho_C)\, V_{COLL'T}\,, \qquad (21)$$

where, according to the definitions of fluid thermal expansion effects and compressibility, to first order in temperature and pressure, separately:

$$\frac{\rho_{COLL'T}}{\rho_C} = [1 - 3\alpha_F (T_{COLL'T} - T_C)]\left[1 + \frac{(P_{COLL'T} - P_C)}{E_F}\right], \qquad (22)$$

where α_F is the linear expansion coefficient for the fluid, the pressures $P_{COLL'T}$ and P_C are, respectively, those for the fluid passing from the valve into the collection tank and in the cylinder of the calibrator, and E_F is the modulus of elasticity of the fluid. It is noted that both α_F and E_F are dependent upon temperature and pressure for the specific fluid, but the values used here and in what follows are assumed to be averages taken over the appropriate ranges of temperature and pressure. It is also noted here that the reciprocal of the modulus of elasticity of the fluid is also the compressibility of the fluid.

In Eq. (22), it is noted that temperature and pressure effects have opposite signs in producing fluid density changes. However, when the temperature differences between the collection vessel and the calibrator are large and where the pressure in the calibrator is much larger than that in the collection vessel, the effects on the fluid can be significant.

If it is assumed that the linear expansion coefficient of a hydrocarbon liquid is $3\times10^{-4}\,{}^\circ\mathrm{C}^{-1}$, a systematic temperature error of only 1 °C will produce a systematic error of 0.1% due to temperature in the determination of the calibrator volume by this draw method. Similarly, if it is assumed that the fluid's modulus of elasticity is 2×10^{9} Pa (2×10^{4} atm), a systematic pressure error of only 2 MPa (20 atm) will produce a systematic error of ±0.1% in the calibrator volume. As mentioned above, such errors will propagate through all of the relationships for calibrating and using meters and these errors will be further altered by additional temperature and pressure corrections.

Furthermore, using Eq. (7) we can write

$$K_{\mathrm{C}}=\frac{N_{\mathrm{E}}}{\left(\dfrac{\rho_{\mathrm{COLL'T}}}{\rho_{\mathrm{C}}}\right)V_{\mathrm{COLL'T}}}, \tag{23}$$

then, from Eq. (22)

$$K_{\mathrm{C}}=\frac{N_{\mathrm{E}}}{V_{\mathrm{COLL'T}}}[1+3\alpha_{\mathrm{F}}(T_{\mathrm{COLL'T}}-T_{\mathrm{C}})]\times\left[1-\frac{(P_{\mathrm{COLL'T}}-P_{\mathrm{C}})}{E_{\mathrm{F}}}\right]. \tag{24}$$

This result is then related to reference conditions via Eq. (10) to give

$$K_{\mathrm{C0}}=\frac{N_{\mathrm{E}}[1+3\alpha_{\mathrm{F}}(T_{\mathrm{COLL'T}}-T_{\mathrm{C}})]\left[1-\dfrac{(P_{\mathrm{COLL'T}}-P_{\mathrm{C}})}{E_{\mathrm{F}}}\right][1+\alpha_{\mathrm{E}}(T_{\mathrm{E}}-T_0)]}{V_{\mathrm{COLL'T}}[1-2\alpha_{\mathrm{C}}(T_{\mathrm{C}}-T_0)]\left[1-\dfrac{(P_{\mathrm{C}}-P_0)D_{\mathrm{C0}}}{T_{\mathrm{C0}}E_{\mathrm{C}}}\right]}. \tag{25}$$

It is noted that the cross-sectional area, $\bar{A}_{\mathrm{C}}$ can be determined via Eqs. (8) and (23) to be

$$\bar{A}_{\mathrm{C}}=\frac{K_{\mathrm{E}}}{N_{\mathrm{E}}}\left(\frac{\rho_{\mathrm{COLL'T}}}{\rho_{\mathrm{C}}}\right)V_{\mathrm{COLL'T}}. \tag{26}$$

Using Eqs. (5), (6) and (22), this can be written in terms of directly measured quantities and related to reference conditions via

$$\bar{A}_{\mathrm{C0}}=\frac{K_{\mathrm{E0}}V_{\mathrm{COLL'T}}[1-\alpha_{\mathrm{E}}(T_{\mathrm{E}}-T_0)][1-2\alpha_{\mathrm{C}}(T_{\mathrm{C}}-T_0)]\left[1-\dfrac{(P_{\mathrm{C}}-P_0)D_{\mathrm{C0}}}{t_{\mathrm{C0}}E_{\mathrm{C}}}\right]}{N_{\mathrm{E}}[1+3\alpha_{\mathrm{F}}(T_{\mathrm{COLL'T}}-T_{\mathrm{C}})]\left[1-\dfrac{(P_{\mathrm{COLL'T}}-P_{\mathrm{C}})}{E_{\mathrm{F}}}\right]}. \tag{27}$$

If K_{C}' is defined as

$$K_{\mathrm{C}}'=N_{\mathrm{E}}/V_{\mathrm{COLL'T}}, \tag{28}$$

then

$$K_{\mathrm{C0}}=K_{\mathrm{C}}'\times\frac{[1+2\alpha_{\mathrm{C}}(T_{\mathrm{C}}-T_0)]\left[1+\dfrac{(P_{\mathrm{C}}-P_0)D_{\mathrm{C0}}}{t_{\mathrm{C0}}E_{\mathrm{C}}}\right]}{[1-3\alpha_{\mathrm{F}}(T_{\mathrm{COLL'T}}-T_{\mathrm{C}})]\left[1+\dfrac{(P_{\mathrm{COLL'T}}-P_{\mathrm{C}})}{E_{\mathrm{F}}}\right][1-\alpha_{\mathrm{E}}(T_{\mathrm{E}}-T_0)]} \tag{29}$$

or, to first order

$$K_{\mathrm{C}}'=K_{\mathrm{C0}}\times\frac{[1-2\alpha_{\mathrm{C}}(T_{\mathrm{C}}-T_0)]\left[1-\dfrac{(P_{\mathrm{C}}-P_0)D_{\mathrm{C0}}}{t_{\mathrm{C0}}E_{\mathrm{C}}}\right]}{[1+3\alpha_{\mathrm{F}}(T_{\mathrm{COLL'T}}-T_{\mathrm{C}})]\left[1-\dfrac{(P_{\mathrm{COLL'T}}-P_{\mathrm{C}})}{E_{\mathrm{F}}}\right][1+\alpha_{\mathrm{E}}(T_{\mathrm{E}}-T_0)]}. \tag{30}$$

When temperatures exceed those of the reference conditions and pressures are those for the reference conditions:

$$K_{\mathrm{C}}'<K_{\mathrm{C0}}. \tag{31}$$

Thus, the observation made above is repeated here, namely, that when pressure effects can be neglected and when temperatures are above the reference conditions, the calibrator delivers, for the same encoder output pulses, more fluid volume than would occur under reference conditions.

It is also noted that Eqs. (23)–(27) can be combined to give:

$$K_C = K_{C0} \frac{[1-\alpha_E(T_E-T_0)]}{[1+2\alpha_C(T_C-T_0]\left[1+\frac{(P_C-P_0)D_{C0}}{t_{C0}E_C}\right]}, \quad (32)$$

which is the same as Eq. (9).

It is noted that, in these two draw procedures, the decision to collect a sufficiently large number of encoder pulses should precede the operation. This number should be selected according to the desired precision for the calibrator constant, see Eq. (3). In the reference conditions

$$N_{E0} = K_{E0} L_{E0}, \quad (33)$$

and in the non-reference conditions

$$N_E = K_E L_E, \quad (34)$$

but, to first order in temperature,

$$K_E = K_{E0}[1-\alpha_E(T_E-T_0)], \quad (35)$$

and

$$L_E = L_{E0}[1+\alpha_E(T_E-T_0)]. \quad (36)$$

Combining Eqs. (33)–(36) therefore yields:

$$N_E = K_E L_E = K_{E0} L_{E0} = N_{E0}. \quad (37)$$

This indicates that the precision criterion specified for the calibrator should be achieved via the number of pulses selected and the choice is not dependent upon whether reference or non-reference conditions prevail.

As stated above following equation (17), the calibrator constants determined via the draw procedure are generally assumed to be independent of piston speed and fluid properties. Where this is not valid, efforts should be made to achieve this assumption, i.e., improving the piston seals or the calibrator should be characterized using techniques analogous to those for turbine meters as will be described below.

It should also be noted that in the above described draw procedures, the valve and pulse counting techniques must not introduce spurious effects. Spurious counting effects may result from the fluid dynamics in the valve as the flow is started and stopped in conjunction with starting and stopping the pulse count. If such an effect is present then it should be eliminated or proper account made for it so that the appropriate fluid volume is associated with the pulse total. This volume can be determined using the valve compensation techniques that are conventionally applied to diverter systems, see [4].

To use the now-characterized calibrator, it is required that appropriate instrumentation be properly installed both to assure that Eq. (12) is satisfied and to measure the quantities involved in Eqs. (9) or (10) or (32) for the calibrator and equations (28) or (29) or (30) for dispensing precise volumes of fluid at specified conditions of temperature and pressure. Appropriate values are needed for the material constants—the thermal expansion coefficients α_E, α_F and α_C, the modulus of elasticity of the material of the calibrator cylinder, E_C, and that of the fluid, E_F, and the pertinent dimensions of the cylinder. Once the appropriate value for the constant K_{C0} has been installed in the calibrator software or the working procedures for the calibrator, the next step is to use the calibrator to calibrate a flowmeter.

3. Calibrator Use in Calibrating a Turbine Type Flowmeter

3.1 Reference Conditions

To calibrate a turbine-type flowmeter at reference temperature and pressure conditions using the calibrator characterized as described above, the arrangement is sketched in Fig. 6. The temperature and pressure are the reference conditions denoted by T_0 and P_0. As stated above, $T_0 = T_{M0} = T_{C0}$ and $P_0 = P_{M0} = P_{C0}$. Applying again the conservation of mass principles, and assuming that there is no change of mass within the control volume with time, Eqs. (11) and (12) indicate that

$$\rho_{C0} \dot{V}_{C0} = \rho_{M0} \dot{V}_{M0}, \quad (38)$$

where ρ_{C0} and ρ_{M0} are the fluid densities in the calibrator and meter, respectively, at the reference conditions. The quantities $\dot{V}_{C0}$ and $\dot{V}_{M0}$ are the volumetric flowrates, respectively, in the calibrator and through the meter at the reference conditions.

Since reference conditions in cylinder and meter are assumed the same, the densities ρ_{C0} and ρ_{M0} are equal and therefore:

$$\dot{V}_{C0} = \dot{V}_{M0}. \quad (39)$$

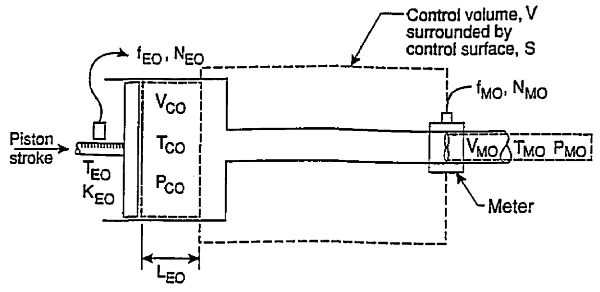

Fig. 6. Arrangement for using characterized calibrator to calibrate a turbine-type flowmeter at reference conditions.

Since the pertinent time intervals are assumed the same:

$$K_{C0}=\frac{K_{E0}}{\bar{A}_{C0}}=\frac{N_{E0}}{\bar{A}_{C0}L_{E0}}=\frac{f_{E0}}{\dot{V}_{C0}}, \qquad (40)$$

where f_{E0} is the encoder frequency, and

$$K_{M0}=\frac{N_{M0}}{V_{M0}}=\frac{f_{M0}}{\dot{V}_{M0}}, \qquad (41)$$

where f_{M0} is the meter frequency.

In Eqs. (40) and (41), the pulse counts N_{E0} and N_{M0} are to correspond to the respective volumes V_{C0} and V_{M0} which are assumed to be the same, or appropriate corrections are made to compensate for any differences between these volumes. Combining Eqs. (40) and (41) gives

$$K_{M0}=\frac{f_{M0}}{f_{E0}}\frac{K_{E0}}{\bar{A}_{C0}}=\frac{N_{M0}}{N_{E0}}\frac{K_{E0}}{\bar{A}_{C0}}=\frac{N_{M0}}{N_{E0}}\cdot K_{C0}=\frac{f_{M0}}{f_{E0}}\cdot K_{C0}, \qquad (42)$$

where K_{M0} has units of pulses per volume at the reference conditions. The quantity K_{E0} is obtained from manufacturer's specifications, testing or Eq. (1).

Conventional non-dimensionalization procedures can be applied to the flowmeter characteristics to produce a set of parameters which interrelate the significant inertial, viscous, and oscillatory effects that constitute the performance of the meter in the calibration conditions, see [6,7]. In this way, the performance of the device can be predicted for other fluid and flow conditions where this set of parameters are the pertinent ones to describe the meter's performance. Of course, when other, different effects such as fluid compressibility or gravitational influences become significant, it should be expected that the initial parameterization needs to be modified to include such effects to obtain satisfactory description of meter performance, see [8,9].

By normalizing the meter factor, K_{M0} and the fluid flowrate using the meter diameter, D_{M0} and the mean flow velocity $\dot{V}_{M0}/A_{M0}=U_{M0}$ and the fluid kinematic viscosity ν_0, we can obtain, for example, the Strouhal number

$$St=\frac{f_{M0}D_{M0}}{U_{M0}}=C_1\,K_{M0}D^3_{M0}\propto K_{M0}D^3_{M0}, \qquad (43)$$

where $C_1=\pi/4$. The Strouhal number is the ratio of characteristic meter frequency effects such as propeller rotation rate to fluid momentum effects. By effects here is meant either forces or energies. As such, the Strouhal number is a dimensionless meter factor.

Conventionally, it is fluid mechanical practice to formulate the Reynolds number as the ratio of fluid inertial to viscous effects,

$$Re=\frac{D_{M0}U_{M0}}{\nu_0}. \qquad (44)$$

This is generally used to describe the domain of the meter calibration for which the corresponding Strouhal numbers specify the range of meter response. A Strouhal-Reynolds characterization of a pulse-producing flowmeter conforms to conventional fluid mechanical procedures and it is analogous to orifice metering practice where discharge coefficient (a ratio of fluid inertia to differential pressure effects) is described functionally or graphically versus Reynolds number. However, as noted in Eq. (44) the Reynolds number requires that the fluid velocity be known. Since this is the purpose for using the meter, an iteration technique is required to calculate the flowrate. To avoid such an iteration, turbine meter manufacturers have designed their products to have high levels of linearity over wide flowrate ranges. As a result of this, it has been conventional turbine meter practice to characterize performance via K-factor vs. frequency to kinematic viscosity ratio—the so-called Universal Viscosity Curve (UVC). In accord with the principles of dimensional similitude, the meter frequency to fluid viscous effects can be formulated using, as characteristic length scale, the meter diameter, D_{M0} as in Eq. (44). This formulation can also be achieved via the product of Strouhal and Reynolds numbers; this product has been recently referred to, see [9], as the Roshko number,

$$R_0=\frac{f_{M0}D_{M0}^2}{\nu_0}. \qquad (45)$$

This Roshko number is the dimensionless version of the frequency-to-kinematic viscosity ratio used for the UVC. It is expected that the dimensionless version of the UVC—the Strouhal-Roshko characterization—should produce superior prediction of meter performance compared to the UVC by virtue of its more complete, i.e., dimensionless description of the inertial, viscous, and oscillatory effects that occur in the meter operation.

The question of which set of parameters best describes a turbine meter's performance should be determined using appropriate data sets. The specific design considerations of blade size and shape, internal meter geometry, bearing features, etc., can be expected to play significant roles in the selection of non-dimensional parameters. Where it may happen that the Reynolds number produces a better description of turbine meter performance, i.e., the data collapses better onto a single curve than achieved using the Roshko number, an iterative sequence of computations may be necessary to produce an accurate determination of flowrate. If the meter is very linear, such an iteration may not be required. Typical flowmeter characterization results are sketched in Fig. 7. Because it is not known whether Reynolds or Roshko number is the better parameter with which to characterize the meter performance, both shall be included in what follows.

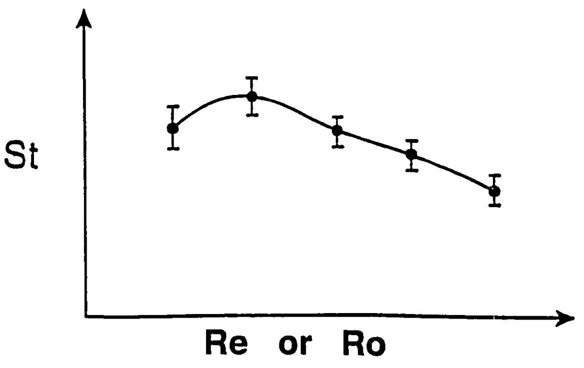

Fig. 7. Normalized calibration results for a turbine-type flowmeter. Points denote averaged results; bars denote standard deviations obtained at each flowrate.

In those instances where meter performance might deviate from the curve shown in Fig. 7, the interpretation would be that additional factors in the deviant conditions have become significant whereas these factors were insignificant in the calibration conditions. Examples might be fluid frictional effects in the turbine bearings produced by extreme viscosity variations from those prevailing in the calibration conditions, or liquid cavitation effects, etc.

The curve shown in Fig. 7 is interpreted as the functional relationship between the Strouhal and Reynolds or Roshko numbers which are assumed to be the salient parameters describing the performance of this flowmeter over these calibration conditions. Inherent in this interpretation is the assumption that in any subsequent use of this functional relationship, the geometries of this meter, for example, the bearings or the propeller diameter are not changed relative to the selected characteristic length of the meter, i.e., the internal diameter, D. If such changes do occur it can be expected that the curve shown in Fig. 7 can change. For example, if a smaller propeller were installed, this curve may retain its shape but lie below that shown in Fig. 7. A non-dimensional parameter which could take into account different propeller diameters is $\beta = d/D$, where d is the propeller diameter. Accordingly, the curve shown in Fig. 7 would pertain to the specific β for which the calibration was done. If other, smaller propellers were also calibrated, these results could be plotted in Fig. 7 and parameterized with the smaller value of β. When the propeller and meter-body materials are the same and where pressure effects can be neglected, the β ratio will remain constant when the temperature changes. When the propeller and the meter-body materials are different, temperature changes can produce different β ratios. These different ratios can be computed using pertinent relationships. The computed results should then be used with calibration data taken for different β ratios to predict the meter performance at the different temperature conditions, see Appendix B.

Figure 7 is different from conventional turbine meter performance plots in which the meter's K-factor is plotted versus the ratio of frequency-to-kinematic viscosity. These conventional quantities are different from the Strouhal and Reynolds or Roshko number parameters by constant factors and by factors of the meter diameter raised to different exponents. These powers of the diameter should change only slightly with small changes in temperature and internal pressure. However, when conditions vary widely, the dimensionless formulations should be used and are expected to produce improved meter performance. Plots in the format of Fig. 7 should then, with the exceptions of deviant phenomena becoming influential, apply to a wide range of specific, dimensional fluid property and flow conditions and produce accurate predictions of turbine meter performance.

Where conventional turbine meter practice is used and plots are produced for K-factor versus the ratio of frequency-to-kinematic viscosity, improved meter performance can be expected when these calibration results are corrected to specified reference conditions. Accordingly, the corrected results should incorporate temperature and internal pressure corrections for the ratios of meter diameters raised to the relevant exponent to predict meter performance for other fluid and flow conditions. For meters having good linearity characteristics, i.e., constancy of the meter factor over specified flowrate ranges, the more important of these two corrections is that for the K-factor, i.e.,

$$K_{M0}=K_M\,(D_M/D_{M0})^3\,. \tag{46}$$

This stipulates that the meter frequency-to-fluid inertial effects ratio, i.e., Strouhal number be the same in the actual conditions as in the reference conditions. To first order in temperature and pressure, separately, the diametral ratio can be written,

$$\left(\frac{D_M}{D_{M0}}\right)^3=[1+3\alpha_M(T_M-T_{M0})]\times\left[1+\frac{3(P_M-P_{M0})\,D_{M0}}{2\,t_{M0}E_M}\right]=\frac{K_{M0}}{K_M}\,, \tag{47}$$

where D_M and D_{M0} are, respectively, the meter diameters at the non-reference conditions, T_M and P_M and reference conditions, T_{M0} and P_{M0}. The quantities α_M and E_M are, respectively, the linear expansion coefficient and the modulus of elasticity of the meter body material for these conditions, and t_{M0} is the thickness of the meter body at reference conditions. The more significant of the two correction factors is usually that for temperature deviations from reference conditions. When the pressure correction can be neglected,

$$K_{M0}=K_M\,[1+3\alpha_M(T_M-T_{M0})]\,, \tag{48}$$

or, to first order:

$$K_M=K_{M0}\,[1-3\alpha_M(T_M-T_{M0})]\,. \tag{49}$$

This relationship duplicates that given in [10].

3.2 Non-Reference Conditions

To calibrate a turbine-type flowmeter using the calibrator characterized as described above, the arrangement is sketched in Fig. 8. The temperature and pressure in the calibrator are the non-reference conditions denoted by T_C and P_C. Applying again the conservation of mass principles, and assuming that there is no change of mass within the control volume with time, Eq. (11) and (12) indicate that

$$\rho_C\dot{V}_C=\rho_M\dot{V}_M\,. \tag{50}$$

Since the fluid conditions in the cylinder and in the meter can be different, the ratio of the densities is

$$\frac{\rho_C}{\rho_M}=[1-3\alpha_F\,(T_C-T_M)]\left[1+\frac{P_C-P_M}{E_F}\right], \tag{51}$$

and from Eq. (32) and in a manner analogous to Eq. (40)

$$K_C=\frac{K_E}{\bar{A}_C}=\frac{f_E}{\dot{V}_C}=K_{C0}\,\frac{[1-\alpha_E\,(T_E-T_0)]}{[1+2\alpha_C\,(T_C-T_0]\left[1+\dfrac{(P_C-P_0)\,D_{C0}}{t_{C0}E_C}\right]}\,. \tag{52}$$

Then, analogously to Eq. (42)

$$K_M=\frac{f_M}{f_E}K_C\frac{\rho_M}{\rho_C}=\frac{N_M}{N_E}K_{C0}\times\frac{[1-\alpha_E(T_E-T_0)][1+3\alpha_F(T_C-T_M)]}{[1+2\alpha_C(T_C-T_0)]\left[1+\dfrac{(P_C-P_0)\,D_{C0}}{t_{C0}E_C}\right]\left[1+\dfrac{(P_C-P_M)}{E_F}\right]}\,, \tag{53}$$

where K_M has units of pulses per volume at the specific, non-reference meter conditions.

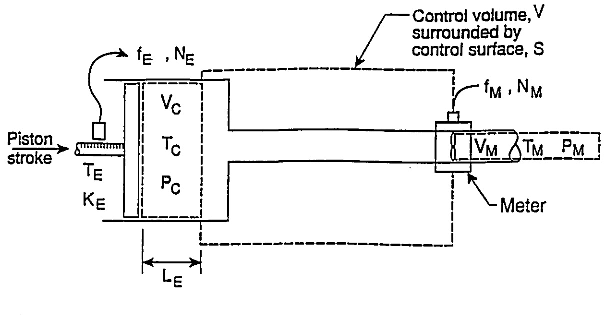

Fig. 8. Arrangement for using characterized calibrator to calibrate a turbine-type flowmeter at non-reference conditions.

As stated above after Eq. (41), the pulse totals from the meter and the encoder have to correspond to the same displaced volume or time interval. If compensations are needed to achieve this correspondence, these should be done and results used in Eq. (53).

By normalizing this meter factor, K_M and the fluid flowrate using the non-reference meter diameter, D_M, and fluid kinematic viscosity, v, we obtain Strouhal and Reynolds or Roshko numbers

$$St = f_M D_M / U_M = C_1 K_M D_M^3 , \qquad (54)$$

where $C_1 = \pi/4$, and

$$Re = D_M U_M / v \qquad (55)$$

or

$$Ro = \frac{f_M D_M^2}{v} . \qquad (56)$$

Using these dimensionless parameters, the performance for the meter can be plotted; results should be as shown in Fig. 7. As noted above in Eqs. (43)–(45), the characteristics of meter factor and diameter at reference and non-reference conditions are interrelated and the dependence of the fluid's kinematic viscosity can be written functionally as

$$v = v_0 [T, T_0, P, P_0] . \qquad (57)$$

With the performance curve given in Fig. 7 and the relationships given in Eqs. (43)–(45), or (54)–(57), one is now ready to use the flowmeter to make a flowrate measurement.

4. Using a Turbine-Type Flowmeter To Make a Measurement

4.1 Reference Conditions

Given that the meter performance characteristics are as shown in Fig. 7, or less preferably but more conventionally as in Fig. 9, one can quantify the meter linearity over a specified flowrate range. The meter linearity is conventionally the average of the maximum and minimum values of the meter factor (Strouhal number) over this range; normalized by the average meter factor, see [3 and 10]. For the meter performance shown in Fig. 7, the mean value of the Strouhal Number, $\overline{St}$ gives the mean meter factor, via

$$\overline{K}_{M0} = \frac{\overline{St}}{C_1 D_{M0}^3} , \qquad (58)$$

where $C_1 = \pi/4$. The flowrate is determined via

$$\dot{V}_{M0} = \frac{f_{M0}}{\overline{K}_{M0}} = \frac{C_1 D_{M0}^3 f_{M0}}{\overline{St}} . \qquad (59)$$

This result would pertain to any flowrate over the range specified for the meter's linearity.

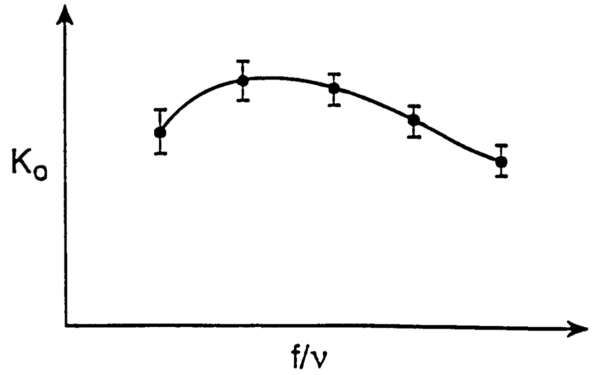

Fig. 9. Conventional performance plot for a turbine-type flowmeter.

If it is desired to improve the accuracy of this flowrate determination, this could be done by using, for example, the curve shown in Fig. 7 or close approximations to it. With advances in today's computer technology, this type of process can be readily installed in the secondary devices used with flowmeters. For the specific frequency from the meter, the Roshko number can be calculated directly and then used to determine the corresponding Strouhal number. For the case where the meter is characterized using Strouhal and Reynolds parameters, the process to determine an accurate flowrate should be iterative. This iteration process should begin using a mean value of meter factor, such as given in Eq. (58), this value of meter factor enables a computation of the flowrate via Eq. (59). Using this flowrate, the Reynolds number can be computed and then used to get the corresponding Strouhal number from the calibration curve and a refined value of flowrate. This process should be repeated until satisfactorily small changes are found in successive results. In this way, the accuracy level for the flowrate determination can be increased over the level associated with the meter's linearity. This can be done to the precision level associated with a specific flowrate as quantified in the calibration process. The resulting enhanced meter performance could amount to significant improvements in measurement accuracy. In the following, a Strouhal-Reynolds characterization of meter performance will be used since it is more conventional in fluid mechanics and since it may require the iteration procedure, described above, to be used.

4.2 Non-Reference Conditions

To describe meter performance in non-reference conditions, the meter characteristics shown in Fig. 7 will be used. The reason for this is that the complete, non-dimensional assessment of meter frequency effects and fluid inertial and viscous effects are not complete in Fig. 9. For this reason, the non-reference meter diameter, D_M, and frequency, f_M, and the fluid's kinematic viscosity, v, should be used, in compatible units, to produce the Reynolds number for the non-reference conditions. This Reynolds number produces, using Fig. 7, the corresponding Strouhal number which with the meter diameter, D_M, gives the meter factor, K_M. The flowrate measurement is then obtained using

$$\dot{V}_M = \frac{f_M}{K_M} = \frac{C_1 f_M D_M^3}{St}. \tag{60}$$

This flowrate is correctly converted to reference conditions by specifying that the Strouhal number is the same for the non-reference and reference conditions, specified by this Reynolds number, i.e.,

$$St = C_1 \frac{f_M D_M^3}{\dot{V}_M} = C_1 \frac{f_{M0} D_{M0}^3}{\dot{V}_{M0}}. \tag{61}$$

Therefore

$$\dot{V}_{M0} = \dot{V}_M \frac{f_{M0}}{f_M} \left(\frac{D_{M0}}{D_M}\right)^3. \tag{62}$$

The reference to non-reference frequency ratio is obtained by specifying that Reynolds number similarity exists for these two conditions, i.e.,

$$Re = \frac{f_M D_M^2}{(St)\, v_M} = \frac{f_{M0} D_{M0}^2}{(St)\, v_{M0}}. \tag{63}$$

It is noted that this is equivalent to stipulating that Roshko number similarity exists for these two conditions. From Eq. (63)

$$\frac{f_{M0}}{f_M} = \frac{v_{M0}}{v_M} \left(\frac{D_M}{D_{M0}}\right)^2 \tag{64}$$

and

$$\dot{V}_{M0} = \frac{C_1 f_M D_{M0}^3}{St} \left(\frac{\mu_{M0}}{\mu_M}\right) \frac{[1+2\alpha_M(T_M-T_{M0})]\left[1+\frac{(P_M-P_{M0})\,D_{M0}}{t_{M0}E_M}\right]}{[1+3\alpha_F(T_M-T_{M0})]\left[1-\frac{(P_M-P_{M0})}{E_F}\right]}. \tag{65}$$

It is apparent that, to obtain high accuracy flowrate measurements using the procedures described above, appropriately high accuracy measurements are required for the component measurement systems and for the pertinent material properties as shown in Eq. (65). In turn, it appears feasible that once systematic uncertainties are satisfactorily removed from calibration facilities, the measurement processes in calibration laboratories, and the measurement systems making on-line measurements will be commensurately improved and the uncertainty levels for these measurements can be predicted using such Eqs. as (2), (10), (25), and (65).

5. Discussion

The above-derived results can, for the sake of brevity, be assessed by considering the effects of temperature and pressure on the respective factors—the calibrator and flowmeter constants and the flowrate measurement at reference conditions. To do this Table 1 shows, for specific material conditions and geometrical sizes, the variations associated with temperature and pressure effects separately and then summed together.

The results shown in the first row of Table 1 present the variations in calibrator constant K_{C0} determined using geometrical measurement methods for variations of ±1 °C in temperature and $\pm 1\times10^5$ Pa (1 atm) in pressure. The material properties and geometrical assumptions are given under the headings of the respective columns. The worst-case combination of temperature and pressure variations taken separately are given in columns 7 and 12, respectively. These results are obtained by adding the absolute values of the component contributions. The total worst-case combination for temperature and pressure variations taken together is given in the column at the right side of the table. Accordingly, the total temperature effect on K_{C0} in the measurement method is five times larger than the pressure effect and the total of these gives an imprecision of ±0.006%.

Table 1. Temperature and pressure effects

Factor affected	Total diff (°C)	Temperature effects				Total temperature combined worst case	Press diff (atm)	Pressure effects			Total pressure combined worst case	Total worst case
		Encoder factor ($\alpha_E=10^{-5}$ °C^{-1})	Calibrator cross-section ($\alpha_C=2\times10^{-5}$ °C^{-1})	Fluid expansion ($\alpha_F=3\times10^{-4}$ °C^{-1})	Meter expansion ($\alpha_M=2\times10^{-5}$ °C^{-1})			Calibrator cross-section ($D/t=20$; $E_C=2\times10^{11}$ Pa)	Fluid expansion ($E_F=2\times10^9$ Pa)	Meter expansion ($D/t=15$; $E_M=2\times10^{11}$ Pa)		
$K_{\mathrm{CU:GEOM}}$[a]	±1	±0.001%	±0.004%			±0.005%	±1	±0.001%			±0.001%	±0.006%
$K_{\mathrm{CU:DRAW}}$[b]	±1	±0.001%	±0.004%	±0.090%		±0.095%	±1	±0.001%	±0.005%		±0.006%	±0.101%
K_{MU}[c]	±1	±0.001%	±0.004%	±0.090%		±0.095%	±1	±0.001%	±0.005%		±0.006%	±0.101%
St[d]	±1	±0.001%	±0.004%	±0.090%	±0.006%	±0.101%	±1	±0.001%	±0.005%	±0.001%	±0.007%	±0.108%
K_M[c]	±1	±0.002%	±0.008%	±0.180%		±0.190%	±1	±0.002%	±0.010%		±0.012%	±0.202%
St[f]	±1	±0.002%	±0.008%	±0.180%	±0.006%	±0.196%	±1	±0.002%	±0.010%	±0.001%	±0.013%	±0.209%
$\dot{V}_{\mathrm{MU}}$[g]	±1	±0.001%	±0.004%	±0.090%		±0.090%	±1	±0.001%	±0.005%		±0.006%	±0.101%
$\dot{V}_M$[h]	±1	±0.002%	±0.008%	±0.180%		±0.190%	±1	±0.002%	±0.010%		±0.012%	±0.202%
$\dot{V}_{\mathrm{MU}}$[i]	±1	±0.002%	±0.008%	±0.270%	±0.012%	±0.292%	±1	±0.002%	±0.015%	±0.002%	±0.019%	±0.311%

[a] Determined via Eq. (10) at non-reference conditions.

[b] Determined via Eq. (29) at non-reference conditions with no additional uncertainty for the encoder or the collection volume.

[c] Determined using $K_{\mathrm{CU:DRAW}}$ via Eq. (42) with no additional uncertainty resulting from encoder or meter outputs.

[d] Determined using $K_{\mathrm{CU:DRAW}}$ via Eq. (43) in reference conditions.

[c] Determined using $K_{\mathrm{CU:DRAW}}$ via Eq. (53).

[f] Determined using $K_{\mathrm{CU:DRAW}}$ via Eq. (54).

[g] Determined using K_{MU} via Eq. (59) with no additional uncertainty resulting from the meter output.

[h] Determined using K_M via Eq. (60) with no additional uncertainty resulting from meter output.

[i] Determined using Eq. (65) with not additional uncertainty for meter output, reference meter dimension, and absolute viscosity.

The results for K_{C0} determined using the draw technique are shown in the second row. These give a total temperature variation of ±0.095% owing mainly to fluid expansion effects. The pressure variation is noted to be a factor of about 16 less than this level and the total imprecision totals ±0.101% which is about a factor of 20 larger than the level achieved using the geometrical measurement technique.

The results for the meter factor, K_{M0}, are given in the third row of the table. Here, at reference conditions, no additional uncertainties are shown over those for K_{C0} in accord with Eq. (42).

The fourth row indicates that the total temperature variation for St is increased over that for K_{M0} by the amount allocated for meter expansion. This produces the ±0.101% uncertainty total for temperature which when added to the increased pressure total gives ±0.108%. This shows that while the Strouhal number is the preferred nondimensional parameter to characterize the frequency effects of a meter, it has more factors than the conventional meter factor, K_{M0} and, therefore, it can have increased uncertainty. However, because the Strouhal number is a dimensionless ratio of frequency to inertial effects in the meter it should be successful in producing more satisfactory metering results for widely ranging conditions than can be done using a dimensional quantity such as K_{M0}.

The fifth and sixth rows express the uncertainties for K_M and the corresponding Strouhal number in a manner analogous to that used to obtain values in rows three and four. However, as shown in Eq. (53) the uncertainties attributed to K_{C0} are increased appropriately due to encoder, calibrator, and fluid effects; and, in the case for St, meter effects. It is noted that the totaled uncertainties have essentially doubled in comparison with those for K_{M0}.

While it is recognized that the conditions of ± 1 °C and $\pm 1 \times 10^5$ Pa (1 atm) pressure variation can be termed large, it should be recognized that no uncertainty has been allocated in Table 1 for the uncertainty with which the material properties and geometrical dimensions are known or have been determined. As well, it should be recognized that these assumed conditions of ± 1 °C and $\pm 1 \times 10^5$ Pa (1 atm) can in reality understate the actual variations that may exist in real situations where flowrate measurements can be attempted in harsh, hostile environments.

It should be emphasized that the above discussion deals only with the uncertainties associated with temperature and pressure imprecision and does not take into account contributions from flowmeter imprecision such as the variability of detecting meter pulses. Additionally, systematic errors which can greatly exceed the levels of imprecision are not included in any of the above.

A summary of the equations derived for characterizing piston-type, encoded-stroke calibrators, their calibration procedures, and the subsequent use of calibrated turbine meters is given in Appendix C. These equations are found to be quite simple when reference conditions prevail. However, reference conditions are practically fictitious and therefore the performance of all of these devices should be considered as occurring in nonreference conditions. Given the capabilities available in today's computers, it is felt that the complete equations for these types of devices should be installed in the controlling and processing software so that when temperature and or pressure conditions become significant in these processes the results are accurate. Using these equations when temperature and or pressure effects are not significant produces negligible differences from the results at reference conditions.

6. Conclusions

High accuracy fluid measurements can be attained when the important factors affecting the performances of both flowmeter calibrators and fluid meters are properly taken into account in the measurement processes of these devices. To do this—to first order temperature and pressure effects on both the calibrator and the meter as well as on the fluid—the equations derived above should be used as the basic system models for calibrator and meter. Specific features of calibrators need to be analyzed and, where pertinent, appropriate modifications to the above-derived equations should be made. Calibrators and metering units need to be properly instrumented and operated according to the required assumptions and techniques for handling the data. Where further increases in flow measurement accuracy are needed, either more accurate descriptions of currently considered factors should be made or additional factors not currently considered should be assessed and included as pertinent, or both.

7. Appendix A. Cross-Sectional Area Changes in the Cylinder of the Calibrator

The fluid pressure and temperature inside the cylinder of the calibrator can enlarge or reduce the cross-sectional areas of this cylinder, see Fig. 1. As well, geometrical changes of the rod or tube connected to the piston can also contribute to changes in this cross-sectional area. Of course, knowledge of specific geometries and material properties are crucial to characterizing these changes. In the following it is assumed that a generic cylinder and rod geometry exist as sketched in Fig. 1.

First, thermal expansion will increase the diameters of the cylinder and the connecting tube or rod via the first order approximations

$$D = D_0 [1 + \alpha_C (T_C - T_0] \qquad \text{(A.1.1)}$$

and

$$d = d_0 [1 + \alpha_r (T_r - T_0] , \qquad \text{(A.1.2)}$$

where, in compatible units, D and d and D_0 and d_0 are the cylinder and tube diameters at non-reference and reference conditions, respectively. The linear expansion coefficients for cylinder and tube or rod are α_C and α_r, respectively, and T_C and T_r are the corresponding temperatures. These diametral enlargements will produce an increased cross-sectional area via the first order approximation

$$\bar{A}_C = \bar{A}_{C0} [1 + 2\alpha_C (T_C - T_0] , \qquad \text{(A.1.3)}$$

where $\bar{A}_C$ and $\bar{A}_{C0}$ are, respectively, the annular areas between cylinder and rod as averaged over the appropriate piston displacement. The linear expansion coefficient of the rod or tube is assumed to be the same as that for the cylinder.

Second, pressure effects can change the cross-sectional area through the enlargement of the calibrator cylinder and the contraction of the rod or tube connected to the piston. The azimuthal or "hoop" stress, σ_θ, produced in the calibrator cylinder can be shown to be

$$\sigma_\theta = (P_C - P_0) D_C / 2t_C , \qquad \text{(A.1.4)}$$

where $P_C - P_0$ is the pressure difference between the pressure in the cylinder and the reference pressure outside the cylinder. The quantities D_C and t_C are, respectively, the inside diameter and the thickness of the cylinder. The azimuthal strain produced by this stress is assumed to be

$$\epsilon_\theta = \sigma_\theta / E_C , \qquad \text{(A.1.5)}$$

where transverse effects are neglected and where E_C is the modulus of elasticity of the material of the calibrator. This azimuthal strain increases the circumference of the calibrator cylinder via

$$C = C_0 (1 + \epsilon_\theta) , \qquad \text{(A.1.6)}$$

where C and C_0 are, respectively, the inside circumferences of the cylinder in stressed and unstressed conditions. This produces an increase, to first order, in the cylinder's averaged cross-sectional area of

$$\bar{A}_C = \frac{\bar{C}^2}{4\pi} = \frac{\bar{C}_0^2}{4\pi} \left[1 + \frac{(P_C - P_0) D_{C0}}{t_{C0} E_C} \right] \qquad \text{(A.1.7)}$$

or since $\bar{A}_{C0} = \bar{C}_0^2 / 4\pi$,

$$\bar{A}_C = \bar{A}_{C0} \left[1 + \frac{(P_C - P_0) D_{C0}}{t_{C0} E_C} \right] , \qquad \text{(A.1.8)}$$

where D_{C0} and t_{C0} are the diameter and thickness, respectively, of the calibrator cylinder at reference conditions. Typical values for the ratio D_{C0}/t_{C0} could be 10 to 20.

In similar fashion, the cylinder pressure in excess of the reference pressure, P_0 at which condition the reference dimensions are determined can reduce the outside diameter of the tube connected to the piston. Since the deformation of a tube should, for the same material and diameter, exceed that for a solid rod, it shall be considered here. Therefore, the cross-sectional area of the tube connected to the piston would be

$$\bar{A}_t = \bar{A}_{t0} \left[1 - \frac{(P_C - P_0) D_{t0}}{t_{t0} E_t} \right] , \qquad \text{(A.1.9)}$$

where D_{t0} and t_{t0} are, respectively, the outside diameter and the thickness of the wall of the tube connected to the piston at reference conditions. The quantity E_T is the modulus of elasticity of the tube material, at reference conditions.

It is generally and safely assumed that the tube contraction effect expressed in Eq. (A.1.9) is negligible in comparison to the effects of temperature on the inner diameter of the calibrator. Therefore, it is assumed that the annular cross-sectional area between cylinder and tube is that expressed in Eq. (A.1.3) and the effect of pressure on this annular area is expressed in Eq. (A.1.8). However, where specifics indicate that other compensations need to be made, other approximations can and should be done. The combined effect of pressure and temperature on the averaged cross-sectional area of the cylinder of the calibrator is,

$$\bar{A}_{C} = \bar{A}_{C0}\,[1 + 2\alpha_{C}\,(T_{C} - T_{C0}]\left[1 + \frac{(P_{C} - P_{0})\,D_{C0}}{E_{C}t_{C0}}\right]. \tag{A.1.10}$$

8. Appendix B. Turbine Meter Data Processing

Conventional practice in processing and using turbine-type flowmeter data began with plotting the meter K factor in pulses per volume units as a function of meter frequency, f; see Fig. A.2.1 and [5-8]. In this figure, the bracketed dots are intended to represent the mean values and the scatter obtained for the K factors at respective frequencies. For fluid and flow conditions which precisely duplicate those for which the meter calibration was performed, this practice produced acceptable results. However, when fluid or flow conditions deviated from those of the calibration, it was found that results could be unacceptable. An example is indicated in Fig. A.2.1. The lines for which the liquid viscosities are μ_1 and μ_2, respectively, indicate that different meter performance occurs at low flowrates when the fluid dynamic viscosity, μ_2 is greater than the value μ_1 used for the calibration.

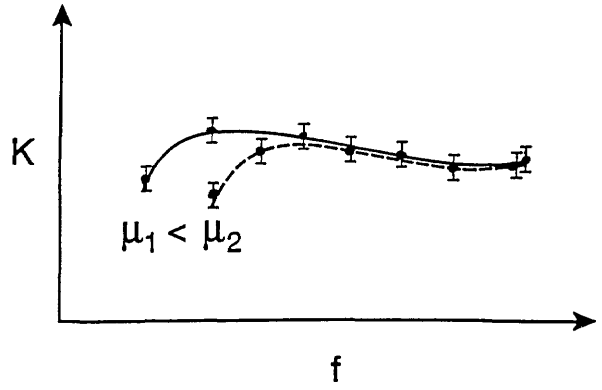

Fig. A.2.1 Conventional format for processing turbine-type flowmeter data.

Flowmeter performance which deviates from that of the calibration conditions at low flowrates is explained by citing the deviant phenomena which have, because of the different fluid or flow conditions, become significant in comparison to the phenomena which prevailed during calibration. Shafer and Lee have resolved several situations involving viscous effects in specific flowmeter geometries [6,8]. From such efforts have come Universal Viscosity Curves (UVC) i.e., plots of meter factor versus the ratio of meter frequency to fluid kinematic viscosity. A typical UVC is shown in Fig. A.2.2. The ordinate, K_0, is the meter factor referenced to a selected reference temperature via, see [10],

$$K_0 = K\,[1 + 3\alpha_{M}\,(T - T_0]\,. \tag{A.2.1}$$

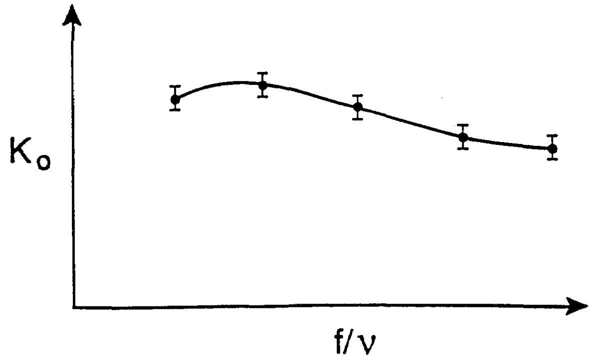

Fig. A.2.2 Universal Viscosity Curve (UVC) for processing turbine-type flowmeter data.

Deviations of flowmeter performance characteristics from UVC's can be explained by citing further deviants, such as lubricity, cavitation, extreme temperature or pressure effects on fluid properties, etc., see [5-8].

When the turbine meter is to be used in temperature conditions different from those of the reference or calibration conditions, temperature effects may be compensated for by producing corrections for the meter factor K, as found in some standards, see [10]. This ISA standard produces an underived correction that is based upon the thermal expansion for the material of the meter body. This correction is effective in predicting trends for the case where the meter body and the turbine wheel material are the same. Where these materials are different, this correction can give erroneous results, for example, in the extreme situation where the turbine wheel has expanded to touch the inner wall of the meter body, thus stopping the wheel's rotation. In such a situation the meter factor should be zero yet the ISA correction would not give this result. Therefore, further evolution is needed for conventional turbine-type flowmeter practice—beyond the UVC methods.

Turbine meter performance is most properly characterized by specifying and quantifying, over the pertinent ranges of fluid and flow conditions, the significant dimensionless parameters which influence meter performance. To do this, the dimensional quantities that are involved in turbine-type flowmetering are cited as shown in Fig. A.2.3. These five dimensional quantities—fluid density ρ, and viscosity μ, the flow velocity U, the meter frequency f, and the meter diameter, D are described in terms of three independent units—length, time, and mass or force. Consequently, there are two dimensionless parameters to characterize the performance of this meter. These dimensionless parameters can take many forms. Conventional fluid mechanical practice would produce parameters expressing ratios of meter frequency effects to fluid inertial effects, i.e., the Strouhal number and the fluid inertial to viscous effects, i.e., the Reynolds number. These are written

$$St=fD/U \qquad \text{(A.2.2)}$$

and

$$Re=\frac{DU\rho}{\mu}=\frac{DU}{v}\,. \qquad \text{(A.2.3)}$$

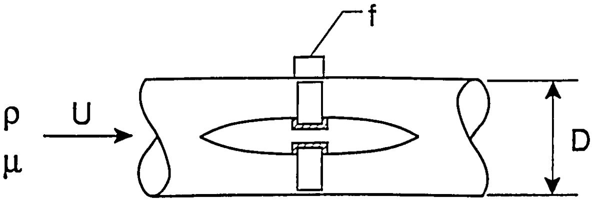

Fig. A.2.3 Turbine meter configuration.

However, turbine meters are designed to have frequencies proportional to volumetric flowrates. The constant of proportionality is the reciprocal of the meter factor. Since the constancy of this meter factor, i.e., the linearity of the meter over the flowrate (frequency) range is generally taken to be a measure of the quality of the meter, it has become conventional turbine meter practice to characterize meters via their K factor versus frequency dependence. In non-dimensional format, this can be done by specifying meter performance using a Strouhal number that is dependent upon the product of the Strouhal and Reynolds numbers, i.e., fD^2/v. This parameterization is essentially that known as the UVC except for the factors involving the meter diameter, D, raised to an exponent. This product has been referred to as the Roshko number, Ro,

$$Ro=\frac{fD^2}{v} \qquad \text{(A.2.4)}$$

see [9]. Alternatively, the pair of parameters, St and Re could also be used to characterize the meter's performance. In either case, only two parameters are needed to characterize the system sketched in Fig. A.2.3.

In all of the above, the effect of different meter geometries or a different turbine wheel is not considered. This is proper where the meter geometry is not changed and where the same turbine wheel and bearings, etc. are used and where the turbine wheel and the meter body are made of the same material. Under these circumstances, the above parameterization of the five dimensional quantities ρ,μ,U,D, and f is completed with the formulation of the Strouhal and Reynolds or Roshko numbers. Using this formulation the performance of the calibrated meter should enable the meter to be satisfactorily used over a range of conditions similar to those encountered in the calibration.

If the situation is changed as shown in Fig. A.2.4 so that the turbine wheel diameter, d, is included to produce six dimensional quantities, then three dimensionless parameters should be formed. The turbine wheels that are considered here are geometrically scaled versions of each other, i.e., they have the same number of blades, the same blade shape and only differ in the diameter, d. The nondimensionalization can be achieved by choosing the third dimensionless parameter to be $\beta=d/D$, the ratio of turbine wheel to inside pipe diameter. The three parameter performance is sketched in Fig. A.2.5. It is noted that when the turbine wheel and meter body are the same material and when only thermal expansion effects are considered, β remains constant with changes in temperature, i.e.,

$$\beta=\frac{d}{D}=\frac{d_0[1+\alpha_r(T_r-T_0]}{D_0[1+\alpha_M(T_M-T_0]}, \qquad \text{(A.2.5)}$$

when $T_r=T_M$ and $\alpha_r=\alpha_M$ this diameter ratio is d_0/D_0.

When turbine wheel and meter body are different materials and when $\alpha_r>\alpha_M$, the beta ratio is not constant and a condition for the linear expansion coefficients and the fluid flowrate can be derived for which $T_M=T_r$ and $\beta=1$. This would indicate that the turbine blade tips touch the inside of the meter body thus stopping the wheel. This condition is, of course, contrived in order to illustrate the point that β variation can produce meter performance variation and in extreme limits can radically alter the graphs of meter performance.

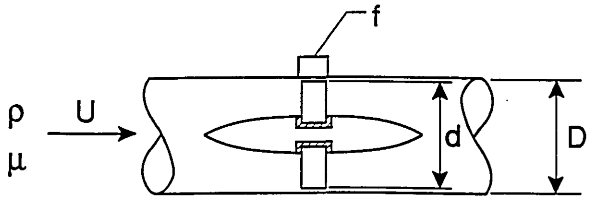

Fig. A.2.4 Turbine meter configuration with the turbine wheel diameter, d, considered as a parameter.

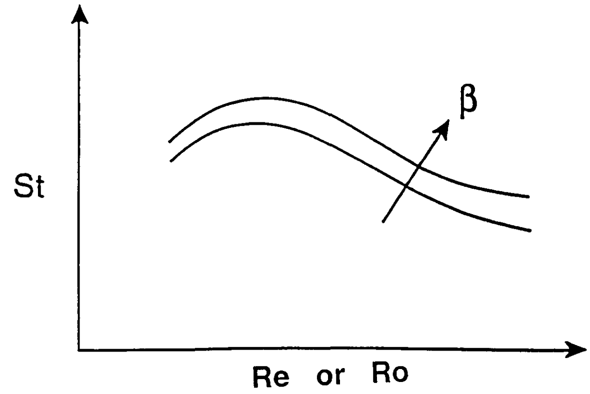

Fig. A.2.5 Non-dimensional turbine meter performance.

If pressure effects are not negligible in altering the diameter of the meter body but are negligible in affecting the diameter of the turbine wheel, β is altered, to first order in temperature and pressure, separately, via

$$\beta=\frac{d_0[1+\alpha_r(T_r-T_0)]}{D_0[1+\alpha_M(T_M-T_0]\left[1+\frac{(P_M-P_0)D_{M0}}{2t_{M0}E_M}\right]}. \tag{A.2.6}$$

By so incorporating thermal and pressure effects using St, Re or Ro, and β parameters into performance curves as sketched in Fig. A.2.6, widely varying metering conditions should be successfully handled.

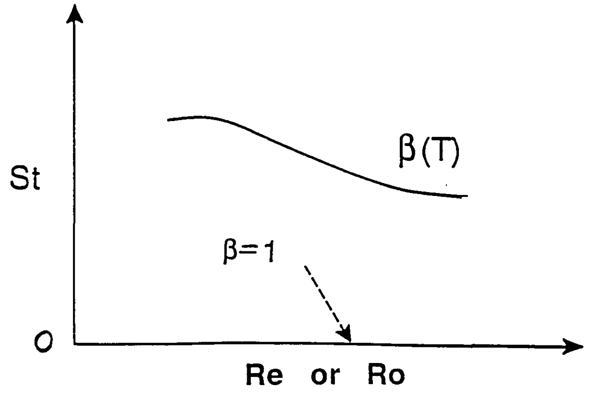

Fig. A.2.6 Sketch of expected turbine meter performance where $\beta\to 1$.

It is concluded that turbine-type flowmeter performance should be handled non-dimensionally. Pertinent corrections are then most clearly seen and most easily performed using the appropriate, first-order, relationships for the thermal and pressure effects. In this way high levels of flowmeter performance can be expected and achieved.

9. Appendix C. Equations Summary

The equations in Appendix C are numbered as in the main text.

1. *Calibrator Characterization*:

   a. Geometrical Measurement Method—Reference Conditions (see p. 513)

$$K_{C0}=\frac{N_{E0}}{V_{C0}}=\frac{L_{E0}K_{E0}}{A_{C0}L_{E0}}=\frac{K_{E0}}{A_{C0}}. \tag{2}$$

   b. Geometrical Measurement Method—Non-Reference Conditions (see p. 515)

$$K_{C0}=K_C\frac{[1+\alpha_E(T_E-T_0)]}{[1-2\alpha_C(T_C-T_0]\left[1-\frac{(P_C-P_0)D_{C0}}{t_{C0}E_C}\right]}, \tag{10}$$

where

$$K_C=\frac{N_E}{V_C}, \tag{7}$$

   c. Draw Technique—Reference Conditions (see p. 516)

$$K_{C0}=N_{E0}/V_{\mathrm{COLL'T0}}. \tag{15}$$

d. Draw Technique—Non-Reference Conditions (see p. 517)

$$K_{C0}=K'_C \frac{[1+2\alpha_C(T_C-T_0)]\left[1+\frac{(P_C-P_0)\,D_{C0}}{t_{C0}E_C}\right]}{[1-3\alpha_F(T_{\mathrm{COLL'T}}-T_C)]\left[1+\frac{(P_{\mathrm{COLL'T}}-P_C)}{E_F}\right][1-\alpha_E(T_E-T_0)]}\,, \quad (29)$$

where

$$K'_C=N_E/V_{\mathrm{COLL'T}}\ . \quad (28)$$

2. *Meter Calibration*:

a. *Reference Conditions*: (see p. 519)

$$K_{M0}=\frac{f_{M0}}{f_{E0}}\,\frac{K_{E0}}{\overline{A}_{C0}}=\frac{N_{M0}}{N_{E0}}\,\frac{K_{E0}}{\overline{A}_{C0}}=\frac{N_{M0}}{N_{E0}}\bullet K_{C0}=\frac{f_{M0}}{f_{E0}}\bullet K_{C0}\,. \quad (42)$$

Data Processing: (see p. 519)

$$St=\frac{f_{M0}D_{M0}}{U_{M0}}=C_1\,K_{M0}D^3_{M0}\propto K_{M0}D^3_{M0}\,, \quad (43)$$

$$Re=\frac{D_{M0}U_{M0}}{v_0}\ , \quad (44)$$

$$Ro=\frac{f_{M0}D_{M0}{}^2}{v_0}\,. \quad (45)$$

b. *Non-Reference Conditions*: (see p. 521)

$$K_M=\frac{f_M}{f_E}K_C\frac{\rho_M}{\rho_C}=\frac{N_M}{N_E}K_{C0} \times \frac{[1-\alpha_E(T_E-T_0)][1+3\alpha_F(T_C-T_M)]}{[1+2\alpha_C(T_C-T_0)]\left[1+\frac{(P_C-P_0)\,D_{C0}}{t_{C0}E_C}\right]\left[1+\frac{(P_C-P_M)}{E_F}\right]}\ . \quad (53)$$

Data Processing: (see p. 522)

$$St=f_MD_M/U_M=C_1K_MD^3_M\ , \quad (54)$$

$$Re=D_MU_M/v\ , \quad (55)$$

$$Ro=\frac{f_MD^2_M}{v}\ . \quad (56)$$

3. *Flow Measurement*:

a. *Reference Conditions*: (see p. 522)

$$\dot{V}_{M0}=\frac{f_{M0}}{\overline{K}_{M0}}=\frac{C_1D^3_{M0}f_{M0}}{\overline{St}}\,. \quad (59)$$

b. *Non-Reference Conditions:* (see p. 523)

$$\dot{V}_M=\frac{f_M}{\overline{K}_M}=\frac{C_1f_MD^3_M}{\overline{St}}\ , \quad (60)$$

$$\dot{V}_{M0}=\frac{C_1f_MD^3_{M0}}{St}\left(\frac{\mu_{M0}}{\mu_M}\right)\frac{[1+2\alpha_M(T_M-T_{M0})]\left[1+\frac{(P_M-P_{M0})\,D_{M0}}{t_{M0}E_M}\right]}{[1+3\alpha_F(T_M-T_{M0})]\left[1-\frac{(P_M-P_{M0})}{E_F}\right]}\ . \quad (65)$$

Acknowledgment

This manuscript has evolved and been assembled as the results of many contributions, direct and indirect, from many sources—NIST staff, DoD metrologists, industrial personnel, and the flow measurement staff members in several national laboratories in Canada, Italy, and the U.K. Special thanks are due to K.R. Benson, NIST, Gaithersburg, for his reactions and contributions all through this effort; ideas and suggestions have also been incorporated from NIST Fluid Flow Group staff members: W. G. Cleveland, D. E. Hess, and N. E. Mease. It is especially pertinent to acknowledge the significant inputs and contributions made to these tests and this paper by V. Grabe, P. Olivier, and D. Ruffner. The secretarial contributions made by Mrs. G. M. Kline, NIST Fluid Flow Group, toward the production of this document are most gratefully acknowledged. In the DoD areas, it is pertinent to cite, alphabetically: Air Force: W. Callis, K. Hartz, B. Keeley, and J. Sharp; Army: J. Miller and D. Sherk; Navy: R. Cheesman, M. Gee, B. McBurney, and D. Todd.

10. References

[1] G. E. Mattingly, Calibration Techniques and Traceability, in Developments in Flow Measurement I, ed. R. W. W. Scott, Applied Science Publishers, New York and London (1982).

[2] G. E. Mattingly, Volume Flow Measurement, in Fluid Mechanics Measurements, Hemisphere Publishing Co., New York (1979).

[3] ASME/ANSI Standard: Glossary of Terms for Fluid Flowrate Measurement, MFC 1 M, 1991, ASME-New York.

[4] ASME/ANSI Standard: Measurement of Liquid Flow in Closed Conduits by Weighing Methods, MFC-9M, 1988, ASME-New York.

[5] R. A. Furness, Turbine Flowmeters, in Developments in Flow Measurement I, ed. R.W.W. Scott, Applied Science Publishers, New York and London (1982).

[6] M. R. Shafer, Performance Characteristics of Turbine Flowmeters, Trans. ASME, J. Basic Eng. **84**, 1369-79 (1962).

[7] H. M. Hochreiter, Dimensionless Correlation of Coefficients of Turbine-Type Flowmeters, Trans. ASME **80**, 1363-68 (1958).

[8] W. F. Z. Lee, and H. Karlby, A Study of the Viscosity Effect and Its Compensation on Turbine-Type Flowmeters, Trans. ASME, J. Basic Eng. **82**, 717-28 (1960).

[9] S. Kohan, and W. H. Schwarz, Low Speed Calibration Formula for Vortex Shedding From Cylinders, Phys. Flds. **16** (9) 1528-9 (1973).

[10] ISA Recommended Practice Specification, Installation and Calibration of Turbine Flowmeters, ISA-RP 31.1, Instrument Society of America, Res. Tri. Pk. NC (1977).

***About the author:** Dr. George E. Mattingly is a mechanical engineer who leads the Fluid Flow Group in the Process Measurements Division of the NIST Chemical Science and Technology Laboratory. The National Institute of Standards and Technology is an agency of the Technology Administration, U.S. Department of Commerce.*

Volume 97, Number 5, September-October 1992
Journal of Research of the National Institute of Standards and Technology

[J. Res. Natl. Inst. Stand. Technol. 97, 533 (1992)]

A General Waveguide Circuit Theory

Volume 97 Number 5 September-October 1992

Roger B. Marks and
Dylan F. Williams

National Institute of Standards
and Technology,
Boulder, CO 80303

This work generalizes and extends the classical circuit theory of electromagnetic waveguides. Unlike the conventional theory, the present formulation applies to all waveguides composed of linear, isotropic material, even those involving lossy conductors and hybrid mode fields, in a fully rigorous way. Special attention is given to distinguishing the traveling waves, constructed with respect to a well-defined characteristic impedance, from a set of pseudo-waves, defined with respect to an arbitrary reference impedance. Matrices characterizing a linear circuit are defined, and relationships among them, some newly discovered, are derived. New ramifications of reciprocity are developed. Measurement of various network parameters is given extensive treatment.

Key words: characteristic impedance; circuit theory; microwave measurement; network analyzer; pseudo-waves; reciprocity; reference impedance; transmission line; traveling waves; waveguide.

Accepted: May 22, 1992

Contents

1. Introduction 534
2. Theory of a Uniform Waveguide Mode 537
   2.1 Modal Electromagnetic Fields 537
   2.2 Waveguide Voltage and Current .. 538
   2.3 Power 538
   2.4 Characteristic Impedance 539
   2.5 Normalization of Waveguide Voltage and Current 540
   2.6 Transmission Line Equivalent Circuit 540
   2.7 Effective Permittivity and Measurement of Characteristic Impedance 543
3. Waveguide Circuit Theory 543
   3.1 Traveling Wave Intensities 543
   3.2 Pseudo-Waves 544
   3.3 Voltage Standing Wave Ratio 546
   3.4 Scattering and Pseudo-Scattering Matrices 547
   3.5 The Cascade Matrix 548
   3.6 The Impedance Matrix 548
   3.7 Change of Reference Impedance . 548
   3.8 Multiport Reference Impedance Transformations 549
   3.9 Load Impedance 550
4. Waveguide Metrology 551
   4.1 Measurability and the Choice of Reference Impedance 551
   4.2 Measurement of Pseudo-Waves and Waveguide Voltage and Current .. 555
5. Alternative Circuit Theory Using Power Waves 555
6. Appendix A. Reduction of Maxwell's Equations 556

7. Appendix B. Circuit Parameter Integral Expressions 557
8. Appendix C. Relations Between p_0 and γ.......................... 558
9. Appendix D. Reciprocity Relations.......................... 559
10. Appendix E. Relations Between Z and S.......................... 560
11. Appendix F. Renormalization Table 561
12. References 561

1. Introduction

Classical waveguide circuit theory, of which Refs. [1,2,3,4] are representative, proposes an analogy between an arbitrary linear waveguide circuit and a linear electrical circuit. The electrical circuit is described by an *impedance matrix*, which relates the normal electrical currents and voltages at each of its terminals, or ports. The waveguide circuit theory likewise defines an impedance matrix relating the *waveguide voltage* and *waveguide current* at each port. In both cases, the characterization of a network is reduced to the characterization of its component circuits. The primary caveat of waveguide circuit theory is that, at each port, a pair of identical waveguides must be joined without discontinuity and must transmit only a single mode, or at most a finite number of modes.

A great deal of confusion regarding waveguide circuits arises from the tendency to overemphasize the analogy to electrical circuits. In fact, important differences distinguish the two. For instance, the waveguide voltage and current, in contrast to their electrical counterparts, are highly dependent on definition and normalization. Also, the general conditions satisfied by the impedance matrix are different in the two cases. Furthermore, only the waveguide circuits, not electrical ones, are describable in terms of traveling waves. The latter two distinctions have been particularly neglected in the literature. In this introduction, we discuss all three of these differences and their relationship to the general waveguide circuit theory.

All waveguide circuit theories are based on some defined waveguide voltage and current. These definitions rely upon the electromagnetic analysis of a single, uniform waveguide. Eigenfunctions of the corresponding electromagnetic boundary value problem are waveguide modes which propagate in either direction with an exponential dependence on the axial coordinate. When limited to a single mode, the field distribution is completely described by a pair of complex numbers indicating the complex intensity (amplitude and phase) of these two counterpropagating *traveling waves*. The waveguide voltage and current, which are related to the electric and magnetic fields of the mode, are linear combinations of the two traveling wave intensities. This linear relationship depends on the *characteristic impedance* of the mode.

The classical definition of the waveguide voltage and current is suitable only for modes which are TE (transverse electric), TM (transverse magnetic), or TEM (transverse electromagnetic). This includes many conventional waveguides, such as lossless hollow waveguide and coaxial cable. However, modes of guides with transversely nonuniform material parameters are generally hybrid rather than TE, TM, or TEM. Thus, the classical theory is inapplicable to multiple-dielectric guides, such as microstrip, coplanar waveguide, and optical fiber waveguide. Neither does it apply to lines containing an imperfect conductor, for a lossy conductor essentially functions as a lossy dielectric. This limitation has become increasingly important with the proliferation of miniature, integrated-circuit waveguides, in which the loss is a nonnegligible factor.

In the absence of a general theory, the most popular treatment of arbitrary waveguides is based on an engineering approach (for example, Ref. [5]). The procedure makes use of the fact that, in TE, TM, and TEM modes, the conventional waveguide voltage and current obey the same telegrapher's equations which govern propagation in a low-frequency transmission line. The characteristic impedance, which enters the telegrapher's equations, can be written in terms of equivalent circuit parameters *C*, *G*, *L*, and *R*. Engineers assume that waveguide voltages and currents satisfying the telegrapher's equations continue to exist for hybrid and lossy modes. Heuristic arguments, based on low-frequency circuit theory, are used to compute the equivalent circuit parameters, and those parameter estimates are used to determine the characteristic impedance from the conventional expression.

In fact, a practical, general definition of waveguide voltage v and current i is easily constructed using methods analogous to those applied to ideal TE, TM, and TEM modes. The basic principle [1, pp. 76–77] is that, for consistency with electrical circuit theory, v and i should be related to the complex power p by $p = vi^*$. This ensures that v and i

are proportional to the transverse electric and magnetic fields. Reference [1] declines to further specify v and i, arguing that their ratio v/i is irrelevant and arbitrary. In fact, v/i is often pertinent. When only the forward-propagating mode exists, then $v/i = Z_0$, the characteristic impedance. As pointed out by Brews [6], Z_0 is not entirely arbitrary; the relationship $p = vi^*$ determines the phase of v/i and therefore of Z_0. The magnitude of Z_0 is formally arbitrary, but its normalization plays a significant role in many problems. The greatest contribution of Ref. [6] is that it defines the equivalent circuit parameters in terms of the characteristic impedance, rather than *vice versa,* and thereby derives explicit expressions for C, G, L, and R in terms of the modal fields.

In Sec. 2 of this paper, we present a complete theory of uniform waveguide modes, beginning from first principles. We modify Brews' definition of the waveguide voltage and current with an alternate normalization devised to simplify the results. We also modify his procedure to simplify the derivation.

In Sec. 3, we proceed to develop a general waveguide circuit theory based on the results of Sec. 2. A number of conclusions presented herein are at odds with not only the electrical circuit theory but also the classical waveguide circuit theory. This is expected, for the classical theory fails to account for losses. The inadequacy of the classical waveguide circuit theory is emphasized by several surprising results of the new theory. For example, the classical theory concludes that the waveguide impedance matrix, like its counterpart in electrical circuit theory, is symmetric when the circuit is composed of reciprocal matter. Here, we demonstrate that this conclusion is not generally valid when lossy waveguide ports are allowed.

Even with the waveguide voltage and current rigorously and consistently defined and with a proper accounting of waveguide loss, another major shortcoming of the classical theory remains: the classical waveguide circuit theory fails to appreciate the subtleties of the *scattering matrix*, which, like the impedance matrix, characterizes the circuit, but which relates the traveling wave intensities instead of the waveguide voltages and currents. A good understanding of the scattering matrix, which is related to the impedance matrix by a one-to-one transformation based on the modal characteristic impedance, is vital to a practical waveguide circuit theory, for the scattering matrix is an essential part of an *operational* definition of the impedance matrix. The reason for this, as we discuss in Sec. 4, is that practical waveguide instrumentation is nearly always based on the measurement of waves or similar quantities. In contrast, waveguide voltages and currents, like the fields with which they are defined, are virtually inaccessible experimentally.

The scattering matrix provides a clear distinction between waveguide and electrical circuits, for the scattering matrix has no direct counterpart in electrical circuit theory. Electrical circuits are *not* subject to a traveling wave/scattering matrix description because electrical circuits are not generally composed of uniform waveguides with exponential traveling waves. This is why it is meaningless to speak of the characteristic impedance of an arbitrary electrical port. Nevertheless, the electrical circuit theory mocks the waveguide theory by introducing an arbitrary *reference impedance*. This parameter is used in place of the characteristic impedance in a transformation identical to that relating the corresponding waveguide parameters, resulting in analogous quantities which are often (confusingly) called "traveling waves." However, since these are not true traveling waves and possess no wave-like characteristics, we prefer to use the term *pseudo-waves*. The relationship between the pseudo-waves is described by a matrix, often (confusingly) called a "scattering matrix," which we instead call a *pseudo-scattering matrix*.

In contrast to the characteristic impedance, the reference impedance is completely arbitrary. Classical waveguide circuit theory, along with electrical circuit theory, has failed to explicitly recognize this distinction.

While the scattering matrix is incompatible with electrical circuit theory, the pseudo-scattering matrix is compatible with both waveguide and electrical theories. In this paper, we define waveguide pseudo-waves exactly as in the electrical circuit theory, using the waveguide voltage and current and an arbitrary reference impedance. These waveguide pseudo-waves cannot be interpreted as traveling waves but are a linear combination of the traveling waves.

By defining the pseudo-scattering matrix for waveguide as well as electrical circuits, we establish a description common to both. On the other hand, such a common description also exists in the form of the impedance matrix. Why do we require both impedance matrix and pseudo-scattering matrix descriptions? This question has at least three answers, which we now enumerate.

The first answer is that the commonality of the two theories allows the common use of tools developed for one of the two applications. These tools include a number of analytical theorems and results as well as a great deal of measurement and computer-aided design software. Users should be able to take advantage of tools using both impedance matrix and pseudo-scattering matrix descriptions. Furthermore, many tools require *both* descriptions. For example, the Smith chart connects the two in a concise and familiar way.

The second answer has to do with measurement. Electrical circuits are measured in terms of voltages and currents and are therefore fundamentally characterized by impedance matrices. In contrast, the waveguide voltage and current are related to electromagnetic fields which are rarely, if ever, subject to direct measurement. Instead, waveguide circuits are measured in terms of traveling waves and pseudo-waves. For example, a slotted line, traditionally used for waveguide circuit measurement, relies on interference between the traveling waves. Most modern waveguide measurements use a network analyzer. We show in this paper that calibrated network analyzers measure pseudo-waves, defined with respect to a reference impedance determined by the calibration. This reference impedance need not equal the characteristic impedance of the waveguide, so the measured pseudo-waves need not be the actual traveling waves.

The third reason that both impedance and pseudo-scattering descriptions are important is that both are needed to analyze the interconnection of a waveguide with an electrical circuit or with a dissimilar waveguide. Such an analysis typically makes use of two assumptions. The first is that the waveguide fields near the interconnection are composed of a single mode; this assumption may lead to an acceptable result even though the discontinuity virtually always ensures that it is inexact. The second assumption is that the (waveguide or electrical) voltage and current in that single mode are continuous at the interface. This is a generalization of a result from electrical circuit theory that is of questionable validity for waveguide circuits. Due to these two assumptions, any simple analysis of this problem is at best approximate. However, if it is to be applied, the matching conditions on the voltage and current may be directly implemented in terms of impedance parameters, while the waveguides are characterized in terms of scattering or pseudo-scattering parameters. Both sets of parameters are therefore required to solve the problem.

A good example of this kind of problem is the interconnection of a TEM or quasi-TEM waveguide with an electrical circuit which is small compared to a wavelength. In this case, the single-mode approximation may be valid, and the conventional impedance-matching method may be useful if the waveguide voltage and current are defined to be compatible with the electrical voltage and current. The canonical problem of this form is the termination of a planar, quasi-TEM waveguide, such as a microstrip line, with a small, "lumped" resistor. Such problems, while unusual in the study of conventional waveguides, are typical of planar circuits and have become increasingly important with their proliferation. The theory presented here supports the experimental study of these problems using conventional microwave instrumentation.

Although our introduction of pseudo-waves entails some new terminology, these quantities are not new discoveries. They implicitly provide the basis of the conventional "scattering matrix" description of electrical circuit theory. Furthermore, while they have not heretofore been explicitly introduced into waveguide circuit theory, they have been applied, perhaps unconsciously, to waveguide circuits by those unaware of the distinctions between the two theories.

An important contrast to the pseudo-wave theory is an alternative known as the theory of "complex port numbers" [7]. This theory defines what it calls "traveling waves" and corresponding "scattering matrices" in a way that is fundamentally different from that described here. The theory itself was originally applied to electrical circuits and remains popular in that context. It has also been extended to waveguide analysis, where it is known as the theory of "power waves" [8]. Here we demonstrate previously-unknown properties of the "power wave scattering matrix" of a waveguide circuit. Furthermore, we show that the power waves are different from not only the pseudo-waves but also the actual traveling waves propagating in a waveguide. As a result, they present some serious complications, discussed in the text. Practitioners of the waveguide arts must be aware that conventional analysis and measurement techniques do *not* determine relations between power waves. Confusion concerning this matter is prevalent.

In this paper, we comprehensively construct a complete waveguide circuit theory from first principles. Beginning with Maxwell's equations in an axially independent region, we define the waveguide voltage and current, the characteristic impedance, and the four equivalent circuit parameters of the mode. We then define traveling wave intensities, which are normalized to the characteristic impedance, and pseudo-waves, which are normalized to some arbitrary reference impedance.

We discuss in detail the significance of the waves and study expressions for the power. We introduce various matrices relating the voltages, currents, and waves in the ports of a waveguide circuit and describe the properties of those matrices under typical physical conditions. We extensively investigate the problems of measuring these quantities.

Although the normalizations in many of the definitions introduced here are unfamiliar, we have striven to ensure that each parameter is defined in accordance with common usage and with the appropriate units. Awkward definitions are occasionally required to achieve convenient results.

2. Theory of a Uniform Waveguide Mode

In this section, we develop a basic description of a waveguide mode. Beginning with Maxwell's equations, we define the waveguide voltage and current, power, characteristic impedance, and transmission line equivalent circuit parameters. We close with a discussion of the measurement of characteristic impedance.

2.1 Modal Electromagnetic Fields

We begin by defining a uniform waveguide very broadly as an axially independent structure which supports electromagnetic waves. In such a geometry, we seek solutions to the source-free Maxwell equations with time dependence $e^{+j\omega t}$. Here we consider only problems involving isotropic permittivity and permeability, although some of the results are easily generalized (see Appendix A). We need to prescribe the appropriate boundary conditions at interfaces and impenetrable surfaces. If the waveguide is transversely open, the region is unbounded, and boundary conditions at infinity, sufficient to ensure finite power, are also required; this excludes leaky modes. The eigenvalue problem is separable and the axial solutions are exponential. In general, there are many linearly independent solutions to this problem, each of which is proportional to a mode of the waveguide. In this paper, we restrict ourselves to consideration of a single mode which propagates in both directions. Most of the results are easily generalized to any finite number of propagating modes.

We introduce complex fields whose magnitude is the root-mean-square of the time-dependent fields, as in Ref. [9], and orient our z-axis along the waveguide axis. For a mode propagating in the forward (increasing z) direction, the normalized modal electric and magnetic fields will be denoted by $\mathbf{e}e^{-\gamma z}$ and $\mathbf{h}e^{-\gamma z}$, respectively, where $\mathbf{e}$ and $\mathbf{h}$ are independent of z. Although it need not be specified here, some arbitrary but fixed normalization is required to ensure uniqueness of $\mathbf{e}$ and $\mathbf{h}$. The modal propagation constant γ is composed of real and imaginary components α and β:

$$\gamma \equiv \alpha + j\beta. \tag{1}$$

Split $\mathbf{e}$ and $\mathbf{h}$ into their transverse ($\mathbf{e}_t$ and $\mathbf{h}_t$) and longitudinal ($e_z\mathbf{z}$ and $h_z\mathbf{z}$) components, where $\mathbf{z}$ is the longitudinal unit vector. As shown in Appendix A, the homogeneous Maxwell equations with isotropic permittivty and permeability can be expanded as

$$\nabla \times \mathbf{e}_t = -j\omega\mu h_z \mathbf{z}, \tag{2}$$

$$\gamma \mathbf{e}_t + \nabla e_z = -j\omega\mu \mathbf{z} \times \mathbf{h}_t, \tag{3}$$

$$\nabla \times \mathbf{h}_t = +j\omega\epsilon e_z \mathbf{z}\ , \tag{4}$$

$$\gamma \mathbf{h}_t + \nabla h_z = +j\omega\epsilon \mathbf{z} \times \mathbf{e}_t, \tag{5}$$

$$\epsilon \nabla \cdot \mathbf{e}_t + \mathbf{e}_t \cdot \nabla \epsilon = \epsilon \gamma e_z\ , \tag{6}$$

and

$$\mu \nabla \cdot \mathbf{h}_t + \mathbf{h}_t \cdot \nabla \mu = \mu \gamma h_z\ . \tag{7}$$

We expressly exclude discussion of the case $\omega = 0$, to which many of the results in this paper do not apply due to the decoupling of $\mathbf{e}$ and $\mathbf{h}$.

To get a better understanding of the eigenvalue problem, we can eliminate either $\mathbf{e}_t$ or $\mathbf{h}_t$ from Eqs. (3) and (5) and thereby derive the explicit expressions for the transverse fields in terms of the axial fields

$$(\omega^2\mu\epsilon + \gamma^2)\mathbf{e}_t = -\gamma \nabla e_z + j\omega\mu \mathbf{z} \times \nabla h_z \tag{8}$$

and

$$(\omega^2\mu\epsilon + \gamma^2)\mathbf{h}_t = -\gamma \nabla h_z - j\omega\epsilon \mathbf{z} \times \nabla e_z\ . \tag{9}$$

Differential equations for the axial fields are

$$(\nabla^2 + \omega^2\mu\epsilon + \gamma^2)e_z = \frac{\gamma}{\epsilon}\mathbf{e}_t \cdot \nabla \epsilon \tag{10}$$

and

$$(\nabla^2 + \omega^2\mu\epsilon + \gamma^2)h_z = \frac{\gamma}{\mu}\mathbf{h}_t \cdot \nabla \mu\ . \tag{11}$$

These equations are in general quite complicated. In many conventional waveguides, ϵ and μ are piecewise homogeneous, so the right sides of Eqs. (10) and (11) vanish. Even so, these equations remain complicated since the various fields components are coupled through the boundary conditions.

In general, the solutions of the boundary value problem possess a full suite of field components. In certain cases, it may be possible to find either a TE ($e_z = 0$) or TM ($h_z = 0$) solution. Equations (8) and (9) ensure that TEM ($e_z = h_z = 0$) solutions exist only in domain of homogeneous $\mu\epsilon$ with the eigenvalue γ satisfying $\gamma^2 = -\omega^2\mu\epsilon$. This forbids TEM solutions in the presence of multiple dielectrics, as exist in open planar waveguides or waveguides bounded by lossy conductors.

Equations (2)–(7) prohibit nontrivial modes with either $\mathbf{e}_t = 0$ or $\mathbf{h}_t = 0$, except when $\gamma = 0$. This degenerate case, which corresponds to mode of a lossless waveguide operating at exactly the cutoff frequency, is discussed in Appendix C.

2.2 Waveguide Voltage and Current

Recall that $\mathbf{e}_t$, $e_z\mathbf{z}$, $\mathbf{h}_t$, and $h_z\mathbf{z}$, satisfying Eqs. (2)–(7) with the propagation constant γ, represent the fields of the mode propagating in the forward direction. Clearly, the fields $\mathbf{e}_t$, $-e_z\mathbf{z}$, $-\mathbf{h}_t$, and $h_z\mathbf{z}$ satisfy the same equations with a propagation constant of $-\gamma$. These latter fields represent the normalized *backward* propagating mode. The distinction between the forward and backward modes is made below.

In general, the *total* fields $\mathbf{E}$ and $\mathbf{H}$ in a single mode of the waveguide are linear combinations of the forward and backward mode fields. Their transverse components can therefore be represented by

$$\mathbf{E}_t = c_+ e^{-\gamma z}\mathbf{e}_t + c_- e^{+\gamma z}\mathbf{e}_t \equiv \frac{v(z)}{v_0}\mathbf{e}_t \tag{12}$$

and

$$\mathbf{H}_t = c_+ e^{-\gamma z}\mathbf{h}_t - c_- e^{+\gamma z}\mathbf{h}_t \equiv \frac{i(z)}{i_0}\mathbf{h}_t . \tag{13}$$

We will call v and i the *waveguide voltage* and *waveguide current*. The introduction of the normalization constants v_0 and i_0 allows v and v_0 to have units of voltage, i and i_0 to have units of current, and $\mathbf{E}_t$, $\mathbf{H}_t$, $\mathbf{e}_t$, and $\mathbf{h}_t$ to have units appropriate to fields. Other waveguide theories omit v_0 and i_0 and therefore require unnatural dimensions.

For basis functions, we have chosen to use the normalized field functions $\mathbf{e}_t$ and $\mathbf{h}_t$, whereas conventional waveguide theories choose arbitrary multiples of $\mathbf{e}_t$, and $\mathbf{h}_t$. The present formulation is conceptually simpler since $\mathbf{e}_t$ and $\mathbf{h}_t$ are the fields in the normalized forward-propagating mode. This mode has propagation constant γ, waveguide voltage $v(z) = v_0 e^{-\gamma z}$, and waveguide current $i(z) = i_0 e^{-\gamma z}$. For the normalized backward-propagating mode, the propagation constant is $-\gamma$, $v(z) = v_0 e^{+\gamma z}$, and $i(z) = -i_0 e^{+\gamma z}$.

2.3 Power

The net complex power $p(z)$ crossing a given transverse plane is given by the integral of the Poynting vector[1] over the cross section S:

$$p(z) \equiv \int_S \mathbf{E}_t \times \mathbf{H}_t^* \cdot \mathbf{z}\,\mathrm{d}S = \frac{v(z)i^*(z)}{v_0 i_0^*} p_0 , \tag{14}$$

where we have defined

$$p_0 \equiv \int_S \mathbf{e}_t \times \mathbf{h}_t^* \cdot \mathbf{z}\,\mathrm{d}S. \tag{15}$$

In accordance with the analogy to electrical circuit theory, we require that

$$p = vi^*. \tag{16}$$

This cannot be achieved with arbitrary choices of the normalization constants v_0 and i_0. Therefore we impose the constraint

$$p_0 = v_0 i_0^*, \tag{17}$$

which allows Eqs. (14) and (16) to be simultaneously satisfied. Either v_0 or i_0 may be chosen arbitrarily; the other is determined by Eq. (17).

The magnitude of p_0 depends on the normalization which determined the modal fields $\mathbf{e}$ and $\mathbf{h}$; in fact, Eq. (15) can even be used to specify the normalization. The *phase* of p_0 does *not* depend on this normalization since the phase relationship between $\mathbf{e}$ and $\mathbf{h}$ is fixed, to within a sign, by Maxwell's equations. This sign ambiguity can be resolved by explicitly distinguishing between the forward and backward modes. The most concise means of making this distinction is to define the forward mode as that in which the power flows in the $+z$ direction; that is,

$$\mathrm{Re}(p_0) \geqslant 0. \tag{18}$$

---

[1] The magnitude of the complex fields was defined to be the root-mean-square, rather than the peak, of the time-dependent fields. This accounts for the absence of the factor 1/2 in the expression for the power.

The ambiguity remains if $\mathrm{Re}(p_0)=0$, as occurs in an evanescent waveguide mode. In this case, we use the alternative condition $\mathrm{Re}(\gamma)>0$, which forces the mode to decay with z. With Eq. (18) or its alternative, the phase of p_0 is unambiguous, except in the degenerate case $p_0=0$.

The average power flow $P(z)$ across S is given by the real part of $p(z)$ as

$$P(z) \equiv \mathrm{Re}[p(z)] = \mathrm{Re}\int_S E_t \times H_t^* \cdot z \,\mathrm{d}S = Re(vi^*). \quad (19)$$

When only the normalized forward mode is present, the complex power is $p(z)=p_0e^{-2\alpha z}$. When only the normalized backward mode is present, the complex power is $-p_0e^{+2\alpha z}$. The associated average powers are $\mathrm{Re}(p_0)e^{-2\alpha z}$ and $-\mathrm{Re}(p_0)e^{+2\alpha z}$, respectively. The signs differ because the forward mode carries power in the $+z$ direction and the backward mode in the $-z$ direction.

The power is *not* generally a linear combination of the forward and backward mode powers, since it is given by the nonlinear expression in Eq. (19). This means that the net real power P is in general *not* simply the difference of the powers carried by the forward and backward modes. This issue is discussed at greater length below.

2.4 Characteristic Impedance

We define the forward-mode characteristic impedance by

$$Z_0 \equiv v_0/i_0 = |v_0|^2/p_0^* = p_0/|i_0|^2 . \quad (20)$$

The equivalence of these expressions again demonstrates the analogy to electrical circuit theory. Brews [6, 10] also defines the voltage, current, power, and characteristic impedance so as to satisfy Eq. (20) and refers to Schelkunoff's point [11] that the equivalence of these three definitions of Z_0 follows from Eq. (17). The three definitions would in general be inconsistent if p_0, v_0, and i_0 were defined independently (for example, in terms of some power, voltage drop, and current in the waveguide) without regard to Eq. (17).

Z_0 is independent of the normalization of the modal fields $\boldsymbol{e}$ and $\boldsymbol{h}$ which affected $|p_0|$. While its magnitude *does* depend on the choice of either v_0 or i_0, its *phase* is identical to that of p_0 and therefore independent of all normalizations. As pointed out by Refs. [6] and [10], the phase of the characteristic impedance Z_0 is a fixed, inherent, and unambiguous property of the mode. A sign ambiguity would have remained had we not imposed Eq. (18) since, due to the sign reversal in the current, the characteristic impedance of the backward mode is $-Z_0$. However, Eqs. (18) and (20) constrain the sign of Z_0 such that

$$\mathrm{Re}(Z_0) \geqslant 0. \quad (21)$$

In particular, as we will see below, the characteristic impedance of any propagating mode of a *lossless* line is real and positive. Equation (21) serves to completely specify Z_0 unless $\mathrm{Re}(Z_0)=0$, in which case the alternative condition $\mathrm{Re}(\gamma)>0$ suffices to make the distinction.

When only a multiple of the forward-propagating mode exists, then $v(z)/i(z)=Z_0$ for all z and at any amplitude. Likewise, when only a multiple of the backward mode exists, then $v(z)/i(z)=-Z_0$. If both forward and backward modes are present, v/i depends on z due to interference between the two.

In order to illustrate the close correspondence between this definition of Z_0 and conventional definitions of the characteristic impedance, we consider the special case of TE, TM, or TEM modes in homogeneous matter. Each of these has fields which satisfy

$$z \times \boldsymbol{e}_t = \eta \boldsymbol{h}_t, \quad (22)$$

where the wave impedance η is constant over the cross section. In this case,

$$Z_0 = \frac{|v_0|^2}{\int_S |\boldsymbol{e}_t|^2 \mathrm{d}S}\,\eta . \quad (23)$$

Since the modal field $\boldsymbol{e}_t$ is normalized, the denominator is fixed. The magnitude of Z_0 therefore depends only on v_0. However, *the phase of the characteristic impedance is equal to that of the wave impedance.* This corresponds to most conventional definitions.

For TEM modes, η is equal to the intrinsic wave impedance $\sqrt{\mu/\epsilon}$ ($\approx 377\ \Omega$ in free space), with the result that

$$\arg(Z_0) = \frac{1}{2}(\arg(\mu) - \arg(\epsilon)). \quad (24)$$

For example, if μ is real then

$$\arg(Z_0) = -\frac{1}{2}\,\delta, \quad (25)$$

where $\tan\delta \equiv \mathrm{Im}(\epsilon)/\mathrm{Re}(\epsilon)$ is the dielectric loss tangent.

When v_0 is chosen to be the voltage between the ground and signal conductors, Z_0 is equal to the conventional TEM characteristic impedance.

For TE and TM modes,

$$\eta = \sqrt{\frac{\mu}{\epsilon}}\left(1-\frac{k_c^2}{\omega^2\mu\epsilon}\right)^{\pm 1/2}, \tag{26}$$

where "+" corresponds to TM and "−" to TE and k_c is the cutoff wavenumber.

2.5 Normalization of Waveguide Voltage and Current

Although the phase of either v_0 or i_0 can be chosen arbitrarily, the choice is of little significance. The important quantity is the phase *relationship* between v_0 and i_0, which, due to the constraint (17) and the fact that the phase of p_0 is fixed, is unalterable. The phase relationship between v_0 and i_0 is a unique property of the mode.

The *magnitude* of Z_0 is determined by the choice of v_0 or i_0. Given the constraint [(Eq. 17)], and having selected a modal field normalization, we may independently assign only one of these two variables. One useful normalization defines the constant v_0 by analogy to a voltage using the path integral

$$v_0 = -\int_{\text{path}} \boldsymbol{e}_t \cdot \mathrm{d}\boldsymbol{l}. \tag{27}$$

The path is confined to a single transverse plane with the restriction that $v_0 \neq 0$. This can always be arranged unless $\boldsymbol{e}_t = 0$ everywhere, but this occurs only in the degenerate case $\gamma = 0$. The integral does not in general represent a potential difference because it depends on the path between a given pair of endpoints. In certain cases, such as when the mode is TM or TEM, the integral depends only on the endpoints, not on the path between them.

Although the path is arbitrary, certain choices are often natural. With a TEM mode, for example, we can put an endpoint on each of two active conductors so that v_0 becomes the path-independent voltage drop across them at $z = 0$ in the normalized mode. In this case, Z_0 is equal to the conventional TEM characteristic impedance. We may not have both endpoints on the same conductor, for then $v_0 = 0$. The same is true of TM modes.

A result of Eq. (27) is that v is also analogous to voltage:

$$v(z) = -\int_{\text{path}} \boldsymbol{E}_t(z) \cdot \mathrm{d}\boldsymbol{l}\,. \tag{28}$$

The normalization in Eq. (27) yields what is known as a "power-voltage" definition of the characteristic impedance, even though the "voltage" is not an actual potential difference. Another useful possibility is a "power-current" definition, choosing i_0 to be a current. Yet another choice, popular for hollow waveguides, is to normalize so that $|Z_0| = 1$. It is not our intent to debate the issue of the optimal definition. However, it is only the magnitude, not the phase, of Z_0 that is open for discussion.

A "voltage-current" definition, popular in the literature, is generally forbidden by Eq. (20), since an arbitrarily specified v_0 and i_0 may not be of the appropriate phase to satisfy $v_0/i_0 = Z_0$.

Appendix F includes a table displaying the effects of renormalizing v_0 and $\boldsymbol{e}_t$ on all of the parameters used in this work.

2.6 Transmission Line Equivalent Circuit

We now develop a transmission line analogy by defining real equivalent circuit parameters C, L, G, and R, analogous to the capacitance, inductance, conductance, and resistance per unit length of conventional transmission line theory. The four parameters are defined by

$$j\omega C + G \equiv \frac{\gamma}{Z_0} \tag{29}$$

and

$$j\omega L + R \equiv \gamma Z_0. \tag{30}$$

Equations (29) and (30) are identical to those derived from the electrical circuit theory description of a transmission line with distributed shunt admittance $j\omega C + G$ and series impedance $j\omega L + R$, as shown in Fig. 1. These quantities also appear in the conventional transmission line equations satisfied by v and i:

$$\frac{\mathrm{d}v}{\mathrm{d}z} = -(j\omega L + R)i \tag{31}$$

and

$$\frac{\mathrm{d}i}{\mathrm{d}z} = -(j\omega C + G)v. \tag{32}$$

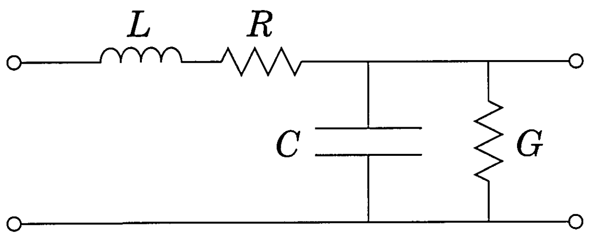

Fig. 1. Equivalent circuit model of transmission line.

Although Eqs. (29) and (30) provide unique definitions of the four circuit parameters, it is possible to cast them into another form which is more convenient for many purposes, as is done by Brews [6]. A simpler derivation, given in Appendix B, shows that the circuit parameters are given exactly by

$$C=\frac{1}{|v_0|^2}\left[\int_S \epsilon'|e_t|^2\mathrm{d}S-\int_S \mu'|h_z|^2\mathrm{d}S\right], \qquad (33)$$

$$L=\frac{1}{|i_0|^2}\left[\int_S \mu'|h_t|^2\mathrm{d}S-\int_S \epsilon'|e_z|^2\mathrm{d}S\right], \qquad (34)$$

$$G=\frac{\omega}{|v_0|^2}\left[\int_S \epsilon''|e_t|^2\mathrm{d}S+\int_S \mu''|h_z|^2\mathrm{d}S\right], \qquad (35)$$

and

$$R=\frac{\omega}{|i_0|^2}\left[\int_S \mu''|h_t|^2\mathrm{d}S+\int_S \epsilon''|e_z|^2\mathrm{d}S\right]. \qquad (36)$$

Here $\epsilon \equiv \epsilon' - j\epsilon''$ and $\mu \equiv \mu' - j\mu''$. In passive media, the four real components ϵ', ϵ'', μ', and μ'' are all nonnegative. Metal conductivity is not included as an explicit term in ϵ but is instead absorbed in ϵ''. In general, of course, ϵ and μ depend on ω.

The parameters C, L, G, and R depend on the same normalization that determines the magnitude of Z_0. For instance, when v_0 is chosen to be the voltage between two active conductors in a lossless TEM line, then C and L are the conventional capacitance and inductance per unit length. Certain combinations of these parameters, notably $G/(\omega C)$, $R/(\omega L)$, RC, RG, LC, and LG, are normalization-independent. For example, $LC=\epsilon'\mu'$ for a TEM line.

Equations (33) through (36) have many applications. In addition to providing a means of numerically calculating the circuit parameters from known fields, they offer opportunities for analytical calculations and approximations as well. The quadratic form in which the fields appear make them particularly useful for these purposes. Another major role they serve is in the attribution of circuit-parameter components to portions of the cross section. For example, it is common to divide the inductance L into an "external" inductance in the dielectric and an "internal" inductance in the imperfect metal. Such a division cannot be undertaken using only Eq. (30) but is readily obtainable by dividing the surface integral in Eq. (34) into dielectric and metal regimes.

Equations (29) and (30) imply the familiar expressions

$$\gamma=\sqrt{(j\omega L+R)\,(j\omega C+G)} \qquad (37)$$

and

$$Z_0=\sqrt{(j\omega L+R)/(j\omega C+G)}\,. \qquad (38)$$

The pairs of roots in Eqs. (37) and (38) correspond to the presence of both forward and backward modes, each of which have identical C, L, G, and R but opposite γ and Z_0. To distinguish the two, recall from Eq. (21) that the forward mode is defined such that $\mathrm{Re}(Z_0) \geqslant 0$. Either Eq. (29) or (30) can then be used to distinguish between the two values of γ. If the waveguide material is passive, then Eqs. (35) and (36) ensure that G and R are both nonnegative, which requires that $\alpha \equiv \mathrm{Re}(\gamma) \geqslant 0$. Thus, the fields of the mode that we have defined as the forward one must decay with increasing z in a lossy system. In general, however, the sign of α does not distinguish the forward and backward modes since $\alpha = 0$ in energy-conserving modes and may be negative in the presence of active media. Nevertheless, Eq. (18) ensures that the forward mode carries power only in the $+z$ direction.

C and L are typically positive for modes of common interest, in which the energy is primarily carried in the transverse fields and the second integrals of Eqs. (33) and (34) are relatively small. On the other hand, C and L may be zero or negative in certain cases. For instance, in the lossless case in which $\epsilon''=\mu''=0$, $G=R=0$ and Eqs. (37) and (38) become

$$(\epsilon''=\mu''=0) \Rightarrow \gamma=j\omega\sqrt{LC} \qquad (39)$$

and

$$(\epsilon''=\mu''=0) \Rightarrow Z_0=\sqrt{\frac{L}{C}} \qquad (40)$$

As shown in Appendix C, the modes of a *lossless* waveguide, except those with $p_0=0$, either propagate without attenuation ($\alpha \equiv \mathrm{Re}(\gamma)=0$) or are evanescent ($\alpha > 0$ but $\beta \equiv \mathrm{Im}(\gamma) = 0$). For the propagating modes, therefore, LC is nonnegative and thus Z_0 and p_0 are real. For the evanescent modes, Z_0 and p_0 are imaginary and the mode carries no average real power. Equation (39) shows that, for evanescent modes, either L or C, but not both, must be negative. For instance, TM modes have $h_z = 0$, so that C cannot be negative. As a result, $L > 0$ for propagating TM modes and $L < 0$ for evanescent TM modes. Complementary statements hold for lossless TE modes.

In lossy waveguides, we can no longer strictly distinguish "propagating" from "evanescent" modes, since generally α and β are both nonzero. Therefore, if we perturb a lossless TM mode by the addition of a minuscule amount of ϵ'', we find a mode that is not evanescent in a strict sense (since $\beta \neq 0$) but nevertheless has $L < 0$. In this way we prove that not all modes with $L < 0$ or $C < 0$ are strictly evanescent.

The allowed range of the phases of γ and Z_0 is determined by Eqs. (37) and (38). We assume for the moment that G and R are nonnegative, as in passive structures. In this case, if C and L are positive, then γ lies in the first quadrant and $-45° \leq \arg(Z_0) \leq 45°$. If in addition $G = 0$, a good approximation in many common quasi-TEM waveguides, then $45° \leq \arg(\gamma) \leq 90°$ and $-45° \leq \arg(Z_0) \leq 0°$. If instead $R = 0$, then again $45° \leq \arg(\gamma) \leq 90°$, but now $0° \leq \arg(Z_0) \leq 45°$. In lossless propagating modes, γ is positive imaginary and Z_0 positive real. Z_0 is also real in lossy lines in the special case $G/(\omega C) = R/(\omega L)$.

Figures (2) and (3) illustrate the allowed range of the phase of Z_0 and γ for various cases, as distinguished by the signs of L and C. G and R are assumed nonnegative in these figures.

Let us compare the current results to the conventional theory of TEM lines. For a lossless TEM line, G and R vanish, as do the second integrals in C and L. The remaining integrals in C and L are simply the energy per unit length stored in the electric and magnetic fields, respectively. Thus the expressions for C and L are simply the conventional expressions for the dc capacitance and inductance per unit length, as given by Collin [3]. When the dielectric is lossy but μ'' is zero, the mode may remain TEM but a shunt conductance G, given by the first term of Eq. (35) as in Ref. [3], is present.

For a general TEM line,

$$\text{(TEM)}: \; Z_0^2 = \frac{\epsilon' \mu}{\epsilon \mu'} \frac{L}{C} = \frac{\mu}{\mu'^2 \epsilon} L^2 = \frac{\mu \epsilon'^2}{\epsilon} \frac{1}{C^2}, \qquad (41)$$

which takes a more familiar form when $\epsilon'' = \mu'' = 0$.

When the metal boundaries are lossy or the dielectric is inhomogeneous, the mode is non-TEM. The second integrals in C and L, which are absent in Ref. [3], are quadratic in the longitudinal fields and may, in some quasi-TEM cases, prove to be negligible compared to the first terms. The expressions for C and G in general include contributions due to fields inside the metal that are not often appreciated. A nonzero series resistance R, given by the second integral in Eq. (36), may also appear whenever e_z and ϵ'' are nonzero; the integral extends over a lossy dielectric as well as an imperfect conductor. Collin does not provide a surface-integral expression for R, but it can be shown that Eq. (36) reduces to Collins line-integral expression when the surface-impedance approximation is invoked and the dielectric is lossless.

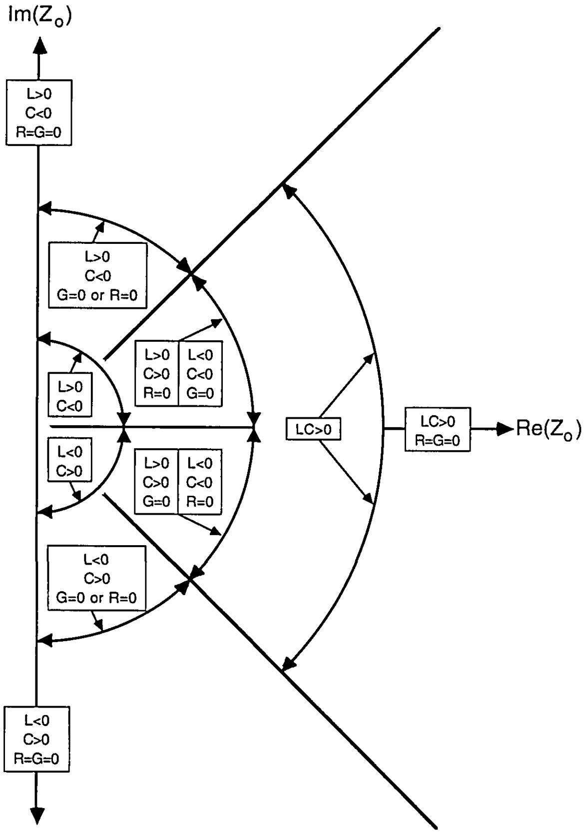

Fig. 2. Allowed ranges of the phase of Z_0 for various signs of the equivalent circuit parameters. The figure gives no indication of the magnitude of Z_0. G and R are assumed to be nonnegative.

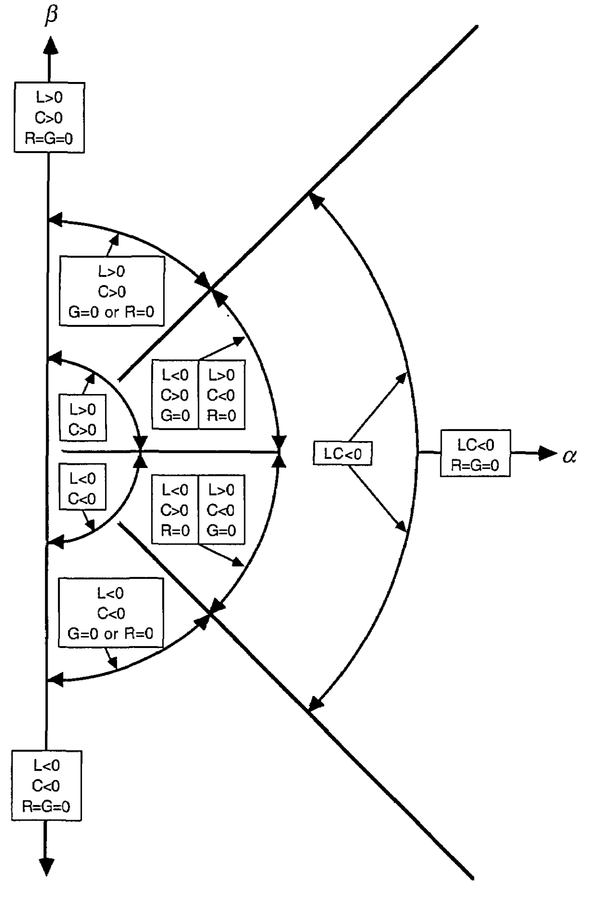

Fig. 3. Allowed ranges of the phase of γ for various signs of the equivalent circuit parameters. The figure gives no indication of the magnitude of γ. G and R are assumed to be nonnegative.

2.7 Effective Permittivity and the Measurement of Characteristic Impedance

It is useful and customary to define the effective relative dielectric constant (or permittivity) by

$$\epsilon_{r,eff} \equiv -(c\gamma/\omega)^2. \tag{42}$$

where c is the speed of light in vacuum. This definition equates γ to the propagation constant of a TEM mode in a fictitious medium of permittivity $\epsilon_{r,eff}\epsilon_0$ and permeability μ_0. We have no need to define an effective permeability.

Using Eq. (37),

$$\epsilon_{r,eff} = \frac{c^2}{\omega^2}[\omega^2 LC - RG - j\omega(LG + RC)]. \tag{43}$$

If, as is most common, C, L, G, and R are nonnegative, then $\mathrm{Im}(\epsilon_{r,eff}) \leq 0$. Although $\mathrm{Re}(\epsilon_{r,eff})$ is typically positive, it becomes negative in lossy lines at low frequencies if $RG > \omega^2 LC$. It is also negative for lossless, evanescent modes.

An alternative form of Eq. (29) is

$$Z_0 = \frac{\sqrt{\epsilon_{r,eff}}}{cC(1 + G/j\omega C)}, \tag{44}$$

which, as discussed in Ref. [12], may be applicable to the determination of Z_0. For example, if $G/(\omega C)$ is known, the phase of Z_0 is determined by the phase of $\epsilon_{r,eff}$. For TM modes in homogeneous dielectric, $G/(\omega C) = \tan\delta$, which is typically much less than 1 and can often be neglected. The same is true for typical quasi-TEM modes. In these cases, C is nearly independent of frequency and may be readily determinable [13]. If so, then Eq. (44) provides the magnitude as well as the phase of Z_0. This provides a practical method of determining Z_0, since $\epsilon_{r,eff}$ may be readily measured using standard microwave instrumentation to measure γ. By contrast, a direct measurement of Z_0 is impractical. For instance, the phase of Z_0 is defined as the phase of the complex power p_0, a quantity which is difficult to assess directly without detailed knowledge of the modal fields.

A similar method of determining Z_0 makes use of the relationship between Z_0, γ, L, and R described by Eq. (30). This method is often difficult to apply, particularly at low frequencies in the presence of lossy conductors, whose internal inductance and resistive loss typically make $R/(\omega L)$ nonnegligible and L and R strongly dependent on resistivity and frequency. In other cases, however, it may prove useful.

3. Waveguide Circuit Theory

In this section, we apply the results of Sec. 2 to develop a waveguide circuit theory. We first discuss traveling waves and pseudo-waves for a single uniform waveguide. These form the basis of the scattering and pseudo-scattering matrices. We also introduce the cascade and impedance matrices and discuss the transformation of reference impedance, concluding with an investigation of the load impedance.

3.1 Traveling Wave Intensities

We define the forward and backward traveling wave intensities (or simply traveling waves) a_0 and b_0 by normalizing the forward and backward modes of Eqs. (12) and (13):

$$a_0 \equiv \sqrt{\mathrm{Re}(p_0)}\, c_+ e^{-\gamma z} = \frac{\sqrt{\mathrm{Re}(p_0)}}{2v_0}(v + iZ_0) \tag{45}$$

and

$$b_0 \equiv \sqrt{\mathrm{Re}(p_0)}\, c_- e^{+\gamma z} = \frac{\sqrt{\mathrm{Re}(p_0)}}{2v_0}(v - iZ_0), \tag{46}$$

where the positive square root is mandated. This power normalization ensures that, in the absence of the backward wave, the unit forward wave with $a_0 = 1$ carries unit power.

It can be shown that a_0 and b_0 are independent of the arbitrary normalization of v_0. While their phases depend on the phase of the modal field e_t in the same way that c_+ and c_- do, a_0 and b_0 are independent of the magnitude of e_t. This normalization-independence suggests that a_0 and b_0 are physical waves rather than simply mathematical artifacts.

Assuming that $\mathrm{Re}(Z_0) \neq 0$, Eqs. (45) and (46) imply

$$v(z) = \frac{v_0}{\sqrt{\mathrm{Re}(p_0)}}(a_0 + b_0) \tag{47}$$

and

$$i(z) = \frac{i_0}{\sqrt{\mathrm{Re}(p_0)}}(a_0 - b_0). \tag{48}$$

From Eq. (19), the real power is therefore

$$P(z) = |a_0|^2 - |b_0|^2 + 2\,\mathrm{Im}(a_0 b_0^*)\frac{\mathrm{Im}(Z_0)}{\mathrm{Re}(Z_0)}. \tag{49}$$

This demonstrates that the net real power P crossing a reference plane is *not* equal to the difference of the powers carried by the forward and backward waves acting independently, except when the characteristic impedance is real or when either a_0 or b_0 vanishes.

Although Eq. (49) is awkward and somewhat counterintuitive, it is not an artifact of the formulation but an expression of fundamental physics. Normalizations do not play a role, for the result is independent of the normalizations of e_t and v_0. Only the phase of Z_0 appears and, as we have seen, this phase is not arbitrary.

In the evanescent case, $\mathrm{Re}(p_0) = \mathrm{Re}(Z_0) = 0$, so that neither the forward nor backward wave individually carries real power. In this case, Eq. (49) is indeterminate. To resolve the problem, we can express Eq. (49) in the form

$$P(z) = |a_0|^2 - |b_0|^2 + 2\,\mathrm{Im}(p_0)\,\mathrm{Im}(c_+ c_-^*), \tag{50}$$

since $\beta = 0$ for evanescent waves. When $\mathrm{Re}(p_0) = 0$, both a_0 and b_0 vanish as a result of the power normalization of Eqs. (45) and (46), but the last term may be nonzero. This means, that, although the forward and backward cutoff waves each carry no real power, power may be transferred if both waves exist. Thus, as we expect, power *may* traverse a finite length of lossless waveguide in which all modes are strictly cut off. This familiar case exemplifies the fact that the net power may fail to equal the sum of the individual wave powers.

The reflection coefficient Γ_0 is defined by

$$\Gamma_0(z) \equiv \frac{b_0(z)}{a_0(z)}. \tag{51}$$

The power can be expressed in terms of Γ_0 by

$$P = |a_0|^2\left[1 - |\Gamma_0|^2 - 2\,\mathrm{Im}(\Gamma_0)\frac{\mathrm{Im}(Z_0)}{\mathrm{Re}(Z_0)}\right], \tag{52}$$

which is similar to a result on p. 27 of Ref. [2]. As noted in Ref. [2], $|\Gamma_0|^2$ is not a power reflection coefficient and may exceed 1 if Z_0 is not real.

3.2 Pseudo-Waves

We now introduce another set of parameters, the pseudo-waves, which, in contrast to the traveling waves, *are* mathematical artifacts but may have convenient properties. We first introduce an arbitrary *reference* impedance Z_{ref}, with the sole stipulation $\mathrm{Re}(Z_{\mathrm{ref}}) \geq 0$. We then define the complex *pseudo-wave amplitudes* (or simply *pseudo-waves*) a and b by

$$a(Z_{\mathrm{ref}}) \equiv \left[\frac{|v_0|}{v_0}\frac{\sqrt{\mathrm{Re}(Z_{\mathrm{ref}})}}{2|Z_{\mathrm{ref}}|}\right](v + iZ_{\mathrm{ref}}) \tag{53}$$

and

$$b(Z_{\mathrm{ref}}) \equiv \left[\frac{|v_0|}{v_0}\frac{\sqrt{\mathrm{Re}(Z_{\mathrm{ref}})}}{2|Z_{\mathrm{ref}}|}\right](v - iZ_{\mathrm{ref}}). \tag{54}$$

Although a and b depend on z (through v and i), we have chosen not to explicitly list z as an argument but instead to concentrate on the parameter Z_{ref}, which plays a more important role in the remainder of this development.

The inverse relationships to Eqs. (53) and (54) are

$$v = \left[\frac{v_0}{|v_0|}\frac{|Z_{\mathrm{ref}}|}{\sqrt{\mathrm{Re}(Z_{\mathrm{ref}})}}\right](a + b) \tag{55}$$

and

$$i = \frac{1}{Z_{\mathrm{ref}}}\left[\frac{v_0}{|v_0|}\frac{|Z_{\mathrm{ref}}|}{\sqrt{\mathrm{Re}(Z_{\mathrm{ref}})}}\right](a - b). \tag{56}$$

Positive square roots are again mandated in Eqs. (53) through (56).

With these definitions, Eq. (19) becomes

$$P = |a|^2 - |b|^2 + 2\,\mathrm{Im}(ab^*)\frac{\mathrm{Im}(Z_{\mathrm{ref}})}{\mathrm{Re}(Z_{\mathrm{ref}})}. \qquad (57)$$

P, v, and i were defined earlier and do not depend on Z_{ref}.

The pseudo-reflection coefficient Γ, defined by

$$\Gamma(Z_{\mathrm{ref}}) \equiv \frac{b(Z_{\mathrm{ref}})}{a(Z_{\mathrm{ref}})}, \qquad (58)$$

depends on Z_{ref}. The analog of Eq. (52) is

$$P = |a|^2\left[1 - |\Gamma|^2 - 2\,\mathrm{Im}(\Gamma)\frac{\mathrm{Im}(Z_{\mathrm{ref}})}{\mathrm{Re}(Z_{\mathrm{ref}})}\right]. \qquad (59)$$

Comparing Eqs. (45) and (46) with Eqs. (53) and (54), we see that $a(Z_0) = a_0$ and $b(Z_0) = b_0$. Although the multiplicative factor in Eqs. (53) and (54) is complicated, it is the only factor that satisfies this criterion and also ensures that a and b satisfy the simple power expression Eq. (57).

Since the pseudo-waves are equivalent to the actual traveling waves when the reference impedance is equal to the characteristic impedance of the mode, this is the natural choice of reference impedance. On the other hand, it is not always the most convenient choice. For instance, when Z_0 varies greatly with frequency, as is often the case in lossy lines [12], the resulting measurements using $Z_{\mathrm{ref}} = Z_0$ may be difficult to interpret; a constant Z_{ref} may be preferable. Furthermore, the characteristic impedance of a given mode is often unknown and difficult to measure. In such cases, the fact that $Z_{\mathrm{ref}} = Z_0$ does not suffice to provide a numerical value for Z_{ref}, which is required in order to make use of Eqs. (55) through (57).

Other choices of reference impedance are also well motivated. In particular, if Z_{ref} is chosen to be *real,* the crossterm in Eq. (57) disappears. The result is the conventional expression in which the power is simply the difference of $|a|^2$ and $|b|^2$. The choice of real Z_{ref} therefore simplifies subsequent calculations and allows the application of a number of standard results which arise from the conventional expression. For example, conservation of energy ensures that the net power P into a passive load is nonnegative. If Z_{ref} is real, Eq. (59) implies that the load's reflection coefficient has magnitude less than 1; that is, it "stays inside the Smith chart." This need not be true for complex Z_{ref}. Another example is the conventional result that the maximum power available from a generator is that power which would be delivered to a load whose reflection coefficient is the complex conjugate of the generators reflection coefficient. In the general case, this result applies only to pseudo-reflection coefficients using a real reference impedance.

One more choice of reference impedance is in common use: that which makes $b(Z_{\mathrm{ref}})$ vanish at a given point on the line. Such a choice ($Z_{\mathrm{ref}} = v/i$) also simplifies Eq. (57), although only at the particular z and for a particular termination.The primary effect of this choice of Z_{ref} is to make the pseudo-reflection coefficient vanish. As discussed later in this paper, many calibration schemes force the pseudo-reflection coefficient of some "standard" termination, usually a resistive load, to vanish. Those schemes thereby implicitly impose this particular choice of reference impedance.

Unfortunately, the quantities a and b are proportional to the forward and backward traveling waves *only* if $Z_{\mathrm{ref}} = Z_0$; otherwise, the pseudo-waves are linear combinations of the forward and backward waves. For example, suppose that we have an infinite waveguide with all sources in $z > 0$. For $z < 0$, we know that $a_0 = 0$; no wave is incident from this side. However, unless $Z_{\mathrm{ref}} = Z_0$, we will find that a and b are both nonzero in this case.

Another contrast is that, as a function of z, a_0 and b_0 have a simple exponential dependence while a and b are complicated functions of z due to interference between the forward and backward traveling waves. For illustration, Fig. 4 plots the magnitudes of a_0 and b_0 for a line which is uniform in $z < 0$ but has an obstacle of reflection coefficient $\Gamma = 0.2$ located at $z = 0$. In contrast, Fig. 5 plots the magnitudes of the associated pseudo-waves a and b with Z_{ref} chosen to make b vanish at $z = 0$. Figure 5 demonstrates not only the complicated behavior of a and b with respect to z but also the fact that the change of reference impedance forces b to vanish at only a *single* point. It is clearly unrealistic to interpret a and b as *"incident"* and "reflected" waves.

In contrast to a_0 and b_0, a and b generally depend on the normalization which determines $|v_0|$, $|i_0|$, and $|Z_0|$. This dependence helps to explain a potential paradox. Assume, for instance, that $Z_0 = 50\ \Omega$. If $Z_{\mathrm{ref}} = 50\ \Omega$, then the pseudo-waves are equal to the traveling waves. Now, since $|Z_0|$ is arbitrary, depending on how we define v_0, we can easily refine Z_0 to, say, 100 Ω. Are not the pseudo-waves still equal to the traveling waves, even though $Z_{\mathrm{ref}} \neq Z_0$? In fact, they are not, for the change in v_0 leads to a renormalization of v and i [see Eqs. (12) and (13)] and therefore a renormalization of a and b through Eqs. (53) and (54). Thus, the pseudo-waves are no longer

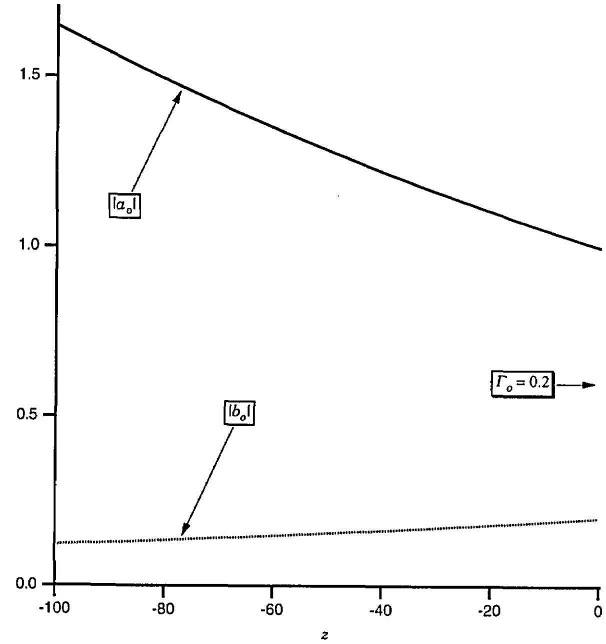

Fig. 4. The magnitudes of the incident (a_0) and reflected (b_0) traveling waves near a termination at $z = 0$ with reflection coefficient $\Gamma_0 = 0.2$. The propagation constant is $0.005 + 0.1j$. The waves depend exponentially on z.

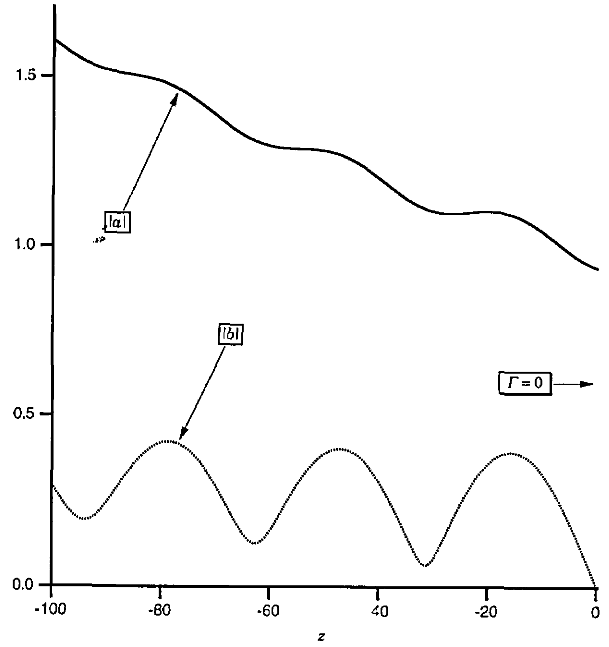

Fig. 5. The magnitudes of the pseudo-waves a and b for the example of Fig. 4. The reference impedance Z_{ref} is chosen so as to make the pseudo-reflection coefficient $\Gamma(Z_{\text{ref}})$ vanish at the termination reference plane. Since the waves depend in a complicated fashion on z, $\Gamma(Z_{\text{ref}})$ vanishes *only* at $z = 0$.

equal to the traveling waves unless we shift Z_{ref} to 100 Ω as well. This normalization dependence of the pseudo-waves, in contrast to the traveling waves, further illustrates the fact that they are not physical waves but instead only mathematical artifacts.

Finally, the condition $\text{Re}(Z_{\text{ref}}) \geq 0$ that we have imposed on the reference impedance corresponds to the condition $\text{Re}(Z_0) \geq 0$ that we imposed earlier on the characteristic impedance. Therefore, it is always possible to choose $Z_{\text{ref}} = Z_0$.

Since the most convenient choice of Z_{ref} depends on the application, it will prove useful to construct a procedure to transform the pseudo-waves in accordance with a change of reference impedance. This is considered below.

3.3 Voltage Standing Wave Ratio

To illustrate the distinction between the traveling waves and the pseudo-waves, we introduce the voltage standing wave ratio (VSWR). For simplicity, we limit discussion to the lossless case $\alpha = 0$, in which case the fields in the waveguide are strictly periodic in z with period $2\pi/\beta$. The VSWR is defined to be the ratio of the maximum to the minimum electric field magnitude, which reduces to

$$\text{VSWR} \equiv \frac{\max\limits_z |E_t(z)|}{\min\limits_z |E_t(z)|} = \frac{\max\limits_z |v(z)|}{\min\limits_z |v(z)|}$$

$$= \frac{|a_0| + |b_0|}{|a_0| - |b_0|} = \frac{1 + |\Gamma_0|}{1 - |\Gamma_0|} \,. \tag{60}$$

In the lossless case, the magnitudes of a_0, b_0, and Γ_0 are independent of z.

Equation (60) illustrates that the VSWR, a quantity which is determined solely from the electric fields, is directly related to the ratio of traveling waves. In fact, it is the interference between these traveling waves that produces the periodicity. The pseudo-waves cannot be measured by such a procedure because they have no physical manifestation.

The pseudo-waves reduce to the traveling waves when the reference impedance is equal to the characteristic impedance. Therefore, the reference impedance of the reflection coefficient derived from a VSWR measurement is equal to Z_0. This provides another argument that Z_0 is the natural choice of reference impedance.

3.4 Scattering and Pseudo-Scattering Matrices

Consider a linear waveguide circuit which connects an arbitrary number of (generally) nonidentical, uniform semi-infinite waveguides which are uncoupled away from the junction. In each waveguide, a cross-sectional reference plane is chosen at which only a single mode exists. If the mode of interest is dominant, this can be ensured by choosing the reference plane sufficiently far from the junction that higher-order modes have decayed to insignificance.

For each waveguide port i, we choose a reference impedance Z^i_{ref}, in terms of which the pseudo-wave amplitudes $a_i(Z^i_{\mathrm{ref}})$ and $b_i(Z^i_{\mathrm{ref}})$ at port i are defined by Eqs. (53) and (54). The orientation is such that the "forward" direction is *toward* the junction. We define column vectors a and b whose elements are the a_i and b_i. The vector of outgoing pseudo-waves b is linearly related to the vector of incoming pseudo-waves a by the pseudo-scattering matrix S:

$$\mathsf{b} = \mathsf{S}\,\mathsf{a}. \tag{61}$$

Although S depends on the choice of reference impedance at each port, we have suppressed notation which would explicitly acknowledge that fact.

We likewise define the vectors of incoming and outgoing traveling wave intensities a_0 and b_0 whose elements are the a_0 and b_0. These two vectors are related by the (true) scattering matrix S^0:

$$\mathsf{b}_0 = \mathsf{S}^0 \mathsf{a}_0 . \tag{62}$$

If $Z^i_{\mathrm{ref}} = Z_0{}^i$ for each port i, then $\mathsf{S} = \mathsf{S}^0$. In other words, the pseudo-scattering matrix is equal to the scattering matrix when the reference impedance at each port is equal to the respective characteristic impedance.

The reflection coefficient Γ_0 is the single element of the scattering matrix S of a one-port. The same is also true of Γ and S.

We can say more about S in special cases. For example, the net power into a *passive* circuit is nonnegative. From (57), this requires that

$$\mathrm{Re}(\mathsf{a}^\dagger[\mathsf{I} - \mathsf{S}^\dagger \mathsf{S} + 2j\mathsf{V}\mathsf{S}]\mathsf{a}) \geqslant 0 . \tag{63}$$

where "†" indicates the Hermitian adjoint (conjugate transpose) and V is a diagonal matrix with elements equal to $\mathrm{Im}(Z^i_{\mathrm{ref}})/\mathrm{Re}(Z^i_{\mathrm{ref}})$. If the circuit is lossless, the inequality in Eq. (63) can be replaced by an equality. If all of the reference impedances are real, then Eq. (63) implies that $\mathsf{I} - \mathsf{S}^\dagger \mathsf{S}$ is positive semi-definite. If, in addition, the circuit is lossless, then $\mathsf{S}^\dagger \mathsf{S} = \mathsf{I}$; that is, S is unitary.

Another useful property of S is a result of electromagnetic reciprocity and is therefore demonstrable when all the materials comprising the junction have symmetric permittivity and permeability tensors; in using Eqs. (2)–(7), we have already assumed as much in the waveguides themselves. As shown in Appendix D and also in Ref. [14], the reciprocity condition is

$$\frac{S_{ji}}{S_{ij}} = \frac{K_i}{K_j}\,\frac{1 - j\ \mathrm{Im}(Z^i_{\mathrm{ref}})/\mathrm{Re}(Z^i_{\mathrm{ref}})}{1 - j\ \mathrm{Im}(Z^j_{\mathrm{ref}})/\mathrm{Re}(Z^j_{\mathrm{ref}})}\,, \tag{64}$$

where the reciprocity factor K_i is given by

$$K_i \equiv \frac{\tilde{p}_{0i}}{p_{0i}{}^*}\,. \tag{65}$$

Here

$$\tilde{p}_0 \equiv \int_S \boldsymbol{e}_t \times \boldsymbol{h}_t \cdot \boldsymbol{z}\ \mathrm{d}S \tag{66}$$

and the additional subscript i refers to the port. When $Z_{\mathrm{ref}} = Z_0$ at each port, Eq. (64) simplifies to

$$\frac{S^0_{ji}}{S^0_{ij}} = \frac{\tilde{p}_{0i}}{\mathrm{Re}(p_{0i})}\,\frac{\mathrm{Re}(p_{0j})}{\tilde{p}_{0j}}\,. \tag{67}$$

The significance of Eq. (64) is that, in contrast to conventional expectations, electromagnetic reciprocity does not necessarily lead to symmetry of the S matrix. In lossless waveguides, $K_i = 1$ and Z_0 is real, so S^0 is symmetric and we need only choose each reference impedance equal to the corresponding characteristic impedance to ensure a symmetric S. In lossy waveguides, K_i is not generally equal to 1. Although $K_i \approx 1$ for typical waveguides, calculations show that it may be much less than 1 in certain guides with very lossy dielectrics [14]. Furthermore, it is not always desirable or even possible to choose a real reference impedance, and a complex reference impedance generally destroys the symmetry of S even when $K_i = 1$. For devices with more than two ports, it is not generally possible to choose the reference impedances so as to make S symmetric. S can always be made symmetric for a two-port, but the phase of the appropriate Z_{ref} at each port depends on K_i at both ports.

Experiments which illustrate the effect of the phase of the reference impedance on the symmetry of S are reported in Refs. [14] and [15].

3.5 The Cascade Matrix

Equation (61) denotes a linear relation between the a_i and b_i. If the circuit of interest is a two-port with $S_{21} \neq 0$, we can express the same relationship using the cascade matrix R, which relates the various pseudo-waves by

$$\begin{bmatrix} b_1(Z^i_{\text{ref}}) \\ a_1(Z^i_{\text{ref}}) \end{bmatrix} = \mathsf{R}^{ij} \begin{bmatrix} a_2(Z^j_{\text{ref}}) \\ b_2(Z^j_{\text{ref}}) \end{bmatrix}. \tag{68}$$

The indices in the superscript of R^{ij} indicate that the reference impedance at port 1 is Z^i_{ref} and that at port 2 is Z^j_{ref}.

Formulas for the conversion between scattering and cascade matrices are readily available [4,16]. For completeness, we repeat them here:

$$\mathsf{R} = \frac{1}{S_{21}} \begin{bmatrix} S_{12}S_{21} - S_{11}S_{22} & S_{11} \\ -S_{22} & 1 \end{bmatrix} \tag{69}$$

and

$$\mathsf{S} = \frac{1}{R_{22}} \begin{bmatrix} R_{12} & R_{11}R_{22} - R_{12}R_{21} \\ 1 & -R_{21} \end{bmatrix}. \tag{70}$$

The cascade matrix of two series-connected two-ports is the product of the two cascade matrices as long as the connecting ports are composed of identical waveguides, with identical reference impedances, joined without discontinuity. Since this holds true regardless of the reference impedances, the introduction of terminology such as "pseudo-cascade matrix" would be needlessly confusing. We will, however, introduce the special notation R^0 to describe the cascade matrix which satisfies

$$\begin{bmatrix} b_{01} \\ a_{01} \end{bmatrix} = \mathsf{R}^0 \begin{bmatrix} a_{02} \\ b_{02} \end{bmatrix}. \tag{71}$$

R is equal to R^0 when $Z^i_{\text{ref}} = Z^i_0$ for each port i.

3.6 The Impedance Matrix

The impedance matrix Z relates the column vectors v and i, whose elements are the waveguide voltages and currents at the various ports:

$$\mathsf{v} = \mathsf{Z}\mathsf{i}. \tag{72}$$

In contrast to S and R, Z is independent of the reference impedance since v and i are also. This makes Z particularly interesting for metrological purposes. Z does, however, depend on the normalization of v_0.

The relation between S and Z is explored in Appendix E. The results are

$$\mathsf{S} = \mathsf{U}(\mathsf{Z} - \mathsf{Z}_{\text{ref}})(\mathsf{Z} + \mathsf{Z}_{\text{ref}})^{-1}\,\mathsf{U}^{-1} =$$

$$\mathsf{U}(\mathsf{Z}\mathsf{Z}_{\text{ref}}^{-1} - \mathsf{I})(\mathsf{Z}\mathsf{Z}_{\text{ref}}^{-1} + \mathsf{I})^{-1}\,\mathsf{U}^{-1} \tag{73}$$

and inversely

$$\mathsf{Z} = (\mathsf{I} - \mathsf{U}^{-1}\mathsf{S}\mathsf{U})^{-1}(\mathsf{I} + \mathsf{U}^{-1}\mathsf{S}\mathsf{U})\mathsf{Z}_{\text{ref}}. \tag{74}$$

Here Z_{ref} is a diagonal matrix whose elements are the Z^i_{ref} and U is another diagonal matrix defined by

$$\mathsf{U} \equiv \text{diag}\left(\frac{|v_{0i}|}{v_{0i}} \frac{\sqrt{\text{Re}(Z^i_{\text{ref}})}}{|Z^i_{\text{ref}}|} \right). \tag{75}$$

The factor U, which does not appear in other expressions relating S with Z [3,4], generalizes the earlier results to problems including complex fields and reference impedances.

Appendix D demonstrates that the off-diagonal elements of Z are related by

$$\frac{Z_{ji}}{Z_{ij}} = \frac{K_i}{K_j} \cdot \frac{v_{0i}^*}{v_{0i}} \frac{v_{0j}}{v_{0j}^*}. \tag{76}$$

Thus Z, like S, is generally asymmetric, even when the circuit is reciprocal and v_0 is chosen real at each port. The asymmetry of Z is *not* a result of wave normalization, for Z is defined without reference to waves.

The admittance matrix Y is the inverse of Z and satisfies

$$\mathsf{i} = \mathsf{Z}^{-1}\mathsf{v} = \mathsf{Y}\mathsf{v}. \tag{77}$$

3.7 Change of Reference Impedance

As discussed earlier, the most convenient choice of reference impedance depends on the circumstances. In order to accommodate the various choices, we consider the relationship between the pseudo-wave amplitudes based on different reference impedances. By expressing $a(Z^n_{\text{ref}})$ and $b(Z^n_{\text{ref}})$ in terms of v and i using Eqs. (53) and (54) and v and i in terms of $a(Z^m_{\text{ref}})$ and $b(Z^m_{\text{ref}})$ using Eqs. (55) and (56), we arrive at the linear relationship

$$\begin{bmatrix} a(Z^n_{\text{ref}}) \\ b(Z^n_{\text{ref}}) \end{bmatrix} = \mathsf{Q}^{nm} \begin{bmatrix} a(Z^m_{\text{ref}}) \\ b(Z^m_{\text{ref}}) \end{bmatrix}, \tag{78}$$

where

$$\mathsf{Q}^{nm} \equiv \frac{1}{2Z^m_{\text{ref}}} \left| \frac{Z^m_{\text{ref}}}{Z^n_{\text{ref}}} \right| \sqrt{\frac{\text{Re}(Z^n_{\text{ref}})}{\text{Re}(Z^m_{\text{ref}})}} \cdot$$

$$\begin{bmatrix} Z^m_{\text{ref}} + Z^n_{\text{ref}} & Z^m_{\text{ref}} - Z^n_{\text{ref}} \\ Z^m_{\text{ref}} - Z^n_{\text{ref}} & Z^m_{\text{ref}} + Z^n_{\text{ref}} \end{bmatrix}. \tag{79}$$

This can be put into more conventional form by defining a quantity N_{nm}, analogous to the "turns ratio" of a conventional transformer, by

$$N_{nm} \equiv \sqrt{\frac{Z^n_{\text{ref}}}{Z^m_{\text{ref}}}}, \tag{80}$$

so Eq. (78) becomes

$$\mathsf{Q}^{nm} \equiv \frac{1}{2|N_{nm}|^2} \sqrt{\frac{\text{Re}(Z^n_{\text{ref}})}{\text{Re}(Z^m_{\text{ref}})}} \begin{bmatrix} 1+N^2_{nm} & 1-N^2_{nm} \\ 1-N^2_{nm} & 1+N^2_{nm} \end{bmatrix}. \tag{81}$$

Equation (81) is similar to the two-port cascade matrix of a classical impedance transformer [4], in which the square root in Eq. (81) is replaced by N^*_{nm}. When Z^m_{ref} and Z^n_{ref} are both real, the two matrices are identical. However, Eq. (81) can be determined neither from the classical result nor from any other lossless analysis. This explains why the result Eq. (79) does not, to our knowledge, appear in previous literature. Equations (78) and (79) are an exact expression of the *complex* impedance transform. We may accurately refer to the pseudo-waves as impedance-transformed traveling waves.

Two consecutive transforms can be represented as a single transform from the initial to the final reference impedance by

$$\mathsf{Q}^{nm}\mathsf{Q}^{mp} = \mathsf{Q}^{np}. \tag{82}$$

Also,

$$\mathsf{Q}^{nn} = \mathsf{I}, \tag{83}$$

where I is the identity matrix. As a result,

$$[\mathsf{Q}^{nm}]^{-1} = \mathsf{Q}^{mn}, \tag{84}$$

which states that the transformation is inverted by a return to the original reference impedance.

The determinant of Q^{nm} is

$$\det[\mathsf{Q}^{nm}] = \left[1 - j\frac{\text{Im}(Z^m_{\text{ref}})}{\text{Re}(Z^m_{\text{ref}})}\right] \left[1 - j\frac{\text{Im}(Z^n_{\text{ref}})}{\text{Re}(Z^n_{\text{ref}})}\right]^{-1}. \tag{85}$$

The scattering matrix associated with Q^{nm} is symmetric if and only if $\det[\mathsf{Q}^{nm}] = 1$, which is true if and only if the phases of Z^m_{ref} and Z^n_{ref} are identical. Equation (85) demonstrates that the scattering matrix representing the transform between a complex and a real impedance is in general asymmetric. In other words, a symmetric scattering matrix cannot remain symmetric when the reference impedance at a single port changes from a real to a nonreal value. This result is closely related to Eq. (64) since, from Eq. (69), the determinant of a cascade matrix is equal to S_{12}/S_{21} of the associated scattering matrix S.

Q^{nm} can be expressed in yet another form:

$$\mathsf{Q}^{nm} = \sqrt{\frac{1 - j\,\text{Im}(Z^m_{\text{ref}})/\text{Re}(Z^m_{\text{ref}})}{1 - j\,\text{Im}(Z^n_{\text{ref}})/\text{Re}(Z^n_{\text{ref}})}} \cdot \frac{1}{\sqrt{1-\Gamma^2_{nm}}} \begin{bmatrix} 1 & \Gamma_{nm} \\ \Gamma_{nm} & 1 \end{bmatrix}, \tag{86}$$

where we use the definition

$$\Gamma_{nm} \equiv \frac{Z^m_{\text{ref}} - Z^n_{\text{ref}}}{Z^m_{\text{ref}} + Z^n_{\text{ref}}}. \tag{87}$$

This form is convenient in the computation of the effect of the complex impedance transform on the reflection coefficient. The reflection coefficient is transformed by

$$\Gamma(Z^n_{\text{ref}}) = \frac{\Gamma_{nm} + \Gamma(Z^m_{\text{ref}})}{1 + \Gamma_{nm}\Gamma(Z^m_{\text{ref}})}. \tag{88}$$

A short circuit, defined as a perfectly conducting electric wall spanning the entire cross section of the waveguide, forces the tangential electric field to vanish at the reference plane. A short therefore requires $v = 0$ and $b = -a$. As a result, the reflection coefficient is $\Gamma_0 = -1$. We can see from Eq. (88) that the transform of a perfect short remains $\Gamma(Z^n_{\text{ref}}) = -1$, independent of the reference impedance. The only other reflection coefficient which is independent of the reference impedance is the perfect open circuit (magnetic wall), at which the transverse magnetic field vanishes so that $i = 0$, $b = a$, and $\Gamma = +1$. The unique status of the short and open is related to their unique physical manifestations.

If $\Gamma(Z^m_{\text{ref}}) = 0$ (perfect match) then $\Gamma(Z^n_{\text{ref}}) = \Gamma_{nm}$. Conversely, if $\Gamma(Z^m_{\text{ref}}) = -\Gamma_{nm}$ then $\Gamma(Z^n_{\text{ref}}) = 0$.

3.8 Multiport Reference Impedance Transformations

A direct, if somewhat complicated, means of computing the transformation of S due to a change of reference impedance begins by computing Z using Eq. (74). Subsequently, Eq. (73) is used with the *new* reference impedance to calculate the transformed S. This procedure works because Z is independent of reference impedance.

If the circuit under consideration is a two-port, the simplest way of computing the transform is to compute the associated cascade matrix R, perform the transform on R, and convert back to an S matrix. To determine the effect of the transform on R, we insert Eq. (78) into the right hand side of Eq. (68). In order to do the same with the left hand side, we need use the result that, due to symmetry of Q^{nm} about both diagonals, Eq. (78) implies that

$$\begin{bmatrix} b(Z_{\mathrm{ref}}^{n}) \\ a(Z_{\mathrm{ref}}^{n}) \end{bmatrix} = \mathsf{Q}^{nq} \begin{bmatrix} b(Z_{\mathrm{ref}}^{q}) \\ a(Z_{\mathrm{ref}}^{q}) \end{bmatrix}. \tag{89}$$

Upon making these replacements and using Eq. (84), we can put Eq. (68) into a form relating $b_1(Z_{\mathrm{ref}}^{p})$ and $a_1(Z_{\mathrm{ref}}^{p})$ to $b_2(Z_{\mathrm{ref}}^{q})$ and $a_2(Z_{\mathrm{ref}}^{q})$. The result is that

$$\mathsf{R}^{pq} = \mathsf{Q}^{pm}\mathsf{R}^{mn}\mathsf{Q}^{nq}. \tag{90}$$

This equation displays the effect on the cascade matrix of altering the reference impedance of port 1 from Z_{ref}^{m} to Z_{ref}^{p} and that of port 2 from Z_{ref}^{n} to Z_{ref}^{q}. This is a concise expression of the complex impedance transform.

In the special but common case in which the two ports use identical reference impedances, Eq. (90) simplifies. In transforming the reference impedance of both ports from Z_{ref}^{m} to Z_{ref}^{p}, the cascade matrix is transformed by

$$\mathsf{R}^{pp} = \mathsf{Q}^{pm}\mathsf{R}^{mm}\mathsf{Q}^{mp} =$$

$$\frac{1}{1-\Gamma_{pm}^{2}} \begin{bmatrix} 1 & \Gamma_{pm} \\ \Gamma_{pm} & 1 \end{bmatrix} \mathsf{R}^{mm} \begin{bmatrix} 1 & -\Gamma_{pm} \\ -\Gamma_{pm} & 1 \end{bmatrix}. \tag{91}$$

This transformation was used in Ref. [16].

3.9 Load Impedance

The load impedance is defined as the single element of the impedance matrix describing a linear one-port. At the reference plane, at which only a single mode exists, the load impedance is defined in terms of v and i as

$$Z_{\mathrm{load}} \equiv \frac{v}{i}. \tag{92}$$

From Eq. (19), the power absorbed by the load can be expressed as

$$P = |i|^2 R_{\mathrm{load}} = |v|^2 \frac{R_{\mathrm{load}}}{|Z_{\mathrm{load}}|^2}, \tag{93}$$

where $R_{\mathrm{load}} \equiv \mathrm{Re}(Z_{\mathrm{load}})$. Power conservation ensures that, for a passive one-port, $R_{\mathrm{load}} \geq 0$. For the remainder of this section, we assume that the load of interest is passive in order to avoid conflict with the requirement that $\mathrm{Re}(Z_{\mathrm{ref}}) \geq 0$.

The load impedance, like v and i, is independent of the reference impedance. Unlike the result of low-frequency circuit theory, however, Z_{load} is *not* a unique property of the one-port itself but instead depends on the fields of the mode incident upon it. Illumination of the same device by a different waveguide, or even a different mode of the same waveguide, may result in a drastically different Z_{load}. Z_{load} also depends on the normalization which determines v_0 and i_0, for this affects v and i.

Using Eq. (92) in Eq. (54), we see that, when the reference impedance is equal to the load impedance, we have $b(Z_{\mathrm{load}}) = 0$. From Eq. (58), this implies that

$$\Gamma(Z_{\mathrm{load}}) = 0. \tag{94}$$

In other words, when $Z_{\mathrm{ref}} = Z_{\mathrm{load}}$, the reflection coefficient vanishes. In this reference impedance, the load looks like a perfect match. Likewise, if we *insist* that the reflection coefficient vanishes when a certain load is connected to our line, we have effectively chosen the reference impedance to be equal to Z_{load}. This is relevant to the calibration problem considered below. Keep in mind, however, that it may be difficult to establish a value for Z_{load} since that depends on the waveguide as well as the load.

Using Eq. (94) along with Eqs. (87) and (88), we find that

$$\Gamma(Z_{\mathrm{ref}}) = \frac{Z_{\mathrm{load}} - Z_{\mathrm{ref}}}{Z_{\mathrm{load}} + Z_{\mathrm{ref}}}. \tag{95}$$

We can also solve for Z_{load}:

$$Z_{\mathrm{load}} = Z_{\mathrm{ref}} \frac{1 + \Gamma(Z_{\mathrm{ref}})}{1 - \Gamma(Z_{\mathrm{ref}})}. \tag{96}$$

This produces the same result regardless of the reference impedance with respect to which Γ is defined. If we choose Z_{ref} equal to the characteristic impedance Z_0, these two equations are identical to those of ordinary waveguide circuit theory and to the theory of Ref. [6].

We see from Eq. (96) that the load impedance of a short is 0 and that of an open is ∞.

As an example of a load, consider the use of a semi-infinite transmission line with characteristic impedance Z_1 to terminate a transmission line with characteristic impedance Z_0. In general, the reflection coefficient and the load impedance are impossible to compute. One common approximation, based on the notions of low-frequency circuit theory, is that both v and i are continuous at the interface. This assumption leads to the result that the load impedance of the line is simply its characteristic impedance. This allows the reflection coefficient to be determined by Eq. (95).

Unfortunately, the assumption leading to this result is not generally valid, since v and i are not generally continuous at an interface. Recall that v and i are not strictly related to true voltage or current. The actual boundary conditions at the interface require continuity of tangential fields, and these cannot in general be satisfied without the presence of an infinity of higher order modes at the discontinuity. By contrast, the waveguide voltage and current are indicative of the intensities of only a *single* mode. The reflection coefficient cannot therefore be determined from waveguide circuit parameters. For an explicit example, consider the case in which $Z_0 = Z_1$ while the two transmission lines are physically dissimilar. In this case, the assumption that the load impedance equals Z_1 leads to the result that there is no reflection of traveling waves. In fact, reflection *must* take place due to the discontinuity at the interface. Exceptions occur only when no higher-order modes are generated. An example is coaxial lines of lossless conductors which differ only in the dielectric material. In this peculiar example, the reflection coefficient can be computed exactly from Z_0 and Z_1. In other examples, the result is at best approximate.

4. Waveguide Metrology

In this section, we apply the theoretical results of the previous sections to the elucidation of the basic problems of waveguide metrology, which aims to characterize waveguide circuits in terms of appropriate matrix descriptions.

4.1 Measurability and the Choice of Reference Impedance

In addition to the slotted line, which measures VSWR directly, the primary instrument used to characterize waveguide circuits is the vector network analyzer (VNA). Here we restrict ourselves to a two-port VNA, which provides a measurement M_i of the product

$$\mathsf{M}_i = \mathsf{X}\mathsf{T}_i\overline{\mathsf{Y}}. \tag{97}$$

Here T_i is the cascade matrix of the device i under test, X and Y are constant, non-singular matrices which describe the instrument, and

$$\overline{\mathsf{Y}} \equiv \begin{bmatrix} 0 & 1 \\ 1 & 0 \end{bmatrix} \mathsf{Y}^{-1} \begin{bmatrix} 0 & 1 \\ 1 & 0 \end{bmatrix} \tag{98}$$

is the reverse cascade matrix corresponding to Y. The problem of network analyzer calibration is to determine X and Y by the insertion and measurement of known devices i. With X and Y known, Eq. (97) determines T_i from the measured M_i.

X, Y, and T_i are commonly considered unique, and a calibration process which determines them uniquely is applied. However, as we have seen in this paper, the cascade matrix T_i depends on the reference impedances with which it is defined. Thus, any number of calibrations lead to legitimate measurements of a cascade matrix and therefore legitimate measurements of pseudo-scattering parameters, although with varying port reference impedances. We refer to these calibrations, each of which is related to any other by an impedance transform, as *consistent.* Any calibration which is not related to a consistent calibration by an impedance transform will not yield measurements of pseudo-scattering parameters. Such a calibration is *inconsistent.* For example, X and Y may be determined in such a way that the resulting measurement of an open circuit is not equal to 1. Such a result is prohibited for pseudo-scattering parameters, so the calibration is inconsistent. It is meaningless to speak of the reference impedance of such a calibration.

The reference impedances of a consistently calibrated VNA are uniquely determined by the calibration. Only when the reference impedance is equal to the characteristic impedance of the line are the resulting pseudo-scattering parameters equal to the actual scattering parameters. Of course, transformation to an alternative reference impedance is possible, but only if the initial reference impedance is *known.* This section analyzes some common calibration methods to determine their reference impedance.

We assume that the waveguides at the two reference planes and the two corresponding basis functions $\boldsymbol{e}_t$ are identical. When Z_{ref} at both ports is equal to the characteristic impedance Z_0, we can express Eq. (97) as

$$\mathsf{M}_i = \mathsf{X}^0\mathsf{T}_i^0\overline{\mathsf{Y}}^0. \tag{99}$$

The single superscript on the network analyzer matrices refers to the reference impedance at the test ports. We do not need to define or discuss a reference impedance at the "measurement ports."

From Eq. (84), the identity matrix can be expressed as $\mathsf{I}=\mathsf{Q}^{0m}\mathsf{Q}^{m0}$. Inserting this into Eq. (99) yields

$$\mathsf{M}_i=(\mathsf{X}^0\mathsf{Q}^{0m})(\mathsf{Q}^{m0}\mathsf{T}_i^0\,\mathsf{Q}^{0n})(\mathsf{Q}^{n0}\,\overline{\mathsf{Y}}^0)=\mathsf{X}^m\mathsf{T}_i^{mn}\overline{\mathsf{Y}}^n, \tag{100}$$

where

$$\mathsf{X}^m\equiv\mathsf{X}^0\,\mathsf{Q}^{0m}, \tag{101}$$

$$\overline{\mathsf{Y}}^n\equiv\mathsf{Q}^{n0}\overline{\mathsf{Y}}^0, \tag{102}$$

and

$$\mathsf{T}_i^{mn}\equiv\mathsf{Q}^{m0}\mathsf{T}_i^0\mathsf{Q}^{0n} \tag{103}$$

are the impedance-transformed cascade matrices. If the calibration procedure determines that $\mathsf{X}=\mathsf{X}^m$ and $\mathsf{Y}=\mathsf{Y}^n$, then subsequent calibrated measurements will determine the matrix T_i^{mn}. If X^m *and* Y^n have the form of Eqs. (101) and (102), the VNA will be consistently calibrated to reference impedances Z_{ref}^m on port 1 and Z_{ref}^n on port 2.

The most accurate method of VNA calibration is TRL [17, 18], a moniker which refers to the use of a "thru," and "reflect," and a "line." The "thru" is a length of transmission line which connects at either end to a test port. The line standard is a longer section of transmission line. The "reflect" is a symmetric and transmissionless but otherwise arbitrary two-port embedded in a section of transmission line. The method assumes that each measured device has an identical transition from the test port to the calibration reference plane. The reference planes are set to the center of the thru.

The TRL method, like other calibration methods, determines the matrices X^m and Y^n. However, as we have seen, these two matrices are nonunique since they depend on the reference impedances. Thus, we need to analyze the algorithm to determine which reference impedances are imposed by the calibration.

Our first standard ($i=1$), an ideal thru, is a continuous connection between two identical lines. Since the traveling waves are not disturbed, the cascade matrix using a reference impedance of Z_0 must be the identity matrix I:

$$\mathsf{T}_1^0=\mathsf{I}. \tag{104}$$

If the calibration is consistent but, instead of Z_0, reference impedances Z_{ref}^m and Z_{ref}^n are used, then the thru has the cascade matrix

$$\mathsf{T}_1^{mn}=\mathsf{Q}^{m0}\mathsf{I}\mathsf{Q}^{0n}=\mathsf{Q}^{mn}. \tag{105}$$

However, the TRL algorithm is constructed so as to force the calibrated measurement of the thru to equal the identity matrix. That is, it imposes the condition that

$$\mathsf{T}_1^{mn}=\mathsf{Q}^{mn}=\mathsf{I}, \tag{106}$$

which, from (86) and (87), is true if and only if

$$Z_{\text{ref}}^m=Z_{\text{ref}}^n. \tag{107}$$

In other words, the algorithm imposes the condition that the reference impedances on both ports be identical. The thru alone cannot provide any information as the value of that reference impedance.

Another result of the TRL algorithm is that the calibrated measurement of the reflect standard is identical on both ports. This again reveals nothing about the port reference impedances except that they are identical.

The ideal line standard ($i=2$) is a length of transmission line identical to that of the two test ports and connected to them without discontinuity. As a result, there is no reflection of the traveling waves. This requires the cascade matrix of the line, with a reference impedance of Z_0, to be

$$\mathsf{T}_2^0=\begin{bmatrix} e^{-\gamma l} & 0 \\ 0 & e^{+\gamma l} \end{bmatrix}, \tag{108}$$

where γ is the propagation constant and l is the line length. Since we require identical reference impedances on both ports, the transformed cascade matrix is

$$\mathsf{T}_2^{mm}=\mathsf{Q}^{m0}\mathsf{T}_2^0\mathsf{Q}^{0m}=$$

$$\frac{e^{+\gamma l}}{1-\Gamma_{0m}^2}\begin{bmatrix} e^{-2\gamma l}-\Gamma_{0m}^2 & (1-e^{-2\gamma l})\Gamma_{0m} \\ -(1-e^{-2\gamma l})\Gamma_{0m} & 1-e^{-2\gamma l}\Gamma_{0m}^2 \end{bmatrix}, \tag{109}$$

where Γ_{0m} is defined as in Eq. (87).

The TRL algorithm ensures that the cascade matrix in Eq. (109) is diagonal and therefore that the calibrated measurement of the line will be such that $S_{11}=S_{22}=0$. The off-diagonal elements of (109) are equal and opposite. Assuming that $e^{-2\gamma l}\neq 1$, T_2^{mm} is diagonal if and only if $\Gamma_{0m}=0$, which implies that $\mathsf{Q}^{0m}=\mathsf{I}$ and

$$Z_{\text{ref}}^m=Z_0. \tag{110}$$

That is, the TRL method using a perfect line and thru results in a consistent calibration with identical reference impedances on each port equal to the characteristic impedance of the line. Recall that the condition $Z_{\mathrm{ref}}=Z_0$ was the condition under which the pseudo-waves are equal to the actual traveling waves. Thus *the TRL method calibrates the VNA so as to measure the unique scattering matrix* S^0 *which relates the actual traveling waves,* not some arbitrary pseudo-scattering matrix S.

In the special case $e^{-2\gamma l}=1$, as occurs in a lossless line whose phase delay is an integral multiple of 180°, T^{mm} is diagonal for *any* Γ_{0m}. Therefore, the reference impedance need not be equal to Z_0 and is in fact indeterminate. This results in the well-known problem of ill-conditioning in such a case.

We have seen that the TRL method calibrates to a reference impedance of Z_0. What happens if we use the TRL *algorithm* but not the TRL *standards*? We consider methods which use the thru and reflect but replace the ideal line by some other passive artifact, which we call the surrogate line. The matrix T_2^0 takes the arbitrary form

$$\mathsf{T}_2^0\equiv\begin{bmatrix}A & B\\ C & D\end{bmatrix}. \tag{111}$$

Since the use of the thru forces any consistent calibration to have identical reference impedances on each port, the transformation of T_2^0 is

$$\mathsf{T}_2^{mm}=\frac{1}{\sqrt{1-\Gamma_{0m}^2}}\begin{bmatrix}A+B\Gamma_{0m}-C\Gamma_{0m}-D\Gamma_{0m}^2 & +A\Gamma_{0m}+B-C\Gamma_{0m}^2-D\Gamma_{0m}\\ -A\Gamma_{0m}-B\Gamma_{0m}^2+C+D\Gamma_{0m} & -A\Gamma_{0m}^2-B\Gamma_{0m}+C\Gamma_{0m}+D\end{bmatrix}. \tag{112}$$

The algorithm attempts to force T_2^{mm} to be diagonal. With a surrogate in place of the line, this may be impossible if T_2^{mm} has the form of Eq. (112), for we have two equations to be satisfied but only the single variable Γ_{0m}. The sum of those two equations produces the requirement

$$C=-B, \tag{113}$$

which is identical to the condition

$$S_{11}^0=S_{22}^0 \tag{114}$$

on the scattering parameters of the standard.

Unless Eq. (114) is satisfied, the analysis reveals a contradiction. The resolution of this problem lies with the realization that Eq. (112) results from the assumption that the calibration is *consistent.* However, unless Eq. (114) is satisfied, the calibration is *inconsistent* and Eq. (112) does not apply. This conclusion is almost obvious, given the fact that both the thru and the surrogate line must appear perfectly matched at each port. In order to meet this condition with a consistent calibration, the thru requires identical reference impedances on each port while the surrogate line demands different reference impedances. Consequently, the calibration is inconsistent and no reference impedance exists.

Clearly, the perfect line meets the symmetry criterion (114). However, so do many other artifacts. Given standards that satisfy (114), a consistent calibration is obtained and the condition of diagonality determines Γ_{0m}. When $B=C=0$, as was the case with the TRL method, then $\Gamma_{0m}=0$ and the reference impedance is Z_0. In any other case, Γ_{0m} is determined by a quadratic equation whose solution is

$$\Gamma_{0m}=\frac{D-A}{2B}\pm\sqrt{\left[\frac{D-A}{2B}\right]^2-1}. \tag{115}$$

The cascade parameters A, B, C, and D can be replaced by the scattering parameters of the standard:

$$\frac{D-A}{B}=S_{11}^0+\frac{1}{S_{11}^0}-\frac{S_{12}^0S_{21}^0}{S_{11}^0}. \tag{116}$$

This formally determines the reference impedance, albeit in a somewhat complicated fashion. In the special case $S_{12}^0S_{21}^0=0$, the insertion of Eq. (116) into (115) leads to the two solutions $\Gamma_{0m}=S_{11}^0$ and $\Gamma_{0m}=1/S_{11}^0$. An analysis lets us reject the second of these. It is then simple to show that

$$Z_{\mathrm{ref}}^m=Z_{\mathrm{load}}. \tag{117}$$

That is, the reference impedance for the calibration is the load impedance of the device used as a standard. As indicated by Eq. (94), this is the appropriate reference impedance so that the calibrated reflection coefficient vanishes.

Since the standard is assumed passive, then, from Eq. (93), $\mathrm{Re}(Z_{\mathrm{load}})\geqslant 0$. Therefore, Eq. (117) presents no conflicts with the requirement that $\mathrm{Re}(Z_{\mathrm{ref}})\geqslant 0$.

This sort of calibration is known as TRM or LRM [19], where the "M" stands for "match." Clearly, the match need not be perfect. If the match *is* perfect ($S_{11}^0=S_{22}^0=0$), then the calibration is identical to that using TRL and will allow the measurement of relations between traveling waves. If the match is symmetric but *im*perfect and $S_{12}^0\,S_{21}^0=0$, *the LRM calibration is related to the TRL calibration by an impedance transform of both ports to a reference impedance equal to the load impedance of the match.* In this case, the VNA calibrated with LRM measures relations not among the traveling waves but among a particular set of pseudo-waves.

Frequently, the match standard is chosen to be a pair of small resistors in the hope that their load impedance is approximately real and constant. This would lead to a useful calibration in which the pseudo-scattering parameters would be measured with respect to a real, constant reference impedance. Unfortunately, it is difficult in practice to design a real and constant load impedance. Furthermore, that impedance is known only after it has been measured with respect to some other calibration. In addition, the load impedance generally depends on the line with respect to which it is measured.

If $S_{11}^0=S_{22}^0\neq 0$ and $S_{12}^0S_{21}^0\neq 0$, as would be the case using a symmetric attenuator, the calibration reference impedance depends on $S_{12}^0S_{21}^0$ as well as S_{11}^0 of the standard. This is an important point to consider in designing the match standard, for any coupling between the two resistors will induce a shift in the reference impedance compared to the load impedance of either resistor alone.

Another useful example is the mismatched line standard. The TRL method using an ideal, matched line led to a reference impedance equal to the characteristic impedance of the line. Since this perfect line is identical to the line at the test port, the traveling waves are not reflected. What happens if the line standard, while uniform, is *not* identical to the test port? The problem is similar to one described in the previous section. In general, the question is impossible to answer. However, for illustration, we consider the approximation that v and i are continuous at the interface. In this case, we can compute the cascade matrix of the line of characteristic impedance Z_l as

$$\mathrm{T}_2^0 =$$

$$\frac{e^{+\gamma l}}{1-\Gamma_{0l}^2}\begin{bmatrix} e^{-2\gamma l}-\Gamma_{0l}^2 & (1-e^{-2\gamma l})\Gamma_{0l} \\ -(1-e^{-2\gamma l})\Gamma_{0l} & 1-e^{-2\gamma l}\Gamma_{0l}^2 \end{bmatrix}, \qquad (118)$$

which can be transformed to

$$\mathrm{T}_2^{mm} =$$

$$\frac{e^{+\gamma l}}{1-\Gamma_{ml}^2}\begin{bmatrix} e^{-2\gamma l}-\Gamma_{ml}^2 & (1-e^{-2\gamma l})\Gamma_{ml} \\ -(1-e^{-2\gamma l})\Gamma_{ml} & 1-e^{-2\gamma l}\Gamma_{ml}^2 \end{bmatrix}. \qquad (119)$$

This is identical in form to the previous result for a perfect line standard. It leads to the result

$$Z_{\mathrm{ref}}^m = Z_l\,. \qquad (120)$$

In this approximation, the reference impedance is the characteristic impedance of the line. This potentially useful result suggests that a particular line may be used as a calibration standard for any network analyzer with identical results. However, the assumption that v and i are continuous, which led to the result, is not generally valid. The example of a 50 Ω, 2.4 mm coaxial standard used on 50 Ω, 3.5 mm coaxial test ports makes this clear, for the standard must reflect the traveling waves even though its characteristic impedance is appropriate for a reflectionless standard. In general, the quality of the approximation depends in detail on the nature of the waveguide interface.

Calibration using any of these devices, as long as $S_{11}^0=S_{22}^0$, leads to solutions differing only by a change of reference impedance. Of course, we can easily transform between any two reference impedances if given the values. A procedure to transform between LRL and LRM calibrations [16] is based on measuring the load reflection coefficient with respect to an LRL calibration. However, this is only a *relative* transformation; the initial and final reference impedances remain unknown. The most comprehensive procedure is to determine the absolute Z_{ref}. A method to accomplish this combines the TRL calibration using a nominally perfect line with a measurement of Z_0, which in this case is identical to Z_{ref} [12]. It is difficult to imagine determining the reference impedance of any of the other calibration methods, even in principle, without comparison to a TRL calibration.

Many calibration methods other than those based on the TRL algorithm are in use. These typically require the measurement of artifacts, such as open and short circuits, whose scattering parameters are presumed known. Although electromagnetic simulations may provide good estimates, the actual scattering parameters can be known accurately only by measurement. Thus the calibration artifacts must be viewed as transfer standards. If the scattering parameters are given incorrectly, the calibration may be inconsistent. However, if perfect short and open circuits are used along with a termination defined as a perfect match, it is possible to obtain a consistent calibration with the reference impedance equal to the load impedance of the termination.

4.2 Measurement of Pseudo-Waves and Waveguide Voltage and Current

The methods of the previous section provide for the measurement of ratios of pseudo-waves. In order to measure the wave amplitudes, an additional magnitude measurement is necessary. The most convenient parameter to measure is the power P. From measurements of P and Γ and a known Z_{ref}, Eq. (59) allows the determination of $|a|$. This applies to $|a_0|$ as well if we replace Z_{ref} by Z_0. The absolute phases of the pseudo-waves and traveling waves cannot be measured without specifying the arbitrary phase of the modal fields. However, the relative phase of a and b is given by Eq. (58).

Once a and b have been determined, $|v|$ and $|i|$ are given by Eqs. (55) and (56). The ratio of these two equations determines the relative phase of v and i.

5. Alternative Circuit Theory Using Power Waves

In addition to the pseudo-waves a and b defined by Eqs. (53) and (54), other quantities may be defined using different linear combinations of v and i. Popular alternatives are the "incident and reflected wave amplitudes" normalized to "complex port numbers" [7]. For a complex port number $\hat{Z}$, these quantities are defined by

$$\hat{a}(\hat{Z}) \equiv \frac{v + i\hat{Z}}{2\sqrt{\mathrm{Re}(\hat{Z})}} \tag{121}$$

and

$$\hat{b}(\hat{Z}) \equiv \frac{v - i\hat{Z}^*}{2\sqrt{\mathrm{Re}(\hat{Z})}}. \tag{122}$$

In Ref. [7], $\hat{Z}$ is arbitrary except that $\mathrm{Re}(\hat{Z}) > 0$; this restriction is lifted in subsequent publications. When $\hat{Z}$ is the load impedance of the device connected to the port, a and b are known as power waves [8]. For simplicity, we shall use the term "power waves" for all quantities of the form (121) and (122).

We take v and i to be the waveguide voltage and current defined in Sec. 2. Like Ref. [7], we limit our discussion to the case $\mathrm{Re}(\hat{Z}) > 0$.

When $\hat{Z}$ is real, the power waves reduce to pseudo-waves (except for a phase factor) with reference impedance $Z_{\mathrm{ref}} = \hat{Z}$. Otherwise they do not correspond. The power waves are *not* equal to the traveling waves for *any* choice of $\hat{Z}$ unless the characteristic impedance is real. For example, Fig. 6 plots the power wave magnitudes corresponding to the example of Fig. 4; $\hat{Z}$ is chosen so that $\hat{b}$ vanishes at $z = 0$. This figure illustrates that the power waves are complicated functions of z; it is clearly unrealistic to interpret them as "incident and reflected waves."

The power waves are devised to satisfy the simple power relation

$$p = |\hat{a}|^2 - |\hat{b}|^2 \tag{123}$$

for any $\hat{Z}$. The pseudo-waves satisfy a relationship of this form only when Z_{ref} is real.

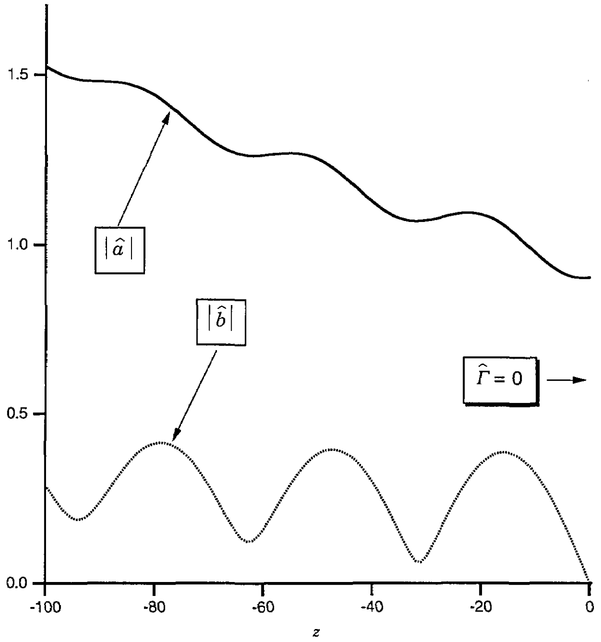

Fig. 6. The magnitudes of the power waves $\hat{a}$ and $\hat{b}$ for the example of Fig. 4. The characteristic impedance is taken to be $1 - 0.2j$. $\hat{Z}$ is chosen so that $\hat{\Gamma}(\hat{Z})$ vanishes at the termination reference plane. Since the waves depend in a complicated fashion on z, $\hat{\Gamma}(\hat{Z})$ vanishes *only* at $z = 0$.

Power wave scattering parameters can be defined analogously to the pseudo-scattering parameters. For example, the power wave reflection coefficient is

$$\hat{\Gamma}(\hat{Z}) \equiv \frac{\hat{b}(\hat{Z})}{\hat{a}(\hat{Z})} = \frac{v - i\hat{Z}^*}{v + i\hat{Z}} = \frac{Z_{\mathrm{load}} - \hat{Z}^*}{Z_{\mathrm{load}} + \hat{Z}}, \tag{124}$$

which should be contrasted to Eq. (95). The power wave reflection coefficient of an open circuit ($i=0$) is equal to 1, the same as the pseudo-wave reflection coefficient defined earlier. However, the result for a short circuit ($v=0$) is

$$v=0 \Rightarrow \hat{\Gamma}(\hat{Z})=-\frac{\hat{Z}^*}{\hat{Z}}, \tag{125}$$

which is equal to the pseudo-wave reflection coefficient -1 only in the special case $\mathrm{Im}(\hat{Z})=0$. This indicates clearly that the power waves are not generally related to the traveling waves by an impedance transform.

The implications of this are significant. For instance, the relationship between the load impedance and the pseudo-reflection coefficient is given by Eq. (95), which is the classical result. It is the basis of the Smith chart as well as most circuit design software. On the other hand, the equivalent relationship in terms of power wave quantities is Eq. (124), to which the Smith chart does not apply since it does not represent a linear fractional transformation. To sharpen this distinction, recall that the Smith chart is based on a *normalized* impedance; that is, the load impedance displayed on the chart is relative to Z_{ref} (Z_0 in the case of traveling waves). The chart is able to accommodate the data in this form because the pseudo-reflection coefficient, as illustrated by Eq. (95), depends only on the *ratio* $Z_{\mathrm{load}}/Z_{\mathrm{ref}}$. The power wave reflection coefficient, however, depends not only on the ratio $Z_{\mathrm{load}}/\hat{Z}$ but also on the phase of $\hat{Z}$. Therefore, an attempt to generalize the Smith chart to display power wave reflection coefficients must lead to a *separate* chart for each phase of $\hat{Z}$.

Recall that the pseudo-wave scattering matrix of a reciprocal circuit is not generally symmetric in lossy waveguides. In contrast, advocates of power waves argue that the power wave scattering matrix of a lossy, reciprocal circuit is symmetric. For waveguide circuits, this is false. The usual derivation of symmetry makes use of the symmetry of the impedance matrix, which, as we have seen, does not hold for waveguides. Thus, one ubiquitous justification of a power wave description of waveguide circuits is invalid. The correct reciprocity relationship is given in Appendix D.

Although a complete circuit theory based on power waves is possible, we have chosen not to develop one, for several reasons. Unlike the power waves, the pseudo-waves are related to the traveling waves by an impedance transform and therefore avoid the problems discussed above. Furthermore, unlike the power waves, the pseudo-waves can generally be set equal to the traveling waves by an appropriate choice of the reference impedance. Although the pseudo-waves do not generally satisfy a simple power expression of the form Eq. (123), they can always be made to do so by an appropriate choice of the reference impedance. Typically this involves choosing Z_{ref} to be real, but the choice of $Z_{\mathrm{ref}}=Z_{\mathrm{load}}$, analogous to the choice $\hat{Z}=Z_{\mathrm{load}}$ made by Ref. [8], will also suffice.

Although a network analyzer may be used to measure power waves, such a use is rare for, as illustrated in the previous section, it is the pseudo-waves that are measured using conventional calibration techniques. None of these methods may be easily modified to directly measure power waves. Methods which apply shorts and opens as calibration standards are inapplicable since only the open, not the short, is a useful power wave standard. Furthermore, the TRL method cannot be applied to power wave measurement since it is closely tied to the measurement of traveling waves.

One method of measuring a power wave reflection coefficient begins with first measuring the pseudo-wave reflection coefficient. If the reference impedance of that calibration can be determined, then the load impedance may be calculated from Eq. (96); the power wave reflection coefficient can then be determined from Eq. (124). Methods which do not require the determination of the pseudo-wave parameters as a prerequisite appear to be unknown at this time. In any case, such methods do *not* exist in the firmware which controls conventional network analyzers, so that these machines are incapable of determining power wave scattering parameters without external software.

6. Appendix A. Reduction of Maxwell's Equations

The electric and magnetic fields of a mode have been designated $\boldsymbol{e}e^{-\gamma z}$ and $\boldsymbol{h}e^{-\gamma z}$. For the moment, we will allow anisotropy and therefore introduce the tensor permittivity $\boldsymbol{\epsilon}$ and tensor permeability $\boldsymbol{\mu}$. Maxwell's equations take the form

$$\nabla\times(\boldsymbol{e}e^{-\gamma z})=-j\omega\boldsymbol{\mu}\cdot(\boldsymbol{h}e^{-\gamma z}), \tag{A1}$$

$$\nabla\times(\boldsymbol{h}e^{-\gamma z})=+j\omega\boldsymbol{\epsilon}\cdot(\boldsymbol{e}e^{-\gamma z}), \tag{A2}$$

$$\nabla\cdot(\boldsymbol{\epsilon}\cdot\boldsymbol{e}e^{-\gamma z})=0, \tag{A3}$$

and

$$\nabla\cdot(\boldsymbol{\mu}\cdot\boldsymbol{h}e^{-\gamma z})=0, \tag{A4}$$

which readily reduce to

$$\nabla\times\boldsymbol{e}-\gamma z\times\boldsymbol{e}=-j\omega\boldsymbol{\mu}\cdot\boldsymbol{h}\ , \tag{A5}$$

$$\nabla\times\boldsymbol{h}-\gamma z\times\boldsymbol{h}=+j\omega\boldsymbol{\epsilon}\cdot\boldsymbol{e}\ , \tag{A6}$$

$$\nabla\cdot(\boldsymbol{\epsilon}\cdot\boldsymbol{e})=\gamma(\boldsymbol{\epsilon}\cdot\boldsymbol{e})\cdot z\ , \tag{A7}$$

and

$$\nabla\cdot(\boldsymbol{\mu}\cdot\boldsymbol{h}\ )=\gamma(\boldsymbol{\mu}\cdot\boldsymbol{h})\cdot z. \tag{A8}$$

If we now divide $\boldsymbol{e}$ and $\boldsymbol{h}$ into their transverse and axial components, Eqs. (A5) and (A6) become

$$\nabla\times\boldsymbol{e}_t=-j\omega(\boldsymbol{\mu}\cdot\boldsymbol{h})\cdot z, \tag{A9}$$

$$\nabla\times\boldsymbol{h}_t=+j\omega(\boldsymbol{\epsilon}\cdot\boldsymbol{e}\ )\cdot z \tag{A10}$$

$$z\times\nabla e_z+\gamma z\times\boldsymbol{e}_t=+j\omega(\boldsymbol{\mu}\cdot\boldsymbol{h}\ )_t\ , \tag{A11}$$

and

$$z\times\nabla h_z+gz\times\boldsymbol{h}_t=-j\omega(\boldsymbol{\epsilon}\cdot\boldsymbol{e})_t\ . \tag{A12}$$

For the isotropic materials discussed in the text, Eqs. (A7)–(A12) reduce to Eqs. (2)–(7). In general, it appears difficult to generalize the text to include materials of arbitrary anisotropy. However, generalization is fairly simple in the absence of terms in $\boldsymbol{\epsilon}$ and $\boldsymbol{\mu}$ coupling between transverse and axial field components. In that case, we can write

$$\boldsymbol{\epsilon}=\boldsymbol{\epsilon}_t+\epsilon_z zz;\ z\cdot\boldsymbol{\epsilon}_t=\boldsymbol{\epsilon}_t\cdot z=0 \tag{A13}$$

and

$$\boldsymbol{\mu}=\boldsymbol{\mu}_t+\mu_z zz;\ z\cdot\boldsymbol{\mu}_t=\boldsymbol{\mu}_t\cdot z=0. \tag{A14}$$

All of the results in the text follow with slight modification. For example, equations Eqs. (B5) and (B6), from which the circuit parameter expressions arise, must be modified by the following replacements:

$$\epsilon|\boldsymbol{e}_t|^2\rightarrow\boldsymbol{e}_t{}^*\cdot\boldsymbol{\epsilon}_t\cdot\boldsymbol{e}_t, \tag{A15}$$

$$\mu|\boldsymbol{h}_t|^2\rightarrow\boldsymbol{h}_t{}^*\cdot\boldsymbol{\mu}_t\cdot\boldsymbol{h}_t, \tag{A16}$$

$$\epsilon|e_z|^2\rightarrow\epsilon_z|e_z|^2, \tag{A17}$$

and

$$\mu|h_z|^2\rightarrow\mu_z|h_z|^2. \tag{A18}$$

7. Appendix B. Circuit Parameter Integral Expressions

Taking the scalar product of both sides of Eq. (5) with $z\times\boldsymbol{e}_t{}^*$ results in

$$\gamma z\cdot\boldsymbol{e}_t{}^*\times\boldsymbol{h}_t+z\cdot\boldsymbol{e}_t{}^*\times\nabla h_z=$$

$$+j\omega\epsilon(z\times\boldsymbol{e}_t{}^*)\cdot(z\times\boldsymbol{e}_t)=+j\omega\epsilon|\boldsymbol{e}_t|^2. \tag{B1}$$

Integrating over the cross section of the waveguide and recognizing the first integral as $p_0{}^*=|v_0|^2/Z_0$, we have

$$\frac{\gamma}{Z_0}=\frac{1}{|v_0|^2}\left[j\omega\int_S\epsilon|\boldsymbol{e}_t|^2\mathrm{d}S-z\cdot\int_S\boldsymbol{e}_t{}^*\times\nabla h_z\mathrm{d}S\right]. \tag{B2}$$

The second integral can be manipulated into a simpler form. First apply Stokes's Law to the vector $h_z\boldsymbol{e}_t{}^*$ to yield

$$\int_S\nabla\times(h_z\boldsymbol{e}_t{}^*)\cdot z\,\mathrm{d}S=\int_S h_z\nabla\times\boldsymbol{e}_t{}^*\cdot z\,\mathrm{d}S-$$

$$\int_S\boldsymbol{e}_t{}^*\times\nabla h_z\cdot z\,\mathrm{d}S=\int_{\partial S}h_z\boldsymbol{e}_t{}^*\cdot\mathrm{d}\boldsymbol{l}, \tag{B3}$$

where ∂S is the boundary of S and $\mathrm{d}\boldsymbol{l}$ is a line element along that boundary. If the waveguide is transversely closed by a perfectly conducting boundary, then S coincides with that boundary and the line integral vanishes. If the waveguide is open, then a portion of S may lie at infinity, but the integral also vanishes as long as $\boldsymbol{e}_t$ vanishes fast enough to ensure that the modal power is finite. Finally, although Stokes' Law cannot formally be applied across material discontinuities, it can readily be shown that the line integrals on both sides of the boundary are equal and opposite. As a result, the line integral in Eq. (B3) vanishes. The insertion of Eq. (2) simplifies Eq. (B3) to

$$z \cdot \int_S e_t{}^* \times \nabla h_z \mathrm{d}S = \int_S h_z \nabla \times e_t{}^* \cdot z \mathrm{d}S =$$

$$j\omega \int_S \mu^* |h_z|^2 \mathrm{d}S, \qquad \text{(B4)}$$

so Eq. (B2) becomes

$$\frac{\gamma}{Z_0} = \frac{j\omega}{|v_0|^2} \left[\int_S \epsilon |e_t|^2 \mathrm{d}S - \int_S \mu^* |h_z|^2 \mathrm{d}S \right]. \qquad \text{(B5)}$$

By an analogous procedure using Eqs. (3) and (4), we may demonstrate that

$$\gamma Z_0 = \frac{j\omega}{|i_0|^2} \left[\int_S \mu |h_t|^2 \,\mathrm{d}S - \int_S \epsilon^* |e_z|^2 \,\mathrm{d}S \right]. \qquad \text{(B6)}$$

The use of Eqs. (B5) and (B6) along with definitions (29) and (30) results in Eqs. (33)–(36) for the circuit parameters C, L, G, and R.

8. Appendix C. Relations Between p_0 and γ

From Eqs. (20), (29), and (30),

$$\gamma p_0{}^* = |v_0|^2 \, [j\omega C + G] \qquad \text{(C1)}$$

and

$$\gamma p_0 = |i_0|^2 \, [j\omega L + R], \qquad \text{(C2)}$$

from which it can readily be shown that

$$2\mathrm{Re}(\gamma)\ \mathrm{Re}(p_0) = +|v_0|^2 G + |i_0|^2 R\ , \qquad \text{(C3)}$$

$$2\mathrm{Re}(\gamma)\ \mathrm{Im}(p_0) = -|v_0|^2\, \omega C + |i_0|^2 \omega L, \qquad \text{(C4)}$$

$$2\,\mathrm{Im}(\gamma)\ \mathrm{Re}(p_0) = +|v_0|^2\, \omega C + |i_0|^2 \omega L, \qquad \text{(C5)}$$

and

$$2\,\mathrm{Im}(\gamma)\ \mathrm{Im}(p_0) = +|v_0|^2\, G - |i_0|^2 R. \qquad \text{(C6)}$$

An interesting alternative form of Eq. (C5) is

$$\mathrm{Re}(p_0) = \frac{\omega}{\beta} \left[\frac{1}{2} |v_0|^2 \, C + \frac{1}{2} \, |i_0|^2 \, L \right]. \qquad \text{(C7)}$$

This is the real average power carried by the forward mode at $z=0$. For TEM modes, it is the product of the group velocity ω/β and the energy density (per unit length), represented by the term in brackets.

If the materials are lossless, then certain useful results apply. In that case, $|v_0|^2 G = |i_0|^2 R = 0$. Aside from the degenerate case in which $\gamma p_0 = 0$, only two sorts of modes may exist. The first, which we denote propagating modes, satisfy

$$\mathrm{Re}(\gamma) = \mathrm{Im}(p_0) = \mathrm{Im}(Z_0) = 0;$$

$$\mathrm{Im}(\gamma) \neq 0;\ \mathrm{Re}(p_0) > 0, \qquad \text{(C8)}$$

which implies that they propagate without decay with a real characteristic impedance. Equation (C4) becomes

$$(\mathrm{Re}(\gamma) = 0) \Rightarrow |v_0|^2 \, C = |i_0|^2 L, \qquad \text{(C9)}$$

leaving free only one of the four parameters R, C, G, and L. Equation (C9) can be expanded as

$$(\mathrm{Re}(\gamma) = 0) \Rightarrow \int_S \mu |h|^2 \,\mathrm{d}S = \int_S \epsilon |e|^2 \,\mathrm{d}S. \qquad \text{(C10)}$$

This states the well-known result [3] that the energy in a lossless propagating wave is divided equally between the electric and magnetic fields.

Modes in lossless media with $\gamma p_0 \neq 0$ that are *not* propagating satisfy

$$\mathrm{Im}(\gamma) = \mathrm{Re}(p_0) = \mathrm{Re}(Z_0) = 0;$$

$$\mathrm{Re}(\gamma) > 0;\ \mathrm{Im}(p_0) \neq 0, \qquad \text{(C11)}$$

and therefore

$$|v_0|^2 \, C = -|i_0|^2 L. \qquad \text{(C12)}$$

These modes are purely evanescent, decaying exponentially and, in isolation, carrying no real power. The inductance and capacitance are of opposite sign.

If we restrict ourselves to passive but not necessarily lossless media, certain converse results apply. Passivity ensures that G and R are nonnegative. Thus, if either $\mathrm{Re}(\gamma) = 0$ or $\mathrm{Re}(p_0) = 0$, then Eq. (C3) requires $|v_0|^2 G = |i_0|^2 R = 0$. Since ϵ'' and μ'' are nonnegative in passive media, Eqs. (35) and (36) require that $\epsilon'' e = \mu'' h = 0$ everywhere. Now, if $e = 0$, then Maxwell's equations imply that $h = 0$ (and *vice versa*), except in the case $\omega = 0$, which we have explicitly excluded. Therefore, in passive media, the possibilities $\mathrm{Re}(\gamma) = 0$ (unattenuated mode) or $\mathrm{Re}(p_0) = 0$ (mode carrying no real power) occur only if $\epsilon'' = \mu'' = 0$; that is, only when the media are lossless. In contrast, there is no apparent prohibition against $\mathrm{Im}(\gamma)$ or $\mathrm{Im}(p_0)$ vanishing in lossy media.

Finally, we treat the degenerate modes in which either γ or p_0 vanishes. From Eqs. (C1) and (C2), these modes satisfy

$$\{\gamma p_0 = 0\} \Rightarrow |v_0|^2 C = |v_0|^2 G = |i_0|^2 L = |i_0|^2 R = 0. \quad \text{(C13)}$$

The second and fourth conditions ensure that such degeneracy occurs only in lossless waveguides.

If $\gamma = 0$, then Maxwell's equations decouple into one set [Eqs. (2), (5), and (6)] involving only e_t and h_z and another set [Eqs. (3), (4), and (7)] involving only h_t and e_z. Therefore, we can decompose the fields into modes with either $e_t = h_z = 0$ or $h_t = e_z = 0$. In the former case, $|v_0|^2 C$ automatically vanishes, due to Eq. (33), and the condition $|i_0|^2 L = 0$ constrains the remaining fields; the opposite holds true in the latter case. In either situation, $p_0 = 0$ since the Poynting vector $e_t \times h_t$ vanishes. In this case $\gamma = p_0 = 0$, exemplified by a lossless waveguide mode operating exactly at the cutoff frequency, the forward and backward modes are indistinguishable.

On the other hand, $p_0 = 0$ does *not* imply that $\gamma = 0$. Furthermore, in contrast to the lossless case with $p_0 \neq 0$ discussed above, γ is *not* restricted to be real or imaginary. "Complex waves," in which γ is neither real nor imaginary even though the materials are lossless, have been discovered in inhomogeneous as well as in anisotropic media. They are discussed in Ref. [20] and references included therein.

9. Appendix D. Reciprocity Relations

Consider two sets of electromagnetic fields (E', H') and (E'', H''), which are produced by two different sets of boundary conditions. Applying the divergence theorem to $E' \times H''$ and using the homogeneous Maxwell's equations produces the well-known result that

$$\int (E' \times H'' - E'' \times H') \cdot n \, \mathrm{d}S = 0, \quad \text{(D1)}$$

whenever the permittivity and permeability tensors are symmetric. In Eq. (D1), the surface encloses a closed region and the unit vector n is the outward normal to the surface. We let the surface enclose an entire waveguide junction and become infinitely large in such a way that the contributions to the integral can be entirely accounted for by the single mode of interest propagating in each waveguide leaving the junction. Expressing the fields in each port n in terms of Eqs. (12) and (13), Eq. (D1) becomes

$$\sum_n \frac{v_n' i_n''}{v_{0n} i_{0n}} \tilde{p}_{0n} = \sum_n \frac{v_n'' i_n'}{v_{0n} i_{0n}} \tilde{p}_{0n}, \quad \text{(D2)}$$

having defined

$$\tilde{p}_{0n} \equiv \int_{S_n} e_{tn} \times h_{tn} \cdot z \, \mathrm{d}S, \quad \text{(D3)}$$

where S_n is the cross section of the nth waveguide. Equation (D2) can be written as the matrix equation

$$\mathrm{i}''^{\mathrm{t}} \mathrm{W} \mathrm{v}' = \mathrm{v}''^{\mathrm{t}} \mathrm{W} \mathrm{i}'. \quad \text{(D4)}$$

As before, i and v are column vectors of i_n and v_n, and "t" stands for "transpose." W is the diagonal matrix

$$\mathrm{W} \equiv \mathrm{diag}(\mathrm{W}_n); \; \mathrm{W}_n \equiv \frac{\tilde{p}_{0n}}{v_{0n} i_{0n}} = \frac{v_{0n}^*}{v_{0n}} \frac{\tilde{p}_{0n}}{\tilde{p}_{0n}^*}, \quad \text{(D5)}$$

where Eq. (20) has been used. Inserting $\mathrm{v} = \mathrm{Z}\mathrm{i}$ into Eq. (D4) and requiring that the result holds for all values of i' and i'', we determine that

$$\mathrm{Z}^{\mathrm{t}} = \mathrm{W} \mathrm{Z} \mathrm{W}^{-1}, \quad \text{(D6)}$$

which is the reciprocity requirement on the impedance matrix. It requires that the elements of Z satisfy

$$\mathrm{Z}_{nm} = \frac{\mathrm{W}_m}{\mathrm{W}_n} \mathrm{Z}_{mn}\,. \quad \text{(D7)}$$

To determine the analogous condition on S, take the transpose of Eq. (E5):

$$\mathrm{S}^{\mathrm{t}} = \mathrm{U}^{-1} (\mathrm{Z}^{\mathrm{t}} + \mathrm{Z}_{\mathrm{ref}})^{-1} (\mathrm{Z}^{\mathrm{t}} - \mathrm{Z}_{\mathrm{ref}}) \mathrm{U}. \quad \text{(D8)}$$

Insert Eq. (D6) and factor out W and W^{-1}, noting that $\mathrm{W}\, \mathrm{Z}_{\mathrm{ref}}\, \mathrm{W}^{-1} = \mathrm{Z}_{\mathrm{ref}}$ since W and $\mathrm{Z}_{\mathrm{ref}}$ are diagonal. The result is

$$\mathrm{S}^{\mathrm{t}} = \mathrm{U}^{-1} \mathrm{W} (\mathrm{Z} + \mathrm{Z}_{\mathrm{ref}})^{-1} (\mathrm{Z} - \mathrm{Z}_{\mathrm{ref}}) \mathrm{W}^{-1} \mathrm{U}. \quad \text{(D9)}$$

The two central terms can be commuted using the fact that any matrices A and B satisfy

$$(\mathsf{A}+\mathsf{B})^{-1}(\mathsf{A}-\mathsf{B})=\mathsf{B}^{-1}(\mathsf{A}-\mathsf{B})(\mathsf{A}+\mathsf{B})^{-1}\mathsf{B} \qquad (D10)$$

as long as the inverses exist. Using Eq. (D10) in Eq. (D9) and using Eq. (E5) to express the result in terms of S, we have

$$\mathsf{S}^{t}=\mathsf{P}^{-1}\mathsf{S}\,\mathsf{P}, \qquad (D11)$$

using the definition

$$\mathsf{P}\equiv \mathsf{Z}_{\rm ref}\,\mathsf{U}^{2}\,\mathsf{W}^{-1}. \qquad (D12)$$

Since P is diagonal, Eq. (D11) requires that the elements of S satisfy

$$\mathsf{S}_{nm}=\frac{\mathsf{P}_{nn}}{\mathsf{P}_{mm}}\,\mathsf{S}_{mn}, \qquad (D13)$$

which is expressed more explicitly as Eq. (64) of the text.

We can also develop a reciprocity relation for the power wave scattering matrix, defined by

$$\hat{\mathsf{b}}=\hat{\mathsf{S}}\hat{\mathsf{a}}, \qquad (D14)$$

where

$$\hat{\mathsf{a}}=\mathsf{F}(\mathsf{v}+\hat{\mathsf{Z}}\mathsf{i}) \qquad (D15)$$

and

$$\hat{\mathsf{b}}=\mathsf{F}(\mathsf{v}-\hat{\mathsf{Z}}^{*}\mathsf{i}) \qquad (D16)$$

are the vector forms of Eqs. (121) and (122). We have defined

$$\hat{\mathsf{Z}}\equiv {\rm diag}\,(\hat{Z}) \qquad (D17)$$

and

$$\mathsf{F}\equiv {\rm diag}\left(\frac{1}{2\sqrt{\hat{Z}}}\right). \qquad (D18)$$

Inserting Eqs. (D15) and (D16), as well as v = Zi, into Eq. (D14) and insisting that the result hold for all i yields

$$\hat{\mathsf{S}}=\mathsf{F}(\mathsf{Z}-\hat{\mathsf{Z}}^{*})\,(\mathsf{Z}+\hat{\mathsf{Z}})^{-1}\,\mathsf{F}^{-1}, \qquad (D19)$$

the transpose of which is

$$\hat{\mathsf{S}}^{t}=\mathsf{F}^{-1}\,(\mathsf{Z}^{t}+\hat{\mathsf{Z}})^{-1}\,(\mathsf{Z}^{t}-\hat{\mathsf{Z}}^{*})\,\mathsf{F}. \qquad (D20)$$

Using Eq. (D6) and some simple manipulation leads to

$$\hat{\mathsf{S}}^{t}=\mathsf{F}^{-1}\,\mathsf{W}(\mathsf{Z}+\hat{\mathsf{Z}})^{-1}\,(\mathsf{Z}-\hat{\mathsf{Z}}^{*})\,\mathsf{W}^{-1}\,\mathsf{F}. \qquad (D21)$$

Reference [8] shows that

$$(\mathsf{Z}+\hat{\mathsf{Z}})^{-1}\,(\mathsf{Z}-\hat{\mathsf{Z}}^{*}) =$$

$$\mathsf{F}^{2}(\mathsf{Z}-\hat{\mathsf{Z}}^{*})(\mathsf{Z}+\hat{\mathsf{Z}})^{-1}\mathsf{F}^{-2}=\mathsf{F}\hat{\mathsf{S}}\mathsf{F}^{-1}, \qquad (D22)$$

so that Eq. (D21) reduces to the simple result

$$\hat{\mathsf{S}}^{t}=\mathsf{W}\hat{\mathsf{S}}\mathsf{W}^{-1} \qquad (D23)$$

The power wave scattering matrix therefore obeys a reciprocity relation identical to the one (D6) satisfied by the impedance matrix. In lossy waveguides, neither is generally symmetric.

10. Appendix E. Relations Between Z and S

Recall that a, b, v, and i are defined as column vectors whose elements are a_m, b_m, v_m, and i_m at the various waveguide ports m. The vector representation of Eqs. (53) and (54) are

$$\mathsf{a}=\frac{1}{2}\,\mathsf{U}(\mathsf{v}+\mathsf{Z}_{\rm ref}\,\mathsf{i}) \qquad (E1)$$

and

$$\mathsf{b}=\frac{1}{2}\,\mathsf{U}\,(\mathsf{v}-\mathsf{Z}_{\rm ref}\,\mathsf{i}), \qquad (E2)$$

where U is a diagonal matrix defined by

$$\mathsf{U}\equiv {\rm diag}\left(\frac{|v_{0m}|}{v_{0m}}\,\frac{\sqrt{{\rm Re}(Z^{m}_{\rm ref})}}{Z^{m}_{\rm ref}}\right). \qquad (E3)$$

Inserting v = Zi into Eqs. (E1) and (E2) eliminates v. The condition b = Sa then implies

$$\mathsf{b}=\frac{1}{2}\,\mathsf{U}\,(\mathsf{Z}-\mathsf{Z}_{\rm ref})\mathsf{i}=\mathsf{S}\mathsf{a}=\frac{1}{2}\,\mathsf{S}\mathsf{U}\,(\mathsf{Z}+\mathsf{Z}_{\rm ref})\mathsf{i}. \qquad (E4)$$

Since this must hold for all i, we can solve for S, yielding

$$\mathsf{S}=\mathsf{U}\,(\mathsf{Z}-\mathsf{Z}_{\rm ref})\,(\mathsf{Z}+\mathsf{Z}_{\rm ref})^{-1}\mathsf{U}^{-1}=$$

$$\mathsf{U}(\mathsf{Z}\mathsf{Z}_{\rm ref}^{-1}-\mathsf{I})\,(\mathsf{Z}\mathsf{Z}_{\rm ref}^{-1}+\mathsf{I})^{-1}\mathsf{U}^{-1}. \qquad (E5)$$

This can be easily inverted to produce

$$\mathsf{Z}=(\mathsf{I}-\mathsf{U}^{-1}\mathsf{S}\mathsf{U})^{-1}\,(\mathsf{I}+\mathsf{U}^{-1}\mathsf{S}\mathsf{U})\mathsf{Z}_{\rm ref}. \qquad (E6)$$

11. Appendix F. Renormalization Table

The text allows for the arbitrarily normalization of the parameters $\boldsymbol{e}_t$ and v_0. This table details the effects of renormalizing these two parameters on the remaining variables. The second column shows the effect on the element in the first column of multiplying $\boldsymbol{e}_t$ by the factor α. The third column shows the results of a change in the voltage integration path which multiplies v_0 by the factor β. No result is shown if the variable is independent of the normalization.

Renormalization table

γ		
$\boldsymbol{E}_t, \boldsymbol{H}_t$		
$\boldsymbol{e}_t, \boldsymbol{h}_t$	$\alpha\boldsymbol{e}_t,\ \alpha\boldsymbol{h}_t$	
c_+, c_-	$c_+/\alpha,\ c_-/\alpha$	
v_0	αv_0	βv_0
i_0	αi_0	i_0/β^*
v		βv
i		i/β^*
p_0	$\lvert\alpha\rvert^2 p_0$	
p		
P		
Z_0		$\lvert\beta\rvert^2 Z_0$
$C,\ G$		$C/\lvert\beta\rvert^2,\ G/\lvert\beta\rvert^2$
$L,\ R$		$\lvert\beta\rvert^2 L,\ \lvert\beta\rvert^2 R$
$a_0,\ b_0$	$\frac{\lvert\alpha\rvert}{\alpha} a_0,\ \frac{\lvert\alpha\rvert}{\alpha} b_0$	
$a(Z_{\mathrm{ref}}), b(Z_{\mathrm{ref}})$	$\frac{\lvert\alpha\rvert}{\alpha} a(Z_{\mathrm{ref}}), \frac{\lvert\alpha\rvert}{a} b(Z_{\mathrm{ref}})$	$a(Z_{\mathrm{ref}}/\lvert\beta\rvert^2), b(Z_{\mathrm{ref}}/\lvert\beta\rvert^2)$
$\tilde{p}_0$	$\alpha^2 \tilde{p}_0$	
K_n	$\left(\frac{\alpha}{\lvert\alpha\rvert}\right)^2 K_n$	
W_n		$\frac{\beta^*}{\beta} W_n$
S_{ij}^0	$\frac{\lvert\alpha_i\rvert}{\alpha_i} \frac{\alpha_j}{\lvert\alpha_j\rvert} S_{ij}^0$	
$S_{ij}(Z_{\mathrm{ref}}^i, Z_{\mathrm{ref}}^j)$	$\frac{\lvert\alpha_i\rvert}{\alpha_i} \frac{\alpha_j}{\lvert\alpha_j\rvert} S_{ij}\ (Z_{\mathrm{ref}}^i, Z_{\mathrm{ref}}^j)$	$S_{ij}(Z_{\mathrm{ref}}^i/\lvert\beta_i\rvert^2, Z_{\mathrm{ref}}^j/\lvert\beta_j\rvert^2)$
Γ_0		
$\Gamma(Z_{\mathrm{ref}})$		$\Gamma(Z_{\mathrm{ref}}/\lvert\beta\rvert^2)$
Z_{ij}		$\beta_i\ \beta_j^*\ Z_{ij}$
Z_{load}		$\lvert\beta\rvert^2\ Z_{\mathrm{load}}$
Y_{ij}		$Y_{ij}/(\beta_i^*\ \beta_j)$
R^0	$\frac{\lvert\alpha_1\rvert}{\alpha_1} \frac{\alpha_2}{\lvert\alpha_2\rvert} \mathsf{R}^0$	
$\mathsf{R}(Z_{\mathrm{ref}}^1, Z_{\mathrm{ref}}^2)$	$\frac{\lvert\alpha_1\rvert}{\alpha_1} \frac{\alpha_2}{\lvert\alpha_2\rvert}\ \mathsf{R}(Z_{\mathrm{ref}}^1, Z_{\mathrm{ref}}^2)$	$\mathsf{R}(Z_{\mathrm{ref}}^1/\lvert\beta_1\rvert^2, Z_{\mathrm{ref}}^2/\lvert\beta_2\rvert^2)$

Acknowledgments

The authors appreciate the contributions of Prof. Robert E. Collin and Dr. David A. Hill, both of whom read the manuscript and offered critical suggestions.

12. References

[1] C. G. Montgomery, R. H. Dicke, and E. M. Purcell, eds., Principles of Microwave Circuits, New York, McGraw-Hill (1948).

[2] N. Marcuvitz, Waveguide Handbook, New York, McGraw-Hill (1951).

[3] R. E. Collin, Foundations for Microwave Engineering, New York, McGraw-Hill (1966).

[4] D. M. Kerns and R. W. Beatty, Basic Theory of Waveguide Junctions and Introductory Microwave Network Analysis, Oxford, Pergamon Press (1967).

[5] F. E. Gardiol, Lossy Transmission Lines, Norwood, Ma, Artech House (1987).

[6] J. R. Brews, Transmission Line Models for Lossy Waveguide Interconnections in VLSI, IEEE Trans. Electron Devices **ED-33**, 1356–1365 (1986).

[7] D. C. Youla, On Scattering Matrices Normalized to Complex Port Numbers, Proc. IRE **49**, 1221 (1961).

[8] K. Kurokawa, An Introduction to the Theory of Microwave Circuits, New York, Academic Press (1969).

[9] R. F. Harrington, Time-Harmonic Electromagnetic Fields, New York, McGraw-Hill (1961) pp. 17–20.

[10] J. R. Brews, Characteristic Impedance of Microstrip Lines, IEEE Trans. Microwave Theory Tech. **MTT-35**, 30–34 (1987).

[11] S. A. Schelkunoff, Impedance Concept in Wave Guides, Quart. Appl. Math. **2**, 1–14 (1944).

[12] R. B. Marks and D. F. Williams, Characteristic Impedance Determination Using Propagation Constant Measurement, IEEE Microwave Guided Wave Lett. **1**, 141–143 (1991)

[13] D. F. Williams and R. B. Marks, Transmission Line Capacitance Measurement, IEEE Microwave Guided Wave Lett. **1**, 243–245 (1991).

[14] D. F. Williams and R. B. Marks, Reciprocity Relations in Waveguide Junctions. Submitted to IEEE Trans. Microwave Theory Tech.

[15] D. F. Williams, R. B. Marks, D. K. Walker, and F. R. Clague, Wafer Probe Transducer Efficiency, IEEE Microwave Guided Wave Lett. **2**, pp. 388–390 (1992).

[16] D. Williams, R. Marks, and K. R. Phillips, Translate LRL and LRM Calibrations, Microwaves & RF **30**, 78–84 (1991).

[17] G. F. Engen and C. A. Hoer, Thru-Reflect-Line: An Improved Technique for Calibrating the Dual Six-Port Automatic Network Analyzer, IEEE Trans. Microwave Theory Tech. **MTT-27**, 987–993 (1979).

[18] R. B. Marks, A Multiline Method of Network Analyzer Calibration, IEEE Trans. Microwave Theory Tech. **39**, 1205–1215 (1991).

[19] H.-J. Eul and B. Schiek, A Generalized Theory and New Calibration Procedures for Network Analyzer Self-Calibration, IEEE Trans. Microwave Theory Tech. **39**, 724–731 (1991).

[20] M. Mrozowski and J. Mazur, Matrix Theory Approach to Complex Waves, IEEE Trans. Microwave Theory Tech. **40**, 781–785 (1992).

About the authors: *Roger B. Marks is a physicist and Dylan F. Williams a project leader in the Electromagnetic Fields Division of the Electronics and Electrical Engineering Laboratory, NIST, Boulder, CO. The National Institute of Standards and Technology is an agency of the Technology Administration, U.S. Department of Commerce.*

Volume 97, Number 5, September-October 1992
Journal of Research of the National Institute of Standards and Technology

[J. Res. Natl. Inst. Stand. Technol. 97, 563 (1992)]

Resistive Liquid-Vapor Surface Sensors for Liquid Nitrogen and Hydrogen

Volume 97 Number 5 September-October 1992

J. D. Siegwarth, R. O. Voth, and S. M. Snyder

National Institute of Standards and Technology,
Boulder, CO 80303

Ten resistance thermometers were tested as point sensors for detecting the liquid-vapor interface in liquid nitrogen and liquid hydrogen. Test results showed that most could be made to detect the liquid surface and lead orientation can be important. A silicon resistive sensor had the fastest response and produced the greatest signal change.

Key words: interface; liquid hydrogen; liquid nitrogen; liquid-vapor; resistance thermometer; surface sensor.

Accepted: July 9, 1992

1. Introduction

In the early 1960s a number of liquid-vapor (L-V) interface sensing devices were tested in liquid hydrogen (LH_2) [1–3]. Part of this work was done at the National Institute of Standards and Technology (then the National Bureau of Standards) for NASA Lewis Research Center. The sensors tested were then commercially available and had various principles of operation. Differences in resistance, capacitance, light reflection, acoustic impedance and viscous damping indicated whether the sensors were in liquid or gas. Since many of the sensors in these early tests were liquid level measuring devices, resolving the liquid surface well in the vertical direction was all they were required to do. Many new level gaging devices are commercially available today but like the sensors examined in the earlier tests, they are still mostly uniaxial devices. Often, the sensing element itself is large in the plane perpendicular to the vertical axis.

The objective of this study was to identify devices to serve as L-V detectors in zero gravity. In zero gravity, the liquid-vapor interface can be moving in any direction. This means the L-V sensor must approximate a point sensor to give the same resolution of the passing of an interface from any direction. Resistance thermometer and optical type sensors approximating point sensors were the only sensors tested in this work. The results of the tests of resistive sensors are reported here. The optical sensor tests results have been reported elsewhere [4].

A resistive L-V sensor has a temperature dependent resistance and when operated at low power dissipation, can serve as a thermometer. The heat transfer from the sensor to the surroundings must be sufficiently large that the temperature difference between the thermometer and the surroundings is below the tolerable measurement error. The difference in the heat transfer from the thermometer to a liquid relative to the heat transfer to equilibrium vapor can be large. A thermometer thus becomes an L-V sensor when the power is raised until the sensor temperature difference between liquid and vapor, hence the resistance difference, becomes large enough to detect easily.

A small sensor size is advantageous not only for spatial resolution but also for sensor response time.

The smaller the mass and surface area, the faster the response upon leaving the liquid. The larger dR/dT, the greater the signal change. Some overlap of these two effects occurs because they are coupled through the magnitude of the temperature change between entry and exit of the liquid. A small mass allows the sensor to respond more rapidly when the sensor enters the liquid. A small sensor surface area however, which is an advantage when the sensor leaves the liquid, slows the response when the sensor enters the liquid.

Since the work of the 1960s, a number of new, miniature resistance thermometers have become available. Many of the resistive L-V sensors tested in this work are commercially available thermometers operated at much higher power than specified by the manufacturer. The time constants and magnitude of the output signal change have been examined over a range of power levels for both liquid hydrogen and liquid nitrogen (LN_2).

2. Apparatus

The apparatus used to test the sensors is shown in Fig. 1. The testing in LH_2 was done in a sealed glass Dewar system to prevent air from contacting the hydrogen. Up to six sensors could be mounted on a holder and tested simultaneously. The holder was cycled rapidly up and down by the manually controlled drive cylinder, which was a double acting air cylinder. The total travel was about 10 cm. Air cushions in each end of the cylinder brought the piston to a stop at the end of its travel. The water driven cylinder served to adjust the vertical position of the drive cylinder and sensor holder so that the sensors passed through the liquid interface somewhere between the 2.5 and 7.5 cm positions of the drive cylinder travel. A linear potentiometer connected to the drive cylinder shaft gave a position signal for which 1 V was equivalent to 2.5 cm of travel. The position at which the sensors crossed the interface could be determined either by placing a sensor at the liquid level and reading the position voltage or by noting the voltage at which a faster L-V sensor started the transition between the gas signal, S_g, and the liquid signal, S_l.

The velocity of the sensor holder at mid stroke was about 3 m/s at the drive air pressures used. The transit time of a sensor through the liquid interface was less than 2 ms for most of the sensors tested. The shortest cycle times of the sensor holder were about 1.5 s.

Individual sensors were mounted on stainless steel blades, 51×17×0.5 mm in dimension. The sensors were centered in 7 mm diameter holes punched near the end of these blades. With a few exceptions, the sensors were supported by their leads. The sensor leads were either clamped mechanically or cemented to the blades. The blades were bolted to the sensor holder at the ends opposite the sensors. Most of the tests were done with the blades mounted so the leads to the sensor were horizontal. One test each in LN_2 and LH_2 was done with the blades mounted so the leads ran vertically down to the sensors.

The electrical leads to the holder were fastened to and guided by a thin steel strip which was attached on one end to a fixed point at the dewar wall and to the moving sensor holder on the other. The rolling loop in this strip allowed the leads to follow the sensor holder.

The sensors were powered either by a constant current or a constant voltage source. The sensor output was the voltage across the sensor for constant current, or the voltage across a fixed resistor in series with the sensor for constant voltage. The constant voltage mode was chosen when the voltage needed to supply the desired power exceeded 10 V or because of the temperature dependence of the sensor resistance was positive.

The output signals from the L-V sensors and the position sensor were sequentially read by a 13 bit high speed 8 channel multiplexer and analog to digital converter card in a laboratory computer. The card was capable of reading at a rate near 10^5 readings/s. Since the reading rate never exceeded 2000 readings/s for one channel, no correction for channel delay was needed. The elapsed time for each test run was limited by the amount of data that could be stored. When only two data channels were recorded, 13,000 readings for each channel was the maximum. The measurement time was added to the data files after the data were taken by multiplying the reading number by the reading period.

The response time of the sensor was defined in these tests as the time elapsed between the time the sensor crossed the liquid surface according to the position sensor voltage and the time at which the L-V sensor signal, S, reached

$$S = (S_l - S_g)/2. \qquad (1)$$

Semiconductor sensors have resistances that increase with decreasing T so $S_l > S_g$ for constant current measurements. Shorter response times than those determined from the S of Eq. (1) could be obtained if the signal processor used a higher

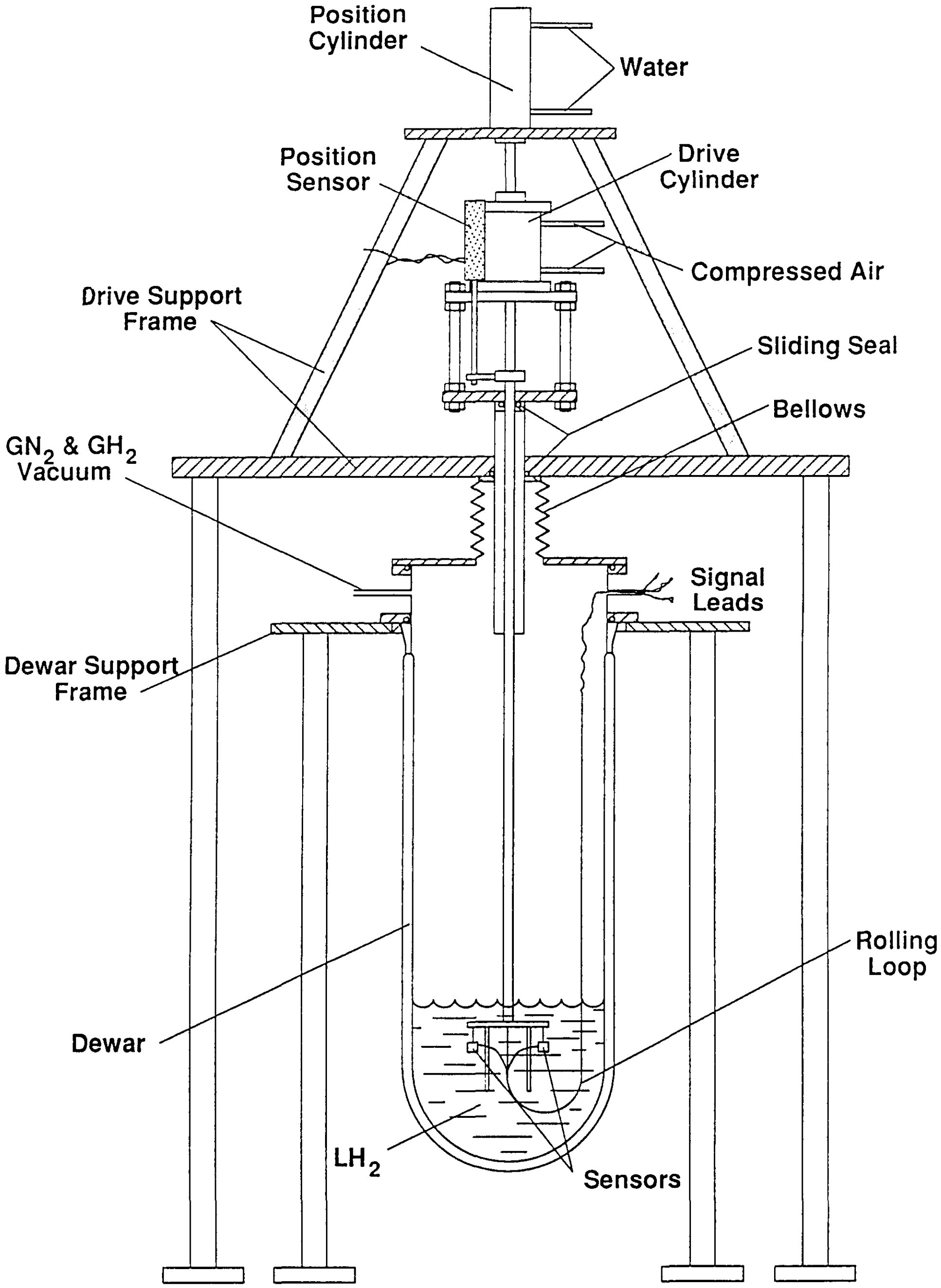

Fig. 1. Test apparatus for liquid-vapor surface sensors.

sensor signal level to indicate entering the liquid surface and a lower one to indicate leaving the surface. The data were analyzed by the computer to determine the response times.

The sensors were cycled in and out several times in these tests. Because the test duration was limited by the amount of data that could be stored, the reading frequency was adjusted to the minimum frequency that could resolve the most important of the signal details. The slowest response time was generally the detail of interest and that was the response time in switching from liquid to gas. The response time from gas to liquid of most sensors was much shorter and was not resolved more accurately, since the response time was less than the measuring period.

3. Resistive Sensors Tested

A brief description of the resistive sensors tested is given in below and in Table 1.

LVD Goddard (LVDG): These sensors were built at Goddard Space Flight Center. The sensor consisted of a small cube of doped silicon with the two leads attached to opposite faces. The design was that used for L-V interface sensors in the SHOOT experiment [5]. The doped silicon chips used in these tests were selected by the Goddard staff for high sensitivity at 20 K (LH_2 temperature at 101 kPa).

Silicon-on-sapphire (SOS): This sensor was built at NIST for use as a fast response thermometer.

K: This sensor is a commercially available thermometer. It was designed to operate over the range where the resistance (R) versus temperature (T) has a positive slope. A minimum in the R versus T curve occurred at about 100 K. A little below LN_2 temperature (77 K at 101 kPa) R, measured by a digital multimeter, exceeded 25 MΩ. This sensor proved to be too fragile to be supported only by its leads. After two sensors so supported broke, a sensor was cemented to some stainless steel shim stock about 0.1 mm thick.

PT1 and PT2: These sensors are commercially available platinum thermometers consisting of platinum films on ceramic substrates. They differ mainly in physical size and resistance. The resistance at 0° C of the smaller is 100 Ω and the larger is 1 k Ω.

DT0, DT1, and S: These three diode thermometers came from a commercial source. DT0, essentially the same thermometer as DT1 but in a different envelope, is no longer made. DT1 and S were built by two different manufacturers but have very similar voltage versus temperature responses. They differed mainly in that DT1 was encapsulated, while S was not.

Mdac: This sensor was a 12 kΩ, 1/4 W resistor in parallel with a 1 kΩ nominal thermistor of unknown manufacture. This sensor is used by an aerospace company both as a L-V sensor and as a thermometer. Two units were tested in this work. One consisted of the bare thermistor and resistor on the end of a probe and connected to small gage copper leads. The other unit consisted of the two elements epoxied together with their leads soldered to two heat sink plates about $7 \times 33 \times 1/2$ mm in dimensions.

CARBON1: This carbon resistor was of unknown manufacture but had sufficient temperature dependence to be a usable carbon thermometer.

4. Test Results

4.1 LVD Goddard, LH_2 Tests

Figure 2 shows several cycles of a rapid cycle test of LVDG in LH_2 at 9 mA constant current. A large signal level change was obtained. The response time for entering and leaving cannot be distinguished from zero on this time scale.

Figures 3a and 3b show the first withdrawal from the liquid and return to the liquid from the same data as Fig. 2 on an expanded time scale. The L-V sensor level defined by Eq. (1) was 3.95 V, and occurred at 0.4090 s. The L-V sensor actually crossed the liquid surface at 0.4075 s, when the position sensor output was 1.9 V. The difference of 1.5 ms was the response time. The slope of the position sensor curve at 1.9 V gives a velocity of the sensor through the liquid surface of over 3 m/s which means the LVDG sensor passed through the liquid surface in less than 0.1 ms. The oscillation in the signal from the position indicator at the end of the holder travel was caused by the air cushion at the end of the drive cylinder stroke.

When the sensor moved from the gas to liquid, Fig. 3b, the sensor voltage at constant current started increasing as soon as the sensor started moving in the gas. The sensor arrived at the liquid surface (1.9 V on the position sensor) at 1.2265 s. The sensor signal (3.95 V) indicating passage through the liquid surface, occurred about 2 ms later.

For the dozen cycles of the test for which four cycles are shown in Fig. 2, the average response times entering and leaving the liquid were 1.5 and 3.5 ms, respectively. The signal level change for this sensor was large at a constant current of 9 mA, changing from about 1 V in the gas to 7 V in the liquid.

The sensor signal should remain stable at the liquid value in liquid or the gas value in gas. LVDG occasionally made transitions to the opposite state without sensor movement. Occasional spikes appear in the sensor signal shown in Fig. 2 that are not associated with transitions through the liquid surface. The upward spikes when the sensor was in the gas may result from splashing from the sensor holder passing through the liquid surface. The downward spikes when the sensor was in the liquid may be caused by splashing, but they may also have resulted from momentary transitions to film boiling on the sensor surface. Considerable splashing occurred both when the sensor holder entered and left the liquid as could be seen through the slits in the silvered Dewar walls.

Table 1. Sensors tested as liquid-vapor surface sensors

Sensor designation	Description	Dimensions	Leads	Support
LVDG	Bulk doped silicon resistor	Cube 1/4 mm	0.05 mm SS	Leads
SOS	Silicon resistor on sapphire	Rectangular 2.8 × 1.9 × 0.25 mm	0.825 mm	SS Wire
K	Silicon resistor on sapphire	Rectangular 1.5 × 0.5 × 0.013 mm	Unknown	0.05 mm SS
PT1	Platinum on ceramic	Rectangular 1 × 4 × 5 mm	Au Pd alloy	Leads
PT2	Platinum on ceramic	Rectangular 1 × 2 × 2.3 mm	Au Pd alloy	Leads
DTO	Encapsulated Si diode	Cylinder 1.45 mm dia. 3.2 mm long	Unknown	Leads
DT1	Encapsulated Si diode	Rectangular 3.2 × 1.9 × 1 mm	Au plated Kovar	Leads
S	Si diode on sapphire	Rectangular 2 × 2 × 0.15 mm	Phosphor bronze	Leads
Mdac	10 kΩ carbon resistor + 100 Ω nominal thermistor	Irregular 15 × 33 × 5 mm	Brass heat sink	Heat sinks
Carbon1	920 Ω, 1/8 W resistor		Copper	Leads

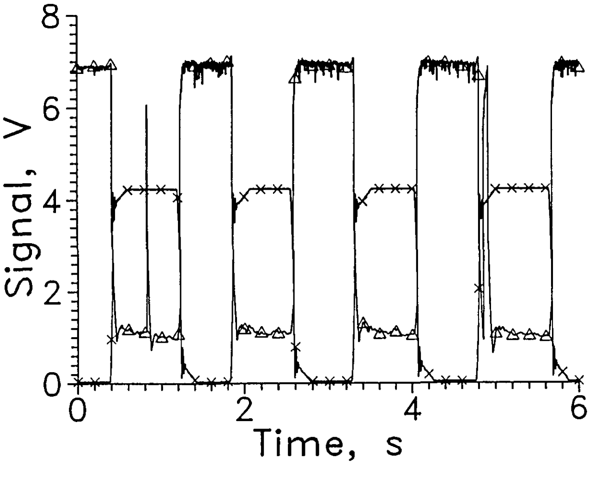

Fig. 2. Output signal from LVDG cycled between LH_2 and GH_2, Δ. Position sensor voltage, ×. Leads horizontal, I = 9 mA, every 100th data point shown. For this and all subsequent graphs of signal versus time, the sensor is in the liquid when the position sensor voltage reading is less than 1 V and out of liquid when the reading is above 3 V.

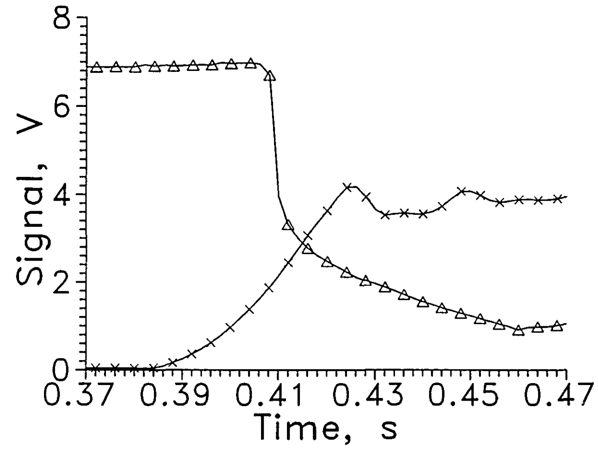

Fig. 3a. Output signal from LVDG at a transition from LH_2 to GH_2, Δ. Data of Fig. 2 on an expanded time scale. Position sensor voltage, ×. Leads horizontal, I = 9 mA, alternate data points shown.

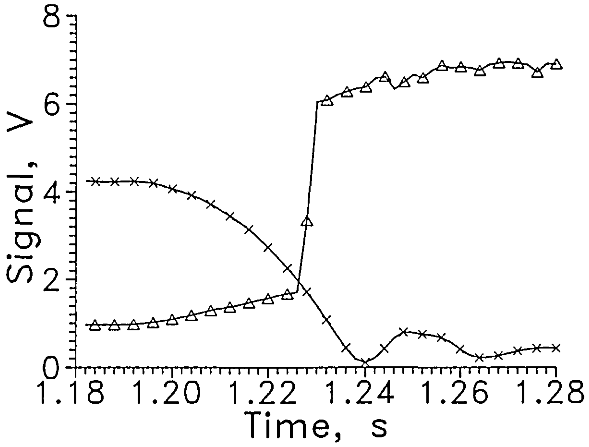

Fig. 3b. Output signal from LVDG at a transition from GH_2 to LH_2, Δ. Data of Fig. 2 on an expanded time scale. Position sensor voltage, ×. Leads horizontal, $I = 9$ mA, alternate data points shown.

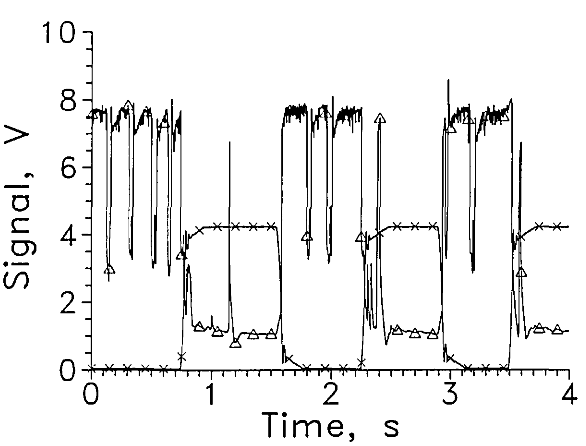

Fig. 4. Output signal from LVDG cycled between LH_2 and GH_2, Δ. Position sensor voltage, ×. Leads horizontal, $I = 11$ mA, every 75th data point shown.

When the sensor current was raised to 11 mA, the sensor voltage in the liquid becomes quite unstable, as shown in Fig. 4. At 20 mA, the in-liquid signal level decreased to less than 4 V (see Fig. 13) and was noisy in the liquid. The voltage in the gas increased to about 1.5 V. The stability of the sensor signal and the amount of signal change decreased while the response time returning to the liquid increased slightly, Fig. 5. The solid lines in Fig. 5 show the response times averaged over about 10 transitions as a function of sensor current. The dotted lines show the envelope of the fastest and slowest responses at each current. The sensor at high currents apparently heated so much above liquid temperature that a longer time was required to cool it back to liquid temperature. When the current was lowered below 9 mA, the response time leaving the liquid increased rapidly as Fig. 5 shows.

The large change of the sensor signal between liquid and gas and the rapid response to the surface crossing suggests that the sensor resistance, R, is a strong function of temperature, T, around 20 K. A measurement of $R(T)$ between 200 and 20 K is shown in Fig. 6. The sensor current was 10 μA, well below the level causing self heating. The scatter in the data between 80 and 120 K probably was caused by low resolution of the signal processing electronics at the low signal level. The slope, dR/dT was large at 20 K as anticipated. The LVDG sensor heated less than 50 K in gas to achieve the 7 to 1 signal level change.

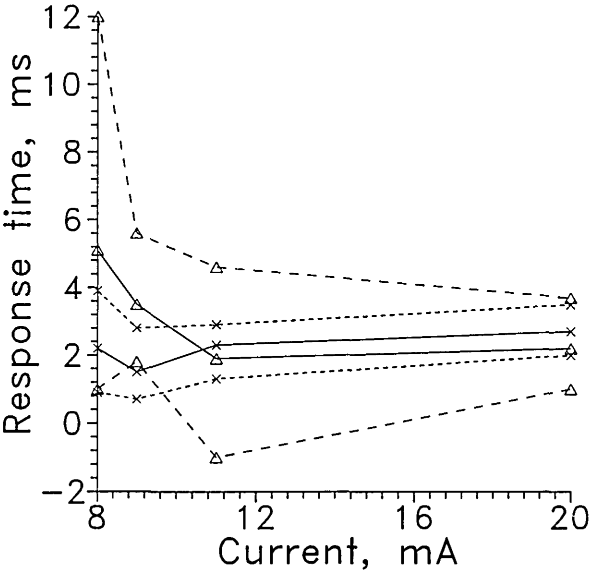

Fig. 5. Averaged response time of LVDG as a function of current for the sensor entering the liquid, ×; leaving the liquid, Δ. Dotted lines show total data scatter.

Figure 7 shows the resistance of the sensor in gas and in liquid as a function of the sensor current at currents in the L-V sensor operating range. The resistance in the gas decreases rapidly with increasing current at lower currents but levels out above about 10 mA as would be expected for an $R(T)$ dependence like that shown in Fig. 6. The resistance in the liquid decreases rapidly above about

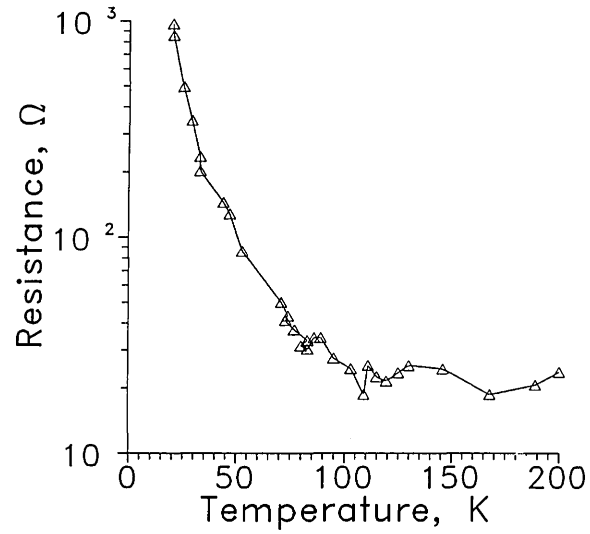

Fig. 6. Resistance of LVDG as a function of temperature, Δ. Leads horizontal. $I = 10\ \mu A$.

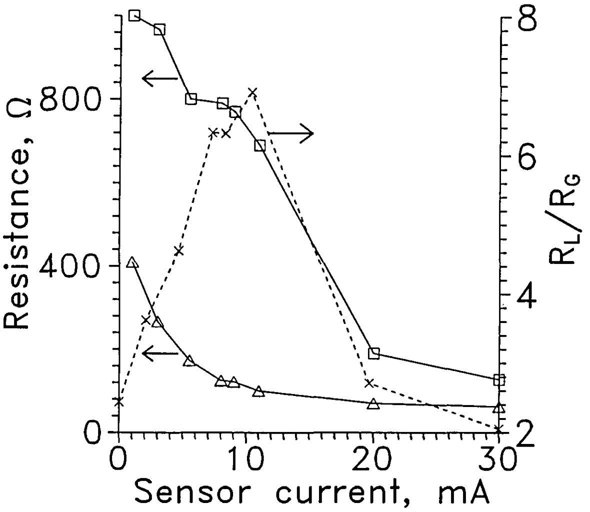

Fig. 7. Resistance of LVDG as a function of current, in GH_2, Δ; and in LH_2; □. R_l/R_g, ×. Leads horizontal.

10 mA current. The decrease of R with increasing sensor current for the sensor in LH_2 results from the increase of temperature needed to transfer the sensor power to the liquid. Above about 10 mA, the heat flux to the LH_2 was sufficient to cause film boiling on the sensor surface which reduced the heat transfer coefficient. This caused the sensor temperature to increase and R to decrease. From Fig. 4, the sensor became a thermoelectric oscillator at 11 mA constant current in liquid. The instability follows from the strong inverse relationship between power level and temperature at constant current.

The ratio of the resistance in liquid to the resistance in gas is also shown in Fig. 7. This ratio was highest at 11 mA, where the sensor oscillation was first seen. The sensor resistance in liquid was only about twice that of gas at 30 mA constant current. The speed and stability was best in these tests for a current around 9 mA for an LVDG sensor of this size, sensitivity and mounting. Any change from this configuration would require a redetermination of the best operating current.

In the first tests in this series, the cycle rate was about one every 4 s and the measurement resolution was 0.1 s. At that rate the response of the LVDG sensor showed only infrequent signal spikes not associated with an actual transition. This suggests that the number of extraneous spikes observed increases at faster cycle times.

To reduce the splashing caused by the sensor holder, the sensor holder was redesigned. The blades to which the sensors were attached were mounted vertically. As a result the sensor leads now ran vertically down to the sensor. The average response time for LVDG in this configuration for entering the liquid was unchanged from that with the leads horizontal. However, in five of the ten cycles recorded at 1 kHz reading rate, an upward spike in the LVDG signal to the liquid reading occurred (Fig. 8a at 9.26 s), between the start of the sensor motion and the entrance to the liquid. In all but one of the remaining five tests, a precursor to the main transition of LVDG was seen. A small precursor occurred at 5.66 s (Fig. 8b).

The average response time of LVDG leaving the liquid increased to almost 21 ms, Figs. 8a and b. The 21 ms response time was measured to the first response of the sensor to vapor. On about half the liquid-to-gas transitions, the LVDG signal cycled between liquid and gas for about 0.1 s after LVDG left the liquid, Fig. 8a. On the remaining half of the test cycles, the LVDG signal cycled back to the liquid reading as much as 0.3 s after the sensor departed the liquid, Fig. 8b.

We believe the increase of the liquid-to-gas response time and the cycling after the initial response was caused by liquid draining down the leads to the sensor from the holder. This source was probably enhanced because the insulation over the leads, which consisted of varnished paper, had partially detached allowing liquid to enter the crack between it and the stainless steel blade holding the sensor.

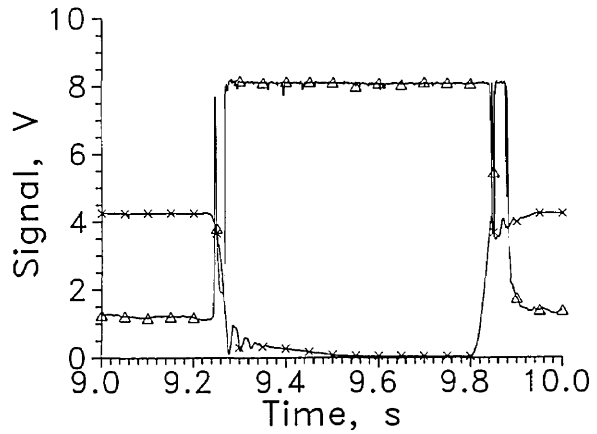

Fig. 8a Output signal from LVDG for one cycle between LH_2 and GH_2, Δ. Position sensor voltage, ×. Leads vertical, $I = 9$ mA, every 50th data point shown.

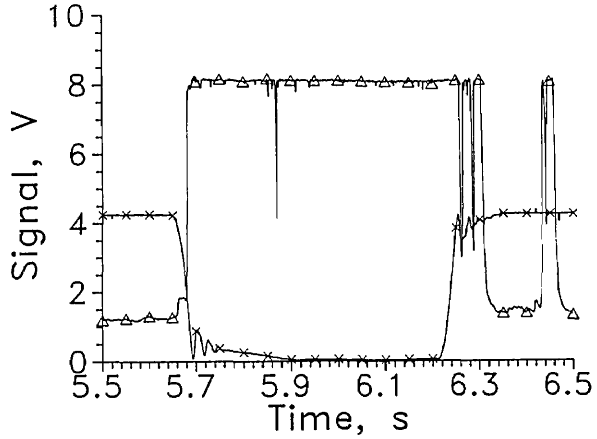

Fig. 8b. Output signal from LVDG for one cycle between LH_2 and GH_2, Δ. Position sensor voltage, ×. Leads vertical, $I = 9$ mA, every 50th data point shown.

The starting position of the sensor relative to the liquid surface appeared to cause differences in the response time when the leads were vertical. The measuring rate of 50/s was too low to measure the gas-to-liquid response accurately but the liquid-to-gas response time appeared to be 5 to 6 ms longer when the sensor holder had completed about 80% of its travel before the sensor left the liquid. The difference in the amount of splashing is the presumed cause. The in-liquid voltage was somewhat larger at a given sensor current than the voltage obtained with horizontal sensor leads.

The sensor holder with the leads vertical was built to reduce splashing in the hope that it would help to eliminate signal transitions that occurred without the sensor crossing the liquid boundary. The performance was definitely poorer than achieved with the original holder. Based on the difference of the test results from the two configurations tried so far, further study of mounting effects would be useful.

4.2 LVD Goddard LN_2 Tests

From Fig. 6, it is clear that dR/dT for LVDG at LN_2 temperature (77 K) was small compared to the slope at 20 K. The resistance only changes from about 40 Ω at 77 K to 20 Ω at ambient. For a four lead measurement, R_l/R_g, which is S_l/S_g at constant current, could be no more than 2. Since we made the measurements with two leads, the 35 Ω leads reduced S_l/S_g to no more than 4/3.

A rapid cycle test of LVDG is shown in Fig. 9 for a 50 mA sensor current. The output signal at this time resolution still approximates a square wave. Unlike the LH_2 tests, no spikes occurred in the LN_2 tests signifying no temporary return to the previous state.

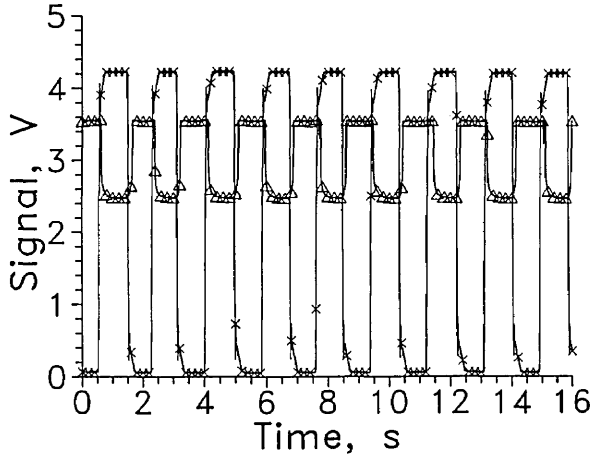

Fig. 9. Output signal from LVDG cycled between LN_2 and GN_2, Δ. Position sensor voltage, ×. Leads horizontal, $I = 50$ mA, every 100th data point shown.

The response times were much longer for LN_2, Table 2, than for LH_2 probably because of the higher sensor heat capacity. The preferred operating current was 50 mA since the liquid-to-gas response was equal to the gas-to-liquid response. Also, the sum of the response times for one cycle was less for 50 mA than for 40 mA.

The liquid-to-gas response time for the LVDG at 40 mA varied more than at 50 mA, as shown in Table 2. The gas-to-liquid response time scatter was much less at both currents than the liquid-to-gas response time scatter. The greater variation in the liquid-to-gas response times probably was caused by varying amounts of liquid retained on the sensor

Table 2. LVD Goddard response time in LN_2

Current (mA)	Power in liquid (mW)	Avg. time constant for liquid entry (ms)	Avg. time constant for liquid exit (ms)	Sum (ms)	Relative holder position
40	64	57	154	211	High
40	64	48	308	356	Low
50	100	118	101	219	High
50	100	106	107	213	Low

though splashing of the liquid when the holder departs the surface may also contribute.

A difference in the responses of the sensor with the different positions of the sensor holder relative to the liquid surface was observed for the 40 mA results as Table 2 shows. The splashing was less when the liquid level was high, but the liquid-to-gas response time was still slower. In one test the sensor failed on some cycles to respond before the sensor returned to the liquid, indicating a response time as long as 1.5 s. At 50 mA, no difference in response time with liquid height was evident.

4.3 K and SOS Sensors

The K and SOS sensors are doped silicon films rather than bulk doped silicon like LVDG. The films were supported on sapphire substrates. The K sensor substrate was so thin that it required support. The doping level was high to give good sensitivity around ambient temperatures. The resistance went through a minimum around 130 K and then rose rapidly below 77 K and became essentially infinite well above 20 K, which rendered the sensor unusable as an L-V sensor for LH_2.

For LN_2, the K sensor gave a 5% change in signal level at 5 mA (10 mW) and had a response time of about 1 s when the sensor left the liquid. The output signal obtained in one test is shown in Fig. 10. When the sensor entered the liquid, the response time was 50 ms or less. The 20 Hz signal reading frequency of the fastest test did not resolve the response time to better than 50 ms. At currents of 6 mA and above, the sensor temperature increased sufficiently to reach the high temperature side of the resistance minimum when the sensor remained out of the liquid for a few minutes. This caused the sensor to respond upon reentering the liquid by a voltage decrease instead of an increase. For short periods out of the liquid, the sensor did not heat above its resistance minimum and responded with a voltage increase as at 5 mA current.

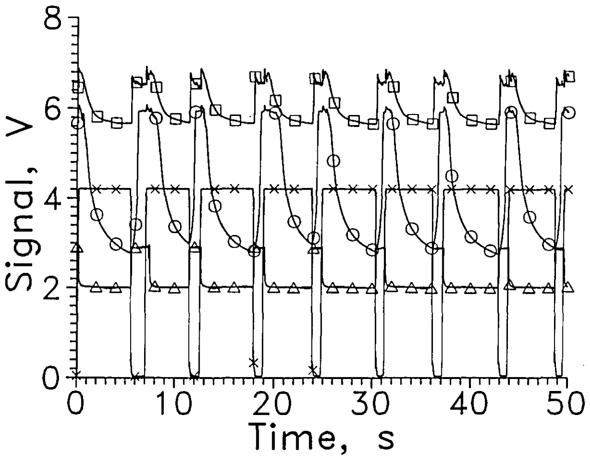

Fig. 10 Output signal from LVDG at 40 mA, Δ; K at 5 mA, □; and PT1 at 20 V, O; cycled between LN_2 and GN_2. Position sensor voltage, ×. Leads horizontal, and every 100th data point shown.

The K sensor was tested at 77 K and below at least three times with many repeated tests each time. The sensor was cemented to 0.1 mm shim stock to prevent breakage.

The SOS sensor in LH_2 at 60 mA constant current (0.4 W) showed a signal level change of more than 30% between liquid and gas. The response time of the sensor leaving the liquid was about 1.5 s for SOS I which had an approximately 1 cm^2 substrate. SOS II had the excess substrate trimmed off and smaller leads attached. The liquid-to-gas response time for SOS II was just under 1 s. The SOS II response time upon re-entering the liquid was no more than 0.1 s.

In LN_2, the change of the resistance of SOS II was only about 5% from gas to liquid. The response time of SOS II was rapid upon entering the LN_2 but the response time to removal from the liquid was as long as 9 s. A lead failed when the current was increased above 60 mA, and no further tests were carried out. SOS II had the disadvantages that the sensor is not commercially available, the response time was slow, and the signal change was small.

Neither the SOS nor the K sensor were tested for effects of lead orientation.

4.4 Thin Film Pt Thermometers

The Pt film thermometers tested have the advantages of being commercially available and inexpensive. PT1 and PT2 had ambient resistances of 1 kΩ and 100 Ω, respectively.

For LH_2 tests, these two sensors were mounted only with the leads vertical. Figure 11 shows an example of one test of PT1 and PT2 in LH_2. The sensors were powered by constant voltage sources, and the series resistances used are given in Table 3. The best performances obtained are given in the table. The size of the signal change between entering and leaving liquid was unexpected since Pt thermometers lose sensitivity below 20 K.

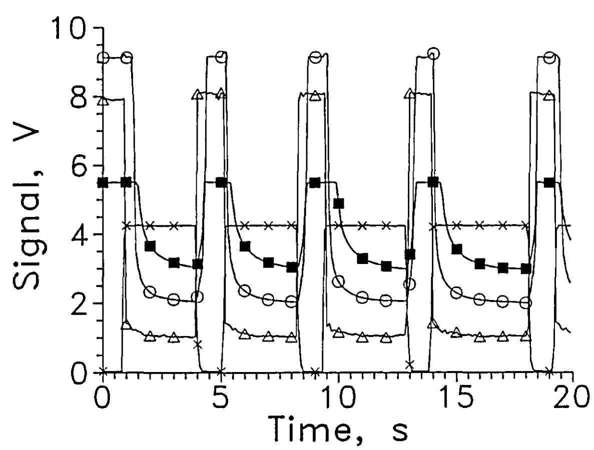

Fig. 11. Output signal from LVDG at 9 mA, Δ; PT1 at 20 V, O; and PT2 at 12 V, ■; cycled between LH_2 and GH_2. Position sensor voltage, ×. Leads vertical, and every 100th data point shown.

Table 3. Operating parameters for best performance

Sensor series R	V or I	Power liquid	Power, vapor	Max S_l/S_g	Avg. response to liquid	Avg. response to gas	Comments
				Hydrogen			
LVDG	9 mA	63 mW	9 mW	7	1.5 ms	3.5 ms	[1]
PT1 46 Ω	20 V	2 W	0.8 W	19	0.3 s	0.4 s	[2,3]
PT2 29 Ω	12 V	1 W	1.3 W	50?	0.25 s	0.6 s	[2,3,4]
DT1	40 mA	120 mW	110 mW	1.1	<2 ms	0.9 s	[4]
S	40 mA	120 mW	100 mW	1.2	<2 ms	0.4 s	
Carbonl 200 Ω	20 V	0.3 W	0.4 W	1.25	60 ms	0.5 s	
Mdac 1000 Ω	100 V	0.36 W	0.5 W	1.4	<1 s	2 s	
				Nitrogen			
LVDG	50 mA	175 mW	125 mW	2	0.11 s	0.11 s	[2]
PT1 100 Ω	20 V	0.84 W	0.5 W	>2	1.4 s	0.6 s	[1]
PT2 29 Ω	10.5 V	0.8 W	0.5 W	>4	1 s	2.1 s	[3]
DT1	40 mA	0.1 W	0.1 W	~1.05	~10 ms	~10 s	
S	40 mA	0.1 W	0.1 W	~1.05	~10 ms	~2 s	
Carbon 1 200 Ω	30 V	1.3 W	1.3 W	1.11	60 ms	0.5 s	
Mdac 1000 Ω	100 V	0.5 W	1.3 W	1.25	~0.5 s	~2 s	
K	5 mA	33 mW	29 mW	1.16	~1 s	~1 s	

[1] Liquid to gas response time increases for vertical leads.

[2] Maximum S_l/S_g is estimate for a four lead measurement.

[3] Tested only with leads vertical.

[4] Did not always make transition to gas reading on rapid cycling.

The liquid-to-gas response of PT2 was slower than that of PT1. In a later test, PT2 failed to respond for more than 3 s when withdrawn from the liquid. The sensor was returned to the liquid before the gas response occurred. The reason for the slower response for a smaller sensor is not known.

Results from a test of PT1 and PT2 in LN_2 are shown in Fig. 12. The signal voltage ratio, S_l/S_g is at least 2 at the cycle rate shown. The ratio is about 2.5 for a slower cycle time. Table 4 gives some characteristics of PT1 in LN_2 for three different voltages. The liquid entry and liquid exit response times of PT1 were closest to equal at 20 V. The percentage scatter of the response times was least for PT1 at 20 V. The signal level change was greater for PT1 in LN_2 than that obtained for LVDG, Fig. 10. The response time was slower than that of LVDG and the power is higher, both of which would be expected because PT1 is larger. The PT1 sensor can be used for LN_2 surface sensing when fast response is not needed.

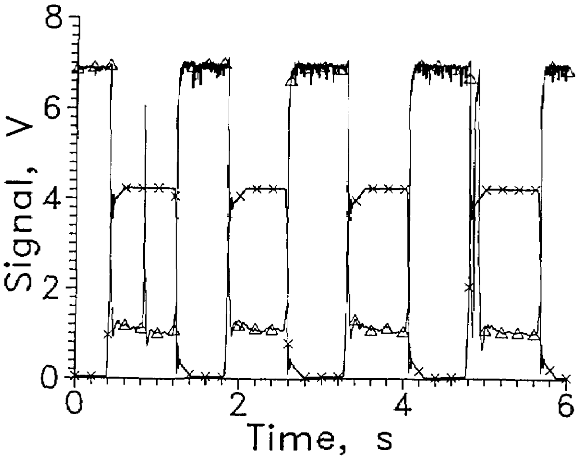

Fig. 12. Output signal from LVDG at 40 mA, Δ; PT1 at 20 V, O; and PT2 at 10 V, ■; cycled between LN_2 and GN_2. Position sensor voltage, ×. Leads horizontal, and every 10th data point shown.

Table 4. PT1 test results in LN_2

Applied volts	Delay in liq. (s)	Range (s)	Delay out liq. (s)	Range (s)	S_l/S_g	Max power (W)
12	0.05	0.01 to 0.17	3.9	1.9 to 6.6	>1.7	0.3
15	0.17	0.07 to 0.29	2.5	1.7 to 3.3	>1.7	0.5
20	0.6	0.47 to 0.68	1.4	1 to 1.8	>2	0.8

When the LN_2 tests were carried out with the leads extending vertically above the sensor, the liquid exit average response time at 20 V increased to about 2 s while the liquid entry time remained unchanged. This lengthening of the response time is again attributed to liquid draining off the sensor holder down the leads to the sensor.

The performance of PT1 in LN_2 was better in terms of signal magnitude than for the smaller sensor PT2, Fig. 12. The response times of PT2 were similar to those of PT1 even though we expected they would respond more quickly because of its smaller surface area and size. The response time of PT1 was often faster than PT2 when entering the liquid which was not expected, but was usually slower upon leaving it. PT2 was only tested in the vertical lead configuration. The long decay of the signal level when the sensor leaves the liquid makes the sensor response time highly sensitive to the voltage level chosen to signify the completion of the transition.

The large signal change and the commercial availability of these sensors make them attractive if the high power dissipation and the slow response are acceptable to the application.

4.5 Diode Thermometers

Some test results for the DT1 and S diode thermometers in hydrogen are shown in Fig. 13. The output signal was the voltage required to maintain a constant current of 40 mA through the sensors. The response time was short for these sensors entering the liquid. In some cases the signal response preceded the time when the sensors entered the liquid. The three sensors of Fig. 13 were all in the same horizontal plane and entered the liquid within about 3 ms of 6.817 s. The early response of the diodes may have been caused by splashing when the holder enters the liquid. Increased cooling due to the motion of the sensor while still in the gas may have caused the early transition by the sensor.

Since the response time of the diodes was so much more rapid entering the liquid than leaving, Fig. 14, a higher power should be used. Figure 15 shows a plot of the response time leaving the liquid as a function of the estimated heat flux for LVDG and a data point for the *S* diode. At heat fluxes below 150 mW/mm^2, the response time is strongly dependent on flux. This curve can be used to estimate the power needed by a sensor with a different surface area if the liquid retained on the surface is the

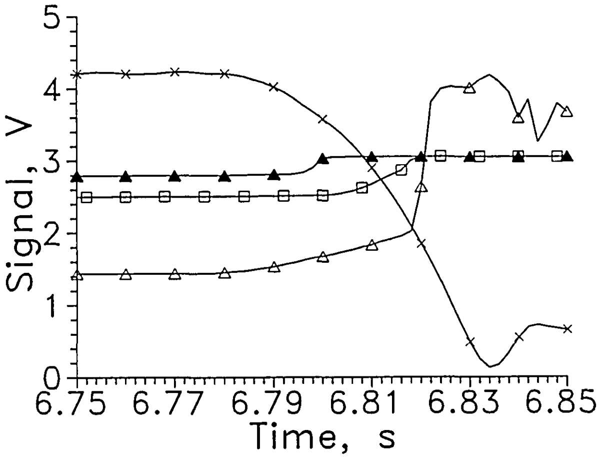

Fig. 13. Output signal from LVDG at 20 mA, Δ; DT1 at 40 mA, ▲; and *S* at 40 mA, □; for one transition from GH_2 to LH_2. Position sensor voltage, ×. Leads horizontal, and every 5th data point shown.

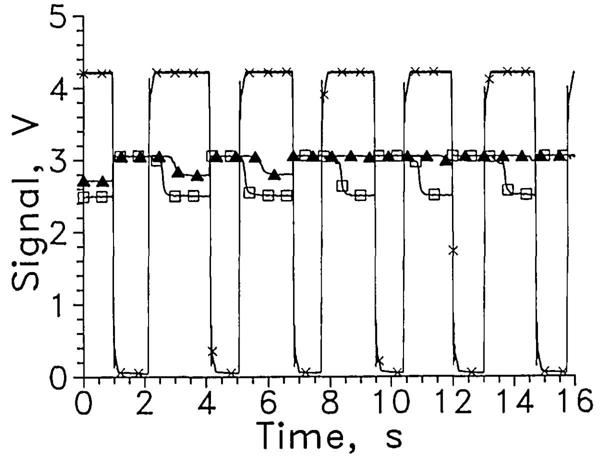

Fig. 14. Output signal from DT1 at 40 mA, ▲; and *S* at 40 mA, □; cycled between LH_2 and GH_2. Position sensor voltage, ×. Leads vertical, and every 300th data point shown except for DT1 which is 305.

dominant factor in the response time. A data point for the highest power to the *S* diode is shown. The *S* sensor had a response time twice as long as LVDG at the same flux. The surface area per unit volume of the *S* diode is about half that of LVDG. The longer response time suggests a contribution from the sensor heat capacity. About 10 times more power would be needed to raise the *S* sensor heat flux up to the 125 mW/mm^2, which should reduce its response time to less than 10 ms. Alternatively, the surface area of the diode could be decreased to raise the heat flux. The manufacturer of one diode sensor suggested that the current not exceed 10 mA. Current above 40 mA was not used for fear of destroying it.

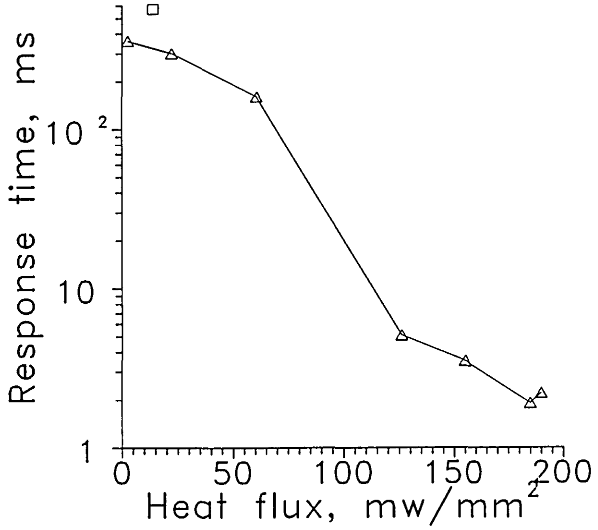

Fig. 15. Response time as a function of heat flux for LVDG; Δ; for *S* diode, □.

Since the unencapsulated *S* thermometer had an area about 2.5 times smaller than the encapsulated DT1, the *S* sensor should heat to a higher temperature in the gas for the same current. The signal voltage should then be lower for *S* in the gas and it was. When the *S* diode was in liquid, however, no heating of the sensor was observed.

The smaller surface area and size of the *S* diode allowed it to respond more quickly than DT1 upon withdrawal from LH_2. The response time for DT1 to withdrawal from LH_2 was long enough that it did not always have time to respond on every cycle before the sensor re-entered the liquid, as shown in Fig. 14. Again, higher currents should speed the out-of-liquid response of these sensors if they are not damaged by higher power dissipation. Higher current should also increase the S_l/S_g ratio which was about 1.2 at 40 mA.

The change of the signal level between LN_2 and GN_2 was so small for the *S* sensor that it was comparable to the noise in the signal channel. The in-to-out response was several seconds. The current through DT1 and *S* must be much greater than the 40 mA maximum current used in these tests if a satisfactory performance as a surface sensor is to be achieved in LN_2.

The DT0 sensor response upon withdrawal from the LH_2 was somewhat faster than DT1. The diodes were not tested with the leads in the vertical orientation.

4.6. Mdac Sensor

One test of the Mdac unit attached to heat sinks is shown in Fig. 16 for LH_2. The sensor responded in a few tenths of a second upon entering the liquid. The response was slow upon leaving the liquid and the noise level was high relative to the signal change until the voltage on the sensor was well in excess of 50 V. The response time leaving the liquid was about 2 s at 100 V.

For liquid vapor surface sensing at 77 K and below, the thermistor is superfluous because its resistance is so high that the carbon resistor carries all the current. Voltages above 100 V were not tried to avoid breakdown of the insulating varnish on the leads. The resistor should be reduced from 12 kΩ to perhaps 1 kΩ to reduce the required voltage. The dependence of R on T for a carbon resistor varies with manufacturer. A brand whose R has a strong dependence on T should be selected. When the Mdac with heat sinks was tested in LN_2, either capacitance effects or momentary shorts in the leads caused signal spikes when the sensor holder moved. A Mdac sensor without heat sinks but with heavier insulation on the leads was tested in LN_2 in a similar test system external to the gas tight dewar assembly of Fig. 1. Test results with 100 V applied are shown in Fig. 17. The response time leaving the liquid was about 2 s. The response time entering the liquid varies from about 0.2 to 1.2 s depending on how long the sensor was out of the liquid. The signal amplitude changed from about 5.2 to 6.7 V for a short cycle time. As Fig. 17 shows, the sensor does not reach equilibrium after withdrawal from the liquid even after 20 s. A lower nominal resistor operating at constant current should reach equilibrium more rapidly. Grinding the shell off the resistor should also speed the response.

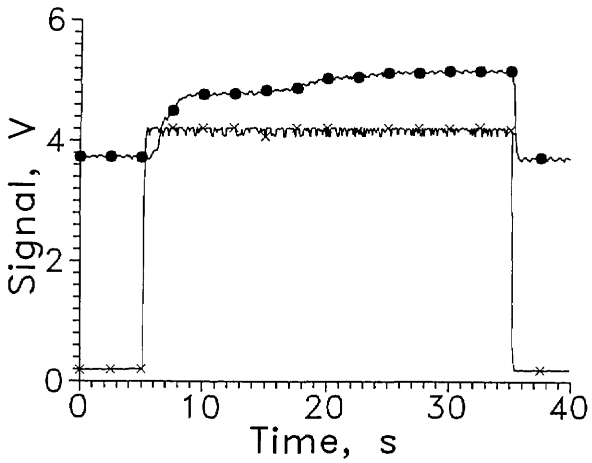

Fig. 16. Output signal from Mdac for one cycle between LH_2 and GH_2, ●. Position sensor voltage, ×. Leads horizontal, $V = 100$ V, every 25th data point shown.

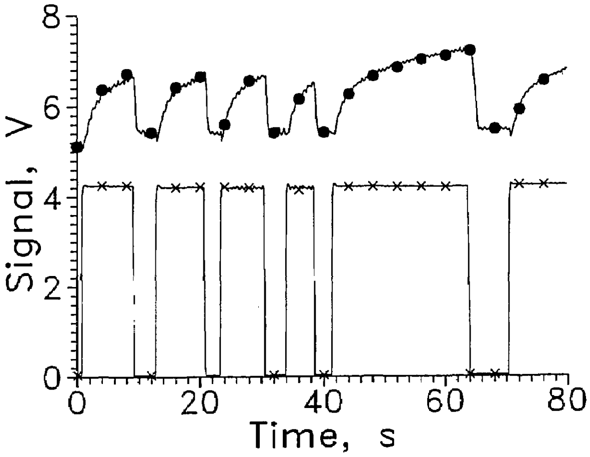

Fig. 17. Output signal from Mdac cycled between LN_2 and GN_2, ●. Position sensor voltage, ×. Leads horizontal, $V = 100$ V, every 20th data point shown.

4.7 Carbon1

For the last LN_2 and LH_2 tests a 925 Ω, 1/8 W carbon resistor (Carbon1) was tested. The signal level change of this resistor was less than for Mdac and the response time similar.

The output voltage change for Carbon1 for hydrogen was from 2.8 to 3.6 V. The signal ratio was about 1.2 for 25 V across the sensor and a 200 Ω resistor in series. The out-to-in response time was about 60 ms. The in-to-out response was about 0.5 s. Both response times increased with increasing current. It is not understood why this should happen on the out transition. It is clear that a carbon resistor with a larger dependence of resistance on temperature is required for the performance of carbon resistors to be satisfactory. Carbon1 did respond faster than Mdac as would be expected because it is smaller.

5. Discussion

An ideal L-V sensor could be described as follows: the signal change should be at least a factor of 10 larger than the combined noise level, drifts of the power supply and drifts of the signal processing electronics; the response time should be less than 10% of the fastest response time required for the measurement and the sensor should not perturb the liquid surface as it passes through.

The response time of a resistive sensor leaving the liquid depends on the integral of the sensor heat capacity between the sensor temperature in the liquid, T_l, and the sensor temperature in the gas, T_g, the amount of liquid in the residual film carried out on the sensor surface, and the power dissipated in the sensor. The amount of liquid in the residual film should be primarily a function of the surface area of the sensor.

The response time of the sensor entering the liquid, however, depends only on the integrated heat capacity of the sensor between T_g and T_l and the surface area through which heat transfers to the liquid.

An ideal resistive sensor should thus consist of the smallest practical resistive element. Any inactive material in the sensor increases the power density in the active part needed to cause a given temperature change. Making the sensor smaller reduces its heat capacity which decreases the response times entering and leaving the liquid. Making it more compact in terms of area decreases the leaving response time. A smaller surface area for the same volume increases the entering response time because the smaller surface reduces the heat transfer rate to the liquid.

Increasing dR/dT of a sensor at a fixed $T_g - T_l$ increases the signal level change, $S_g - S_l$. Conversely, at constant $S_g - S_l$, $T_g - T_l$ is decreased as dR/dT increases thus the amount of heat transferred to or from the sensor in moving between the two states is reduced. In the latter case, the response times both entering and leaving the liquid decrease.

At LH_2 temperature, the LVDG sensor has characteristics of the ideal L-V sensor discussed above. The small size and large dR/dT of LVDG, Fig. 6, give it both a fast response and a large signal change when it is powered by a constant current. At 9 mA, the voltage signal ratio $V_l/V_g = 7$. Thus the power dissipated in the gas 1/7 is that dissipated in the liquid. This inherent decrease in power reduces $T_g - T_l$ which reduces the response time. Even at 20 mA where the sensor is insulated by the formation of a vapor layer, the signal ratio is still 2.7 and the time constants are nearly the same as at 9 mA. No advantage is achieved at the higher current and the disadvantages of a noisy signal and higher power into the LH_2 make higher currents unattractive.

Most of the other sensors tested did not have large values of dR/dT at LH_2 temperatures, hence their signal ratios were modest compared to LVDG. Many did respond rapidly when entering the liquid. Often this was true because the power to the sensor was too low which caused a slow response upon withdrawal to the gas. To speed their response leaving the liquid, a higher sensor power was needed. Since a higher sensor power raises the liquid entry response time especially when dR/dT is small, smaller size is the only way to improve response time.

The active portion of many of these sensors was small with respect to their overall size. Applying sufficient power to rapidly remove the liquid film risks destroying the sensor. The long equilibrium time on the liquid to gas transition of some of the sensors probably came from the large heat capacity of the sensor. A sensor that can withstand a higher power could be driven by a logic controlled power supply that decreases sensor power as soon as the L-V sensor begins responding to gas. This would reduce heating of the sensor in the gas, which shortens the response time entering the liquid. The magnitude of $S_l - S_g$ is decreased by this approach, however.

At LN_2 temperature, LVDG still showed a relatively square signal pulse for a transition from liquid to gas to liquid, but the smaller dR/dT resulted in a greatly reduced ratio of V_l/V_g. The sensor power in liquid was about the same as that for the LH_2 tests. The response times are about 0.1 for both, 50 times longer than found for LH_2. The long response time entering the liquid is caused by a large total sensible heat content of the sensor between T_l and T_g.

The large change in sensor resistance and the fast response time make the LVDG sensor the best of those tested for use in LH_2. Of the sensors tested, LVDG had the fastest response in LN_2 for withdrawal from the liquid. The response was slower and the signal level change reduced from that in LH_2. Possibly a stronger signal could be obtained for LVDG in LN_2 if the doping level of the silicon sensor was increased. The sensor has the disadvantage in that it is not commercially available at present.

These tests have shown that sensor lead orientation relative to the liquid surface can be important to the response time of the liquid to gas transition. The different behavior for the two lead geometries of LVDG in LH_2 and PT1 in LN_2 illustrates this. Liquid draining down the leads from crevices in the insulation and lead anchoring hardware probably caused delays in the sensor response. Bending the lead wires into a *J* shape, with the sensor on the short leg, might eliminate any flow down the leads to the sensor. The orientation effect observed in this work was caused by gravity driven flows. In zero gravity, the lead orientation with respect to the direction of motion of the liquid surface could still affect the response time. Changing the direction of the leads relative to the surface could cause a variation in the amount of liquid remaining in the sensor.

Since the sensors and their supports will always have a finite size, splashing will occur when the liquid surface moves by. Smaller sensors should generate less surface disturbance. The support structure for the sensors may be a much stronger source of disturbance. A large amount of splashing and bubble introduction occurred during these tests, but the switching of the sensors between states tended to be fairly independent of other disturbances.

Table 3 shows the best operating power found during these tests for each of the sensors and the resulting signal ratio and time constants. The optimum performance of a sensor might be expected to occur at the power level that gave equal time delays for entering and leaving the liquid. This was the case for sensors tested at high power. For some sensors, in particular the diode sensors, this power was not reached.

It should be emphasized that the commercially available sensors tested here are meant to be thermometers and not liquid-vapor sensors. These sensors were not designed to be used as they were used in these tests. The results given here do not reflect in any way upon the ability of these sensors to measure temperature. Only LVDG was specifically designed to be a liquid-vapor detector.

Acknowledgments

The authors would like to thank D. Ladner of Martin Marietta Corporation and Kulite Semiconductor Products Corporation for supplying sensors. A special thanks goes to A. Serlemitsos and M. DiPirro of NASA Goddard who provided the LVDG sensor for these tests.

6. References

[1] D. Burgeson and R. Richards, Test results of liquid level point sensor operation in liquid hydrogen, NBS Report No. 9231 (May 16, 1966).

[2] D. Burgeson and R. Richards, Selecting liquid level transducers for cryogenic service, NBS Report No. 8784 (April 1, 1965).

[3] D. Burgeson, W. Pestalozzi, and R. Richards, The performance of point level sensors in liquid hydrogen, Advances in Cryogenic Engineering **9**, Plenum Press, New York (1964).

[4] J. Siegwarth, R. Voth, and S. Snyder, Liquid-vapor surface sensors for liquid nitrogen and hydrogen, Cryogenics **32**, 236 (1992).

[5] M. DiPirro and S. Serlemitsos, Discrete liquid/vapor detectors for use in liquid helium, Advances in Cryogenic Engineering **35B**, Plenum Press, New York (1990) pp. 1617–1623.

About the authors: *James D. Siegwarth is a Physicist and Roland O. Voth is a Mechanical Engineer (now retired) in the Chemical Engineering Division of the National Institute of Standards and Technology. Steven M. Snyder is a Chemical Engineer who held a temporary position with NIST during this work. The National Institute of Standards and Technology is an agency of the Technology Administration, U.S. Department of Commerce.*

Volume 97, Number 5, September–October 1992
Journal of Research of the National Institute of Standards and Technology

[J. Res. Natl. Inst. Stand. Technol. 97, 579 (1992)]

Fracture Toughness of Advanced Ceramics at Room Temperature

Volume 97 Number 5 September–October 1992

George D. Quinn
National Institute of Standards
and Technology,
Gaithersburg, MD 20899

Jonathan Salem
National Aeronautics and Space
Administration,
Lewis Research Center,
Cleveland, OH 44135

Isa Bar-on and Kyu Cho
Worcester Polytechnic Institute,
Worcester, MA 01609

Michael Foley
St. Gobain, Norton Industrial
Ceramics Corp.,
Northboro, MA 01532

and

Ho Fang
Allied-Signal, Garrett Auxiliary
Power Division,
Phoenix, AZ 85010

This report presents the results obtained by the five U.S. participating laboratories in the Versailles Advanced Materials and Standards (VAMAS) round-robin for fracture toughness of advanced ceramics. Three test methods were used: indentation fracture, indentation strength, and single-edge precracked beam. Two materials were tested: a gas-pressure sintered silicon nitride and a zirconia toughened alumina. Consistent results were obtained with the latter two test methods. Interpretation of fracture toughness in the zirconia alumina composite was complicated by R-curve and environmentally-assisted crack growth phenomena.

Key words: advanced ceramic; alumina; fracture; fracture toughness; indentation; round-robin; silicon nitride; zirconia.

Accepted: July 15, 1992

1. Introduction

The Versailles Advanced Materials and Standards (VAMAS) project is an international collaboration for prestandardization research. The participating countries are Canada, France, Germany, Italy, Japan, the United Kingdom, the United States and the Commission of European Communities. Technical Working Area #3, Ceramics, has the objective of undertaking research on the reliability and reproducibility of test procedures for advanced technical ceramics.

Fracture toughness is an important property of advanced ceramics and is one measure of brittleness. The Japan Fine Ceramics Center (JFCC) in 1988 organized a VAMAS round-robin to evaluate fracture toughness by three methods on two advanced ceramics. All testing was to be performed at room temperature. This round-robin was designated the '89 Fracture Toughness Round-Robin Test (RRT) by the JFCC. Twenty-three laboratories agreed to participate, including six in the United States.

The three test methods chosen were: indentation fracture (IF), indentation strength (IS), and single-edge precracked beam (SEPB). These methods are schematically illustrated in Fig. 1. The SEPB and IF methods are standards in Japan and the procedures in this round-robin were in accordance with JIS R 1607 [1].

The IF test is a variant of the scheme originally proposed by Evans and Charles [2]. A polished sample is indented with a Vickers hardness indenter and the length of the resultant median cracks measured. The fracture toughness is related to the indentation load, the size of the median cracks, the elastic modulus and hardness of the material. The test has the virtues that it measures a "micro" fracture toughness, (that is, a toughness relevant to the scale of naturally-occurring defects) and requires only a small amount of material. Drawbacks include the need to rely on a calibration constant to deal with the complex deformation and residual stress fields, and the plethora of equations that have developed for computing fracture toughness by this method as discussed in Refs. [2–6].

The indentation strength (IS) method involves the implantation of an artificial flaw on the surface of a flexure specimen and fracture of the specimen in three- or four-point flexure [7]. A Vickers indentation is used to create the artificial flaw. It is not necessary to measure the initial crack size, since the crack will extend stably during subsequent loading in response to the external load and the residual stress field associated with the indentation. Fracture toughness is calculated from the elastic modulus, indentation load, Vickers hardness and flexural strength.

The single-edge precracked beam (SEPB) method [8,9] is a variation on the traditional single-edge notched beam method. In the latter test, a precrack is formed by a thin saw cut since fatigue precracking is difficult with advanced ceramics. The saw cuts are nevertheless blunt and measured toughness are typically too high. The SEPB method solves the precracking problem by means of a "bridge indentation" scheme, wherein an indented or saw cut flexure specimen is compression loaded in a bridge anvil until a precrack pops in. The precracked beam is then fractured in three-point flexure and the fracture toughness evaluated from an equation by Srawley [10]. The crack size must be measured in some manner, often by dye penetration or by subsequent fractographic analysis. An advantage of this method is that, with the choice of suitable specimen and flexure fixture dimensions, the test is similar to ASTM standard test method E-399, Plane-Strain Fracture Toughness of Metallic Materials [11].

The Japan Fine Ceramic Center accumulated the available results from thirteen laboratories in 1990 and prepared reports summarizing the findings [12–14]. Five U.S. laboratories completed their testing in the round-robin by the summer of 1991 and this report presents their results and findings. The five participating U.S. laboratories are listed in Table 1. These labs will hereafter be referred to as USA labs 1–5.

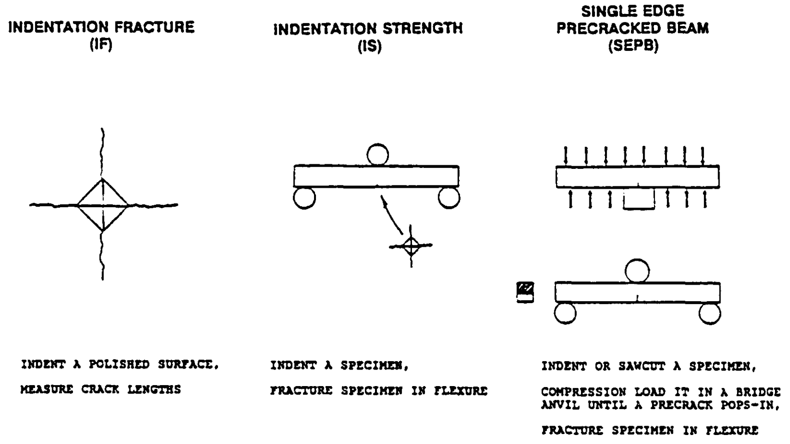

Fig. 1. The test methods used for the VAMAS Round-Robin.

Table 1. U.S. participants

Laboratory
NIST Ceramics Division, Gaithersburg, MD
Allied-Signal, Garrett Auxiliary Power Division, Phoenix, AZ
St. Gobain Norton Industrial Ceramics Corp., Northboro, MA
NASA/Lewis Research Center Cleveland, OH
Worcester Polytechnic Institute Department of Mechanical Engineering, Worcester, MA

2. Materials

The Japan Fine Ceramic Center furnished all specimens for the round-robin. Two materials were used:

Gas-pressure sintered silicon nitride,
Grade EC-141[1,2], (hereafter designated silicon nitride)

Zirconia alumina composite
Grade UTZ-20[1,2], (hereafter designated ZAC).

Twenty specimens of each material were sent to the participants. Specimen dimensions were $3 \times 4 \times 40$ mm. One of the 4 mm wide sides was ground and polished by a #2000 diamond grinding wheel to provide a good reference surface for indentations.

The silicon nitride is a commercial grade sintered silicon nitride that is used for automotive turbochargers [14,15]. Yttria and alumina are used as the sintering aids. The microstructure has fine (1–2 μm), equiaxed β-silicon nitride grains and a glassy boundary phase [16]. The room-temperature flexure strength is approximately 900 MPa. Strength gradually drops to about 60% of this value at 1200 °C [17,18]. Young's modulus is 310 GPa at room temperature. The gas-pressure sintering process is expected to produce a homogeneous and isotropic material.

ZAC, a composite with about 50% zirconia and alumina, was fabricated by pressureless sintering. The Young's modulus was given as 280 GPa. Figure 2 shows the microstructure. X-ray diffraction on the polished surface of a specimen indicated the primary phases are alpha alumina and tetragonal zirconia. Some monoclinic and cubic zirconia were also detected. Energy dispersive spectroscopy on the scanning electron microscope revealed only aluminum and zirconium. Silicon was not detected.

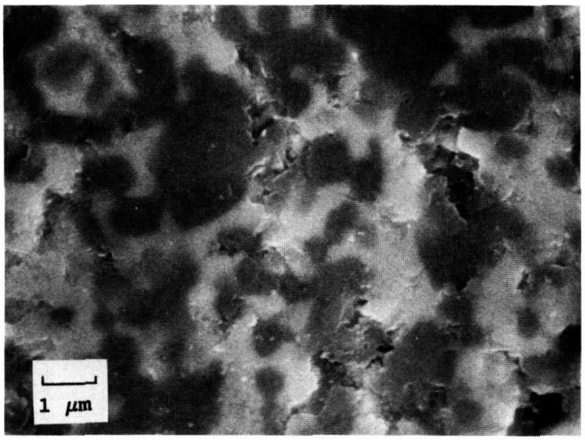

Fig. 2. A scanning electron micrograph of the zirconia alumina composite (ZAC). The white phase is zirconia, the dark phase, alumina. Some residual porosity is also evident.

Two important issues regarding advanced ceramic crack growth are whether there are environmental effects and whether the material has *R*-curve behavior. Both these phenomena interfere with the goal of measuring fracture toughness.

Environmentally-assisted crack extension is usually depicted on a V-K_I graph as depicted in Fig. 3. The conventional interpretation is that Region I and II behavior is controlled by the environment, whereas Region III crack extension is intrinsic to the material [19]. The point is that environmentally-assisted, slow crack growth can occur at stress intensities less than K_{Ic} and thereby interfere with attempts to measure the latter. Tetragonal zirconia and zirconia alumina composites are known to have glassy boundary phases and are susceptible to slow crack growth phenomena [20,21].

---

[1] NTK Technical Ceramics, NGK Spark Plug Co. Nagoya Japan.

[2] Certain commercial equipment, instruments, or materials are identified in this paper to specify adequately the experimental procedure. Such identification does not imply recommendation or endorsement by the National Institute of Standards and Technology, nor does it imply that the materials or equipment identified are necessarily the best available for the purpose.

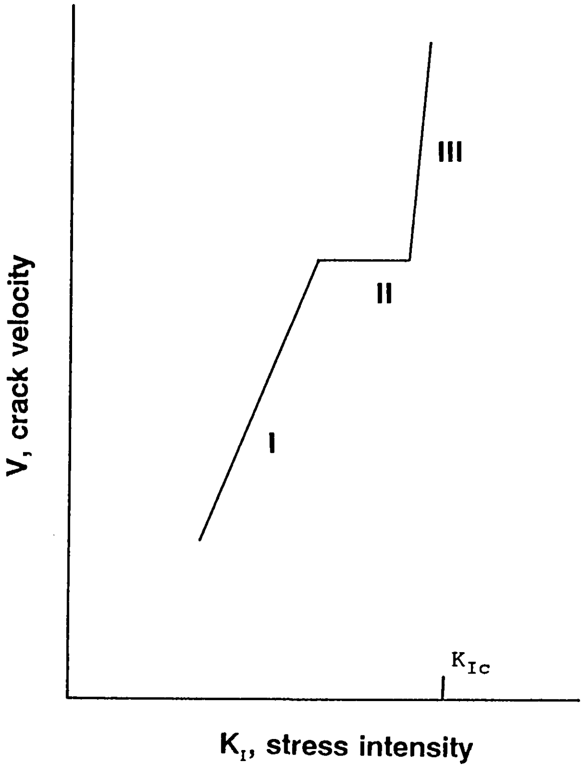

Fig. 3. Environmentally-assisted crack growth occurs at stress intensities less than K_{Ic} and can interfere with measurements of fracture toughness.

R-curve phenomena, illustrated in Fig. 4, are common in advanced ceramics [22–28] and are attributed to interactions of a crack with the microstructure. Resistance to crack extension increases as the crack extends. In advanced ceramics this is often due to wake (behind the crack tip) phenomena such as grain bridging, fiber reinforcement, or dilation from phase transformations. The ZAC with a transformable tetragonal zirconia phase likely will cause rising R-curve behavior, but the fine grain, equiaxed silicon nitride is not likely to do such.

Figure 5 illustrates one possible framework suggested by Fuller for categorizing advanced ceramics [29]. The simplest condition is a material that has no R-curve behavior (i.e., brittle) and which has no environmentally-assisted crack growth. It is not unreasonable to characterize such a material as having a specific fracture toughness, K_{Ic}, and test methods could be tailored to measuring such value. It is expected that the silicon nitride will approximate these conditions when tested at room temperature.

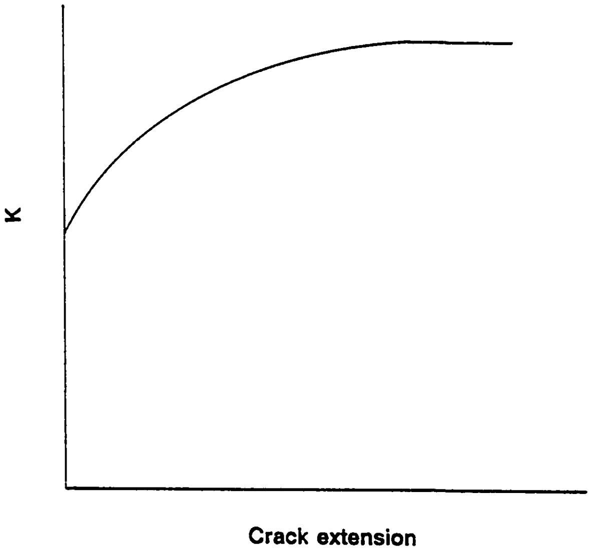

Fig. 4. R-curve phenomena can also complicate fracture toughness testing. The resistance to crack extension increases as the crack extends. It is not clear what constitutes K_{Ic} in such a material.

BRITTLE NO SCG	BRITTLE SCG
R-CURVE NO SCG	R-CURVE SCG

Fig. 5. The crack growth behavior of advanced ceramics can be categorized by whether R-curve phenomena, and/or slow crack growth phenomena are active. After Fuller [29].

If, on the other hand, environmental effects influence crack growth, then results will be very sensitive to the testing conditions, especially the rate of loading and humidity. If R-curve phenomena are active, then a serious question ensues as to what fracture resistance is being measured by a given test. In general, different tests will give different results for toughness, depending upon the precracking history, the amount of crack extension during the test, the amount of crack opening displacement, and the precracking and final loading rates. A material which manifests both environmentally-assisted crack growth and R-curve phenomena poses a formidable challenge, both in testing and interpretation of results [22,23]. The zirconia alumina composite may very well fall into this category.

The test matrix and testing conditions in this round-robin were specified primarily with two objectives: detecting environmental effects through the use of variable loading rates, and observing the sensitivity of the results in the IF and IS methods to the use of different indentation loads. No procedures were specified to detect or quantify R-curve phenomena, although as will be shown, some inferences can be made from the results.

3. Experimental Procedure

The experimental procedures were specified in the instructions JFCC furnished to all participants and are summarized below.

3.1 Indentation Strength (IS) Method

The polished 4 mm wide surface of each specimen was indented by a Vickers indenter at the individual laboratories. Two loads each were used for the two materials: 49 and 249 N for silicon nitride, and 98 and 490 N for ZAC. Use of two loads permitted an assessment of whether there was a dependence of fracture toughness on indentation load. Ten specimens of each material were indented at each load in the middle of the specimen. The 490 N load for the ZAC is higher than what most microhardness machines can produce, so most laboratories mounted a Vickers indenter onto a universal testing machine and loaded the specimen in a simulated indentation cycle. It is not clear how proper this procedure is and how successfully it was done in the different laboratories. Hardness measurements themselves are notoriously sensitive to loading rate, vibration, and impact. For example, it was very difficult with displacement control machines to simulate the constant load portion of a hardness cycle. NIST held the crosshead stationary for 15 s to simulate that portion of the cycle. NIST was able to control the peak loads to within 1% for 7 of 10 specimens, and within 2.5% for the remaining three. In addition, it was very difficult to control the exact peak load with such machines when they were loading at rates simulating a microhardness machine cycle. During the customary hold time of about 15 s, the crosshead was held stationary and a relaxation of 2% in load was noted for all specimens. In contrast, USA lab 5 unloaded immediately upon reaching the peak load.

The indented specimens were then loaded into a three-point flexure fixture with a 30 mm span, taking care that the indent was loaded in tension directly under the middle load pin. The flexure strength was measured with a crosshead speed of 0.5 mm/min. The specimen and fixture sizes, and the rate-of-loading are consistent with the Japanese flexure strength standard test method: JIS R 1601 [30].

The JFCC instructions specified that the fracture toughness should be calculated by the following equation:

$$K_{Ic} = 0.59\ (E/H_v)^{1/8}\ (\sigma_c\ P^{1/3})^{3/4} \qquad (1)$$

where E is the elastic modulus, H_v is the *Vickers hardness*, σ_c is the flexure strength, and P is the indentation load. Unfortunately, the hardness in Eq. (1) is not the same hardness as specified in the original Ref. [7]. Vickers hardness is defined as the load divided by the *actual contact area* of the indenter into the specimen (the surface of the four facets of the pyramidal impression which penetrate into the sample):

$$H_v = 1.854\ P/(2a)^2 \qquad (2)$$

where $2a$ is the indentation diagonal size. In Ref. [7], the hardness was defined as the load divided by the *projected area* on the surface:

$$H = 2\ P/(2a)^2. \qquad (3)$$

The fracture toughness as originally derived in Ref. [7] is:

$$K_{Ic} = 0.59\ (E/H)^{1/8}\ (\sigma_c\ P^{1/3})^{3/4}. \qquad (4)$$

The use of the wrong hardness leads to a systematic error of 1% (calculated values are too high) in fracture toughness if Eq. (1) is used. Equations (3) and (4) are *the proper equations to use for the IS method* as specified in Ref. [7].

3.2 Single-Edge Precracked Beam (SEPB) Method

The fractured halves of the IS tested specimens were subsequently used for SEPB testing. Indentations were implanted on the 3 mm wide face, the specimen precracked with a bridge-anvil, the precrack dye-penetrated, the specimen fractured in three-point loading, and the precrack size measured on the fracture surface.

Either an indentation or saw cut can be used as a precursor to the precrack in the middle of the specimen. The JFCC instructions for this round-robin specified use of one Vickers 98 N indent for the silicon nitride, and three 196 N indents for the ZAC as shown in Fig. 6a.

Next, the specimen was inserted into the bridge-anvil as shown in Fig. 6b with the indents located directly over the groove whose dimensions could be varied from 3 to 6 mm as needed. The assembly was inserted into a universal testing machine and load was increased until a precrack popped in. This could be monitored by acoustic emission equipment or by ear. No loading rate was specified, but slow rates are advisable to permit detection of the pop-in and to minimize the risk of load cell overload. Although not specified in the instructions, once the pop-in load had been established, it was acceptable to preload at a moderate rate up to some fraction of the expected pop-in load (e.g., 80%), and then load slowly until pop-in. Loads between 10000 and 20000 N (2200–4400 lb) were needed for this step, which precluded the use of most small table-top universal testing machines. (NIST utilized a heavy duty machine[3] for precracking, and a small table-top model[4] for three-point fracture.) The pop-in load and the precrack length could be adjusted by the selection of different groove widths; the larger the width, the lower the pop-in load and the longer the precrack.

A specific design for a bridge-anvil was furnished by JFCC along with instructions on how to order a set from Japan. Several U.S. participants attempted to acquire such an anvil, but encountered administrative difficulties and ultimately fashioned their own apparatus. This is important since some foreign and U.S. participants had problems obtaining proper precracks with their own designs, whereas the labs using the JFCC design had few such problems. The JFCC reports suggested that improper alignment with the former may have been a problem [12,13].

The depth of the precrack was then measured. The instructions recommended the use of dye penetrants, possibly diluted by acetone. If dye penetrants were used, the instructions specified that the specimens were to be dried at 50 °C for 1 h.

The specimens were then loaded in a three-point flexure fixture with a rather short 16 mm span and loaded to fracture. The specimens were tested at two different crosshead rates (1.0 and 0.005 mm/min) thereby permitting an assessment of whether environmental phenomena affected the results.

After fracture, the precrack length was measured at three locations as shown in Fig. 7. The average of the three measurements was used as the crack length to calculate fracture toughness. The difference between any two of the three length measurements could not exceed 10% of the average, and the plane of the crack had to be perpendicular to the specimen long axis within 10 ° or else the specimen was rejected. These criteria are from the ASTM fracture toughness standard E 399 [11]. In addition, although it was not clearly stated in the instructions, the precrack length had to be between 1.2 and 2.4 mm. This is a requirement of JIS R 1607 [1], but is not in ASTM E 399 [11].

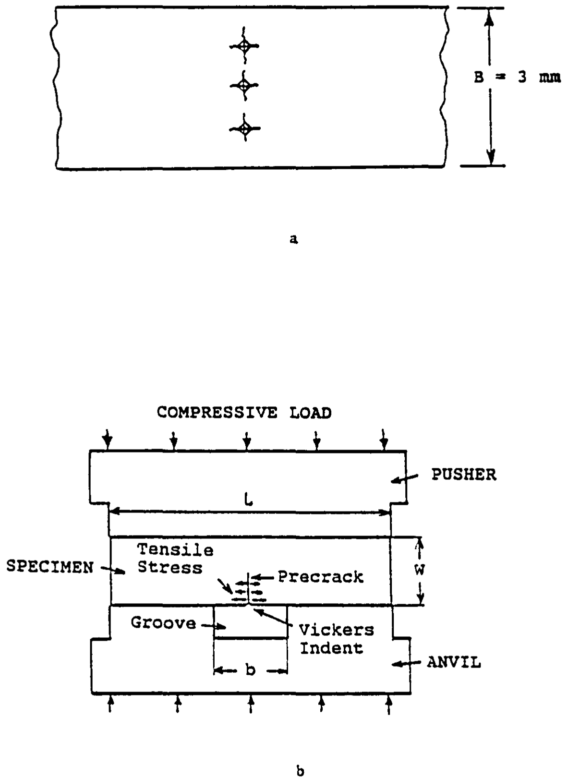

Fig. 6. The precracking procedure for the SEPB specimens. Three 196 N indents were used on the ZAC as shown in (a). After indentation, the precrack was popped-in by loading the specimen in a bridge-anvil as shown in (b).

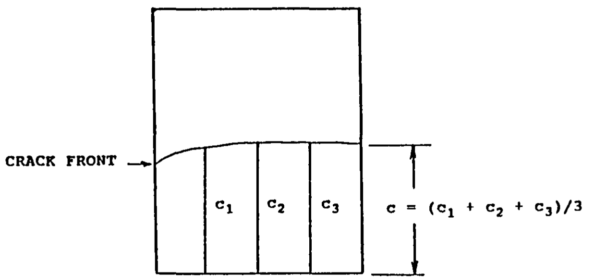

Fig. 7. After fracture, the SEPB precrack size was measured on the fracture surface.

---

[3] Instron model TTCML with a 50000 N load cell.

[4] Instron model 1122 with a 5000 N load cell.

Fracture toughness was then calculated from Srawley's equation [13] (which is also the same as in ASTM E 399) which is accurate within ±0.5% for all crack lengths from 0 to W [10,11]:

$$K_{Ic}=\frac{3SP}{2BW^2}\,c^{0.5}\,F(\alpha) \tag{5}$$

$$\alpha=c/W \tag{6}$$

$$F(\alpha)=\frac{1.99-\alpha(1-\alpha)(2.15-3.93\alpha+2.7\alpha^2)}{(1+2\alpha)(1-\alpha)^{1.5}} \tag{7}$$

where:

S is the moment arm of the three-point fixture (16 mm)
c is the precrack length
α is the normalized precrack length
W is the specimen height
B is the specimen width
P is the load at fracture.

3.3 Indentation Fracture (IF) Method

One of the fractured halves of an IS specimen was used for this method. Ten Vickers indentations were placed on the polished surface. Two loads each were used for the two materials: 98 and 196 N for the silicon nitride, and 294 and 490 N for the ZAC. No instructions on loading rate were given. The 294 N load (30 kg) is at the limit of many commercial microhardness testers. As discussed above in the IS section, the 490 N indentation had to be simulated on a universal testing machine and this could have introduced a serious additional source of error or scatter in the IF method. (Microhardness measurements are notoriously sensitive to vibrations and rate of loading.)

The indentation diagonal length, $2a$, and the crack length, $2c$, were measured for each impression. If the ratio of the crack length to indentation length, c/a, was less than 2.3, or if there was crack branching, the data was to be rejected.

Two different equations were to be used for calculation of fracture toughness. Unfortunately, the instructions for the round-robin furnished two forms for each of the equations (for a total of four equations) which led to some confusion.

The derivation by Miyoshi et al. [31] gives:

$$K_c=0.018\,(E/H_v)^{0.5}\,(P/c^{1.5}) \tag{8}$$

$$=0.0264\,E^{0.5}\,P^{0.5}\,c^{-1.5}\,a. \tag{9}$$

Equation (9) properly follows from Eq. (8) *if the hardness is* $H_v=1.854P/(2a)^2$. The instructions for the round-robin specified that Eq. (9) was to be used but also included Eq. (8), but without the subscript "v". Regretably, some U.S. participants utilized Eq. (8), but with $H=2P/(2a^2)$. This leads to a 3.9% error in the IF results. In the results that follow, all data have been corrected to be in accordance with Eq. (9) as specified by the round-robin instructions and by Miyoshi et al. [31].

An alternate equation derived by Marshall and Evans [32] was also prescribed by the round-robin instructions:

$$K_c=0.036\,E^{0.4}\,P^{0.6}\,a^{-0.7}\,(c/a)^{-1.5} \tag{10}$$

$$=0.036\,E^{0.4}\,P^{0.6}\,a^{0.8}\,c^{-1.5}. \tag{11}$$

In this instance, there is no confusion with hardness since it does not appear. Equations (9) and (11) are very similar and have the same c dependence. The E, P, and a dependencies are slightly different and reflect a small difference in the dependence of the E/H ratio used in the original derivations. Dividing Eq. (9) by (11) gives:

$$K_c,\ \text{Eq. (9)}/K_c,\ \text{Eq. (11)}=0.689\,(E/H)^{0.1}. \tag{12}$$

Equations (9) and (11) give values of K_c that are about 7% different since E is constant and H varies only a slight amount over the range of indentation loads used. The Miyoshi et al. [31] Eq. (9) gives the smaller value of K_c. (The difference is also about 7% if H_v is used.)

Several laboratories also measured the Vickers indentations and cracks from the precracking of the IS specimens (described above) and thus were able to obtain additional data for IF analysis. The indentation loads available for IF analysis are shown in Table 2.

Table 2. Indentation loads for IF analysis

Material	Load (N)				
silicon nitride	49	98[a]	196[a]	294	
ZAC		98		294[a]	490[a]

[a] Specified by the IF instructions.

4. Results and Discussion

The U.S. laboratory results are presented here in the same format as used by JFCC for the earlier partial results. This is done to permit easy comparison of the U.S. results to those of the other participants. The results from the U.S. labs are identified in the figures as U.S. labs 1–5.

4.1 Indentation Strength (IS) Results and Discussion

Figures 8 and 9 show the results for silicon nitride and the zirconia alumina composite respectively. The U.S. data are completely consistent with the other data and show the same trend of apparent increasing toughness with indentation load. The within-laboratory standard deviations of the results are also consistent with the other laboratory results and are typically 0.1 to 0.2 $MN/m^{1.5}$ (Figs. A1–A4 in Appendix A). (Foreign lab 2 did not follow instructions and annealed the specimens prior to testing thereby relieving the residual stress. This procedure invalidates the use of Eqs. (1) or (4).) For silicon nitride, the average fracture toughness for all laboratories (excluding lab 2) is approximately 5.8 and 6.3 $MN/m^{1.5}$ at the 49 and 294 N loads, respectively. For the ZAC, the averages are 6.9 and 7.4 $MN/m^{1.5}$, at 98 and 490 N loads, respectively. None of the Japanese labs (8–11) performed IS measurements.

A material with constant fracture toughness would have a fracture load dependent upon the indentation load, *P*, to the minus one third power. Since this dependence is factored into Eqs. (1–4) there should be no dependence of IS toughness on indentation load. The apparent variation in Figs. 8 and 9 could be attributed to a rising "R-curve", and indeed, techniques to analyze such data have been devised [26–28].

An alternative explanation can be found by noting that the controlled flaw is often quite large relative to the specimen cross section. The flaw is not exposed to a uniform stress field, but is actually in a gradient which diminishes to zero axial stress at

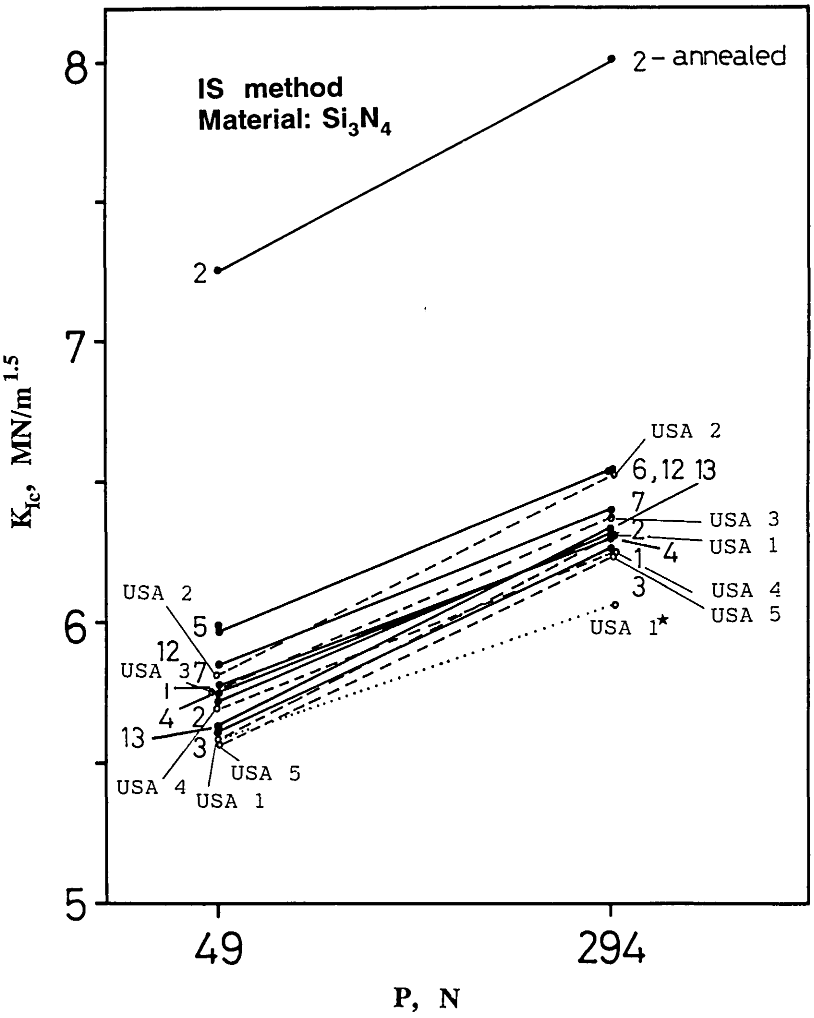

Fig. 8. Fracture toughness for the silicon nitride as measured by the indentation strength (IS) method. The dotted line shows the USA lab 1 data for the 294 N indentation load corrected for the stress gradient (USA 1*).

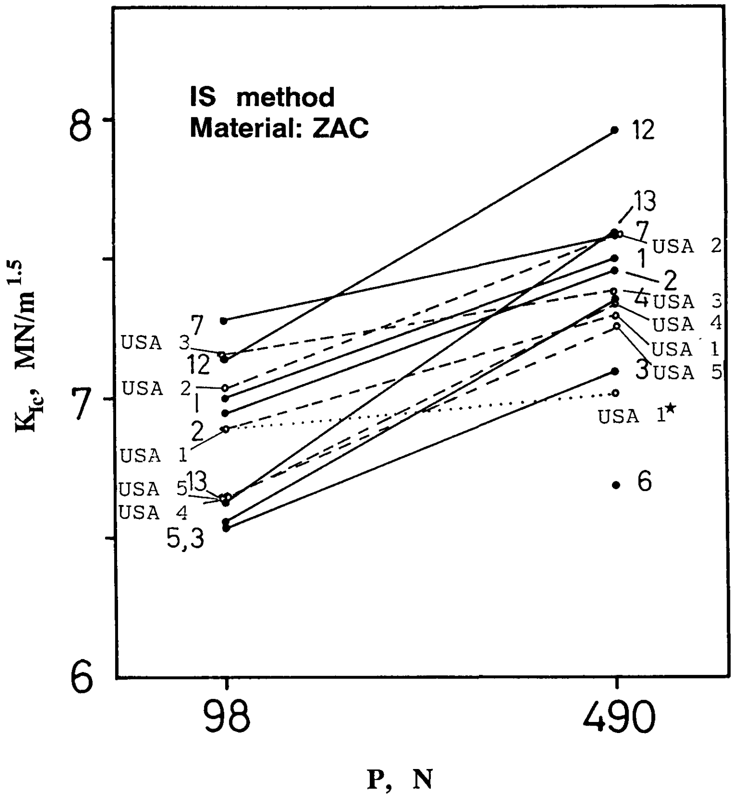

Fig. 9. Fracture toughness for the ZAC as measured by the indentation strength (IS) method. The dotted line shows the USA lab 1 data corrected for the stress gradient.

the neutral axis. The stress intensity around a crack can be expressed as:

$$K_I = Y \sigma \sqrt{c} \quad (13)$$

where Y is the shape factor, σ is the far-field stress, and c is flaw depth. The derivation of Eq. (4) assumes that the applied far-field stresses are acting uniformly on the surface crack and that the shape factor, Y, for the crack is uniform and remains constant as the crack extends. The shape factor is incorporated into the constant, 0.59, in Eq. (4). An expanded version of Eq. (4) from Ref. [7] is:

$$K_I = [(256/27)(\pi Y)^{3/2} \S]^{1/4} (E/H)^{1/8} (\sigma P^{1/3})^{3/4} \quad (14)$$

where § is a constant for the Vickers produced radial cracks.

Assuming a constant Y is only an approximation for surface cracks loaded in bending. Although it is adequate for shallow cracks in large bend specimens, it is more accurate to adjust the stress intensity shape factor, Y, for the stress gradient. In recent years, the shape factors corrections derived by Newman and Raju [33,34] have been commonly used. An estimate of the effect of the stress gradient upon the computed fracture toughness is derived below.

The indentation loads used in the present round-robin had to be sufficiently large to ensure fracture from the artificial flaw. Table 3 illustrates that the artificial flaws were quite large relative to the specimen thickness (3 mm). (The surface lengths were measured and the depths shown assume the crack shape is semicircular.)

Table 3. Indentation strength (IS) specimen initial crack sizes

Material	Indent load P (N)	Surface length $2c$ (mm)	Flaw depth c (mm)	Depth ratio c/W
Si_3N_4	49	0.165	0.083	0.028
Si_3N_4	294	0.570	0.285	0.095
ZAC	98	0.179	0.090	0.030
ZAC	490	0.622	0.311	0.104

The initial crack sizes are *not* the crack size at fracture, however. During loading to fracture, the residual stresses from the indentation will combine with the applied external stresses to cause the initial crack, c_0, to extend stably to a size $c_{\max}$ at which point unstable fracture will occur [7]. The value of $c_{\max}$ can be estimated from the indentation parameters and, thus, it is not necessary to measure a crack length for this method. (Note that Eqs. (1) and (14) do not include a crack size term.) Not having to measure precrack size is a great experimental advantage. If the plastic indentation zone exerts a constant residual force upon the crack as it extends, the original analysis shows that the precrack will extend $2.52\times$ its original size in a uniform stress field for a flat R-curve material [7]. The crack extension would be less if the plastic indentation zone behaves as a rigid (fixed-displacement) wedge [27]. The latter study reported experimental extensions along the specimen surface of 2.1 and $2.3\times$ for a SiC-alumina composite and silicon nitride, respectively.

The extent of crack extension into the depth will be much less, however, due to the stress gradient. Thus, the controlled flaw will change shape from a semicircle to a semiellipse. Raju and Newman showed several instances where crack shape changed ellipticity during fatigue growth [33]. Dusza [35] and El Aslabi et al. [36] reported that crack extension was entirely along the surface in ceramic IS specimens, with nearly no extension into the depth. The latter study was on a silicon nitride with similar indentation loads as in the VAMAS round-robin. Ramachandran and Shetty [27], Krause [26], and Anderson and Braun [28] also noted the change of crack shape. Each of these investigators observed that the change in shape would affect their shape factors, but resorted to the use of an average value for Y.

Ideally, the final crack shape at instability could be measured and the correct shape factor could be used in the Eq. (13). The silicon nitride and ZAC specimens tested at NIST were examined to determine if the final crack shape could be measured. The semicircular initial cracks were evident, but the final crack shapes were not clear (Fig. 10). It was therefore necessary to estimate the final crack shape.

The Raju and Newman [33] and most other [34] analyses show that for the semicircular cracks of Table 2, the shape factor, Y, is severest at the surface by about 10%. The cracks will grow into semiellipses with an aspect ratio somewhere between 0.7 and 0.9, depending upon the penetration into the flexure stress gradient. Assuming such extension, and taking into account the different initial crack depths of Table 3, it can be estimated from the graphs of Raju and Newman [33] that Y for the larger-precracked specimens will be 10% less at fracture than for the smaller-precracked bars. This is for both the ZAC and silicon nitride. The calculated fracture toughness for the larger initial cracks is therefore reduced by $Y^{3/8}$ [Eq. (14)], or 4% (relative to the small-load IS specimens). This reduction is shown as a dotted line for the NIST data in Figs. 8 and 9. Much of the apparent dependence of fracture toughness upon indentation load can thus be accounted for.[5]

In summary, the indentation strength (IS) results are quite consistent between the different laboratories, and give an average fracture toughness of 5.7 $\text{MN/m}^{1.5}$ for the silicon nitride, and 6.7 $\text{MN/m}^{1.5}$ for the ZAC at the lower indentation loads. The scatter in toughness values within each laboratory was quite low, typically 0.1 to 0.2 $\text{MN/m}^{1.5}$. The method is simple to conduct and rather popular. One shortcoming of the method is that the true crack shape, the stress intensity factor, the simplifications of the elastic-plastic analyses for the residual stress driving force, and the assumptions of the general similitude of the indentation patterns from material to material, are all embodied in the constant 0.59 in Eq (4). This value was empirically derived by comparison of indentation strength results to results on "standard" materials of "known" toughness. Finally, the specification that three-point loading was to be used added an additional, unnecessary complicating factor in that the precrack had to be precisely located in the three-point flexure fixture. Four-point testing would have been much easier, and possibly more accurate.

4.2 Single-Edge Precracked Beam Results and Discussion

Figures 11 and 12 show the results obtained from the SEPB method as a function of crosshead rate. The use of two widely different crosshead rates permits an assessment of whether environmentally-assisted crack growth was a factor. Most of the laboratories used the recommended speeds of 1 and 0.005 mm/min. USA lab 2 overlooked this, however, and tested all 20 specimens at a single rate.

---

[5] This stress intensity shape factor variability is a serious interfering factor on measurements of R-curves in IS testing. Krause [26] and Anderson and Braun [28] have also made this observation.

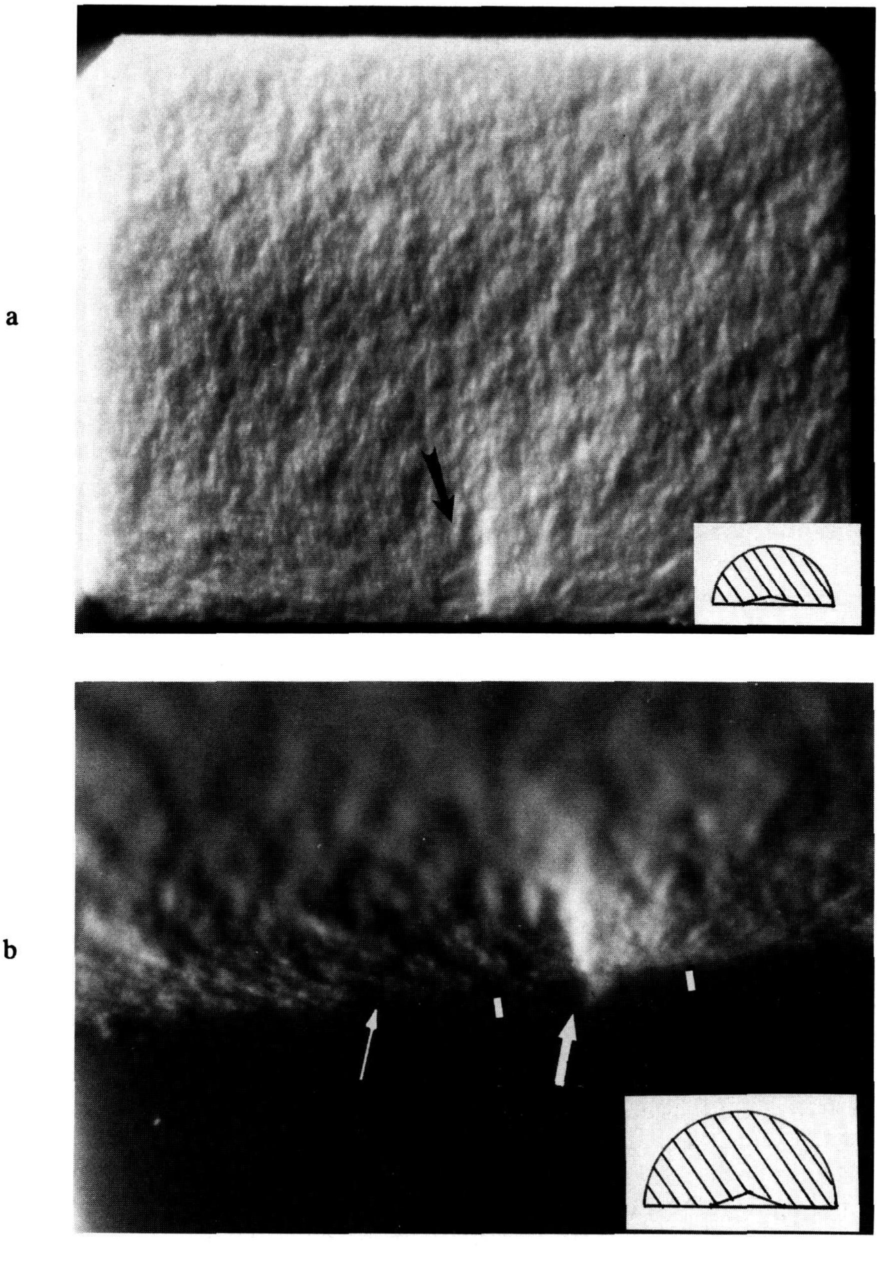

Fig. 10. Fracture surface of an indentation strength ZAC specimen with a 490 N indent. An insert in each figure shows (at correct scale) the size of the indentation and the precrack. (a) shows the entire fracture surface. The black arrow points to the area where the indentation fracture origin lies. (b) is a closeup with the specimen tilted to accentuate both the indent and the fracture surface. The large white arrows marks the Vickers indent; the white bars, the precrack; and the small white arrow, the probable extent of stable crack extension prior to catastrophic fracture.

The silicon nitride is, for the most part, insensitive to the rate of loading, whereas the ZAC exhibited pronounced sensitivity. If the fracture toughness is lower at the lower loading rate, the usual interpretation is that environmentally assisted slow crack growth is active. This interpretation will be reconsidered below.

The toughness values for the silicon nitride are, for the most part, in very good agreement between the laboratories and cluster about 5.6 MN/m$^{1.5}$. The standard deviations within the all labs are usually between 0.1 and 0.4 MN/m$^{1.5}$. The U.S. laboratories are between 0.1 and 0.3 MN/m$^{1.5}$ as shown in the figures in the appendix. The exceptions are USA

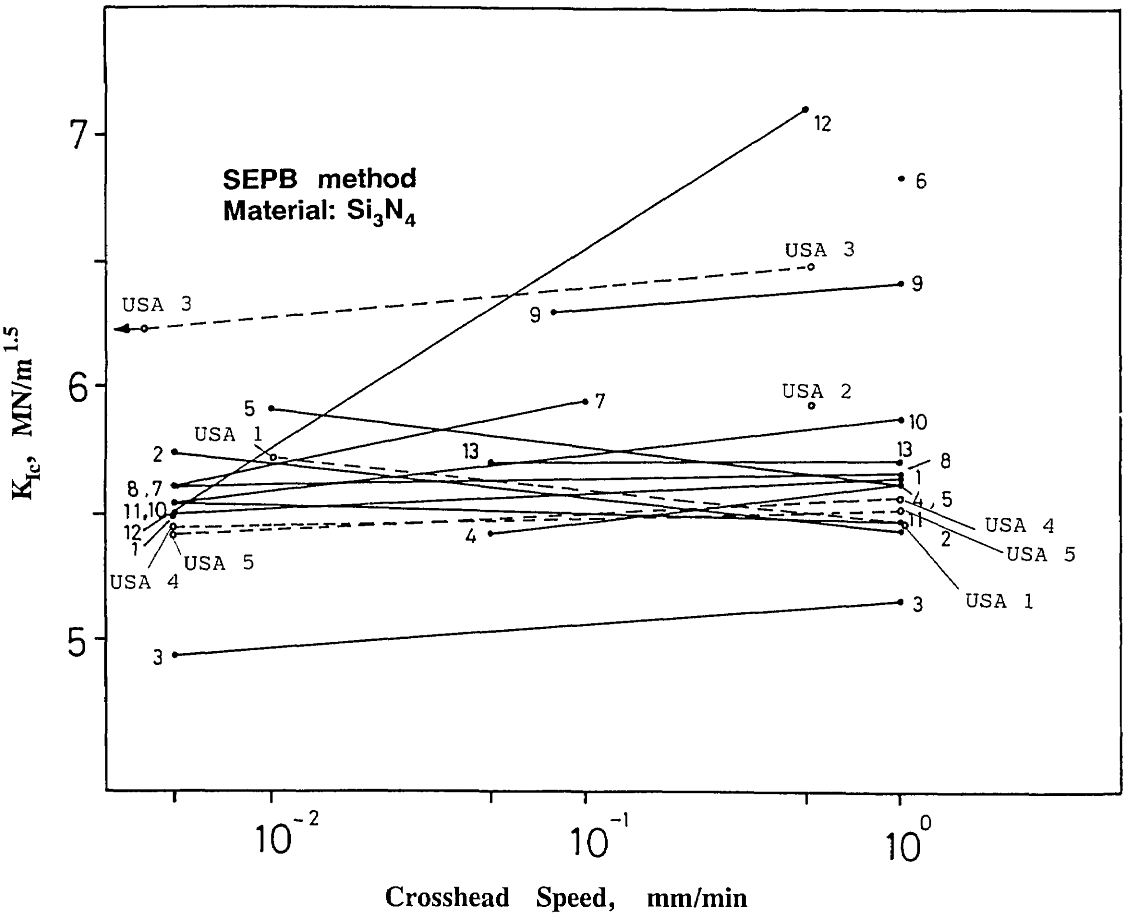

Fig. 11. Fracture toughness for the silicon nitride as measured by the single edge precracked beam (SEPB) method. There is a negligible loading rate effect indicating that environmentally assisted crack growth is not a factor.

lab 3 and labs 3, 6, 9, and 12 from the original reporting labs. Of the four Japanese labs (8–11), labs 8, 10, and 11 had very consistent results with low scatter (Figs. A5–A8 in Appendix A), but lab 9 seemed to be systematically high.

The ZAC results have higher scatter as shown in Fig. 12. Most results are within a range of 0.75 MN/m$^{1.5}$ and show the trend of higher toughness with higher loading rate, although sometimes, *individual* labs (such as labs 2 and 4, and USA labs 3 and 4) concluded there was *no* such dependence. USA lab 4 had drastically divergent results and it is tempting to conclude the results are erroneous. They are not, and USA lab 4 discerned an important phenomenon that raises important questions about the interpretation of the SEPB test results which are deferred until later in this section.

The initial reports by JFCC on the round-robin suggested there may have been confusion and problems by some of the participants who had never tried the SEPB test method before [12,13]. One problem proved to be in measuring the precrack size, a task which required some experience and skill. Several labs that were unfamiliar with the bridge-anvil precracking method reported difficulties in obtaining properly precracked specimens. Figure 13 shows two silicon nitride SEPB specimens: one with and one without straight precracks. Alignment of the homemade bridge-anvils is the probable source of the difficulty. JFCC suggested that some of the precracking jigs may not have been adequate to the task. On the other hand, there were sufficient fragments left over from the IS testing that a large number of specimens could be tried until an adequate number of SEPB specimens could be tested. The high compression loads also posed a severe risk of universal testing machine or load cell damage if the operator inadvertently pressed a wrong crosshead speed button.

The flexibility of precracking conditions led to some differences in precise procedures with unknown attendant effects on the final results. For

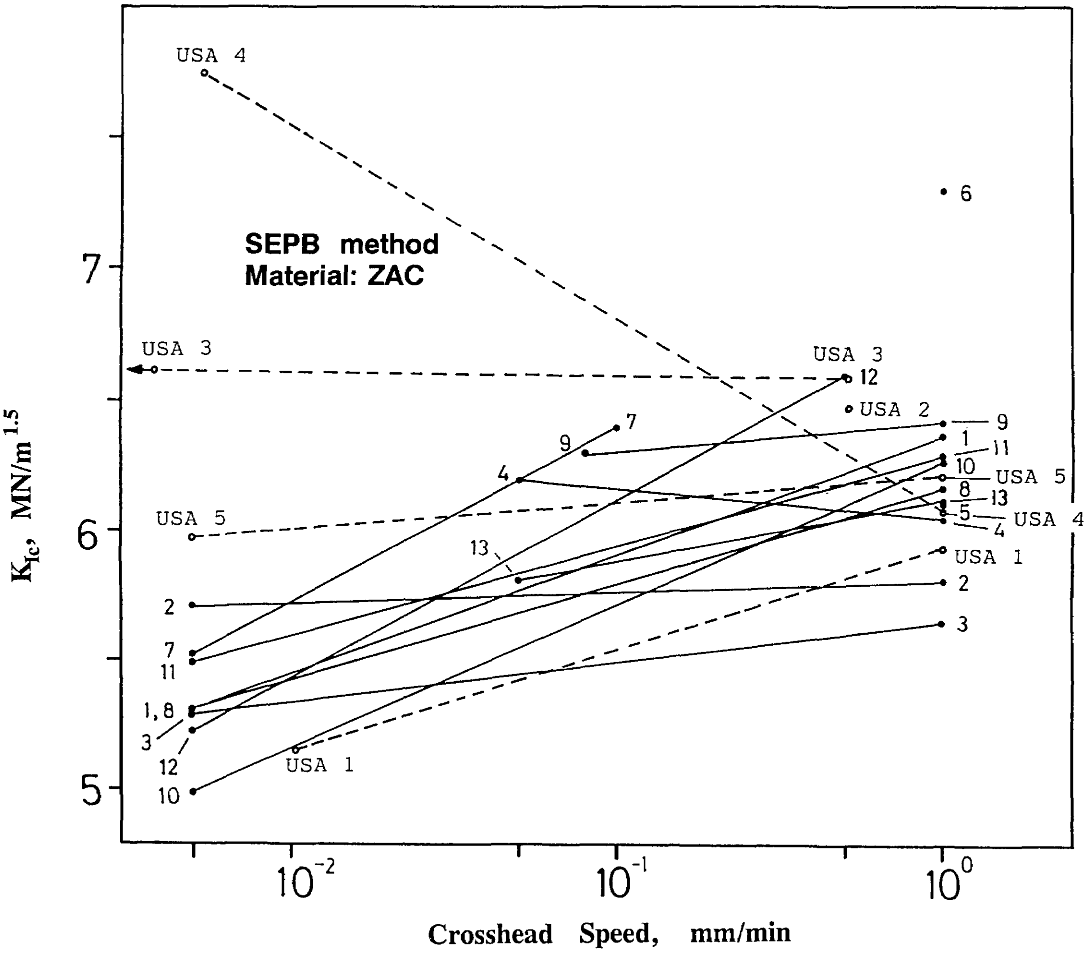

Fig. 12. Fracture toughness for the ZAC as measured by the single-edge precracked beam (SEPB) method. The rate dependence of fracture toughness probably is a consequence of R-curve and environmentally assisted crack growth phenomena.

example, the rate of loading was unspecified in the instructions: "Increase the load gradually until a pop-in sound is detected by ear or a sonic sensor." Some laboratories used older, screw-driven machines and crosshead rates had to be kept low to hear the pop-in against the background machine noise. Other laboratories with quieter machines precracked at faster rates.

NIST and USA lab 3 (at least initially) used a stethoscope attached to the bridge-anvil support to detect pop-in. USA labs 3 and 5 visually observed precracking through a hole in the side of the bridge-anvil at the same time that the crack was exposed to a dye penetrant. Most other laboratories applied dye penetrant *after* precracking. The use of a dye penetrant *during* precracking may alter the precracking process by enhancing intergranular, environmentally assisted crack growth as opposed to stable fast crack pop-in. The rate of precracking has been shown to have a strong effect upon the type of precrack (trans- versus intergranular) and upon the final toughness result in materials with R-curve producing microstructures [8,37].

The silicon nitride specimens precracked with a distinct (albeit faint) pop and it is believed that the material was less sensitive to details of precracking than the ZAC. USA lab 5 used load control (rather than displacement control) and reported that it was easier to detect a distinct pop-in at *higher* loading rates. NIST used a slow loading rate for the ZAC and observed (by interrupting the procedure, removing the specimen, and dye penetrating it) that precracking commenced at loads as low as 9000 N, and stably propagated in short extensions (with attendant sound emissions) as load was increased. NIST and USA lab 3 discerned a series of faint snapping noises during the ZAC precracking. The evidence strongly suggests R-curve phenomena. Differences in precracking may have affected the ZAC results as will be discussed below.

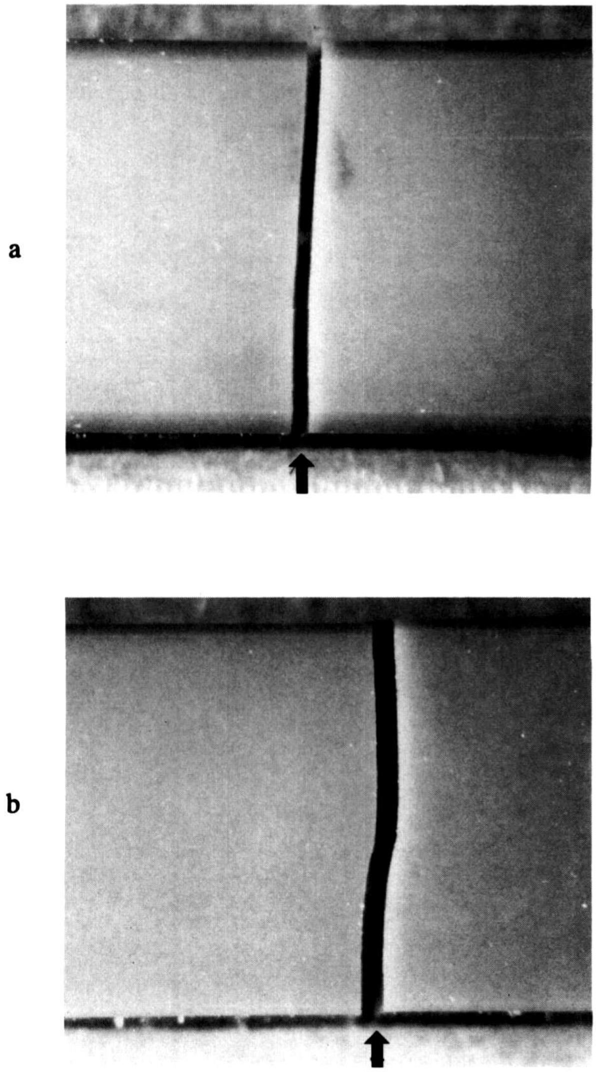

Fig. 13. Side views of fractured silicon nitride SEPB specimens. The arrows mark the precrack.

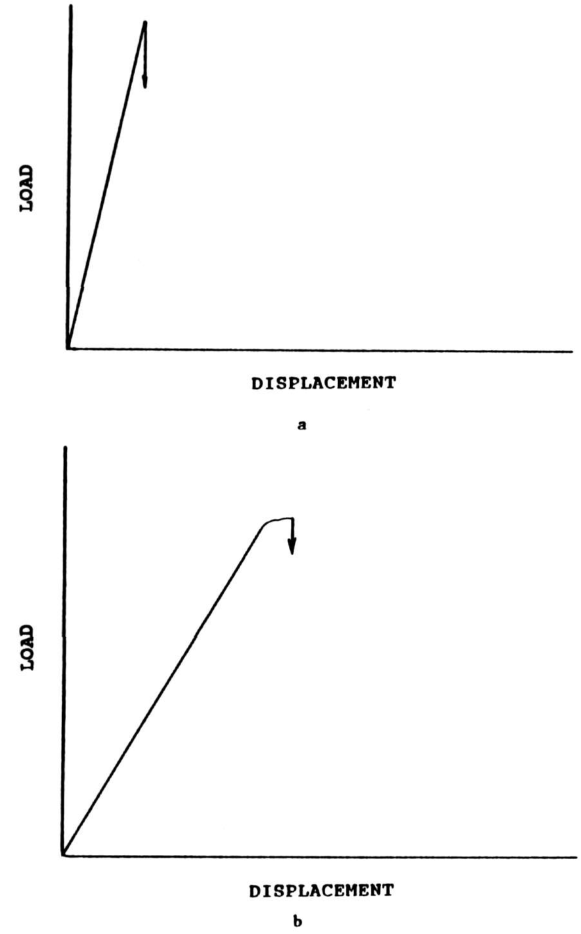

Fig. 14. Silicon nitride SEPB specimens at both loading rates, and the ZAC at the fast loading rate, had linear loading to fracture as shown in (a). The ZAC at the slow loading rates had several seconds of stable crack growth prior to catastrophic fracture as shown schematically in (b).

After precracking, the specimens were loaded to fracture in three-point flexure. The silicon nitride at all loading rates, and the ZAC at the fast rates, exhibited an essentially linear load-deflection curve as illustrated in Fig. 14. NIST and USA lab 4 reported that the ZAC, in contrast, had a slight nonlinearity at the slower loading rates as illustrated in Fig. 14. This is an important observation and means that the *crack grew stably prior to catastrophic fracture.* The stable growth can be interpreted as coming either from environmentally assisted crack growth, or from rising *R*-curve behavior. The environmental growth probably does not fully explain the observed results since, for a flat R-curve material, any crack extension in a single-edge loaded beam usually leads to unstable-crack extension (for "soft" testing machines and fixtures, and for the precrack sizes of the specified ranges of this round-robin[6].) Therefore, rising R-curve phenomena probably exists in the ZAC.

One minor observation at NIST during the three-point loading was that alignment of the precracked beam in the three-point fixture was a nuisance. The SEPB specimens had a very short length (~20 mm) and were tested on a 16 mm

---

[6] Stable crack extension is possible in flat *R*-curve materials for the precrack sizes specified in the VAMAS round-robin, but only if the testing system is extremely rigid. Baratta and Dunlay [38] and Sakai and Inagaki [39] have defined the geometries, specimen and system compliances that lead to stable crack extension. The testing systems used in the present round-robin were usually "soft" or compliant, and would not promote stable crack growth.

span. A 1% error in positioning the precrack is only 0.08 mm (0.003 in)! It is not known what effect such misalignments had upon the measured values of toughness. Four-point fixtures would have been easier to use and would have eliminated this potential error source.[7]

After fracture, all labs measured the "precrack" size on the fracture surfaces and rejected any specimens where the crack was misaligned, uneven, or not in the specified size range. Measurements were made using optical microscopes or photos taken with a microscope. Figure 15a shows a typical precrack in the ZAC. Table 4 shows some of the procedures used by the U.S. labs. Each lab developed a procedure after a few trial and error steps. The easiest and most reliable method for the ZAC was application of a felt-tip pen to the precrack which stained the white material quite effectively. The opaque silicon nitride was much more problematic (Figs. 15b,c) and none of the dye penetrants worked effectively. Most bled during subsequent fast fracture and storage which led to false crack length measurements. Two labs reported this occurred despite drying cycles or protracted periods of storage prior to fracture. The best procedure for the silicon nitride was optical microscopy with low-incident angle lighting.

Table 4. Precrack inspection procedures

Lab	Procedure ZAC	 Silicon nitride
NIST	Green felt-tip pen	(Fluorescent dye penetrant-unsuccessful) Low-angle incident lighting
USA lab 2	Commercial blue dye penetrant	Commercial blue dye penetrant
USA lab 3	Felt-tip pen	Blue food coloring, applied under load
USA lab 4	(Red dye penetrant unsuccessful) Low-angle incident lighting	(Red dye penetrant unsuccessful) Low-angle incident lighting
USA lab 5	Acetone and dye, fractographic inspection	Acetone and dye, fractographic inspection

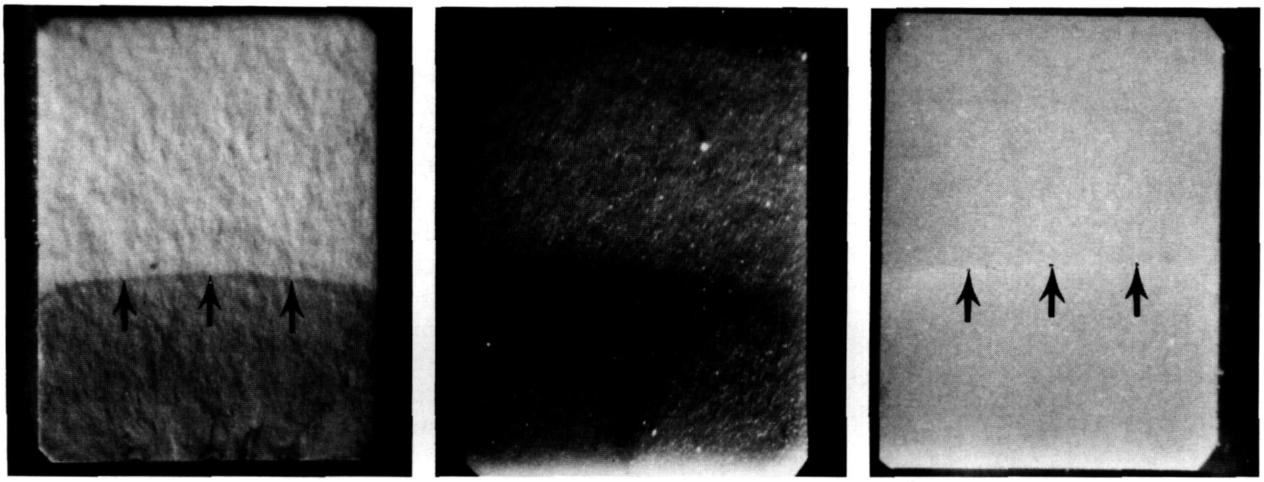
a b c

Fig. 15. Fracture surfaces of ZAC (a) and silicon nitride (b) SEPB specimens. The colored penetrant on the ZAC is quite definitive. The silicon nitride was more difficult to dye penetrate and low-angle incident lighting was necessary. The position of the shadow in (b) could be altered significantly, however, depending upon the lighting angle. Considerable care had to be taken to make proper size measurements as marked by the arrows in (c).

---

[7] In defense of the choice of three-point loading, it should be stated that the scheme was presumably chosen to be in compliance with the loading configurations of ASTM standard E-399 [11]. The latter standard uses much larger specimen sizes that are easier to set-up however.

The apparently unusual results of USA lab 4 for the ZAC (Fig. 12) can now be reexamined in light of the known R-curve phenomena and of the USA lab 4 precracking procedure. Their procedure for staining the precrack was unsuccessful and they resorted to measuring the "precrack" by low-angle incident lighting. The ridge or feature that they observed in the ZAC is almost certainly *not the original crack from the precracking step, but instead, the crack length at the point of instability.* This crack length was considerably longer ($\sim$0.4 mm) than the pop-in crack size because of stable crack extension during the slow loading to fracture. The longer precracks that USA lab 4 used in Eqs. (5–7) account for their apparently high values of fracture toughness.

This is further reflected in Fig. 16 which shows the apparent fracture toughness as a function of crack size for USA labs 4 and 5. USA lab 4 concluded there was a strong dependence of fracture toughness on crack length and USA lab 5 concluded there was none.

This raises a rather fundamental question about what crack size is appropriate for the computation of fracture toughness for the ZAC: the pop-in precrack length or the crack length at instability? Indeed, this raises the additional question of what point on the R-curve (Fig. 4) does the measured fracture toughness lie.

One aspect of SEPB testing that was not addressed in the round-robin is the possible residual influence of the indents upon the final results. The indents are intended to act strictly as precrack starters and are presumed to have no result on the final fracture. Several investigations have concluded that this is not correct, and that proper results are only obtained if the indentations and their residual stress fields are removed prior to testing [40–43]. Further work is warranted to further clarify whether this is true only for short precrack lengths.

In summary, for the SEPB method, very consistent results were obtained by four of the five USA labs for the silicon nitride. The results were in agreement with the bulk of the other reported data from the international participants. There were negligible effects from loading rate or R-curve phenomena. The ZAC results were somewhat less consistent. Interpretation is severely complicated probably by both R-curve and environmentally assisted crack growth phenomena. The meaning of the measured fracture toughness in this material is unclear.

4.3 Indentation Fracture (IF) Results and Discussion

The IF results for silicon nitride and ZAC are shown in Figs. 17 and 18, respectively. The scatter in these results is shown in the appendix as Figs. A9–A12.

The USA lab results for the silicon nitride are consistent with the main body of data. There was no explanation for the very deviant results from foreign labs 5 and 6 [12–13]. The four Japanese labs 8–11 obtained systematically higher toughness values than the other participants. (The scatter in results within an individual lab are typically 0.15–0.3 MN/m$^{1.5}$, so the differences shown in Fig. 17 are systematic.) High values of fracture toughness correspond to shorter measured crack lengths.

The IF results for the ZAC are widely scattered and it is not possible to dismiss the results of any laboratory as being deviant. Toughness ranged from 5.3 to 9.2 MN/m$^{1.5}$. Scatter in results within each lab varied widely from as low as 0.1 MN/m$^{1.5}$ to as high as 1.3 MN/m$^{1.5}$.

Both Eqs. (9) and (11) show that fracture toughness depends upon crack length, c, raised to the minus 1.5 power. A $\pm 10\%$ variation in c therefore causes a $+17$ to -13% variation[8] in K_c or a net scatter (ratio) of $1.17/.87 = 1.34$. This variability probably accounts for most of the scatter in the results. The ZAC scatter at 294 N is from 9.2 to 5.3 MN/m$^{1.5}$, $=1.7$, and the silicon nitride at 196 N is from 6.6 to 5.0 MN/m$^{1.5}$, $=1.32$.

Several USA labs reported that the crack lengths measured were highly dependent upon the mode of viewing. All labs observed that there was considerable interpretation as to where the exact crack tip was and that there was difficulty in measuring this point. Different viewers were apt to obtain different results on the same specimen. Most agreed that the optics furnished with the microhardness machines were woefully inadequate for measuring crack lengths. (Most used more powerful microscopes.) NIST utilized a reflected light microscope[9] at up to 400× with a video camera connected to a 32 cm television monitor. Crack length measurements were made on the monitor with a mouse-driven set of cross hairs and length measuring software. The software included calibration corrections for the video system. This enabled accurate measurements to be taken in a very short time with

---

[8] $(0.9)^{-1.5} = 1.17$; to $(1.1)^{-1.5} = 0.87$.

[9] Optiphot, Nikon, Melville, N.Y.

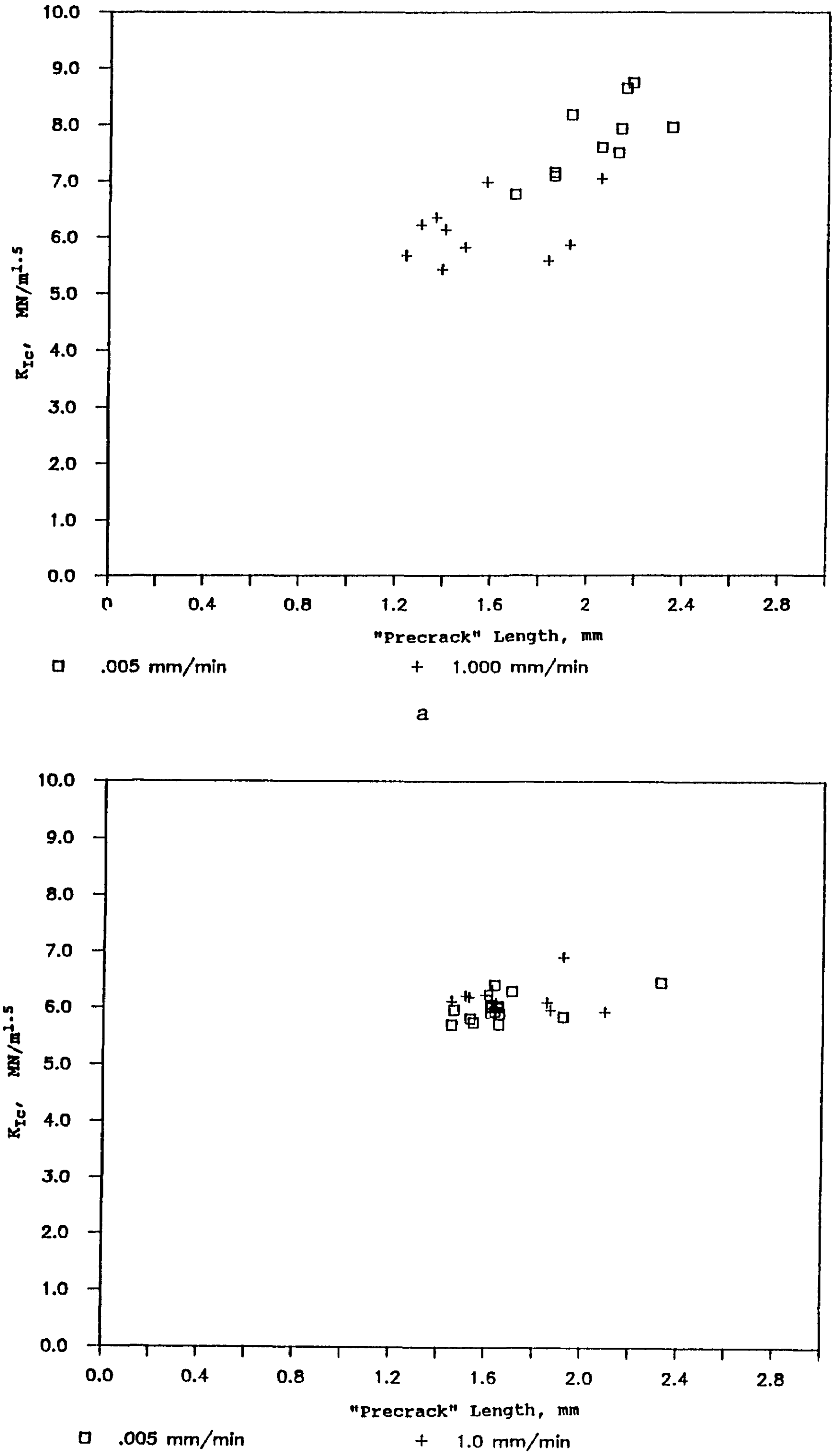

a

b

Fig. 16. Apparent SEPB fracture toughness versus "precrack" size for the ZAC. (a) is from USA lab 4, and (b) is from USA lab 5. The precrack lengths in (a) are the initial crack lengths after bridge anvil precracking; whereas those in (b) represent the crack length at instability.

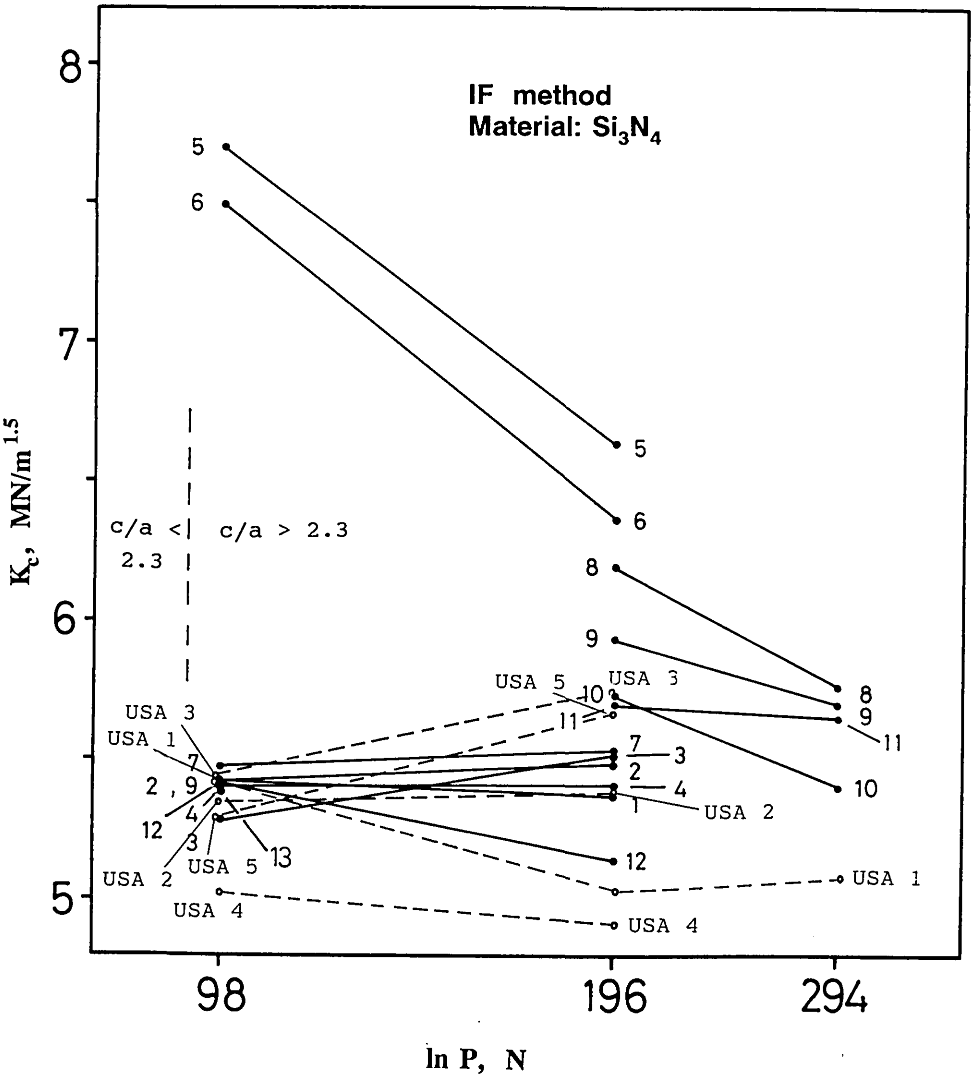

Fig. 17. Indentation fracture (IF) fracture toughness for the silicon nitride.

minimum effort. A few silicon nitride measurements were repeated on a different optical system, also equipped with a video monitoring system, but without the measurement software. Measurements from the two systems agreed within 3–4%. USA lab 4 reported that their experience was that measurements taken by a scanning electron microscope were typically 10 μm longer than optical measurements.

The indentation loads prescribed by the round-robin instructions were intended to produce cracks sufficiently long that the assumptions entailed in the derivations of Eqs. (9) and (11) would be valid. If the ratio of crack length to indentation diagonal size ratio (c/a) was less than 2.3, the data were to be ignored. Approximate locations for this threshold as determined with the NIST data set are shown as dashed vertical lines in Figs. 17 and 18. It is evident that the indentation load of 98 N was marginal for the silicon nitride, and the load of 294 for the ZAC was unacceptable. The instructions specified that 10 measurements be made, and only those indentations that were satisfactory would be used.

The need for a $c/a > 2.3$ comes from the requirement that the cracks be fully developed median (and not Palmqvist) cracks. A number of recent studies (e.g., [44]) have carefully studied subsurface crack morphologies and report that the transition from Palmqvist to a median crack form can actually occur at ratios as high as 3.0.

There were dramatic differences in whether this c/a criterion was met from lab to lab since they were measuring different crack lengths for a given

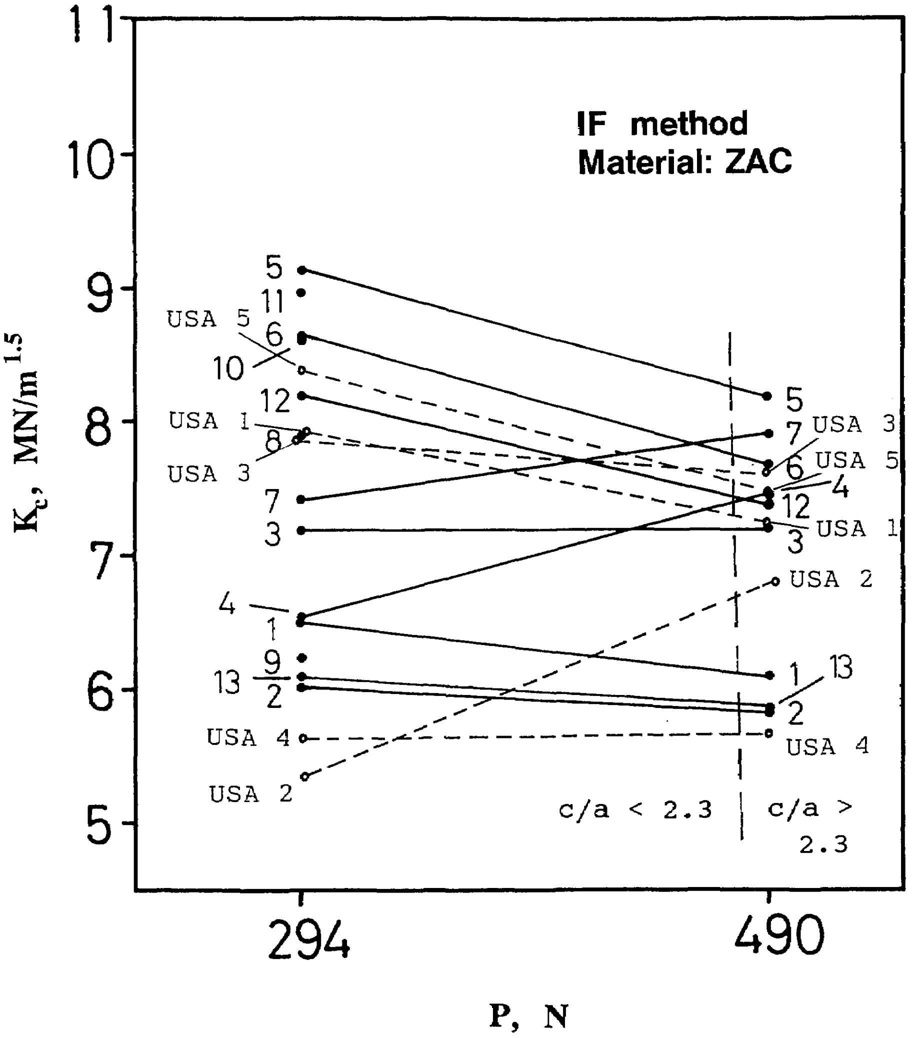

Fig. 18. Indentation fracture (IF) fracture toughness for the ZAC.

set of test conditions. Table 5 shows how the USA labs responded. The international participants also had wildly mixed results on meeting this criterion [12,13]. None of the Japanese labs (8–11) reported results at 98 N for the silicon nitride, suggesting that all their c/a ratios were <2.3.

Statistical bias problems can arise in situations such as this, depending upon the sampling procedures. The average value can be quite different if (a), of the 10 indentations, only those that meet the criterion are accepted, as opposed to (b), indentations are repeatedly made *until* 10 acceptable patterns are made. (For example, consider representativeness of taking the average of 10 valid indentations if, in fact, 300 indentations had to be made overall.) USA lab 5 reported that there was a pronounced dependence of fracture toughness on the c/a ratio as shown in Fig. 19. This was the case for both materials and at all indentation loads. Taking only those values for which $c/a > 2.3$ leads to using only the lower values of fracture toughness, leading to a clear bias.

Table 5. Indentation fracture sampling. Fraction of indentations that met the $c/a > 2.3$ criterion

	Material			
	ZAC		Silicon nitride	
USA lab	294 N	490 N	98 N	196 N
1	0/10	7/10	7/10	10/10
2	20/20	18/20	29/32	29/29
3	5/10	3/10	6/10	10/10
4	10/10	10/10	10/10	10/10
5	0/20	10/20	8/20	14/18

There are several complications to the IF method including environmentally assisted crack growth, the decelerating nature of the crack, and R-curve influences. Environmentally assisted crack growth, which can occur in response to the residual stress, tends to make the cracks longer than they would otherwise be. This would lead to underestimates of the fracture toughness. As discussed above in the SEPB results, there seems to be negligible environmental effects for the silicon nitride. Environmentally assisted slow crack growth may be active in the ZAC, but it was difficult to distinguish the rate effects from the R-curve phenomenon. USA lab 5 reported that ten specimens of each material were indented with a drop of oil over the indent but *no difference* in crack lengths was noted.

The conventional interpretation is that the IF median cracks form during the unloading sequence [7], but some instances of formation during the loading have also been reported [45]. In either instance, the crack opens up from, and extends away from the indentation impression until it arrests. Polycrystalline materials have the potential for the microstructure to interfere with the decelerating IF crack, whereas in most fracture mechanics test methods the cracks are accelerating at critical load.

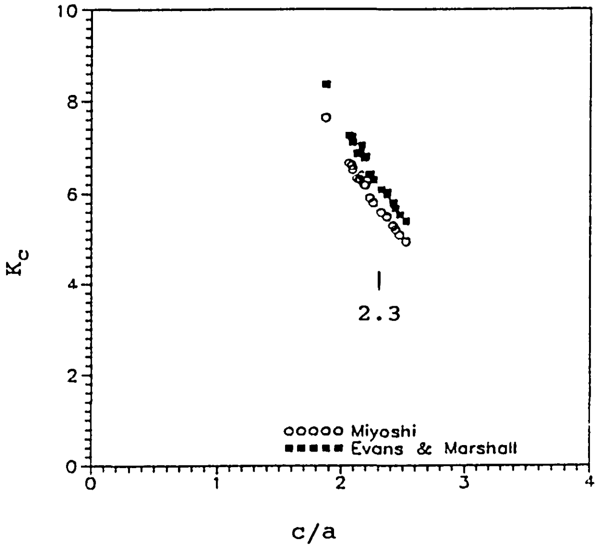

Fig. 19. The (IF) fracture toughness varied strongly with the *c/a* ratio for the silicon nitride indented at 98 N. Data and figure from USA lab 5.

This difference may tend to make the IF cracks shorter than they otherwise would be (if the microstructure were amorphous or very fine and homogeneous) and overestimates of fracture toughness may result from IF testing.

In conclusion, the IF results were disappointing primarily because of the high scatter and failure to obtain consistent interlaboratory results. The strong dependence of the computed fracture toughness upon the crack length ($c^{-1.5}$), and the difficulty in measuring such, combined to cause high scatter. Refinements to the measurement technique in principle could improve the accuracy of this method.

5. Summary

Table 6 summarizes the apparent fracture toughness values for the different methods. These numbers are estimates based upon the "average" values from the figures presented previously with emphasis on the most reasonable test conditions. The concurrence of values at about 5.5 MN/$m^{1.5}$ for the silicon nitride is encouraging. It is plausible that this material has a constant fracture toughness (flat R-curve) and a negligible loading rate dependence. The variability in the estimates for the ZAC probably reflects R-curve and environmentally assisted crack growth phenomena. The different test methods may be giving fracture toughness values corresponding to different points on the R-curve.

Table 6. Summary of fracture toughness values (MN/$m^{1.5}$)

Method	Silicon nitride	ZAC
IS (low load)	**5.7**[a]	6.7[b]
(high load)	6.3[b]	7.4[b]
SEPB	**5.6**[a]	5.4 (slow rate) 6.1 (fast rate)
IF	**5.4**[a] (very high scatter)	?

[a] Denotes the most probable value for K_{Ic} for silicon nitride.
[b] No correction for stress gradient.

The scatter in IF results for the silicon nitride shows that any one lab could stray typically as much as 0.5 MN/$m^{1.5}$ off the mainstream results, although in some instances there was even more deviation. The scatter in IF results for the ZAC, both within a lab and between labs, was so high as to render the results highly suspect. The effects of R-curve phenomena upon the IF test method values are uncertain.

The IS method had lower scatter and very plausible results for the silicon nitride, making this a very attractive, simple laboratory test for estimating fracture toughness. The ZAC results also had a relatively low scatter, about equal to that obtained by SEPB. Once again, the R-curve and environmentally assisted crack growth phenomena had an uncertain effect upon the ZAC results. Either low indentation loads (for small crack sizes) or large specimen cross-sections are recommended for IS testing to minimize the stress gradient problem. Four-point loading may be preferable for small specimens.

The generally consistent results obtained on the SEPB method for the silicon nitride are also encouraging. Some questions, both in testing procedure and in interpretation, were again raised about using this method for the ZAC in the context of R-curve behavior. Careful attention needs to be placed on specifying exactly which "precrack" length should be measured in such instances. Testing in four-point loading would simplify the SEPB procedure.

Table 7. Participants utilization of the fracture toughness methods

Laboratory	VAMAS round-robin tests IS	IF	SEPB	Other tests
NASA-Lewis	[a]	[d]	[a]	[a]CN (Chevron Notch)
Norton	[a]	[b]	[b]	
Allied Signal (Garrett)	[d]	[d]	[d]	[a]CN (Chevron Notch)
Worcester Polytechnic	[b]	[b]	[a]	
NIST	[a]	[a]	[c]	[b]DCB (Double Cantilever Beam) [b]AM-DCB (Applied Moment DCB)

[a] Test method already in routine usage, and is preferred.
[b] Test method already in routine usage.
[c] Test method will be used.
[d] Test method not ordinarily used.

6. Conclusions

Table 7 summarizes the fracture toughness test methods that are normally used by the participating USA labs. The indentation fracture (IF) method is not commonly used and several laboratories complained that interpretation of the method is "ambiguous." All agreed that it is difficult to accurately and precisely measure the cracks, that there is significant variability between observers. Four of the five labs felt the method was not reliable. The method is not suitable for elevated-temperature testing. The high scatter in the results of the present round-robin indicate that, at the least, better procedures for measuring the cracks are necessary. The participants for the most part felt that the method may be adequate in the laboratory as a research tool, but is not suitable as a standard for general engineering purposes. These findings are consistent with those of Binner and Stevens in their review paper on this method [46].

The same distrust about the indentation cracks seems to be held by three of the five labs towards the indentation strength (IS) method. This method is widely cited in the ceramics literature, and is felt to provide a good estimate of fracture toughness despite a concern with its empirical roots and "calibration" constants. The method is not applicable to high-temperature testing. The experimental ease of the method (indent and break, without the need to measure cracks) and the fairly consistent results obtained in this round-robin may encourage the broader use of this method as a simple, fast means of estimating fracture toughness for quality control or comparison purposes.

There was a generally favorable reaction to the SEPB method. Three of the labs routinely use it despite its recent development. One other lab reported that it will be adopted for routine work. Most participants felt that fracture toughness values obtained were technically rigorous for a flat R-curve material in the absence of environmental effects. The extra work entailed in precracking was felt to be worthwhile in terms of the quality of the result. Several labs reported problems with SEPB elevated-temperature testing since precracks are prone to heal.

In overall summary, the round-robin was felt to be a success. Reasonably consistent results were obtained for the IS and SEPB methods between most laboratories for two different materials. Several areas were identified where refinements could be made and there now is greater confidence by the U.S. participants in these two methods. Participants either successfully tried the IS or SEPB methods for the first time, or refined their usual procedures. The IF method was less successful in this round-robin.

A single value of fracture toughness for the silicon nitride seems to be appropriate. No R-curve or environmentally assisted crack growth phenomena were detected. Several questions of interpretation of fracture toughness were raised for the case of the ZAC, which exhibited R-curve and environmentally assisted crack growth. There is no simple interpretation of fracture toughness for this material.

A direct result of this round-robin is that the IS and SEPB methods are now under consideration in ASTM Committees C-28, Advanced Ceramics and E-24, Fracture Testing as candidates for standard test methods for advanced ceramics.

7. Appendix A. Scatter in Results

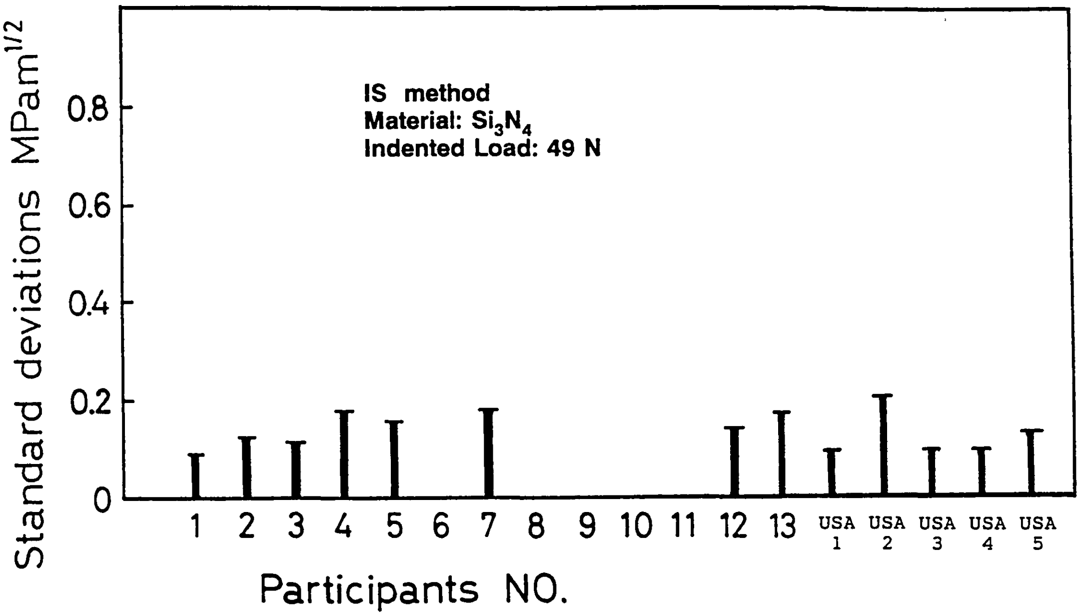

Fig. A1. Standard deviations of the indentation strength results (IS) for the silicon nitride at 49 N.

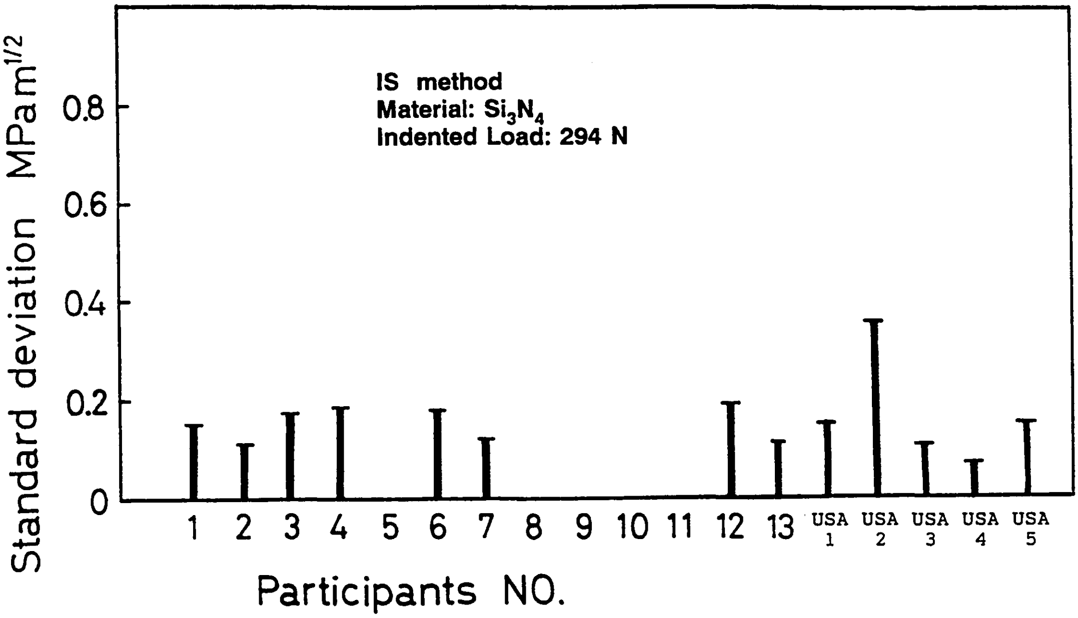

Fig. A2. Standard deviations of the IS results for the silicon nitride at 294 N.

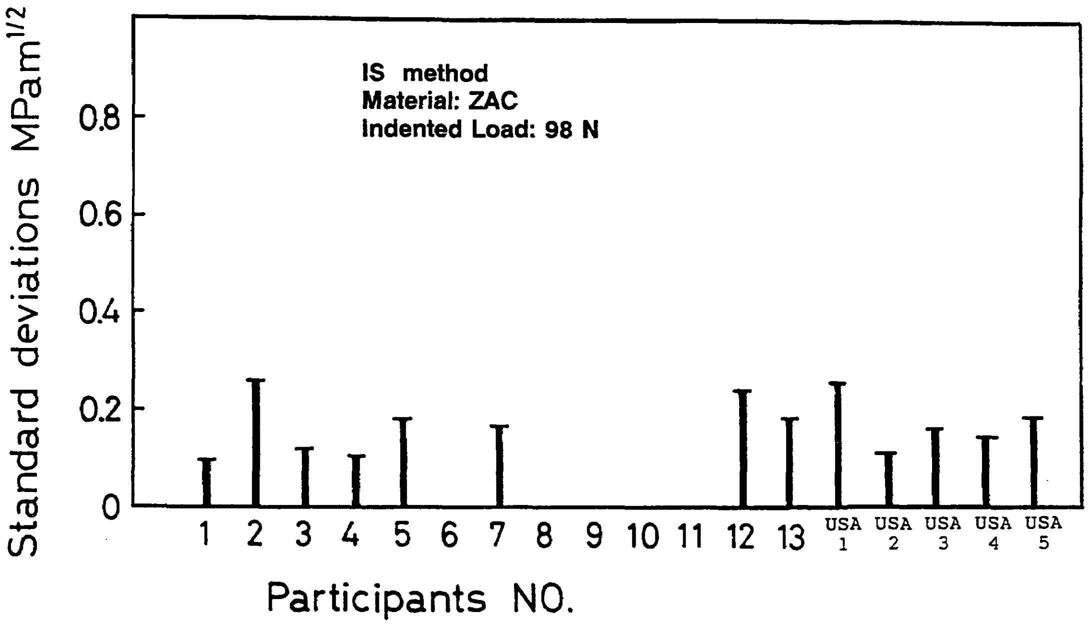

Fig. A3. Standard deviations of the IS results for the ZAC at 98 N.

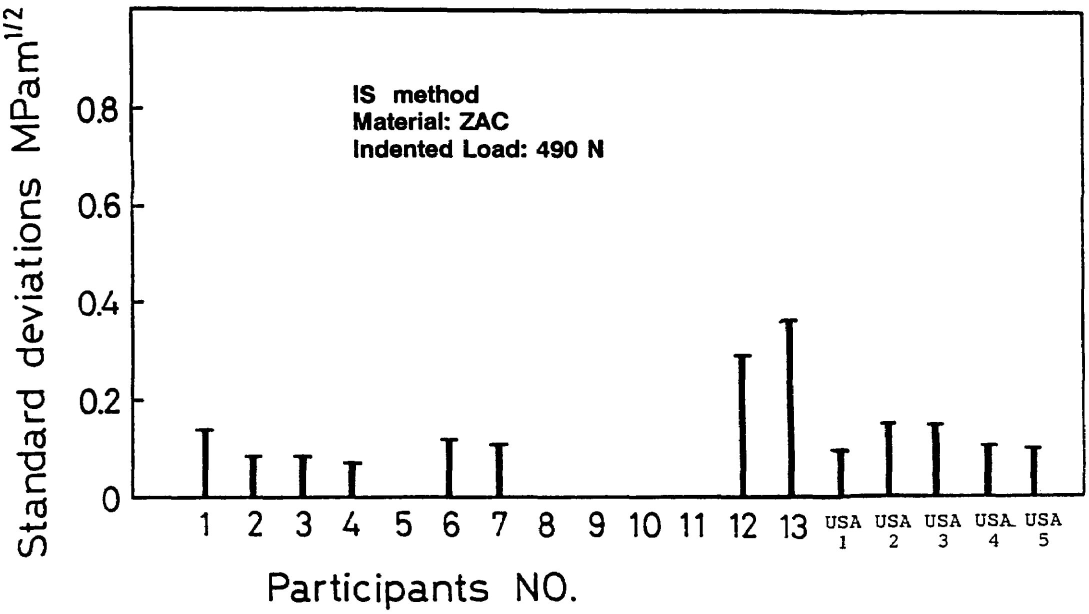

Fig. A4. Standard deviations of the IS results for the ZAC at 490 N.

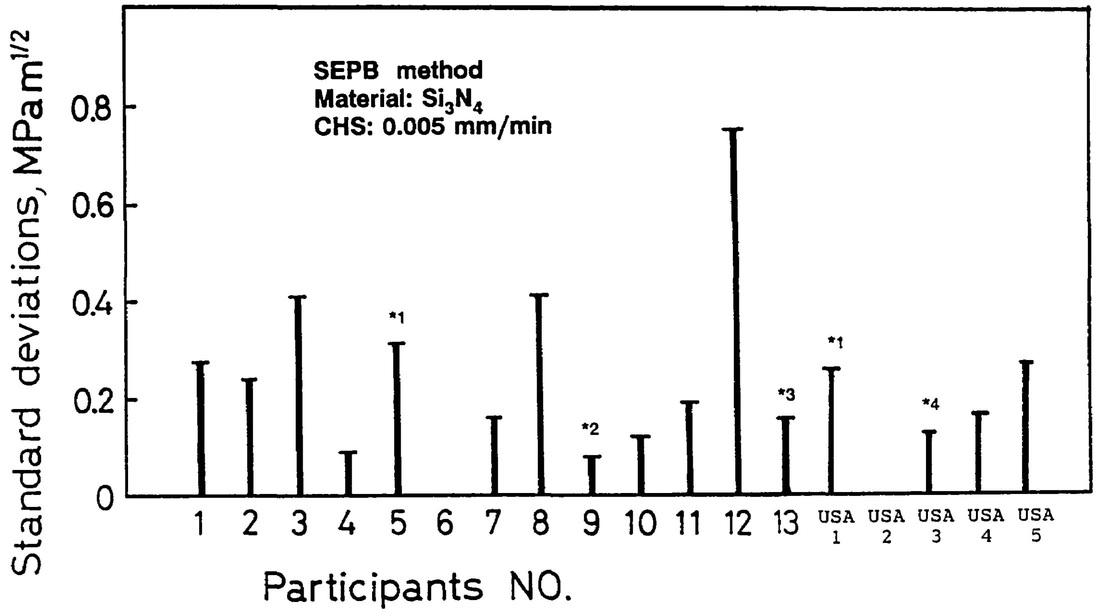

Fig. A5. Standard deviations for the SEPB results for the silicon nitride at the slow loading rates.
*1. Crosshead speed = 0.01 mm/min.
*2. Crosshead speed = 0.08 mm/min.
*3. Crosshead speed = 0.05 mm/min and eight specimens only.
*4. Crosshead speed = 0.0025 mm/min.

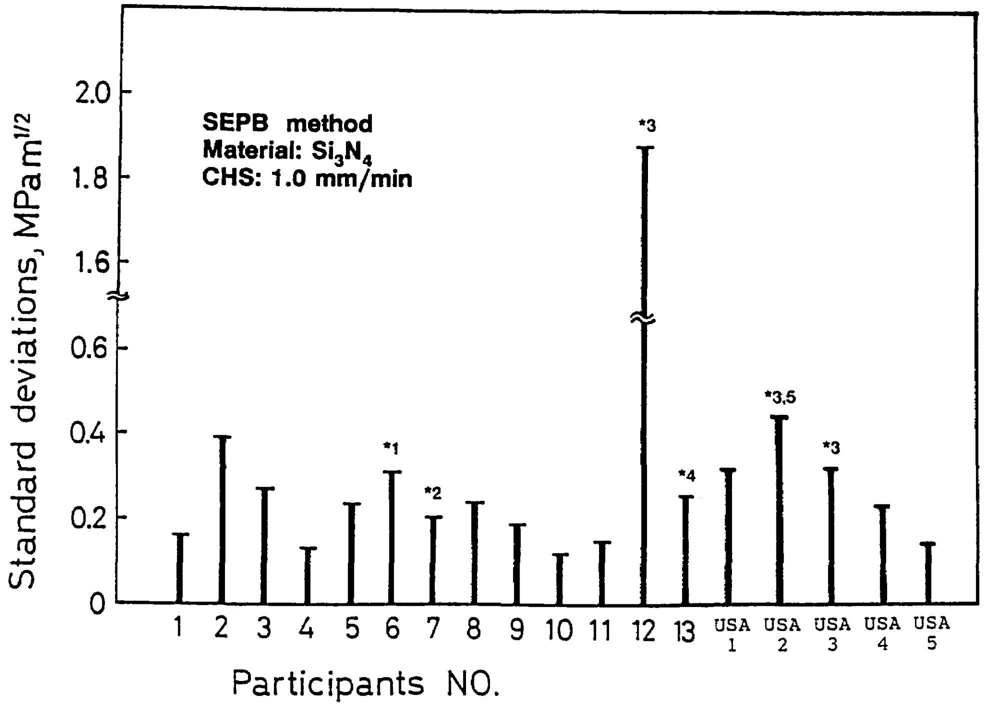

Fig. A6. Standard deviations for the SEPB results for the silicon nitride at the fast loading rates.
*1. Span = 15 mm.
*2. Crosshead speed = 0.1 mm/min.
*3. Crosshead speed = 0.5 mm/min.
*4. Seven specimens only.
*5. 18 specimens.

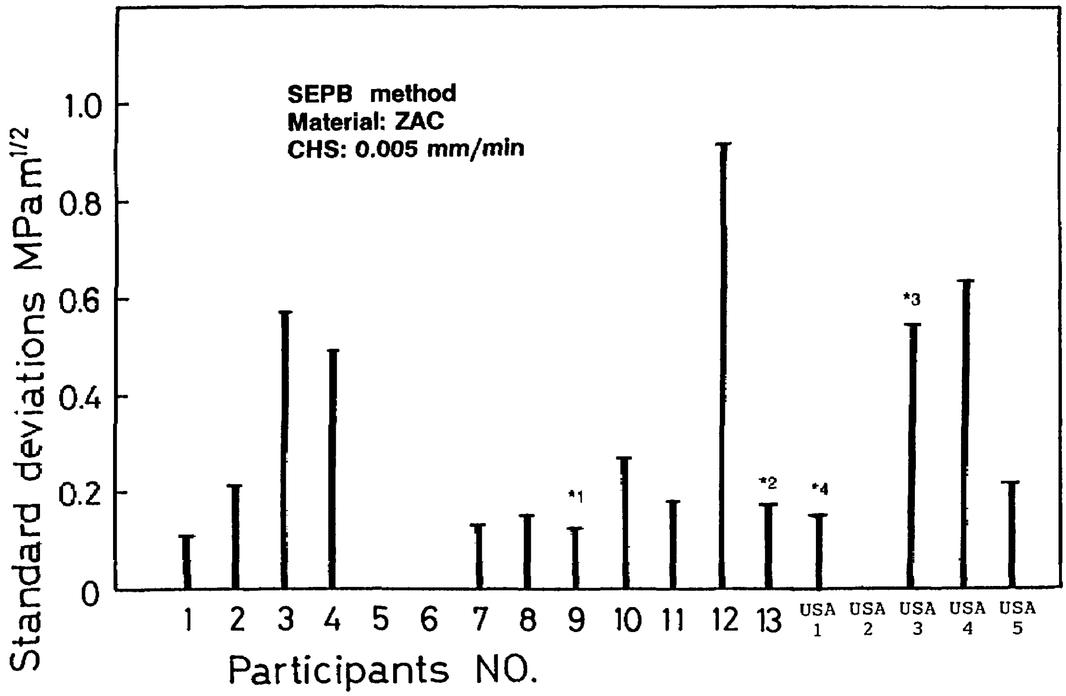

Fig. A7. Standard deviations for the SEPB results for the ZAC at slow loading rates.
*1. Crosshead speed = 0.08 mm/min.
*2. Crosshead speed = 0.05 mm/min and seven specimens only.
*3. Crosshead speed = 0.0025 mm/min.
*4. Crosshead speed = 0.001 mm/min.

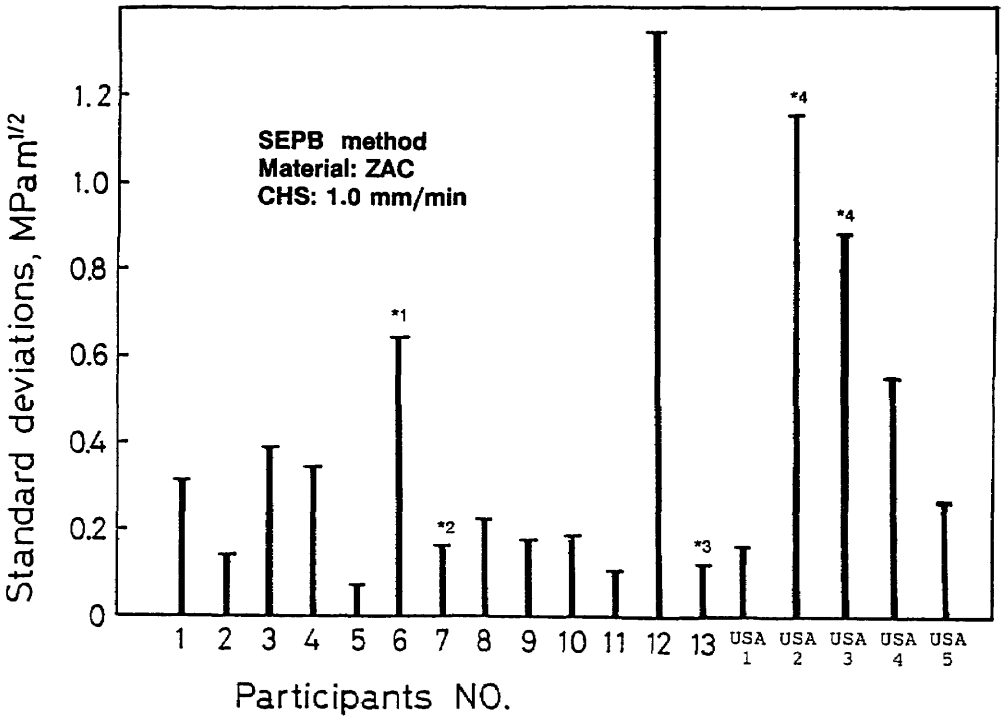

Fig. A8. Standard deviations for the SEPB results for the ZAC at fast loading rates.
*1. Span = 15 mm.
*2. Crosshead speed = 0.1 mm/min.
*3. Seven specimens only.
*4. Crosshead speed 0.5 mm/min.

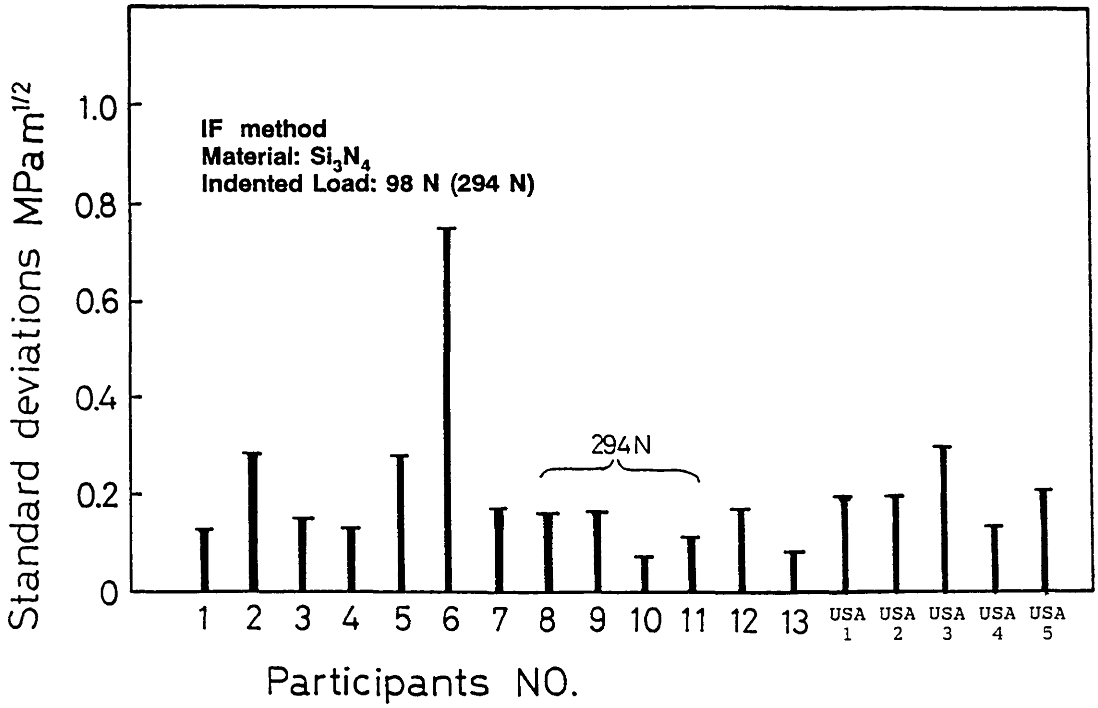

Fig. A9. Standard deviations for the indentation fracture (IF) results for the silicon nitride at 98 or 294 N loads.

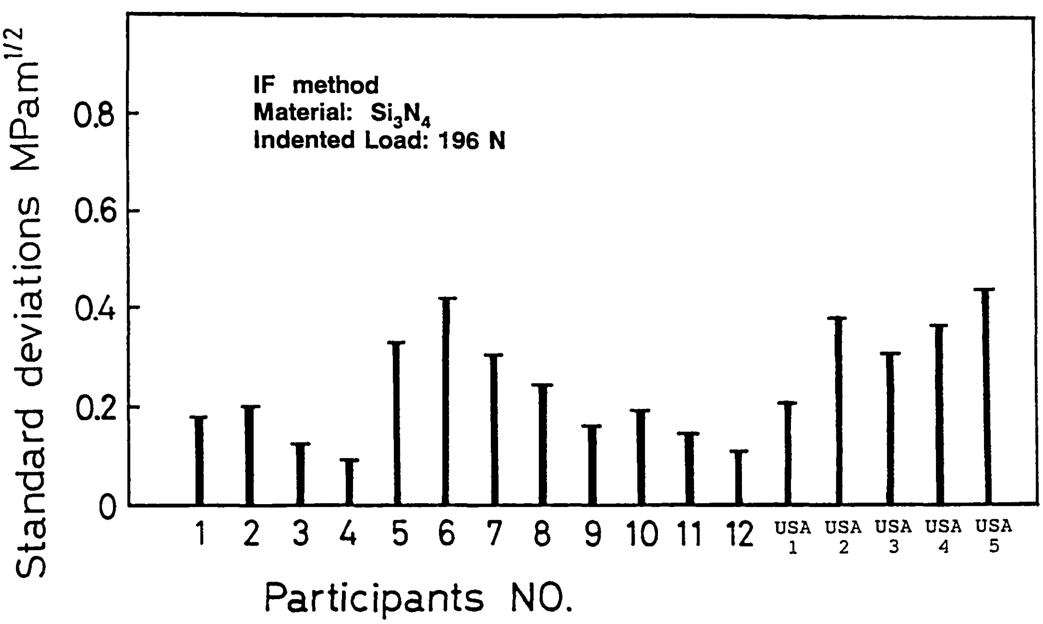

Fig. A10. Standard deviations for the IF results for the silicon nitride at 196 N.

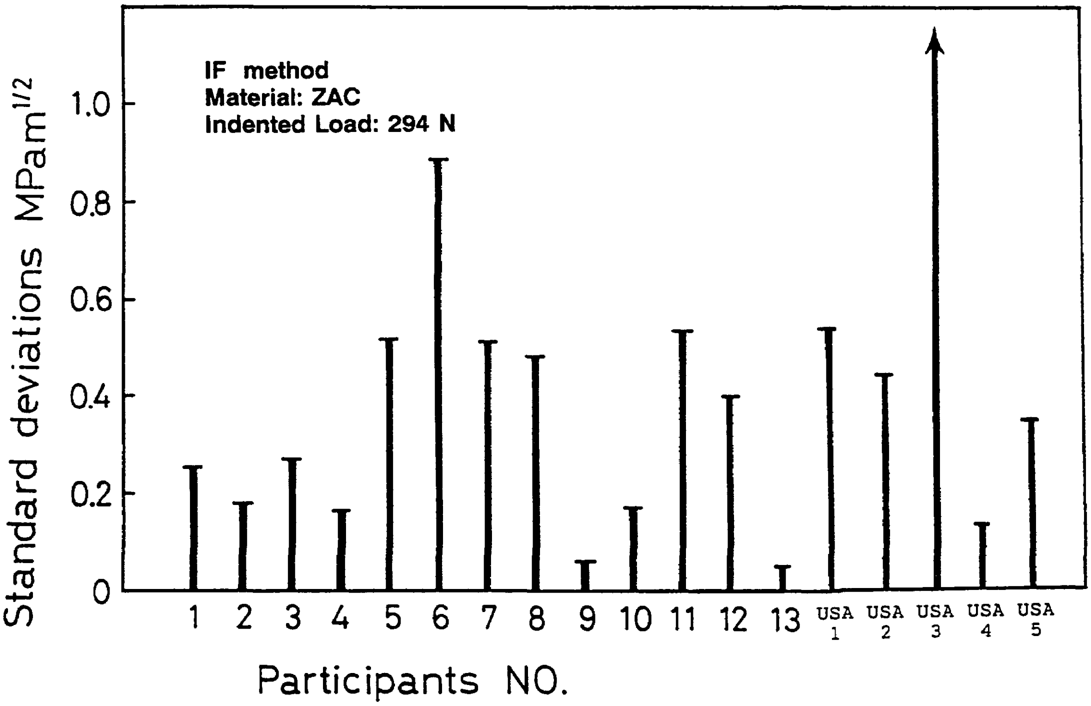

Fig. A11. Standard deviations for the IF results for the ZAC at 294 N.

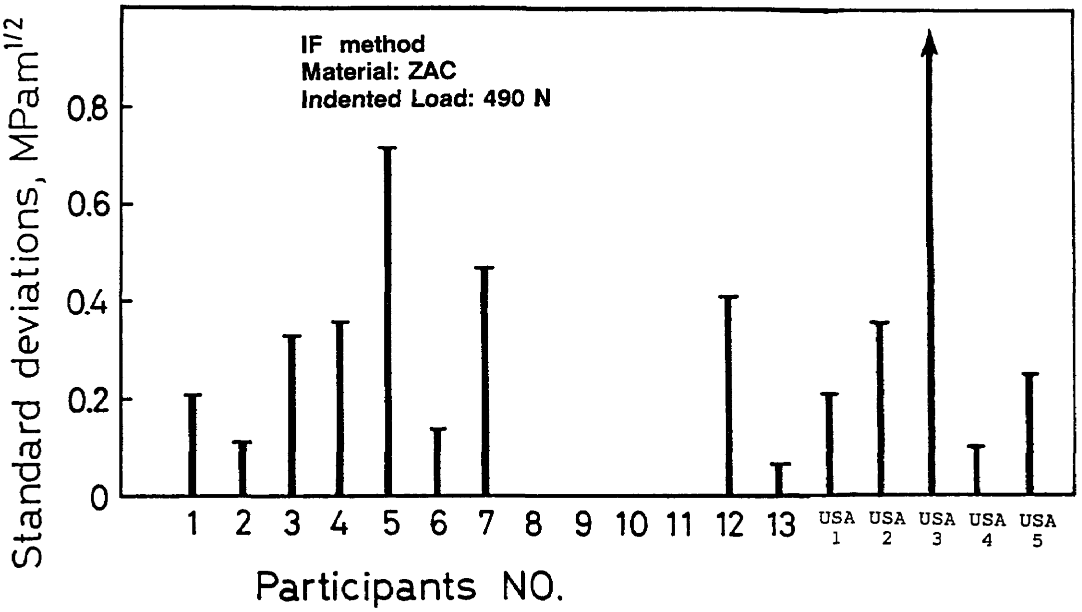

Fig. A12. Standard deviations for the IF results for the ZAC at 490 N.

Acknowledgments

The authors wish to thank the Japan Fine Ceramic Center for furnishing the materials at no cost to the U.S. participants and for their assistance in setting up and coordinating this exercise. Special thanks go to Drs. Hiroshi Okuda, Hideo Awaji, and Mineo Mizuno.

The authors also thank Dr. Edwin Fuller, Jr. of NIST for initially organizing the U.S. participation, for reviewing the manuscript, and for helping with technical discussions.

At NIST, Dr. A. Shapiro helped with the optical microscopy system, Mr. James Evans assisted with the mechanical testing, Dr. James Cline furnished the x-ray diffraction data, and Dr. L. Braun contributed several consultations.

Partial support for this program was provided by the Ceramic Technology Project, U.S. Department of Energy, Office of Transportation Technologies, under contract DE-AC05-84OR21400 with Martin-Marietta Energy Systems, Inc.

8. References

[1] JIS R 1607 (1990), Testing Methods for Fracture Toughness of High Performance Ceramics, Japanese Industrial Standard, Japanese Standards Association, Tokyo.

[2] A. G. Evans and E. A. Charles, Fracture Toughness Determination by Indentation, J. Am. Ceram. Soc. **59** (7–8), 371–372 (1978).

[3] C. B. Ponton and R. D. Rawlings, Dependence of the Vickers Indentation Fracture Toughness on the Surface Crack Length, Br. Ceram. Trans. J. **88**, 83–90 (1989).

[4] R. Matsumoto, Evaluation of Fracture Toughness Determination Methods as Applied to Ceria-Stabilized Tetragonal Zirconia Polycrystal, J. Am. Ceram. Soc. **70** (12), C366–C368 (1987).

[5] Z. Li, A. Ghosh, A. Kobayashi, and R. Bradt, Indentation Fracture Toughness of Sintered Silicon Carbide in the Palmqvist Crack Regime, J. Am. Ceram. Soc. **72** (6), 904–911 (1989).

[6] Research Report on the Standardization of Fine Ceramics, Japan Fine Ceramic Association, Tokyo, March 1985.

[7] P. Chantikul, G. R. Anstis, B. R. Lawn, and D. B. Marshall, A Critical Evaluation of Indentation Techniques for Measuring Fracture Toughness: II, Strength Method, J. Am. Ceram. Soc. **64** (9), 539–543 (1981).

[8] T. Fujii and T. Nose, Evaluation of Fracture Toughness for Ceramic Materials, IJIS Int. **29** (9), 717–725 (1989).

[9] T. Nose and T. Fujii, Evaluation of Fracture Toughness for Ceramic Materials by a Single-Edge-Precracked-Beam Method, J. Am. Ceram. Soc. **71** (5), 328–333 (1988).

[10] J. E. Srawley, Wide Range Stress Intensity Factor Expressions for ASTM E 399 Standard Fracture Toughness Specimens, Int. J. Fract. **12**, 475–476 (1976).

[11] ASTM E-399, Standard Test Method for Plane-Strain Fracture Toughness of Metallic Materials, Annual Book of ASTM Standards, Vol. 03.01., ASTM, Philadelphia, PA (1991).

[12] H. Awaji, J. Kon, and H. Okuda, The VAMAS Fracture Toughness Test Round-Robin on Ceramics, VAMAS Report #9, Japan Fine Ceramics Center, Nagoya, Japan, Dec. 1990.

[13] H. Awaji, T. Yamada, and H. Okuda, Results of the Fracture Toughness Test Round-robin on Ceramics, J. Jap. Cer. Soc. **99** (5), 417–422 (1991).

[14] H. Awaji, T. Yamada, H. Okuda, H. Tanaka, S. Nagai, F. Wakai, and S. Sakaguchi, Results of the Fracture Toughness Round-robin on Ceramics in Proceedings of the International Symposium on Pre-standards Research for Advanced Materials, Tokyo, Japan, Dec. 1991.

[15] Y. Akimune, Y. Katano, and K. Matoba, Spherical-Impact Damage and Strength Degradation in Silicon Nitrides for Automobile Turbocharger Rotors, J. Am. Ceram. Soc. **72** (8), 1422–1428 (1989).

[16] Y. Akimune, Y. Katano, and K. Matoba, Correction to Spherical-Impact Damage and Strength Degradation in Silicon Nitrides for Automobile Turbocharger Rotors, J. Am. Ceram. Soc. **72** (11), 2172 (1989).

[17] Ceramic Technology for Tomorrow's Heat Engines, Ceram. Ind., March 1989, pp. 41–43.

[18] NTK Technical Information Data Sheet, OC-2061-8603.

[19] S. W. Freiman, Environmentally Enhanced Fracture of Ceramics, Mat. Res. Soc. Symp. Proc. **125**, 208–215 (1988).

[20] P. Becher, Slow Crack Growth Behavior in Transformation-Toughened Al_2O_3-$ZrO_2(Y_2O_3)$ Ceramics, J. Am. Ceram. Soc. **66** (7), 485–487 (1983).

[21] M. L. Mecartney, Influence of an Amorphous Second Phase on the Properties of Yttria-Stabilized Tetragonal Zirconia Polycrystals (Y-TZP), J. Am. Ceram. Soc **70** (1), 54–58 (1987).

[22] E. K. Beauchamp and S. L. Monroe, Effect of Crack-Interface Bridging on Subcritical Crack Growth in Ferrites, J. Am. Ceram. Soc. **72** (7), 1179–1184 (1989).

[23] T. Fett and D. Munz, Subcritical Crack Growth of Macro- and Microcracks in Ceramics, to be published in the proceedings of the conference, Fracture Mechanics of Ceramics, Nagoya, Japan, 1991.

[24] J. Wang and R. Stevens, Review: Zirconia-Toughened Alumina (ZTA) Ceramics, J. Mat. Sci. **24**, 3421–3440 (1989).

[25] S. J. Bennison and B. R. Lawn, Flaw Tolerance in Ceramics with Rising Crack Resistance Characteristics, J. Mat. Sci. **24**, 3169–3175 (1989).

[26] R. F. Krause, Jr., Rising Fracture Toughness form the Bending Strength of Indented Alumina Beams, J. Am. Ceram. Soc. **71** (5), 338–344 (1988).

[27] N. Ramachandran and D. Shetty, Rising Crack-Growth-Resistance (*R*-Curve) Behavior of Toughened Alumina and Silicon Nitride, J. Am. Ceram. Soc. **74** (10), 2634–2641 (1991).

[28] R. Anderson and L. Braun, Technique for the *R*-curve Determination of Y-TZP Using Indentation Produced Flaws, J. Am. Ceram. Soc. **73** (10), 3059–3062 (1990).

[29] E. Fuller, Jr., private communication.

[30] Testing Method for Flexural Strength (Modulus of Rupture) of High Performance Ceramics, Japanese Industrial Standard, JIS R 1601 (1981), Japanese Standards Association, Tokyo.

[31] T. Miyoshi, N. Sagawa, and T. Sassa, Trans. Jap. Soc. Mech. Eng. **51A**, 2489 (1989).

[32] D. B. Marshall and A. G. Evans, Reply to Comment on Elastic/Plastic Indentation Damage in Ceramics: The Median/Radial Crack System, J. Am. Ceram. Soc. **64** (12), C-182–183 (1981).

[33] J. C. Newman and I. S. Raju, An Empirical Stress Intensity Factor Equation for the Surface Crack, Eng. Fract. Mech. **15** (1–2), 185–192 (1981).

[34] Y. Murikami, Stress Intensity Factor Handbook, Vol. 1 and 2, Pergamon Press, NY (1987).

[35] J. Dusza, Comparison of Fracture Toughness Testing Methods Applied to Si_3N_4 and Si_3N_4-Whisker System, submitted to Scripta Met. and Mat., 1991.

[36] A. M. El Aslabi, G. Kleist, R. Steinbrech, and H. Nickel, Fortschritt der Deutsch. Ker. Ges. **6**, 133 (1991).

[37] J. Salem, J. Shannon, Jr., M. Jenkins, and M. Ferber, Effects of Precracking Methods on the Fracture Properties of Alumina, in Proc. of the Society of Experimental Mechanics Conference, Milwaukee, Wisc. (1990).

[38] F. I. Baratta and W. A. Dunlay, Crack Stability in Simply Supported Four-point and Three-point Loaded Beams of Brittle Materials, Mec. Mater. **10**, 149–159 (1990).

[39] M. Sakai and M. Inagaki, Dimensionless Load-Displacement Relation and Its Application to Crack Propagation Problems, J. Am. Ceram. Soc. **72** (3), 388–394 (1989).

[40] R. Warren and B. Johannesson, Creation of Stable Cracks in Hardmetals Using 'Bridge' Indentation, Powder Met. **27** (1), 25–29 (1984).

[41] T. Nishida, T. Shiono, and T. Nishikawa, On the Fracture Toughness of Polycrystalline Alumina Measured by SEPB Method, J. Eur. Ceram. Soc. **5**, 379–383 (1989).

[42] T. R. Lai, C. L. Hogg, and M. V. Swain, Comparison of Fracture Toughness Determination of Y-TZP Materials Using Various Testing Techniques, in Ceramic Developments, eds. C. Sorrell and B. Ben-Nissan, Materials Science Forum, Vols. 34–36, Trans Tech Publ., Switzerland (1988) pp. 1071–1075.

[43] T. Fett, G. Martin, and D. Munz, V-K Curves for Borosilicate Glass Obtained from Static Bending Tests with Cracks Introduced by the Bridge Method, J. Mat. Sci. Let. **10**, 220–222 (1991).

[44] S. L. Jones, C. J. Norman, and R. Shahani, Crack-Profile Shapes Formed Under a Vickers Indent Pyramid, J. Mat. Sci. Let. **6**, 721–723 (1987).

[45] R. F. Cook and G. M. Pharr, Direct Observation and Analysis of Indentation Cracking in Glasses and Ceramics, J. Am. Ceram. Soc. **73** (4), 787–817 (1990).

[46] J. G. P. Binner and R. Stevens, The Measurement of Toughness by Indentation, Br. Ceram. Soc. Trans. and Journal **83** (6), 168–172 (1984).

About the authors: *George Quinn is a research ceramic engineer in the Ceramics Division of NIST. Jonathan Salem is a materials research engineer in the Structural Integrity Branch at NASA-Lewis Research Center, Clevelend, Ohio. Isa Bar-on and Kyu Cho are associate professor and research engineer, respectively, in the Department of Mechanical Engineering at Worcester Polytechnic Institute, Worcester, Massachusetts. Michael Foley is the Supervisor of the Mechanical Properties Testing Laboratory at St. Gobain, Norton Industrial Ceramics Corp. in Northboro, Massachusetts. Ho Fang is a materials engineer in the Garrett Auxiliary Power Division of Allied-Signal Company, Phoenix, Arizona. The National Institute of Standards and Technology is an agency of the Technology Administration, U.S. Department of Commerce.*

[J. Res. Natl. Inst. Stand. Technol. 97, 609 (1992)]

Errata

Erratum: Optical Calibration of a Submicrometer Magnification Standard

**Jon Geist, Barbara Belzer,
Mary Lou Miller, and
Peter Roitman**

National Institute of Standards
and Technology,
Gaithersburg, MD 20899

[J. Res. Natl. Inst. Stand. Technol. Volume 97, Number 2, March-April 1992, p. 267]

The figures over figure captions 1 and 3 should be interchanged.

Volume 97, Number 5, September–October 1992
Journal of Research of the National Institute of Standards and Technology

Conference Report

DATA ADMINISTRATION MANAGEMENT ASSOCIATION SYMPOSIUM Gaithersburg, MD May 12-13, 1992

Report prepared by

Judith Newton

Information Systems Engineering,
Computer Systems Laboratory,
National Institute of Standards and Technology,
Gaithersburg, MD 20899

1. Introduction

Along with capital and human resources, an organization's data represents one of its fundamental assets. Data administration (DA) attempts the effective planning, organization, and management of an enterprise's data resource, with the intention of empowering the organization to achieve its mission and goals. Very often, however, this endeavor is received with skepticism and limited support by those who could most benefit from data administration practices and products.

The Data Administration Management Association (DAMA) is the professional organization for data administrators. An international board oversees a loose federation of local chapters in the United States, Canada, and Australia. The National Capital Region Chapter (NCR DAMA) has monthly meetings from September through April, as well as a Symposium in May.

NCR DAMA held its fifth annual Symposium at NIST on May 12-13, 1992. The theme this year was *Data Administration—A Value Added Service*. Attended by 275 Federal and private industry data administrators, the Symposium was cosponsored by NIST and NCR DAMA.

It emphasized the practices, technologies, activities, initiatives and ideas that deliver clearly visible value to the users, or "customers" of data administration. In addition to presentations by nationally recognized experts and practitioners, it included workshops, panel discussions, and a tutorial. Topics ranged from the keynote speech on the politics of successful data sharing to the latest implementation of the Information Resource Dictionary System (IRDS) standard.

2. Speakers

The keynote speaker was Barbara von Halle, a principal at Spectrum Technology Group, Inc. She described how enterprise-wide data sharing can be a vision and eventually a reality. Because it is a significant cultural change, it can happen in an orderly manner, chaotically, or not at all. She presented practical tips and techniques that have been successful in various organizations, with insight into reasons for failures. There is a delicate balance of short term and long term deliverables and realistic expectations.

Charles Bachman of Bachman Information Systems, Inc. described the IBM AD/Cycle Enterprise Model as "the foundation of the most important technical advance in application development since the advent of COBOL." The key challenges it must meet are: first, it must be acceptable to the data processing community as the next step in the definition of application systems. Second, it must serve as the semantic target for reverse engineering existing applications. Third, it must be understandable by knowledgeable functional managers. Fourth, it must represent a complete and executable functional specification, subject to logic level debugging. Finally, it must serve as the basis for forward engineering the business requirements to a number of diverse information technology platforms.

Sooner or later, claims Cynthia L. Walker of Software Solutions, Inc., all data administrators are faced with the challenge of justifying their existence by demonstrating true return on investment (ROI). Their challenge is to attempt not only to prove that their organization is performing better and saving time and money as a result of data administration, but also to identify just how much better performance is and exactly how much time and money the organization is saving. The solution has five points of attack: be creative; emphasize tangible, measurable benefits; select an ROI approach that matches your organization's development stage; avoid initiation stage "quicksand"; and reduce investment (costs).

Andrea Tyndall Norris presented an overview of information architecture activities at NASA, where she is data administrator for the Automated Information Management (AIM) program.

The business view of data management was discussed by Dan Appleton of D. Appleton Co., Inc. During the past 20 years, business management has been steadily reengineering business into more adaptive structures. Adaptive organizations cannot be effective without order of magnitude increases in information quality. The key to achieving these increases lies with data management, particularly with its ability to effectively develop, manage, and employ business rules.

Anthony J. Winkler of ASYSA, Inc. asserted that data administration is a function that exists in many different enterprises, but remains ill-defined as to purpose. It has a critical role in supporting the cost-effective acquisition and operation of information systems, but its role is not always well understood. A model for developing a data administration activity must be driven by a stated set of objectives, engineering the activity to achieve its proper role.

"Winning friends and influencing people" through data administration was the topic of Cathy Hirsh's presentation. The AMS principal explored how DA programs have been successful in the past and what organizations can do to ensure they remain so in the future. Historically, these have involved three approaches: the "control," the "you better not.." and the "try it, you'll like it" approach. Four of the challenges in today's environment are: the need for more integrated data; the need for using new systems and technology without discarding the old; poor quality data; and faster and better quality development of information technology capabilities.

3. Tutorial

Sandra K. Perez of Concept Technology, Inc., presented a tutorial session on "Adding Value with Conceptual Modeling." She described the method of conceptual modeling, compared and contrasted its expressiveness with different modeling paradigms, and demonstrated its use. These techniques and methods can add value to data administration and effect a positive flow for the effective management of enterprise information resources.

4. Panels

The following panel discussions were presented:

- "CASE Studies," Margaret H. Law, NIST, moderator;
- "Federal Experiences in Data Adminstration," Bruce K. Rosen, NIST, moderator;
- "DA and the System Life Cycle or DA Versus the System Life Cycle," Dennis Berg, AMS, moderator;
- "Data Administration Practitioners," Joseph H. Oates, Life Cycle Technologies, moderator;
- "IRDS Implementation," Alan Goldfine, NIST, moderator.

5. Standards and Procedures Workshops

The Working Group on Standards and Procedures has been meeting monthly during the past year. It has produced a draft Model Data Administration Standards Manual, which was distributed for comment. When finalized, the document will be circulated as a guide to the administration of information standards and include procedures for standards implementation. The group plans to resume monthly meetings in the fall.

Four workshops at the Symposium presented aspects of the working group's results.

- Data Standardization, Dan Wahl, Vector Research, Inc., and Judith Newton, NIST, moderators;
- Automated Tools, Joan Sziede, U. S. Geological Survey, moderator;
- Data Administration and Security, David Stowell, Stowell Associates, moderator;
- Repository Management, Bill Brimberry, National Park Service, moderator.

6. Proceedings

The proceedings of this Symposium were distributed at the event. The Proceedings of the First,[1] Second,[2] and Fourth[3] Annual DAMA Symposia were published by NIST and copies are still available. The Sixth Annual Symposium will be held at NIST May 11-12, 1993.

---

[1] Judith J. Newton and Frankie E. Spielman, eds., Data Administration: Management and Practice, Proceedings of the First DAMA Symposium, NIST Special Publication 500-159, National Institute of Standards and Technology, Gaithersburg, MD, October, 1988.

[2] Judith J. Newton and Frankie E. Spielman, eds., Data Administration: Standards and Techniques, Proceedings of the Second Annual DAMA Symposium, NISTIR 90-4292, National Institute of Standards and Technology, Gaithersburg, MD, April 1990.

[3] Judith J. Newton, Mary Lou Melley, and Holly Higgins, eds., Managing Data: From Vision to Reality, Proceedings of the Fourth Annual DAMA Symposium, NISTIR 4843, National Institute of Standards and Technology, Gaithersburg, MD, May 1992.

News Briefs

General Developments

Inquiries about News Briefs, where no contact person is identified, should be referred to the Managing Editor, Journal of Research, National Institute of Standards and Technology, Administration Building, A635, Gaithersburg, MD 20899; telephone: 301/975-3572.

CONSORTIUM TO DEVELOP CERAMIC MACHINING DATA

Ten manufacturers that produce or use components made from silicon nitride and silicon carbide are joining NIST in a program to develop machining data and guidelines to improve grinding processes for advanced structural ceramics. The consortium will focus on cost-effective production. Machining information will be developed in two phases. The first calls for consortium members to machine test bars using in-house procedures and then send specimens to NIST for characterization and testing. During the second phase, test bars will be ground in accordance with a detailed plan that specifies grinding wheel type, grinding fluid, wheel surface speed and other conditions. Finished specimens will be tested by NIST for surface quality and fracture strength. Fracture surfaces of selected samples will be examined for critical flaws and probable sources. Two federal research groups are co-sponsoring parts of the effort, and a university is participating in theoretical studies of the machining process. For information, contact Said Jahanmir, A329 Materials Building, NIST, Gaithersburg, MD 20899, (301) 975-3671.

INDUSTRY/NIST TO IMPROVE ADVANCED POLYMER SYSTEMS

A private company and NIST have established a cooperative program to improve the performance and manufacture of advanced systems using composite polymer materials. Researchers from the private company will work with NIST scientists to use a NIST-developed neutron reflection technique to examine the molecular level structure of polymers and how it affects adhesion with a second material (or substrate). Proper interface structure of polymers at solid interfaces controls the durability, mechanical performance, and environmental resistance of advanced polymer systems. The NIST measurement method will help producers in the automotive, aerospace, and electronics industries improve their ability to characterize protective coatings of polymers on metals, the adhesion of polymer matrices to reinforcing fibers in composites, and the bonding of polymer thin films to various components in electronic packaging. For information, contact Wen-li Wu, A209 Polymer Building, NIST, Gaithersburg, MD 20899, (301) 975-6839.

FREQUENCY CALIBRATIONS USING LORAN-C EXPLAINED

For companies needing very accurate frequency calibrations at low cost, using the U.S. Coast Guard's LORAN-C long-range navigation system may be the answer. A new paper from NIST explains the system and how it can be used for automated frequency calibrations. LORAN-C is the world's most accurate ground-based radio system, producing a frequency "good enough to meet the requirements of nearly any calibration laboratory," the paper reports. LORAN-C consists of 20 networks of stations (all broadcasting on 100 kHz) covering most of the United States, Canada, Europe, the North Atlantic, the Central and West Pacific, and the Philippines and Japan. The NIST paper discusses types of receiving equipment, how to use a certain receiver pulse as the reference frequency, creation of an automated frequency calibration system, and the expected performance from LORAN-C. For a copy of paper 34-92, contact Jo Emery, Div. 104, NIST, Boulder, CO 80303, (303) 497-3237.

TECHNOLOGY CENTERS CREATED FOR CALIFORNIA, MINNESOTA

NIST has selected Los Angeles, CA, and Minneapolis, MN, as sites for two new Manufacturing Technology Centers (MTCs). The California MTC, headquartered at El Camino College in Torrance, CA (in Greater Los Angeles), is sponsored jointly by the California Community Colleges and the California Department of Commerce. Its primary focus will be supporting the thousands of hard-pressed aerospace industry suppliers in the region. The Upper Midwest MTC will use the existing facilities of its sponsor, Minnesota Technology Inc., a public, non-profit corporation. Its main clients are expected to be from the computer, industrial machining, and metal and plastics/composites fabrication industries. The NIST MTCs are designed to help small and mid-sized manufacturers become more competitive by adopting modern technologies. NIST provides up to half of a center's funding for the first 3 years and then reduces funding for the following 3 years. MTCs must be self-supporting by the seventh year of operation.

CRADA PARTNERS TO STUDY CONCRETE FAILURE DURING FIRE

NIST and the Portland Cement Association have signed a cooperative research and development agreement (CRADA) to examine the effect fire has on concrete building partitions such as walls, ceilings and floors. In particular, the researchers are interested in predicting how long it takes for a concrete partition to fail during a fire. Current fire computer models, such as NIST's HAZARD I, focus on the fire and the effect it has on the building's environment and occupants. For example, HAZARD I can predict the temperature, smoke concentrations, and toxic gas levels in each room of a building. It also can be used to predict the behavior and movement of the building occupants, as well as their ultimate fate. However, little information is available concerning the fire behavior of building partitions, so models like HAZARD "assume" they are impenetrable and do not change during a fire. Under the CRADA, a computer model will be developed that can predict a fire's effect on concrete. The NIST researchers believe this future model, and one currently being tested for wooden walls, can be extended to other materials as well. For information, contact Walter Jones, B356 Polymer Building, NIST, Gaithersburg, MD 20899, (301) 975-6887.

HAVE YOU HEARD? NEW NOISE STANDARD DEVELOPED

NIST has created a new portable standard to evaluate the accuracy of phase modulation (PM) and amplitude modulation (AM) noise measurement equipment at 5, 10 and 100 MHz, as well as the noise floor (minimum level of noise) for such devices. The new standard should benefit both companies that make equipment for calibrating noise measurement apparatus and industrial laboratories (such as those in the aerospace industry) that conduct these calibrations. Previously, calibration equipment had to be sent to NIST for accuracy and noise floor evaluation, or users had to rely on a manufacturer's specifications. Comparisons of measurement systems in different laboratories using commercially available oscillators as transfer standards were limited to a typical repeatability of plus or minus 3 dB. The accuracy of the portable standard for both PM and AM noise is plus or minus 0.14 dB. Additionally, the temperature coefficient is less than 0.02 dB/K and the stability is better than 0.4 dB over 1 year. A patent is pending for this new standard. A paper, number 35-92, describing the standard is available from Jo Emery, Div. 104, NIST, Boulder, CO 80303, (303) 497-3237.

"SUPERCONDUCTIVITY REPORT" NOW AVAILABLE ON VHS

A new videotape, "Superconductivity: A Report from NIST," which highlights NIST research in both high- and low-temperature superconductivity, was recently released. The 12 min tape describes the two goals of the superconductivity program: to establish techniques and standards for characterizing superconducting materials, and to use these materials in advancing the art of electrical measurements and standards. VHS copies are $12 (shipping included) and may be purchased from Video Transfer Inc., 5709-B Arundel Ave., Rockville, MD 20852, (301) 881-0270.

TWO VIEWS OF PROTEIN PUZZLES PROVE BETTER THAN ONE

Protein molecules are like giant puzzles that scientists solve with one of two methods: showering laboratory-grown protein crystals with x rays or placing dissolved proteins in magnetic fields to get a picture of where individual atoms lie. While both techniques are very useful, scientists find discrepancies between the crystal and solution models, and, therefore, have not previously integrated the two methods. But a new study by the National Institutes of Health and the Center for Advanced Research in Biotechnology (CARB) shows for the first time that combining data from both techniques can produce clearer pictures of protein structures than is obtainable by either single method. To achieve this conclusion, scientists at NIH and CARB pooled data from studies of interleukin-1 beta, a lymphokine that stimulates the body's immune response. Their work, described in the Aug. 14, 1992, issue of Science, opens a new door for accurately solving the structures of large biological molecules. CARB is operated jointly by NIST and the University of Maryland.

NEW BIOSENSOR CONSORTIUM SEEKS MEMBERS

Biosensors are small electronic devices that use biological molecules (such as enzymes, antibodies, antigens or nucleic acids) to detect a specific substance. Industry and government scientists are teaming up to hasten the development of advanced biosensors that could change dramatically the laboratory analysis of medical, environmental, and industrial samples by the end of the century. More than a dozen companies are joining NIST in the Consortium on Advanced Biosensors (CAB). To meet CAB's goal of fostering biosensor development and commercialization, the consortium will support generic research projects to solve the common problems biosensor producers face. For more information, contact Howard Weetall, Biosensor Technology Group, A353 Chemistry Building, NIST, Gaithersburg, MD 20899, (301) 975-2628, fax: (301) 330-3447.

NIST/INDUSTRY TO STUDY CRYPTOGRAPHY INFRASTRUCTURES

NIST and a private company are investigating the merits and cost implications of various infrastructures that will support planned federal cryptography standards. There are several possible alternatives for such infrastructures, elements of which include support organizations, distribution systems, directory services and message authentication. NIST's proposed Digital Signature Standard (DSS), which allows users to "sign" an outgoing message digitally and verify signatures in incoming messages, requires such support. Before DSS technology can become operational, a sound infrastructure must be implemented to ensure efficient, secure use of resources for government agencies and the public customers they serve. The NIST/industry study aims to identify the best and most cost-effective infrastructure alternatives. Numerous government agencies, including the U.S. Postal Service, the Internal Revenue Service, the Federal Bureau of Investigation and the Defense Department, support the infrastructure study.

STANDARDS NEEDS ON DIAMOND FILMS CITED

Foremost among conclusions from a recent NIST workshop on diamond films is the need to characterize methods so that experimental data, measured at different sites by different workers, may be meaningfully compared. At the meeting, producers and potential users of diamond films made by chemical vapor deposition methods, focused on two technical topics: measurement of thermal conductivity or thermal diffusivity for heat dissipation applications, and measurement of mechanical properties of diamond for cutting tools. Researchers gave presentations on topics relevant to commercial applications, and companies described their needs for standards. The workshop was held in response to a recommendation in a NIST report assessing diamond technology in Japan (Workshop on Characterizing Diamond Films, NISTIR 4849) that called for increased information exchanges among members of the U.S. diamond community. NISTIR 4849 is available for $19 prepaid from the National Technical Information Service, Springfield, VA 22161, (800) 553-6847. Order by number PB 92-205426.

CRITICAL TECHNOLOGIES DOMINATE ATP PROPOSALS

The NIST Advanced Technology Program (ATP) received 140 proposals for the first of two recently announced competitions, according to program officials. Nearly half of the proposals were for research on advanced materials or electronics. Significant numbers of proposals in manufacturing, information technology and computing, energy technologies, biomedical and biotechnology, and chemistry also were logged. The ATP funds research on generic, precompetitive technologies with the potential to enhance the competitiveness of U.S. industry. A second ATP competition will accept proposals from Jan. 25, 1993, to Feb. 24, 1993. An estimated $15 million to $20 million will be available for ATP awards in each competition. Full application packages are available from the Advanced Technology Program, A430 Administration Building, NIST, Gaithersburg, MD 20899, (301) 975-2636.

EXPLORING MATH AND MANUFACTURING IN THE CLASSROOM

Mathematics teachers say awareness of their subject's practical value needs to grow. Meanwhile, manufacturers maintain that technical pursuits do not receive adequate emphasis in U.S. schools. "Technology Learning Modules" being developed by a NIST mechanical engineer working with a software firm, aim to respond to both concerns. Intended initially for seventh- and eighth-graders, the lessons begin with students sketching out part designs on graph paper and end with computer programs that instruct a tabletop milling machine to make wax renderings of the children's creations. In between, students explore and use mathematical concepts, as well as experiment with 3-D computer modeling and design programs that rival the graphic capabilities of even the best video games. Still in the prototype stage, the modules were evaluated this summer by four Washington, DC-area teachers and could be ready for a trial run in classrooms by late fall. "Technology Learning Modules" for high-schoolers are in the works. For more information, contact Denver Lovett, Rm. 136 Shops Building, NIST, Gaithersburg, MD 20899, (301) 975-3503.

MOBILE MACHINERY GROUP DEFINES STANDARDS ISSUES

Private-sector panelists at a recent workshop co-sponsored by NIST and the Equipment Manufacturers Institute identified several important issues to U.S. industry as they relate to international standards development and conformity assessment. This was the fourth in a series of meetings to determine how the Federal government can increase U.S. industry acceptance within other markets such as the European Community (EC). Panelists cited the following needs: mobile machinery technical standards need international harmonization, information on EC standards and directives needs to be disseminated adequately in the United States, U.S. regulatory bodies should harmonize their regulations with EC directives, U.S. public and private sectors must adopt international standards whenever possible, and improved coordination is needed between the public and private sectors in developing U.S. positions on EC 92 issues. The report, Conformity Assessment Workshop: Mobile Machinery (NISTIR 4853), is available from the National Technical Information Service, Springfield, VA 22161, (800) 553-6847 for $26 (print) and $12.50 (microfiche) prepaid. Order by PB 92-205368.

PROPOSALS SOUGHT FOR PRECISION MEASUREMENT GRANTS

NIST is seeking project proposals for its 1994 Precision Measurement Grants. The grants are for $50,000 for 1 year, and may be renewed for up to two additional years. Prospective candidates must submit summaries of their proposed projects and biographical information to NIST by Feb. 1, 1993, to be considered for the current grants, which will run from October 1993 through September 1994. NIST's Precision Measurement Grants are awarded each year to scientists in U.S. academic institutions for work in determining values for fundamental constants, investigating related physical phenomena, or developing new, fundamental measurement methods. For further information, contact Barry N. Taylor, B160 Physics Building, NIST, Gaithersburg, MD 20899, (301) 975-4220.

SECURITY TRAINING COMPENDIUM AVAILABLE FROM NIST

As part of its mandate under the Computer Security Act of 1987, NIST has issued a catalog of computer security training and awareness courses available from a variety of vendors nationwide. The document lists hundreds of courses aimed at executives, managers, security and audit personnel, ADP management and operations, and end users. Course subject categories include computer security basics, security planning and management, contingency planning, computer security policy and procedures, and systems life cycle management. Course topics range from disaster recovery to auditing fraud to detecting and preventing viruses. Computer Security Training & Awareness Course Compendium (NISTIR 4846) is available on-line through the NIST computer security bulletin board by dialing (301) 948-5717 or (301) 948-5140 (9600 baud only).

FIFTEEN INVENTIONS NOW AVAILABLE FOR LICENSING

NIST recently announced that the following 15 government-owned inventions are now available for licensing:

- Method for Production of Predetermined Concentration Graded Alloys (Docket No. 86-001);
- Predetermined Concentration Graded Alloys (Docket No. 86-008);
- Ultrasensitive Force Detector Employing Servo-stabilized Tunneling Junction (Docket No. 87-026);

- A Method for Making Single Crystals (Docket No. 88-022);
- Process for the Preparation of Fiber-Reinforced Ceramic Matrix Composites (Docket No. 88-044);
- Tunnel-Stabilized Magnetic Reading and Recording (Docket No. 90-002);
- Matrix Modification in the Electrophoretic Separation of Nucleic Acids (Docket No. 90-014);
- Method and Apparatus for Assessment of Surface Smoothness Using Reflected Energy (Docket No. 90-016);
- Localized Plasma Processing (Docket No. 90-021);
- Hard X-Ray Magnification Apparatus and Method with Submicrometer Spatial Resolution of Images in One, Two or Three Dimensions (Docket No. 90-038);
- Azeotropic Refrigerant Comprising Bis-(Difluoromethyl) Ether and 1,1,2-Trifluoroethane (Docket No. 91-003);
- Two-Dimensional, Josephson-Array, Voltage-Tunable, High-Frequency Oscillator (Docket No. 91-005);
- Object/Anti-Object Neural Network Segmentation (Docket No. 91-011);
- Apparatus and Method for Evaporative Concentration of a Liquid Sample (Docket No. 91-012); and
- Calibration System for Determining the Accuracy of Phase Modulation and Amplitude Modulation Noise Measurement Apparatus (Docket No. 91-014).

For technical and licensing information on these inventions, contact Bruce E. Mattson, B256 Physics Building, NIST, Gaithersburg, MD 20899, (301) 975-3084.

NIST AND AUTO INDUSTRY COOPERATE ON WELDING RESEARCH

To assist industries that use welding, NIST has developed arc current/voltage signal monitoring systems and arc diagnostics software to improve the control of automated gas metal arc welding. Recently, a research associate from an automobile manufacturer spent 6 months working with NIST researchers to learn about this welding technology hardware/software, study weld droplet transfer characteristics, and determine how NIST's weld-sensing strategies might be applied to automotive exhaust system (catalytic converter) manufacturing processes. The manufacturer hopes that a welding research laboratory similar to NIST's can be set up at its research center. The Cooperative Research and Development Agreement (CRADA) under which this program operates is expected to be a model for future cooperation between NIST and other industrial partners in the field of welding research.

NIST TO LEAD DEVELOPMENT OF NEW IEEE STANDARD FOR POWER-FREQUENCY FIELD-MEASURING INSTRUMENTS

A NIST scientist will lead the development and drafting of a new document for specifications of instruments for measuring electric and magnetic power-frequency fields.

The IEEE activity responds to increasing societal interest in the effects of power-frequency and power-frequency harmonic electric and magnetic fields and new interest in the measurement of these fields in practical environments, such as in homes, in business and industry, and in transportation systems. A number of instruments having a range of capabilities have been developed and marketed for carrying out these measurements, but at present there are no standards prescribing specifications for instrumentation used in the various environments. The Magnetic Fields Task Force and the Subcommittee 1 working group will jointly prepare the draft of the proposed standard P1308, "Recommended Practice for Instrumentation: Specifications for Electric Field Strength and Magnetic Flux Density Meters—10 Hz to 2 kHz." The resulting draft standard will be submitted to the IEEE Standards Board.

NIST SCIENTIST SHARES PATENT AND R&D 100 AWARD ON DIAMOND-TURNING OF FERROUS METALS

A NIST scientist along with two co-workers at Los Alamos National Laboratory (LANL), has been awarded a U.S. patent for a process for diamond-tool machining of materials that react with diamond. Development of the long process allows diamond turning of mirror-like surface finishes on ferrous materials. One application is direct machining of stainless steel to optical-quality tolerances as molds for aspheric lenses. In the process, controlled cryogenic cooling of the tool post and workpiece prevents detrimental temperature-dependent chemical interaction of the workpiece material with the carbon in the diamond cutting tool. The process has been named a winner of the 1992 R&D 100 Award.

NON-METHANE ORGANIC COMPOUND GAS STANDARDS DEVELOPED TO SUPPORT ATMOSPHERIC MEASUREMENTS OF AUTO EMISSIONS

Scientists at NIST have developed a series of gas mixtures consisting of trace level concentrations of 15 different organic compounds in nitrogen. The compounds are constituents of automobile exhaust and have been identified as reactants in the formation of ozone. The standards are difficult to produce since some of the reference compounds are gases under normal conditions, and others are liquids. To prepare these standards, scientists had to develop a procedure to quantitatively weigh and blend numerous substances in two different physical states, gas and liquid, into one complex mixture so the amount of each substance could be determined with an uncertainty of 1 percent. These standards are also difficult to analyze since the concentration levels are low, approximately 5 ppb (0.0000005 percent), and the analyzers are not sensitive enough to directly detect the substances. Therefore, the organic constituents in the samples had to be preconcentrated, and parameters such as cryogenic temperature and substrate material needed to be optimized for both the gaseous compounds and the liquids.

These standards allow scientists to better understand and follow the complex atmospheric chemistry of ozone formation. Ozone at high altitudes is essential to regulating the Earth's atmosphere. However, ozone at ground level is a pollutant that adversely effects human health and is a major contributor to plant and crop damage. Ground-level ozone is formed by complex interactions involving hydrocarbons, oxygen, and sunlight, and is one of the constituents of photochemical smog. Current concern with high pollution levels has caused environmental agencies to embark on studies to determine sources and levels of pollutants so they can recommend remediation steps and measure whether these steps are effective. The standards developed at NIST contain the hydrocarbon compounds involved in the reactions to form ozone and will calibrate instruments used to accurately measure these components in the atmosphere.

CARBONYL SULFIDE MEASURED IN AUTOMOTIVE EMISSIONS USING TUNABLE DIODE LASER ABSORPTION SPECTROSCOPY

Carbonyl sulfide (COS) is the most abundant gaseous sulfur species in the Earth's unpolluted atmosphere. This gas is believed to be the primary precursor of the stratospheric aerosol sulfate layer during non-volcanic time periods. Modeling studies have raised the concern that long-term perturbations to this layer from increasing COS emissions could significantly influence the Earth's radiative budget and climate through increased solar scattering. The possibility of increased heterogenous reactions on such aerosols also may increase stratospheric ozone destruction.

COS measurements were made over several years both at NIST and at the National Center for Atmospheric Research (NCAR) in Boulder, CO. Groups at both locations used tunable diode laser absorption spectroscopy because of its high selectivity and sensitivity for detecting COS. Measurements were made on ambient COS as well as on the emissions of numerous automobiles, both gasoline and diesel powered. The measurements at NIST were made using the P(24) or P(25) transition in the 100-000 band of COS. The primary technique used was to split a portion of the infrared beam off to a line locking cell (containing COS) and use a first derivative frequency lock. The majority of the beam was passed through a long path multipass cell (up to 200 m) and detected in the second derivative mode. The measurements were calibrated using low COS emitting permeation devices. The determined value of COS in clean ambient air was 500 ± 10 ppt ($1 \text{ ppt} = 1 \times 10^{-12}$). Measurements of automobile emissions of COS made both at NIST and NCAR, ranged between 2 and 300 ppb ($1 \text{ ppb} = 1 \times 10^{-9}$). Based on NCAR data concerning the average emission of the vehicles studied (about 50 ppb), and the total number of automobiles and trucks (about 200 million worldwide), the increase to the atmospheric budget per year from automobile and truck emissions will not exceed 0.1 percent of the global concentration of 500 ppt.

GOLD-PLATINUM THERMOCOUPLES: A NEW HIGH-STABILITY, HIGH-ACCURACY INDUSTRIAL TRANSFER STANDARD

Scientists at NIST recently completed a study of the stability of gold-platinum thermocouples to determine their applicability as accurate and rugged secondary reference thermometers, and as transfer standards at temperatures up to 1000 °C. This effort includes the determination of a new, highly accurate reference function based on the International Temperature Scale of 1990. The thermocouples were fabricated from 0.5 mm diameter wires of the highest purity material commercially available. These thermocouples were determined to be stable to within 0.016 °C when heated for 1000 h at about 965 °C. This is an order of magnitude improvement over the stability of currently available reference standard thermocouples (types S, R, and B), and is at least 10 times better than the stability of industrial platinum resistance thermometers at temperatures above 550 °C. These thermocouples also compare favorably with high-temperature standard platinum resistance thermometers at temperatures above 900 °C. This type of thermocouple will be useful for measuring and controlling temperature in semiconductor production, for determining the efficiency of gas turbines used by the electric utilities, for aerospace applications, and for general laboratory and industrial use.

This work was reported to the scientific and industrial community at the recently held Seventh International Symposium on Temperature.

DARK-STATE VIBRATIONAL QUASI-CONTINUUM PROBED WITH MOLECULAR "SEARCHLIGHT" TECHNIQUE

As part of a project to develop new methods for studying energy migration and transfer in medium to large sized molecules, NIST scientists have discovered a novel method of using an electric field to tune a spectroscopically accessible "bright" state across a wide range of inaccessible "dark" states belonging to the vibrational quasi-continuum. This new method is in some ways analogous to sweeping through a dark sky with a searchlight until the desired objects are lit up by reflected radiation and come into view. The method will permit a much more controlled study of the vibrational continuum, including the transition from Poisson statistics to Wigner statistics which is involved in the passage of vibrating molecular systems from periodic to chaotic motion. The present observations also help explain the unexpected "disappearance" of electrical polarity (i.e., the electric dipole moment) in excited vibrational states embedded in the quasi-continuum. Further experiments are being carried out to determine the full potential of this new method, particularly the relationship of these measurements to the reaction dynamics of highly excited molecules.

MAGNETISM IN NANOMETER-SIZED IRON PARTICLES

The dynamics of domain rotation in single-domain particles can be much faster than in materials where this process is dominated by domain-wall motion. This domain switching by coherent rotation has potential applications for high-speed data storage media. A collaborative research effort between the neutron scattering group at NIST and Johns Hopkins University has prepared nanometer-sized iron particles embedded in alumina, so that the interparticle magnetic interactions are very weak. Small-angle neutron scattering has characterized this material as having a mono-dispersed particle size distribution with the average particle size at about 4 nm. This is well below the critical size for single domain formation and allows detailed studies of the dynamics to be performed. Recent inelastic neutron scattering results suggest that the spins at the surface of the nanometer-sized iron particles tend to become thermally disordered with increasing temperature, while the interior spins remain ordered. Future high resolution inelastic scattering studies at the CNRF are expected to measure the coherent single-domain fluctuation times and to determine the influence of surface melting and anisotropy on the domain fluctuation process.

THIRD INDUSTRY WORKSHOP IDENTIFIES CHALLENGES FOR IMPROVED POLYMER COMPOSITE PROCESSING

A group of 22 industry experts, representing companies that make or use polymer composites, gathered at NIST to review the NIST program in composite processing and to identify the important scientific and technical barriers preventing more cost-effective fabrication with these materials. The attendees represented automotive, aerospace, and electronic companies, as well as organizations involved in the supply, design, and manufacture of materials. The group expressed strong support for the NIST program and its priorities, particularly the emphasis on liquid molding which the two previous NIST workshops had identified as a most important fabrication method for the future. These experts then identified four critical issues where advances are needed: process monitoring and control technology, knowledge and control of the fiber-matrix interface, recycling, and standardized test methods and data reporting procedures (databases). In the area of liquid molding, they identified two topics as particularly critical: mold filling and preform preparation. Mold filling was singled out because of the need for both improved process simulation models and better characterization data for input to these models. Attendees considered better preform technology as critical to reduce the time required for preform preparation and improving reliability. The workshop's conclusions will guide the NIST program in composite processing.

PULSED LASER DEPOSITION OF NANOCOMPOSITE THIN FILMS

Nanocomposite magnetic thin films of Ag-Fe_3O_4 have been prepared by researchers at NIST using, for the first time, a pulsed laser deposition technique. Initial results were presented at a special laser materials processing symposium of the Materials Research Society. Depending on the processing conditions, the films exhibited either ferromagnetic or superparamagnetic behavior. The films were formed by condensation of vapors generated by excimer laser excitation of Ag-Fe_3O_4 targets. The composition of the laser induced vapor plumes was determined using molecular beam mass spectrometry, in conjunction with optical emission spectroscopy. Both neutral and ionic species were found to be present. The plume composition was found to correlate well with that of the target. A uniform target stoichiometry was found to be crucial to the successful deposition of a nanocomposite structure, which was verified using Mössbauer spectroscopy. Currently, correlations are being made between the plume species temporal and spatial distributions and the film's stoichiometry, morphology and magnetic properties for the purpose of modeling and optimizing the deposition process.

GAS-COUPLED ACOUSTIC MICROSCOPE

The first images were obtained with a high-pressure, gas-coupled, transmission, scanning, acoustic microscope that was designed and built by NIST. The gas-coupled system enables high-resolution ultrasonic inspection of complex material systems such as electronic packages without the need for immersion in a liquid. Images of a ceramic lead frame were obtained at 20 MHz in nitrogen gas at 3 MPa. The use of high pressure reduces acoustic losses to a manageable level (50-60 dB). A resolution of 25 μm was achieved; however, lens improvements and higher frequencies offer promise of improving resolution tenfold. The novel system consists of a pressure chamber (30 cm diameter, 60 cm long); a precision (±0.05 μm) computer-controlled, six-axis, sample stage; impedance matched transducers; and associated electronics.

HIGH-RESOLUTION EXPERIMENTAL MECHANICS BY E-BEAM MOIRÉ

The resolution of strain measurements has been improved fivefold at NIST by using a scanned-electron-beam moiré technique. This new method uses electron-beam lithography to write a grating of regularly spaced lines at a density of 10 000/mm on a flat, sensitized specimen surface. The specimen is loaded mechanically under the scanning electron microscope. Moiré fringes of high contrast are produced in the SEM image when the pitch of the raster scan nearly matches the pitch of the line grating. One fringe corresponds to a relative displacement of 100 nm.

In the first study, deformation at the interface between plies of longitudinal and transverse fibers in a fiberglass-epoxy composite was examined under tensile loading. Next, NIST will use this technique to study the mechanical behavior of interfaces in various fine-scale interconnect structures found in electronics packaging, for example, the plated-through-hole structure commonly used in printed wiring boards.

NON-INTRUSIVE TECHNIQUE DEVELOPED FOR SURFACE COOLING STUDIES

NIST scientists have developed an infrared thermographic technique to study surface cooling induced by the evaporation of an impinged droplet. This is a first step in better understanding the reduction in the burning rates of materials as they are subjected to sprays of a fire suppressant. In the study, a single drop of purified water is reproducibly deposited on a cleaned ceramic surface of known initial, elevated temperature. Digitization of time-dependent 2D video imaging of the surface provides data on the difference in the radiance level between a reference surface of known emissivity and temperature and the unknown target surface of interest. Calibrations against point surface probes indicate agreement of 1–2 °C. Typical results show a sharp temperature drop in the initial portion of the evaporative transient. Such an induced thermal stress can affect the material's physical characteristics and even its local structural integrity. The method, including typical results, appears in Experimental Thermal and Fluid Science **5**, 136–141 (1992).

NIST DEVELOPS FINGERPRINT CLASSIFICATION SYSTEM FOR THE FEDERAL BUREAU OF INVESTIGATION (FBI)

NISTIR 4880, Massively Parallel Neural Network Fingerprint Classification System, describes an automated system for fingerprint classification that uses image-based, ridge-valley features; Karhunen Loeve (K-L) transforms; and neural networks to perform pattern-level classification. On a massively parallel computer, the system achieves a speed of classification of 0.54 s per fingerprint and is capable of 88 percent classification accuracy with 10 percent rejects. As part of the FBI-sponsored development activity, a sample of 4000 fingerprints (2000 matched pairs) was collected and publicly released as NIST Special Database 4.

Neural networks have had the potential for massively parallel implementation for some time, but system-level, image-based applications employing neural networks have been realized only recently due to the complex requirements for an image system, including image isolation, segmentation, and feature extraction as well as recognition. The NIST developed system uses two neural-network-based methods for feature extraction and classification. Researchers used the K-L technique for feature extraction; this is a self-organizing method that uses no class information to select fingerprint characteristics. The image processing prior to classification takes more than 99 percent of the total processing time, while classification requires only 0.03 percent of the system's time.

RASTER GRAPHICS VALIDATION PROGRAM DEVELOPED

In support of the Department of Defense's Computer-aided Acquisition and Logistics Support initiative, NIST has been developing conformance testing programs for various standards including raster graphics conformance testing. NISTIR 4848, Raster Graphics Validation, describes the guidelines for establishing and managing raster graphics validations, which include conformance testing and, when conformance is demonstrated, the issuance of a certificate of validation. The publication provides policies, procedures, and general information needed to establish a conformance testing program for FIPS 150, Facsimile Coding Schemes and Coding Control Functions for Group 4 Facsimile Apparatus, a planned FIPS (Open Document Architecture [ODA] Raster Document Application Profile [DAP]), and related DoD standards and specifications. Federal agencies may specify raster graphics validation as a part of their procurement requirements.

HARDWARE DESCRIPTION LANGUAGE APPROVED AS FIPS

The Secretary of Commerce has approved FIPS 172, VHSIC Hardware Description Language (VHDL), for federal agency use. To be effective Dec. 31, 1992, FIPS 172 adopts American National Standard Hardware Description Language VHDL (ANSI/IEEE 1076-1987), which specifies the form and establishes the interpretation of programs expressed in VHDL. The new standard will promote the portability of VHDL programs for use on a variety of data processing systems.

VALIDATED PRODUCTS LIST EXPANDED

NIST has expanded the scope of its Validated Products List (VPL) which identifies information technology products tested for conformance to various FIPS in accordance with NIST's conformance testing procedures. Conformant products are issued a current validation certificate or a registered test report.

The expanded VPL includes computer language processors for programming language Ada, C, COBOL, Fortran, MUMPS, Pascal, and database language SQL; computer graphics implementations for Graphical Kernel System and Computer Graphics Metafile; operating system implementations for POSIX; open systems interconnection implementations for GOSIP; and computer security implementations for the Data Encryption Standard, the Message Authentication Code, and Key Management.

The testing of products to assure conformance to FIPS may be required by federal agencies in accordance with the FIPS, Federal Information Resources Management Regulations (FIRMR), and the associated Federal ADP and Telecommunications Standards Index issued by the General Services Administration. The VPL is updated and published quarterly; the current version is NISTIR 4871, Validated Products List 1992 No. 3, dated July 1992.

GUIDANCE ON COMPUTER SECURITY TRAINING PUBLISHED

NISTIR 4846, Computer Security Training & Awareness Course Compendium, assists federal agencies in locating computer security training resources nationwide. The publication is a compilation of information on training courses supplied by the vendors of the courses. Target audiences for training include executives, managers, and users. Requirements to conduct computer security training and awareness activities are mandated under the Computer Security Act of 1987.

77TH NATIONAL CONFERENCE ON WEIGHTS AND MEASURES MEETS IN NASHVILLE

The 77th Annual Meeting of the National Conference on Weights and Measures (NCWM), which is sponsored by NIST, was held in Nashville, Tenn., July 19–23. The meeting was attended by 316 delegates, including voting delegates representing 42 states, the District of Columbia, Puerto Rico, and the U.S. Virgin Islands. The status of EC 92 from the perspectives of Germany and the United Kingdom was provided. Canada's Legal Metrology Branch participated in substantial portions of the technical committee work.

The conference:

- established a Petroleum Subcommittee under the Laws and Regulations Committee to focus on issues relating to petroleum and motor fuels;
- adopted a new section on Home Food Service Sales Plans for inclusion in the Uniform Method of Sale of Commodities Regulation. The new section establishes requirements for the sale of any food item or items, alone or in combination with nonfood products or services, in a consumer's home; formed a Metric Working Group under the Laws and Regulations Committee to help guide NCWM response to recent amendments made to the Fair Packaging and Labeling Act;
- postponed voting on a proposal to establish minimum criteria for electronic audit trails used in connection with weighing and measuring devices;
- exempted certain scrap commodities from NIST Handbook 44 requirements for minimum net load to be weighed on a vehicle scale; the exemption permits smaller loads of scrap to be weighed on vehicle scales and, consequently, will reduce expensive handling costs and help to keep down the costs of recycling; and
- adopted a certification program for trainers participating in the conference's National Training Program for weights and measures officials.

NIST TRANSFERS MEASUREMENT EXPERTISE TO POWER ELECTRONICS INDUSTRY

Recent activities at NIST have resulted in three transfers to industry of NIST-developed methods of characterizing and modeling power electronic devices, in one case resulting in the development of a commercial product. A private company has announced the introduction of a power device thermal test system based upon measurement procedures developed by NIST scientists.

In the second transfer, a NIST scientist provided consultation for a private company which is interested in applying his work to industrial and commercial motor control systems. The NIST scientist presented a half-day tutorial on insulated-gate bipolar transistor (IGBT) modeling, circuit simulation, and parameter extraction. The IGBT is a significant device for applications such as motor control. As a result of his visit, company members expressed interest in supporting NIST work relating to a new class of power device, the metal oxide-semiconductor controlled thyristor.

In the third instance, a seminar was presented on the NIST power device and thermal characterization work. The private company is developing power integrated circuits for aerospace and automotive applications. One of the goals is to develop a compound semiconductor-on-silicon process using wafer-bonding techniques in order to fabricate electro-optic devices.

NIST ASSISTS INDUSTRY WITH MEASUREMENTS OF MEDIA AND HEADS FOR HIGH-DENSITY MAGNETIC RECORDING

A NIST scientist has used the recently acquired atomic force microscope (AFM) to help a private company in a study of the friction properties of high-density storage magnetic hard disks. These disks are of polished aluminum with the magnetic media applied in a spin-coating step; the resulting roughness of such a disk is in the range of 30 nm. The drive for increased storage density of hard disks leads to smaller bit sizes and, consequently, reduced distance between the head and disk. The reduced spacing (known as flying height) in turn increases the likelihood of direct contact between the head and the disk (head crash). To make a head crash less disastrous, private companies are applying very thin films of a lubricating material; for example, in the past a few tenths of a nanometer of sputtered carbon have been used. The private company is investigating both the use of lubricants and the effects of surface texture; the NIST scientist has used the AFM to image the surfaces of specimen disks that have different observed friction qualities, including disks with and without the lubricating layer. Radial line scans of the surface provide a measure of roughness that can be correlated with disk performance. The NIST scientist also has provided AFM images of the insulating gap between pole pieces from a thin-film head; the resulting measurement of 0.25 μm is in good agreement with other methods. NIST and the company are considering a joint paper describing the work to date; future interactions with the company are likely to involve studies of disk and head topography and their magnetic signatures.

NIST HELPS ASSURE LOTTERY FAIRNESS

The mass group examined the weight of 430 ping-pong balls used by the Federal Communications Commission (FCC) to issue new licenses. With the rapid growth in communications, lotteries are conducted by the FCC as an unbiased means to give the public access to new opportunities in cellular phone communications, cable TV, and low power TV ventures that create about $1 billion worth of new business each year. The ping-pong balls are used by the FCC field offices as mechanical random number generators for lottery drawings and arrived at NIST as 17 discrete sets. NIST provides the data that give the FCC assurance that the within group weight variation is within acceptable limits.

ROBOT CHAUFFEUR

Using a video camera on the windshield and motors attached to the steering wheel, brake, and throttle, control computers are driving a vehicle along NIST's roads. This work is being performed by NIST and Florida University in support of the Department of Transportation's Intelligent Vehicle Highway System and the Department of Defense's Robotic Testbed programs. The goal is to increase highway safety, increase traffic flow, and reduce driver workload, if not replace him altogether.

The primary challenge in autonomous driving is to detect and locate the road, other vehicles, and obstacles. The system must be quick to allow high-speed driving and must be reliable under extreme variation in outdoor conditions.

The current system uses the following steps to track the painted stripes on the road and steer the vehicle along the center of the lane: First, edges are extracted from the video image. Edges occur where the brightness of the image changes, such as where the image changes from the gray road to the white stripe. Then, two quadratic curves that represent each lane boundary as it appears in the video image are updated. The system computes the coefficients of the curves using a recursive least-squares fit that filters out edges caused by shadows and other image noise. Finally, the steering wheel angle that steers the vehicle along the center of the perceived lane is calculated by steering an amount proportional to the horizontal position of the lane at a given distance in front of the vehicle. This process cycles at 15 Hz and can drive the vehicle at 40 km (25 mph) in bright sunlight, cloudy days, and at night.

RATE OF KEY PHYSIOLOGICAL REACTION DETERMINED

NIST scientists have determined the rate constant and reaction product for the key physiological reaction of nitric oxide, NO, with the superoxide anion, $O_2^{-\cdot}$. Previous studies had concluded that the reaction was too slow to be of physiological importance in biological systems. The results of this study, soon to appear in Free Radical Research Communications, demonstrate that this reaction is very fast and could be biologically significant.

The NIST work showed that this rapid reaction leads to the formation of the unstable species peroxynitrite ($^-$OONO), which then decomposes to produce highly reactive free radicals. This finding is significant because the relatively unreactive O_2^- species generates a highly reactive product radical that may be of considerable physiological importance in the cell-killing activity of macrophages and neutrophils, which are key defense mechanisms in the body.

NIST PARTICIPATES IN X-RAY BEAMLINE DEVELOPMENT AT THE ADVANCED PHOTON SOURCE

A NIST scientist recently participated in a workshop for the Synchrotron Radiation Instrumentation Collaborative Access Team at Argonne National Laboratory. The workshop's purpose was to lay out the initial design principles for x-ray beamlines that will be built at the newest synchrotron light source under construction, the Advanced Photon Source.

The Advanced Photon Source will ultimately be the national facility for experiments that require intense high energy x-ray beams, such as for x-ray diffraction. The collaborative access team (known as CAT) is a consortium of scientists from academia, government, and industry laboratories who have joined forces to submit a funding proposal to build a series of beamlines at the synchrotron light source when it comes on line in 1997. The initial proposal from a smaller number of scientists interested in x-ray physics was combined with proposals from several groups with related interests at Argonne National Laboratory to create the CAT, which encompasses a total of six beamlines, one of the largest collaborative efforts so far. The beamlines will be dedicated to research on high resolution x-ray spectroscopy, materials microanalysis, x-ray diffraction, and x-ray optics.

The NIST scientist will coordinate the design of a beamline dedicated to x-ray diffraction and efforts to use x-ray standing waves to analyze the structure of interfaces and surfaces on an atomic scale.

SUBPICOSECOND PROBES OF LASER SURFACE HEATING

NIST scientists used femtosecond laser techniques to measure the coupling of visible light pulses to molecules bound to a metal surface. The measurements represent the first time-resolved characterization of electronic energy transfer between an excited solid and the molecules bound to its surface, and are critically important in determining new procedures to modify surfaces at low temperatures.

In these experiments, a clean Pt(111) crystal is prepared under ultrahigh vacuum conditions. Two laser pulses arrive at the crystal: an initial visible pulse that excites the crystal and a time-delayed infrared probe. Absorption of the visible pulse initially excites electrons in the metal, which rapidly relax and heat the crystal. When the experiment is repeated with a chemisorbed monolayer of CO (carbon monoxide) on the crystal, the high energy (261.0 meV) CO stretching vibration does not couple directly to the excited electrons. Rather, the data show that energy is transferred to the low frequency Pt-CO bending or rocking motions of the CO layer on the same time scale as thermal heating of the lattice.

Understanding and controlling the coupling of optical radiation to surface reactions is receiving considerable attention in catalysis, semiconductor processing, and solar energy conversion. Much of the current interest arises from the need to develop low-temperature processing methods, where the selective coupling of energy is used to modify the surface rather than in unwanted heating. These measurements demonstrate the potential of femtosecond laser diagnostics for tracking interface processes and determining whether they are electronically or thermally driven.

USING LASERS TO CONFINE ATOMS ON A LATTICE OF LIGHT

NIST scientists recently observed the quantized, oscillatory motion of atoms trapped in microscopic potential wells formed by interfering light beams. This kind of atomic behavior was predicted as long ago as 1968, but its observation has only recently been made possible by new techniques of laser cooling and spectrum analysis developed at NIST. Rubidium atoms are trapped and cooled using laser beams so their temperature is reduced to only a few microdegrees above absolute zero. These ultra cold atoms are then placed in a counterpropagating pair of interfering laser beams that create a periodic potential well. The oscillation of atoms in the wells creates a phase modulation of the light emitted by the atoms and appears as sidebands in the spectrum of that light. The spectrum has features almost a thousand times finer than the linewidth of the optical transition and contains information about the temperature of the atoms and their spatial distribution. At the lowest temperature of 2 μK, the atoms are localized to 1/15 of the optical wavelength. Using a different technique, workers in Paris have made similar observations.

The NIST work was described in the July 6 issue of Physical Review Letters.

BROADBAND PICOSECOND INFRARED SPECTROSCOPY OF SOLUTION-PHASE PHOTOCHEMISTRY

A long-standing goal in chemistry is to unravel the detailed mechanisms and energetics of how complex molecular reactions occur. Of particular interest is the development of experimental methods to probe directly short timescale reaction dynamics of industrially relevant chemical processes and biological functions. NIST scientists have pioneered a novel spectroscopic technique for directly monitoring energy flow in reaction intermediates and the appearance of products in real time with up to 10 fs (10^{-14} s) time resolution.

This method has been used to measure extremely rapid events, such as fragment ejection, product solvation, and vibrational energy flow in photochemical reactions of inorganic metal-carbonyl species in room temperature solution. Metal carbonyls are important because they function as homogeneous catalysts and are models for heterogeneous catalysis. Using a picosecond laser, a UV light pulse is absorbed by molecules such as $Cr(CO)_6$, $Rh(CO)_2(C_5H_7O_2)$ and $Co(CO)_2(C_5H_7)$ in

Hexane (C_6H_{14}). The appearance of products is observed with vibrational and structurally sensitive infrared time-resolved spectroscopy. A broadband IR pulse tuned to the CO-stretching region of the spectrum interrogates the excited sample, is subsequently upconverted into the visible spectral region, and dispersed onto a CCD multichannel detector. In this way, spectroscopic "snapshots" of the transient and product species are obtained. In all cases, CO fragment ejection occurs and solvated species are formed in 30 ps or less. The $Cr(CO)_5(C_6H_{14})$ product is found to contain CO bond excitation and cooling of this species takes about 100 ps. While the other two product species are not comprised of many more atoms or internal degrees of freedom, they surprisingly show no evidence for being formed vibrationally hot. Studies underway at higher time resolution should determine the position and energy content of chemical bonds in the reactants and products before and during solvation, thus leading to a fundamental understanding of the reactivity of these and related molecules.

NIST/NPL INTERCOMPARISON OF RADIANCE TEMPERATURE SCALES

An equivalency agreement for radiance temperature calibrations has existed since 1986 between NIST and the National Physical Laboratory (NPL) in the United Kingdom. This agreement states that the radiance temperature scales realized by NIST and NPL are equivalent over the temperature range of 630 to 1500 °C to within 0.3 K (one standard deviation estimate), and from 1500 to 2200 °C to within 1.0 K. For the first time since the 1971 radiometric intercomparison of ribbon filament lamp standards at 660 nm, the uncertainties stated in the equivalency agreement have been verified for the temperature range 1000 to 2500 °C.

In May 1992, NIST and NPL scientists intercompared the radiance temperature scales at 1000 nm using a commercially available near-infrared pyrometer, with modified optics and electronics, as the transfer standard. A second intercomparison, for the temperature range 800 to 2200 °C at 660 nm, using high-stability vacuum and gas ribbon filament standard lamps is planned for this fall.

NIST STRONGLY REPRESENTED AT SOLID STATE DOSIMETRY CONFERENCE

NIST researchers made substantial contributions to the 10th International Conference on Solid State Dosimetry held at Georgetown University, July 13–17, 1992. More than 200 participants from 30 countries attended. An invited paper on electron spin resonance dosimetry by a NIST scientist reviewed new trends and expanding applications in clinical radiography, bone dosimetry in nuclear medicine, the detection and analysis of irradiated foods, quality control for industrial radiation processing, investigations of radiation accidents such as Chernobyl, radiation imaging and microscopy for materials and biological studies, and dating of geological, archeological artifacts.

Other NIST contributions included an invited paper on the development of NIST alanine dosimeters for use as a reference standard; a report on radiation dose to bone in patients administered radiopharmaceuticals internally; a presentation on the high-resolution measurement of radial dose distributions around small beta-particle sources; and a poster paper on imaging and response characteristics of novel radiochromic films irradiated by electrons and proton beams. A paper by a NIST scientist raised considerable interest. It described a collaboration between NIST and private industry dealing with the development of novel bubble detectors for real-time imaging of gamma-ray and alpha- and beta-particles from low-level radioactive sources.

ANOMALIES IN RESONANCE IONIZATION MASS SPECTROMETRY MEASUREMENTS EXPLAINED

Resonant ionization mass spectrometry (RIMS) plays an important role in isotopic analysis, especially when the quantity of sample to be studied is very small. By combining the advantages of both lasers and mass spectrometers, RIMS has become a technique with high sensitivity and selectivity.

However, NIST scientists previously observed anomalous isotopic ratios of even and odd isotopes using broad-band radiation. This led to some doubts about the widespread applications of the technique. Stimulated by this observation, Lambropoulis and Lyras provided a theoretical explanation of the anomalous isotopic ratios observed in the tin transitions (286.3 nm), and predicted the dependence of this odd-even effect with laser intensity.

The effect is essentially due to the intensity-dependent nature of the atomic state from which the atom is ionized. For intermediate intensities, the atomic populations are equally distributed among the ground and excited states. Because the relative number of (degenerate) states differs from odd to even, the fraction that can be ionized is also different from odd to even. In the case of tin, the odd to even ratio is approximately 4/3.

Using a RIMS system at NIST, the odd to even responses in tin samples were examined for a range of laser intensities from 10^5 to 10^{10} W/cm^2. The results agreed well with the theoretical predictions. This result is convincing evidence that the effect is now understood physically and that the resonance ionization method can be applied with significantly improved accuracies to ultrasensitive measurements of trace elements in biological or environmental samples.

NIST DEVELOPS TRANSPORT STANDARDS FOR PHASE NOISE MEASUREMENT SYSTEMS

A NIST scientist has developed the first convenient transfer standards for testing phase noise measurement systems. Phase noise considerations have been rising in importance in radars, telecommunications, and other systems where high spectral purity of signals is critical. Its presence in signal channels degrades the spectral purity and thus the performance of the system. The scientist's measurement concept is very general and can be applied from subaudio to visible frequencies. The transfer standards operate at 5, 10, and 100 MHz and are the first systems with verifiable phase noise ever produced. The accuracy is nominally 1 dB and can be improved to 0.1 dB with special calibration. The phase noise is constant in amplitude to 0.2 dB from about 1 Hz to 10 percent of the carrier frequency. This is extremely important since most commercial phase noise measurement systems have frequency dependent errors. The system also produces a standard for amplitude noise with similar flatness and accuracy. This too is a first for this area of metrology.

Commercial systems for phase noise measurements have been available for several years, but there has been no satisfactory method for assuring that such systems were indeed giving accurate readings. User measurements with these new transfer standards could eventually be used in a measurement assurance program since the transfer standard provides for testing of the entire measurement process. The measurements are currently being offered as a special test, since evaluation of the full range of user needs has not yet been completed.

SYNCHRONIZATION INTERFACE STANDARDS FOR TELECOMMUNICATIONS NETWORKS

NIST has just completed a special "Workshop on Synchronization Standards for Telecommunications Systems." A key objective of the event was to familiarize industry representatives with new, NIST-developed measures of system performance recently adopted as standards by both U.S. industry and the international telecommunications community.

The performance measures developed for specification of phase noise in components of telecommunications systems are variations of the two-sample variance developed by NIST to deal with the nonwhite noise processes found in all clocks and oscillators. Traditional statistical measures cannot be applied to such devices. NIST developed the new measures in response to an industry request for assistance arising from a recognition that traditional industry measures could not adequately support specifications for new optical fiber telecommunications systems now entering the market.

The response of the industry to NIST work in the field has been very positive, suggesting that NIST will remain heavily engaged with the industry in this area for some time to come.

ENHANCED MAGNETOCALORIC EFFECT IN IRON-DOPED GARNET MATERIALS

A class of materials with enhanced properties for cryogenic magnetic refrigeration was developed at NIST; they show a much larger field-induced entropy change than $Gd_3Ga_5O_{12}$ (GGG), the most commonly used refrigerant material for cryogenic magnetic refrigeration. This material is the first material to confirm the results of Monte Carlo and mean field calculations which predict that materials containing superparamagnetic magnetic clusters can have significant field-induced entropy changes over a range of temperatures. The new materials are formed by replacing nonmagnetic Ga atoms in GGG with Fe atoms that interact magnetically with nearby Gd atoms. At temperatures below about 30 K, the Gd moments are thought to form magnetically aligned clusters which give rise to the enhanced magnetocaloric effect.

Currently, cryogenic magnetic refrigerators have been operated in the temperature range below ~15 K, where the specific heat of GGG is low and the field-induced entropy change is large. Under an applied field of 0.9 T, the iron-doped garnet materials exhibit a field induced entropy change that is nearly five times greater than that of GGG at 20 K, opening an avenue for development of higher temperature magnetic refrigerators having potential importance for the manufacture of liquid hydrogen in a hydrogen economy.

SMALL-ANGLE NEUTRON SCATTERING STUDIES OF NANOSTRUCTURED CERAMICS

Nanostructured powders are of technological interest because they can be processed to small-grained, fully dense ceramics that exhibit novel properties related to their unique microstructures. NIST scientists followed the microstructure evolution during sintering of nano-structured yttria using small angle neutron scattering (SANS). The results have shown that pores in the 70 nm range are clearly present in the as-pressed compacts (60-65 percent theoretical density) and in the material that had been sintered at temperatures up to 600 °C. Higher sintering temperatures produced material with increasingly larger pore sizes until, at 1200 °C, the measured scattering curve resembled that of a conventional ceramic material containing micrometer-sized pores. In contrast, compacts that had been hot-pressed (550 °C) to a higher density without sintering retained the original 70 nm pores. Further SANS studies of isochronally and isothermally sintered nanostructured yttria as well as preliminary studies of nanostructured zirconia are presently underway at the NIST Cold Neutron Research Facility. A new collaboration with a participating company in NIST's Advanced Technology Program, will result in a systematic SANS investigation of nanophase microstructure evolution during processing of extremely small-grained alumina and silicon nitride.

NIST RECOMMENDS MOISTURE CONTROL MEASURES FOR MANUFACTURED HOUSING

A NIST scientist has used his finite-difference simulation model MOIST, which predicts combined heat and moisture transfer through multilayer structures, to recommend moisture control guidelines for walls and ceiling/roofs of manufactured housing. The Department of Housing and Urban Development (HUD) is responsible for the nation's Manufactured Home Construction and Safety Standards. HUD is currently revising the standards and asked NIST to determine if changes were needed in the moisture control provisions. For controlling winter moisture accumulation in walls, manufacturers currently are allowed to install a vapor retarder at the interior wall surface, use permeable sheathing and siding, or provide an outside ventilated cavity between the siding and wall insulation.

Through yearly simulations in four cold U.S. climates, NIST found only the first practice to be effective in all climates and has recommended the others be eliminated. For ceiling/roofs, the manufacturer is required only to install a ceiling vapor retarder. Using similar simulations, NIST found that a detrimental amount of moisture accumulates in the roof sheathing of homes located in cold winter climates even with ceiling vapor retarders unless the penetrations and openings in the ceiling construction are sealed and outdoor ventilation openings are provided to the ceiling/roof cavity.

NIST AND TAIWAN COLLABORATE ON OPEN SYSTEMS INTERCONNECTION (OSI) ROUTING PROTOCOLS

In a cooperative venture with the Telecommunication Laboratories (TL) of the Directorate General of Telecommunications, Ministry of Transportation and Communications of Taiwan, NIST researchers designed and prototyped a reference implementation of and a test system for the Intermediate System to Intermediate System (IS-IS) Intra-Domain Routing Exchange Protocol. IS-IS is an OSI protocol designed to dynamically facilitate effective routing and to help provide connectionless data communications services.

Major accomplishments of the 2 year project included expediting the progression of the IS-IS protocol from a draft standard to an international standard; using a formal description technique (FDT) and developing FDT tools to automate the development of an IS-IS Protocol reference implementation; and using a FDT and NIST-developed tools to automate the development of the IS-IS Multi-Party Conformance Test System (IS-IS MPCTS). The system was used to test commercial IS-IS products for conformance to the IS-IS standard in NIST's Cooperative Routing Laboratory.

SPATIAL DATA TRANSFER STANDARD APPROVED AS FEDERAL INFORMATION PROCESSING STANDARD (FIPS)

On July 29, 1992, the Secretary of Commerce approved the Spatial Data Transfer Standard (SDTS) as FIPS 173. To be effective Feb. 15, 1993, FIPS 173 will facilitate the transfer of digital spatial data between dissimilar computer systems.

The SDTS provides specifications for the organization and structure of digital spatial data transfer, definition of spatial features and attributes, and data transfer encoding. The standard was developed through a government and industry cooperative effort headed by the Department of the Interior. In addition to serving as the national spatial data transfer mechanism for federal agencies, the SDTS is being made available for use to state and local governments, the private sector, and academia.

NEW PUBLICATION FOCUSES ON GRAPHICAL USER INTERFACES (GUIs)

NISTIR 4876, An Introduction to Graphical User Interfaces and Their Use by CITIS, describes GUIs and the options for their use within the Contractor Integrated Technical Information Service (CITIS). A GUI is a powerful tool used for simplifying a computer environment. The report provides a tutorial on the various meanings of the term GUI, describes the usefulness of GUIs, identifies problems with GUIs, and recommends that the X Window System GUI be used within the CITIS specification. The work supports the Department of Defense (DoD) Computer-aided Acquisition and Logistics Support (CALS) initiative.

CATALOG OF CODE SETS UPDATED

Federal Information Processing Standard (FIPS) 19-1, Catalog of Widely Used Code Sets, has been updated and is being published as FIPS 19-2. The catalog lists and briefly describes code sets in wide use in the United States that may be useful in federal data systems. The standard format that describes each code set specifies code characteristics, maintenance agency, source document, and other relevant data. FIPS 19-2 will assist federal agencies and other organizations in selecting appropriate code sets and in avoiding duplication.

MAINFRAME COMPUTER TAPES SUBJECT OF NEW PUBLICATION

NIST Special Publication 260-118, Calibration of NIST Standard Reference Material 3202 for 18-Track, Parallel, and 36-Track, Parallel Serpentine, 12.65 mm (0.5 in), 1491 cpmm (37871 cpi) Magnetic Tape Cartridge, focuses on the square cartridge tapes used by mainframe computers. The report describes the testing methodology, the measurement system, the procedure for selection of a Master Standard Reference tape, and the procedure for use of the Standard Reference Material.

Standard Reference Materials

ACCURATE DNA FINGERPRINTS ASSURED BY NEW SRM

To help ensure DNA profiles are as accurate as possible, NIST has developed a new quality assurance standards set, the first of its kind for forensic and medical labs. Known as Standard Reference Material 2390, it was developed at NIST with support from the National Institute of Justice. DNA profiles, also called "DNA fingerprints," are being used with increasing frequency as evidence in criminal cases involving rape or murder, in civil suits over paternity, and as "DNA dog tags" for soldiers. Eventually, the improved accuracy in DNA typing established by the SRM could make this new technology acceptable in more courtrooms. The SRM contains male and female DNA molecules extracted from living cells, as well as precut fragments of a viral DNA that can be used as a genetic ruler. It also includes tubes, each containing 3 million human cells from which DNA can be extracted and tested. SRM 2390 is available for $374 from the Standard Reference Materials Program, Rm. 205, Building 202, Gaithersburg, MD 20899, (301) 975-6776, fax: (301) 948-3730.

STANDARD REFERENCE MATERIAL 1842, X-RAY STAGE CALIBRATION BOARD

Automated x-ray inspection systems frequently are used to assure the quality of mechanical parts. Individual turbine blades destined for assembly in jet engines serve as one example.

This new SRM is intended as a reference standard for checking the operation of automated x-ray inspection systems. It is used to establish the accuracy of the X and Y stage encoders and for measuring long-term drift in the drives or encoders. It also is used to calibrate variable magnification systems. The board contains a calibrated pattern of through-thickness holes which can be imaged by the x-ray system. It is expected that various x-ray system manufacturers will develop software routines that will perform automatic evaluation of their systems and generate reports that can be used to monitor system performance.

STANDARD REFERENCE MATERIAL 676, ALUMINA INTERNAL STANDARD FOR QUANTITATIVE ANALYSIS BY X-RAY POWDER DIFFRACTION

X-ray powder diffraction long has been the primary technique for obtaining information about the crystalline structure of materials, such as ceramics. In turn, this information can be used to predict material characteristics and performance in order to select the best process for production.

The Standard Reference Materials Program announces the availability of Standard Reference Material (SRM) 676 for use as an internal standard for quantitative analysis and I/I_c determinations by x-ray powder diffraction. The SRM is composed of phase-pure alumina (corundum structure) powder that is characterized by sub-micrometer equi-axial grains that have been de-aggregated and calcined to eliminate preferred orientation effects and to ensure homogeneity. An extensive study determined the character of this material to be optimal for accurate x-ray powder diffraction intensity measurements.

Certified lattice parameters, a and c, and certified relative intensity data at various scan angles (low/high) 2θ over the scan range are given. The lattice parameter values were determined by means of the least-squares refinement of measurements from 40 peak positions. The relative intensity data were collected and processed with an algorithm that scans specific peaks for an integrated intensity measurement.

STANDARD REFERENCE MATERIAL 659, PARTICLE SIZE DISTRIBUTION STANDARD FOR SEDIGRAPH CALIBRATION

The Standard Reference Materials Program announces the availability of Standard Reference Material (SRM) 659 for calibrating and evaluating equipment used to measure particle size distributions in the 0.2 to 10 μm range. Measurement of such powders is important to the success of industries making products as diverse as Portland cement and cosmetics. The SRM's primary impact will be in the advanced ceramics industry where knowledge of the particle size distribution is necessary for process control.

The SRM is composed of silicon nitride powder that is characterized by equi-axial primary particles with a mean dimension of ~1 μm and a minimal amount of large agglomerates. Certified size distribution values are reported at five selected cumulative weight percentiles (20, 25, 50, 75, and 90) and were established with measurements generated on two x-ray sedimentation instruments.

STANDARD REFERENCE MATERIAL 2579—LEAD PAINT FILM ON MYLAR SHEET FOR PORTABLE X-RAY FLUORESCENCE ANALYZERS

Portable hand-held x-ray analyzers are being used to field test building surfaces, both interior and exterior, to identify buildings requiring lead abatement treatment. Abatement is a national priority, to reduce lead poisoning, as public health officials now recognize that serious adverse affects from lead exposure occur in children at blood levels previously believed to be safe. Most of the exposure cases originate from the home environment and are directly related to the extensive past use of lead-based paint.

The Standard Reference Materials Program announces the availability of Standard Reference Material (SRM) 2579 for checking the calibration of portable x-ray analyzers used in mandated lead screening programs. The SRM consists of a series of five color-coded mylar sheets, one a blank, and the other four coated with lead paint at different concentration levels. The lowest of these is 0.29 mg/cm^2, and the highest is 3.53 mg/cm^2. The sheets are over-coated with a lead-free lacquer to protect the surface from damage in field use.

Standard Reference Data

CHEMICAL KINETICS PC DATABASE EXPANDED

A major resource for research chemists, environmental scientists, and combustion engineers now includes information on 6900 chemical reactions with more than 20 000 individual data entries. The Chemical Kinetics Database, NIST Standard Reference Database 17, Version 4.0, is an important tool for modeling combustion systems or chemical processes occurring in the atmosphere. These data are necessary, for example, in predicting the atmospheric lifetimes of chemicals that may impact on the depletion of the Earth's ozone layer. The database provides the bench scientist with fast, easy access to information. In a few minutes, a user can examine all available data for many different reactions, compare the rates measured to their own data, generate files for inclusion in a modeling program, or produce literature citations that can be used in a word processor. NIST SRD 17, Version 4.0, is available for $390 from the Standard Reference Data Program, A320 Physics Building, NIST, Gaithersburg, MD 20899, (301) 975-2208, fax: (301) 926-0416. Owners of a previous version can update for $125.

PC DATABASE AVAILABLE ON TRANSIENT MOLECULES

NIST has expanded the personal computer (PC) database for spectroscopic information on short-lived molecules. Information on the sequence of chemical reactions is important to physical chemists, environmental researchers, combustion engineers and others concerned with complex chemical processes. The Vibrational and Electronic Energy Levels of Small Polyatomic Transient Molecules Database (VEEL), Version 2.0, now contains more than 1300 transient molecules with 3 to 16 atoms. The program has been improved from an earlier version to permit faster searches and provide more flexible formula entry requirements. The expanded VEEL database is available for $390 from the Standard Reference Data Program, A320 Physics Building, NIST, Gaithersburg, MD 20899, (301) 975-2208, fax: (301) 926-0416. Owners of a previous version can upgrade for $50.

Calendar

November 16–20, 1992

ELECTRICAL MEASUREMENT ASSURANCE PROGRAMS WORKSHOP

Location: San Diego Princess Hotel
San Diego, CA

Purpose: To provide instruction on the design and statistical quality control of calibration systems as applied to industrial standards laboratory operations. The workshop is given by the staff of the Electricity and Statistical Engineering Divisions of the National Institute of Standards and Technology.
Topics: Design and statistical quality control of calibration systems.
Format: Lectures are intermingled with computerized workshops where participants work in small groups to reinforce concepts and understanding.
Audience: Professional and senior technical personnel, particularly personnel working in electrical measurements. It is not recommended for entry-level people, unless they have a background in electrical engineering or physics. Attendees should, at a minimum, have a thorough knowledge of high school algebra.
Sponsor: NIST, National Conference of Standards Laboratories.
Contact: Norman Belecki, B146 Metrology Building, NIST, Gaithersburg, MD 20899, (301) 975-4223.

July 12–16, 1993

THIRD INTERNATIONAL CONFERENCE ON CHEMICAL KINETICS: REACTIONS IN GAS AND CONDENSED MEDIA

Location: National Institute of
Standards and Technology
Gaithersburg, MD

Purpose: To bring together scientists interested in gas and condensed phase chemical kinetics to facilitate the interchange of concepts and data, and to apply this knowledge to the solution of applied problems.
Topics: The rates and mechanisms of gas and condensed phase reactions of: carbon-centered radicals including carbenes; peroxyl radicals; hydroxyl radicals; halogen and hydrogen atoms; nitrogen-containing radicals; sulfur-centered and other radicals; metal-containing radicals; and ozone and its reaction products. These reactants are of considerable interest for industrial and environmental processes.
Format: Seven non-parallel sessions consisting of invited lectures, contributed lectures, contributed poster sessions, and general discussions.
Audience: Industry, government agencies, and academia.
Sponsors: NIST.
Contact: Robert Huie, A260 Chemistry Building, NIST, Gaithersburg, MD 20899, (301) 975-2559.

June 27–July 1, 1994

CONFERENCE ON PRECISION ELECTROMAGNETIC MEASUREMENTS – CPEM '94

Location: Clarion Harvest House Hotel
Boulder, CO

Purpose: To exchange information on a wide range of problems in the area of precise electromagnetic measurements. A number of special sessions on the fundamental constants will be held in anticipation of a new adjustment of the constants scheduled for 1995.
Topics: Direct current and low-frequency measurements; fundamental constants and special standards; time and frequency; rf, microwave, and millimeter-wave measurements; lasers, optical fibers, and optical electronics; superconducting and other low-temperature systems; dielectrics and antennas; automated measurement methods; and advanced instrumentation, including new sensors and novel measurement methods.
Format: General sessions, plenary sessions, and poster sessions.
Audience: Industry, government agencies, and academia. Emphasis is on standards activities and measurement methods.
Sponsors: NIST, IEEE Instrumentation and Measurement Society, Union Radio Scientifique Internationale.
Contact: Donald B. Sullivan, Div. 847, NIST, Boulder, CO 80303, (303) 497-3772.